Schweizerische Eidgenossenschaft
Confédération suisse
Confederazione Svizzera
Confederaziun svizra

Eidgenössisches Departement für Umwelt, Verkehr, Energie und Kommunikation UVEK
Département fédéral de l'environnement, des transports, de l'énergie et de la communication DETEC
Dipartimento federale dell'ambiente, dei trasporti, dell'energia e delle comunicazioni DATEC

Bundesamt für Strassen
Office fédéral des routes
Ufficio federale delle Strade

Contribution to the assessment of the safety and fatigue of concrete structures based on advanced in-situ measurements

Contribution à l'évaluation de la sécurité structurale et de la fatigue d'ouvrages en béton sur la base de mesures in-situ avancées

Beitrag zur Bewertung der Tragsicherheit und der Ermüdungsfestigkeit von Betontragwerken aufgrund detaillierten in-situ Messungen

École Polytechnique Fédérale de Lausanne,
Structural Concrete Laboratory

Prof. Aurelio Muttoni
Enrique Corres
Marko Pejatović

Forschungsprojekt AGB 2019/017 auf Antrag der AGB (Arbeitsgruppe Brückenbau)

December 2025 **1809**

Schweizerische Eidgenossenschaft
Confédération suisse
Confederazione Svizzera
Confederaziun svizra

Eidgenössisches Departement für Umwelt, Verkehr, Energie und Kommunikation UVEK
Département fédéral de l'environnement, des transports, de l'énergie et de la communication DETEC
Dipartimento federale dell'ambiente, dei trasporti, dell'energia e delle comunicazioni DATEC

Bundesamt für Strassen
Office fédéral des routes
Ufficio federale delle Strade

Contribution to the assessment of the safety and fatigue of concrete structures based on advanced in-situ measurements based on advanced in-situ measurements

Contribution à l'évaluation de la sécurité structurale et de la fatigue d'ouvrages en béton sur la base de mesures in-situ avancées

Beitrag zur Bewertung der Tragsicherheit und der Ermüdungsfestigkeit von Betontragwerken aufgrund detaillierten in-situ Messungen

École Polytechnique Fédérale de Lausanne,
Structural Concrete Laboratory

Prof. Aurelio Muttoni
Enrique Corres
Marko Pejatović

Forschungsprojekt AGB 2019/017 auf Antrag der AGB (Arbeitsgruppe Brückenbau)

December 2025 **1809**

Impressum

Forschungsstelle und Projektteam

Projektleitung
Prof. Aurelio Muttoni

Mitglieder
Dr Enrique Corres
Dr Marko Pejatović

Begleitkommission

Präsident
Jean-Christophe Putallaz

Mitglieder
Stéphane Cuennet
Dr Pascal Kronenberg
Dr Ana Spasojević

Antragsteller

Arbeistgruppe Brückenforschung (AGB)

Bezugsquelle

Das Dokument kann kostenlos von http://www.mobilityplatform.ch heruntergeladen werden.

Table of contents

Summary

The inspection and monitoring of reinforced concrete structures are fundamental for detecting potential problems affecting the structural safety (ultimate limits state and fatigue resistance). The final decision on whether or not to intervene is always based on the interpretation of the available data. Recent technological developments such as the Digital Image Correlation (DIC) allow to capture the crack displacements over large surfaces, thus providing a significantly larger amount of data and a more detailed information than the conventional in-situ measurement techniques. For instance, this type of innovative measurements can provide valuable information on the consequences and risks associated with the presence of abnormal cracks.

The aims of this research are:

- To verify the possibility of using DIC for short-term and long-term in-situ measurements on bridges and other engineering works;
- To verify the reliability of DIC measurement to the quantification of the internal forces in a structure (axial and shear forces in the reinforcement bars and forces carried by concrete through the cracks by aggregate interlocking);
- To contribute to the estimation of the stresses in the reinforcement based on the measurement of crack displacements to be used for a fatigue verification. This concerns the estimation of the axial force and the bending moments in the bar and their corresponding stresses due to the crack displacements. The estimation of the axial force is indirectly treated in the crack formulations, that allow to estimate the crack width as a function of the calculated stress in the bar. The estimation of the bending moment is conducted on the basis of the models developed to describe the so-called dowel action.

On this basis, the following topics are treated:

- The limits of applicability of DIC in existing structures.
- The comparison of existing tools to overcome some of the limitations of DIC.
- The improvement of the relationship between the crack opening in the direction of the bar and the longitudinal stresses generated in the bar.
- The improvement of the relationship between the crack opening in the direction perpendicular to the bar and the longitudinal stresses generated in the bar.

Limits of applicability of Digital Image Correlation in-situ

Digital Image Correlation (DIC) is a technique that consists tracking subgroups of pixels across different images. The position of the subgroups is compared with the reference image to determine the displacement field of the tracked region. The measurement system is composed of one or two cameras, their supports, a lighting system and a computer for the data acquisition. Various commercial software can be used to run the correlation. DIC measurements can be performed using a single camera (which yields planar displacements, 2D-DIC) or two cameras (which yields three-dimensional displacements, 3D-DIC). Nowadays, most applications use 3D-DIC measurement systems. For this reason, the research presented in this report focuses on 3D-DIC and will be referred to simply as DIC.

The displacement field obtained from DIC measurements can be used to determine the strain field of the studied region. In the case of reinforced concrete structures, the tensile deformations are small as the tensile strength is soon reached, leading to the formation of cracks. Consequently, the strain field measurements in cracked regions strongly depend on the crack displacements. For this reason, the strain field can be used to detect the crack pattern and crack kinematics (opening and sliding) over large surfaces. This is precisely the main advantage of DIC compared with the traditional crack measurement systems that provide unidirectional information at discrete points.

DIC measurements are known to be affected by multiple factors including the relative movements between the camera and the measurement surface, the lighting conditions or the currents of air between the cameras and the measurement surface. These influencing parameters can be reasonably well controlled in laboratory conditions. This is reflected in the high-accuracy that is obtained in applications of DIC in laboratory tests of reinforced concrete elements. Nevertheless, the conditions that can be found when performing such measurements in existing structures can differ considerably. Wind and traffic loads cause vibrations in the structure which will then affect the camera supports. For measurements in the external faces of structures, light variations can occur. For this reason, two series of tests to quantify the influence of the aforementioned parameters in the measurement uncertainty of absolute displacements were performed.

First a series of tests to characterize the influence of lighting was performed by varying the exposure time in the acquired images. This changes the brightness of the images. Since the variable lighting is a known effect, special algorithms have been developed to account for this and are available in most commercial correlation software. This was the case in the performed measurements, that show little influence of the brightness of the image within an exposure time ±50% of the ideal exposure time. However, it was observed that differences in lighting within the image lead to small variations in the measurement uncertainty. For this reason, the uncertainty in the measurement area should be evaluated before performing the measurements to determine if the expected accuracy is sufficient in all the important regions of the studied region.

A second series of tests was performed to evaluate the influence of vibrations. Identical measurements were performed on the ground in laboratory conditions, on the ground outside the building and on a footbridge. The results show that the measurement uncertainty increases for the measurements performed outside the laboratory. However, for the measurement of relative displacements between two points, the differences are not so significant.

A final verification of these findings was done by performing DIC measurements in the Chillon Viaducts. A crack near the anchorage of one of the prestressing tendons in the bottom slab of the box girder section was studied. The crack opened and closed under the passage of heavy trucks by approximately ±15 µm (0.015 mm). Two omega gauges were installed across the crack for validation of the measurements. The DIC results show good agreement with the gauge measurements with a certain variation that corresponds to the estimated measurement uncertainty.

Complementary image-based techniques for initial and long-term crack characterization

DIC measurements are accurate and versatile as they can provide information across an entire three-dimensional region of the structure. For this purpose, a series of images is compared with a reference image. A necessary condition for the correlation is that the images must be taken with the same relative position between cameras. This condition presents two limitations for the application of DIC in existing structures:

- If an existing crack is already present in the reference image, the total crack kinematics cannot be determined and the crack geometry can only be assessed if there is at least a slight modification of opening (or/and sliding) due for instance to traffic loading or temperature variations.
- The disassembly of the measurement system between inspections will invariably lead to different relative camera positions in the successive inspections. Consequently, the images of the new inspections cannot be correlated to the first inspection. Therefore, no information about the change between inspections can be obtained. The only way to achieve this would require leaving the DIC measurement system in place. This is highly inconvenient as it would require one DIC measurement system per inspected structure, including its maintenance.

To overcome these limitations, two alternative techniques are proposed. The first technique aims to characterize the initial crack based on direct detection algorithms. In a first step, the crack properties are detected from the information contained in a single image. In a second step, the detected crack lips are superposed to determine the crack kinematics. Two open-access tools have been used for this purpose. Tests have been conducted to quantify the measurement uncertainty of the crack kinematics in laboratory conditions. The results show that the crack geometry can be well characterized with an uncertainty of ±1 pixel for the crack opening and ±2 pixels for the crack sliding. The measurement uncertainty is larger than using conventional DIC. However, the only required tools are a digital camera and a computer.

The second technique aims to determine the crack displacements for long-term monitoring. The technique relies on tracking the position of markers placed on both lips of the crack. By comparing the position of the markers in successive inspections and considering one lip of the crack as reference, the markers on the other side reflect the displacements of the crack. Consequently, they can be used to determine the crack kinematics that took place between the measurements. The temperature variations have to be considered given the larger distance from the centre of the markers to the crack lips. A model to estimate the expected uncertainty based on the number of markers and their disposition is proposed. A test for of the system in laboratory conditions was performed using a four-point bending test on a small reinforced concrete beam. The marker-based technique captures the crack kinematics, giving similar results to those measured using conventional DIC. The results fall within the tolerance estimated by the uncertainty model.

A final validation of these techniques was performed in the same crack used for the validation of the short-term measurements using conventional DIC. The initial crack characterization technique could accurately detect the crack. The measured crack lip displacements were compared with the results obtained using a crack microscope and a crack ruler. The results in most points fall within the tolerances observed in the laboratory tests. In some cases, larger differences were observed. This is reasonable, as in many cases the lips of existing cracks are slightly deteriorated or eroded. A test of the marker-based technique has also been performed over half a day. The results are compared with conventional short-term DIC measurements, showing good agreement. In conclusion, the proposed techniques can be used to overcome the conventional DIC limitations with a certain increase in the measurement uncertainty.

Pull-out tests to investigate the bond stress development

Bond forces between the reinforcement bars and the concrete are a fundamental part of the cracked response of reinforced concrete elements. For this reason, an experimental programme was carried out to establish a better relationship between the local bond–slip response (obtained from short pull-out tests) and the response of medium-length anchorages. The influence of various parameters that can typically vary in common structural applications was studied, including the clear concrete cover, the casting position, the rib geometry and the lug orientation with respect to the nearest concrete surface. The tested bars were instrumented with distributed fibre optical sensors and the concrete surface tracked with DIC. A specifically designed testing frame was used to minimize the influence on the development of secondary conical cracks near the loaded end of the bar.

The influence of the concrete cover agrees with previous research. An increase of the cover increases the confinement and therefore the activated bond stresses for small slips and at the anchorage resistance. The failure mode of specimens with a clear cover of one bar diameter is caused by the spalling of the concrete cover. For clear covers of 3 and 5 diameters, the failure was caused by splitting induced pull-out. All the results show a considerable reduction of the activated bond stresses within a distance of around 1 to 3 bar diameters. In that region, the response follows the same ascending branch as the rest of the bar with a sudden loss of the bond stresses.

The influence of the casting conditions has been confirmed for all the considered concrete covers and agrees with previous research. The bars in poor casting conditions (placed at

the top of the concrete mass during pouring) have the smallest anchorage resistance. The bars in good casting conditions (placed at the bottom near to the formwork) have the largest anchorage resistance. The response of bars oriented parallelly to the casting direction is between the poor and good casting conditions.

The influence of the rib orientation on the anchorage resistance is small and falls within typical bond test scatter. The orientation seems to have an influence in the redistribution capacity of bars in poor casting conditions. Bars with the lugs placed perpendicularly to the concrete surface (one side of the rib lugs was at the position of the plastic settlement and concrete bleeding voids) displayed more uniform bond stress distributions. For the same reason, these bars showed lower bond stresses for small slips, indicating that this effect could have a bigger influence in service conditions.

The influence of the rib geometry for specimens with a cover of 1 bar diameter showed some differences that can be explained by the rib orientation with respect to the surface. For specimens with a cover of 5 bar diameters, differences can be observed that do not correspond to the differences in the bond index of the bars.

The detailed measurements with DIC and fibre optical measurements have shown that the reduction of the local bond-slip responses for low and moderate confinements, with respect to the pull-out failure, can be explained by the development of spalling cracks (parallel to the bar and approximately parallel to the concrete surface), splitting cracks (parallel to the bar and approximately perpendicular to the concrete surface) and conical cracks leading to concrete cone breakouts near the loaded end of the bar (which typically corresponds to the crack plane).

Enhancement of the bar stress - crack width relationship

Extensive research can be found in the literature concerning the relationship between the stress in the reinforcement and the crack width. This is typically addressed by the crack width formulations in codes of practice which are used to verify the predicted crack opening at serviceability limit state as a function of the calculated steel stress in the design of a new structure. The goal of this research is the opposite, taking advantage of the fact that in the case of an existing structure, additional information is available so that it should be possible to estimate the steel stress for a fatigue verification on the basis of the variation of the measured crack opening.

The mechanical model that serves as base for crack formulations in current codes of practice is considered. Based on a sensitivity analysis, the assumed bond stress is one of the main influencing parameters after the crack spacing, which is known in the case of an existing structure. Shrinkage can influence considerably the cracking force and the stresses in the bar. However, neglecting this effect results in a conservative estimation of the bar stresses. This is favourable, as the uncertainty in the estimation of the shrinkage-induced effects in real structures is significant.

An experimental campaign has been performed to evaluate the activation of bond stresses in reinforced concrete elements using DIC and distributed fibre optical sensors. Furthermore, additional tests from the literature using the same measurement techniques have been analysed. The experimental results show that in most cases, the activated bond stresses are lower than the assumed values in current codes. The activated bond stresses in the stirrups are an exception, as the experimental results show bond stresses that are similar or larger than the proposed values of current codes. The analysis of cyclic tests show that a considerable reduction occurs in the first 10 to 15 cycles, and a slower deterioration with the following cycles.

A refined local model to characterize the bond activation is proposed, based on mechanical considerations and the experimental results from the pull-out tests. Using this local model, an expression to estimate the bond stresses in a cracked element is derived. This expression accounts for the crack width, the casting conditions, the presence of longitudinal

cracks and the cyclic loading. The results are compared with the experimental values providing satisfactory results given the inherent variability of bond results.

Using the measured crack spacing, the application of the considered crack formulation with the proposed bond stresses improves the steel stress estimation compared with current code formulations. The estimations using the code formulations and the calculated mean crack spacings differ considerably from the experimental results. The improvement is more relevant for small crack widths. For large crack widths, the relative error in the stress estimations is smaller. This is due to the fact that, stresses in the bar are larger. Therefore, the error in the calculated bar stress as a result of the misestimation of the bond stresses has a smaller relative impact.

Experimental investigation of dowel action in reinforcing bars using refined measurements

In typical reinforced concrete design, reinforcement is designed to carry axial forces, but it can also resist transversal forces by dowel action. The latter develops in case of sliding of cracks which are perpendicular to the reinforcing bar or in case of opening of cracks which are inclined with respect to the bar. Dowel actions is usually neglected for simplicity's sake in the design phase, but it can be accounted for either explicitly in mechanical models or implicitly in empirical relationships. Furthermore, there are cases where the connection between various concrete elements explicitly depends on dowel action, as for example in connections between precast elements or between two concrete parts cast at different times. On the other side, dowel action can have a negative impact on the fatigue resistance of reinforcing bars subjected to cyclic loading, because of the local stress concentrations near interfaces due to relative movements, either in sliding or in opening of cracks not perpendicular to the bar. For the assessment of the remaining capacity of existing structures, improved models of the behaviour are needed, including realistic models of the behaviour of concrete, steel and their interfaces. To that aim, Section 6 presents a contribution to a better understanding of dowel action by two test series.

The first test series focused on the behaviour of a reinforcing bar submitted to dowel action: the concrete specimens with the embedded bars were placed in a custom-made test setup and subjected to monotonic or low stress-level cyclic actions with a longitudinal and a transversal crack opening component, up to developing the full plastic capacity of the dowel and rupture at the peak of catenary action. The measurement system included tracking the displacement field at the surface of the concrete and the strains in the dowel by optical fibres glued in longitudinal grooves on its surface. The latter measurements allow to derive the internal forces in the reinforcing bar and its deformed shape as well as the contact pressure between the bar and the surrounding concrete. The results show a strong dependency on the test variables: diameter of the bar, imposed crack kinematics and angle between the bar and the crack. The larger dowel resistance is associated with a larger bar diameter and a larger angle between the bar and the crack. The first-order dowel resistance is characterized by concrete crushing under the bar near the crack and yielding of the bar due to bending. Further increments of the dowel force are possible by activating the catenary action associated with significant transversal displacements. Optical fibre measurements indicate that the most stressed cross-section in the bar due bending related to dowel action is approximately 1.5 times the bar diameter away from the crack. The concrete stiffness is observed to degrade substantially at approximately 40% to 60% of the first-order dowel resistance.

The second test series looked more closely at the behaviour of concrete underneath the bar, in the presence of a point load introduced at various locations into concrete through a reinforcing bar. The increase in both the peak force and the initial stiffness was observed for the point load applied farther away from the concrete edge. This increase occurs due to the larger concrete area carrying the applied force. It was observed that the proposed tests can reproduce the comparable dowel tests for the load position of 0.9 times the bar diameter from the concrete edge. This alignment occurs because this force position roughly

corresponds to the location of the resultant of the pressure distribution along the bar observed in the dowel tests.

Dowel models to predict the resistance and the relationship between transverse displacement and stress in the reinforcing bar

The accurate modelling of dowel action for fatigue, serviceability and ultimate limit states represents a challenge due to scarce refined measurements concerning steel reinforcement, the concrete and the steel-concrete interaction under cyclic and monotonic loads. In this context, Section 7 presents a new formulation for the bearing stiffness of concrete under the reinforcing bar to be used in Winkler's model. The formulation accounts for various effects and is developed based on mechanical considerations and calibrated on the basis of the optical fibre measurements described in Section 6. Regarding the ultimate limit state, existing models to calculate the dowel resistance are compared to the new experimental data.

A new formulation for the bearing stiffness of concrete under the reinforcing bar to be used in Winkler's model (beam on elastic foundation) is proposed. The formulation accounts for various effects: angle between the crack and the bar, bar diameter, concrete strength, casting conditions, thickness of the concrete cover, number of load cycles and secondary cracks near to ribs in concrete due to the axial force. Good casting conditions were observed to yield approximately 2 times larger stiffness underneath the rebar than poor conditions. The stiffness increases with the concrete cover, reaching its maximum for the cover-to-bar diameter ratio of approximately 3. The bearing stiffness starts to gradually decrease when the transverse displacement increases, due to splitting cracks, concrete crushing and spalling near the crack. This decrease is accounted for in an empirical expression calibrated based on optical fibre measurements. The enhanced model accurately predicts the shear force-transverse displacement response observed in monotonic tests. Additionally, it demonstrates good accuracy in predicting the peak longitudinal stress, aligning well with optical fibre measurements from both monotonic and cyclic tests.

Regarding the ultimate limit state, the Rasmussen's model based on limit analysis is used to evaluate the dowel resistance for the 90°-angle between the bar and the crack, including different values of the confinement factor. For the angles smaller than 90°, Dulacska's model is used. The prediction of the considered models shows a good agreement with the tests considered.

Résumé

L'inspection et la surveillance des structures en béton armé sont fondamentales pour détecter les problèmes potentiels affectant la sécurité structurelle et la résistance à la fatigue. La décision finale d'intervenir ou non est toujours basée sur l'interprétation des données disponibles. Des développements technologiques récents tels que la corrélation numérique d'images (DIC) permettent de détecter les déplacements dans les fissures sur de grandes surfaces, fournissant ainsi une quantité de données beaucoup plus importante et des informations plus détaillées que les techniques de mesure in situ conventionnelles. Par exemple, ce type de mesures innovantes peut fournir des informations précieuses sur les conséquences et les risques associés à la présence de fissures anormales.

Les objectifs de cette recherche sont les suivants :

- Vérifier la possibilité d'utiliser le DIC pour des mesures in situ à court et à long terme sur des ponts et d'autres ouvrages d'art ;
- Vérifier la fiabilité de la mesure DIC pour la quantification des efforts dans une structure (forces axiales et de cisaillement dans les barres d'armature et forces transmises par le béton à travers les fissures par engrainement des agrégats) ;
- Contribuer à l'estimation des contraintes dans les armatures sur la base de la mesure des déplacements de fissures à utiliser pour une vérification de la fatigue. Cela concerne l'estimation de l'effort axial et des moments de flexion dans la barre et leurs contraintes correspondantes dues à l'ouverture et au glissement des fissures. L'estimation de la force axiale est traitée indirectement dans les relations effort-ouverture des fissures, qui permettent d'estimer la largeur de la fissure en fonction de la contrainte calculée dans la barre. L'estimation du moment de flexion se base sur les modèles développés pour étudier le phénomène appelé effet goujon.

Sur cette base, les thèmes suivants sont traités :

- Les limites de l'applicabilité de la DIC dans l'auscultation des structures existantes.
- La comparaison des outils existants pour surmonter certaines des limites de la DIC.
- L'amélioration de la relation entre l'ouverture de la fissure dans la direction de la barre et les contraintes longitudinales générées dans la barre.
- L'amélioration de la relation entre l'ouverture de la fissure dans la direction perpendiculaire à la barre et les contraintes longitudinales générées dans la barre.

Limites d'applicabilité de la corrélation d'images numériques in situ

La corrélation numérique d'images (DIC) est une technique qui consiste à suivre des sous-groupes de pixels sur différentes images. La position des sous-groupes est comparée à l'image de référence pour déterminer le champ de déplacement de la région suivie. Le système de mesure est composé d'une ou deux caméras, de leurs supports, d'un système d'éclairage et d'un ordinateur pour l'acquisition des données. Différents logiciels commerciaux peuvent être utilisés pour effectuer la vidéo-corrélation. Les mesures DIC peuvent être effectuées à l'aide d'une seule caméra (ce qui donne des déplacements dans le plan, 2D-DIC) ou de deux caméras (ce qui donne des déplacements dans l'espace, 3D-DIC). De nos jours, la plupart des applications utilisent des systèmes de mesure 3D-DIC. C'est pourquoi la recherche présentée dans ce rapport se concentre sur la 3D-DIC et sera simplement appelée DIC.

Le champ de déplacement obtenu à partir des mesures DIC peut être utilisé pour déterminer le champ de déformation de la zone étudiée. Dans le cas des structures en béton armé, les déformations de traction avant la formation de fissures sont faibles. Par conséquent, les mesures du champ de déformation dans les régions fissurées dépendent fortement des déplacements concentrés dans les fissures. C'est pourquoi le champ de déformation peut être utilisé pour détecter la configuration et la cinématique des fissures (ouverture et glissement) sur de grandes surfaces. C'est précisément le principal avantage

de la DIC par rapport aux systèmes traditionnels de mesure des fissures qui fournissent des informations unidirectionnelles en des points discrets.

Les mesures DIC sont connues pour être affectées par de multiples facteurs, notamment les mouvements relatifs entre la caméra et la surface de mesure, les conditions d'éclairage ou les courants d'air entre les caméras et la surface de mesure. Ces paramètres peuvent être raisonnablement bien contrôlés en laboratoire. Cela se reflète dans la grande précision obtenue dans les applications de la DIC dans les essais en laboratoire sur des éléments en béton armé. Néanmoins, les conditions dans lesquelles ces mesures peuvent être effectuées dans des structures existantes peuvent varier considérablement. Les actions dues au vent et au trafic provoquent des vibrations dans la structure qui affectent ensuite les supports de la caméra. Pour les mesures effectuées sur les faces externes des structures, des variations de lumière peuvent se produire. C'est pourquoi deux séries d'essais ont été réalisées afin de quantifier l'influence des paramètres susmentionnés sur l'incertitude de mesure des déplacements absolus.

Tout d'abord, une série d'essais visant à caractériser l'influence de l'éclairage a été réalisée en faisant varier le temps d'exposition des images. Cela modifie la luminosité des images. La variation de l'éclairage étant un effet connu, des algorithmes spéciaux ont été développés pour en tenir compte et sont disponibles dans la plupart des logiciels de corrélation commerciaux. C'était le cas dans les mesures effectuées, qui montrent une faible influence de la luminosité de l'image dans un temps d'exposition de ±50% du temps d'exposition idéal. Toutefois, il a été observé que les différences d'éclairage dans l'image entraînent de légères variations dans l'incertitude de la mesure. C'est pourquoi il convient d'évaluer l'incertitude dans la zone de mesure avant d'effectuer les mesures afin de déterminer si la précision attendue est suffisante dans toutes les zones importantes de la zone étudiée.

Une deuxième série d'essais a été réalisée pour évaluer l'influence des vibrations. Des mesures identiques ont été effectuées sur le sol en conditions de laboratoire, sur le sol à l'extérieur du bâtiment et sur une passerelle. Les résultats montrent que l'incertitude de mesure augmente pour les mesures effectuées en dehors du laboratoire. Cependant, pour la mesure des déplacements relatifs entre deux points, les différences ne sont pas si importantes.

Une dernière vérification de ces résultats a été faite en effectuant des mesures DIC sur les viaducs de Chillon de l'autoroute A9. Une fissure près de l'ancrage d'un des câbles de précontrainte dans la dalle inférieure du caisson a été étudiée. La fissure s'est ouverte et refermée sous le passage des poids lourds d'environ ±15 µm (0,015 mm). Deux jauges oméga ont été installées en travers de la fissure pour la validation des mesures. Les résultats DIC montrent une bonne correspondance avec les mesures des jauges de déformation, avec une certaine variation qui correspond à l'incertitude de mesure estimée.

Les mesures DIC sont précises et polyvalentes car elles peuvent fournir des informations sur toute une région tridimensionnelle de la structure. Pour ce faire, une série d'images est comparée à une image de référence. Une condition nécessaire à la corrélation est que les images soient prises avec la même position relative entre les caméras. Cette condition présente deux limites pour l'application de la DIC dans les structures existantes :

- Si une fissure existante est déjà présente sur l'image de référence, la cinématique totale de la fissure ne peut pas être déterminée et la géométrie de la fissure ne peut être évaluée que s'il y a au moins une légère modification de l'ouverture (ou/et du glissement) due, par exemple, à l'action du trafic ou aux variations de température.
- Le démontage et le remontage du système de mesure entre les inspections entraînera inévitablement des positions relatives différentes de la caméra lors des inspections successives. Par conséquent, les images des nouvelles inspections ne peuvent pas être corrélées à la première inspection. Il n'est donc pas possible d'obtenir des informations sur les changements survenus entre les inspections. La seule façon d'y parvenir serait de laisser le système de mesure DIC en place. Cette solution est très peu pratique car elle nécessite un système de mesure DIC par structure inspectée, y compris son entretien.

Techniques complémentaires basées sur l'imagerie pour la caractérisation initiale et à long terme des fissures

Pour surmonter ces limitations, deux techniques alternatives sont proposées. La première technique vise à caractériser la fissure initiale sur la base d'algorithmes de détection directe. Dans un premier temps, les propriétés de la fissure sont détectées à partir des informations contenues dans une seule image. Dans un second temps, les lèvres détectées de la fissure sont superposées pour déterminer la cinématique de la fissure. Deux outils en libre accès ont été utilisés à cette fin. Des essais ont été effectués pour quantifier l'incertitude de mesure de la cinématique des fissures dans des conditions de laboratoire. Les résultats montrent que la géométrie de la fissure peut être bien caractérisée avec une incertitude de ±1 pixel pour l'ouverture de la fissure et de ±2 pixels pour le glissement de la fissure (l'incertitude en unités de distance dépend de la taille du pixel et, en conséquence, de l'appareil utilisé et sa position par rapport à la surface étudiée). L'incertitude de mesure est plus grande qu'en utilisant le DIC conventionnel. Cependant, les seuls outils nécessaires sont un appareil photo numérique et un ordinateur.

La seconde technique vise à déterminer les déplacements des fissures pour un suivi à long terme. Cette technique repose sur le suivi de la position de marqueurs placés sur les deux lèvres de la fissure. En comparant la position des marqueurs lors d'inspections successives et en considérant une lèvre de la fissure comme référence, les marqueurs de l'autre côté reflètent les déplacements de la fissure. Par conséquent, ils peuvent être utilisés pour déterminer la cinématique de la fissure qui a eu lieu entre les mesures. Les variations de température doivent être prises en compte étant donné la plus grande distance entre le centre des marqueurs et les lèvres de la fissure. Un modèle permettant d'estimer l'incertitude attendue en fonction du nombre de marqueurs et de leur disposition est proposé. Un essai du système en laboratoire a été réalisé au travers d'un essai de flexion à quatre points sur une petite poutre en béton armé. La technique basée sur les marqueurs détecte la cinématique de la fissure, donnant des résultats similaires à ceux mesurés à l'aide de la méthode DIC conventionnelle. Les résultats se situent dans la tolérance estimée par le modèle d'incertitude.

Une validation finale de ces techniques a été effectuée dans la même fissure que celle utilisée pour la validation des mesures à court terme à l'aide du DIC conventionnel. La technique initiale de caractérisation des fissures a permis de détecter la fissure avec précision. Les déplacements mesurés entre les lèvres de la fissure ont été comparés aux résultats obtenus à l'aide d'un microscope de fissure et d'une règle de fissure. Dans la plupart des cas, les résultats se situent dans les tolérances observées lors des essais en laboratoire. Dans certains cas, des différences plus importantes ont été observées. Ceci est explicable du fait que dans de nombreux cas, les lèvres des fissures existantes sont légèrement détériorées ou érodées. Un test de la technique basée sur les marqueurs a également été réalisé sur une demi-journée. Les résultats sont comparés aux mesures DIC conventionnelles à court terme et montrent une bonne concordance. En conclusion, les techniques proposées peuvent être utilisées pour surmonter les limites des mesures DIC conventionnelles avec une certaine augmentation de l'incertitude des mesures.

Essais d'arrachement pour étudier l'évolution de la contrainte d'adhérence

Les forces d'adhérence entre les barres d'armature et le béton constituent un élément fondamental du comportement à la fissuration des éléments en béton armé. C'est pourquoi un programme expérimental a été mis en œuvre pour établir une meilleure relation entre la loi locale contrainte d'adhérence - glissement (obtenue à partir d'essais d'arrachement avec des faibles longueur d'ancrage) et le comportement des ancrages de longueur moyenne. L'influence de divers paramètres susceptibles de varier dans les applications structurelles courantes a été étudiée, notamment l'enrobage des barres, la position des barres lors du bétonnage, la géométrie des nervures et l'orientation des nervures par rapport à la surface de béton la plus proche. Les barres testées ont été équipées de capteurs optiques à fibres réparties et la surface du béton a été suivie à l'aide d'un système

DIC. Un bâti d'essai spécialement conçu a été utilisé pour minimiser l'influence sur le développement de fissures coniques secondaires près de l'extrémité chargée de la barre.

L'influence de l'enrobage est conforme aux recherches précédentes. Une augmentation de l'enrobage augmente le confinement et donc les contraintes d'adhérence activées pour les petits glissements ainsi que la résistance de l'ancrage. Le mode de rupture des échantillons avec un enrobage correspondent à un diamètre de barre est causé par l'éclatement de l'enrobage. Pour les enrobages de 3 et 5 diamètres, la rupture a été causée par un arrachement induit par la fissuration. Tous les résultats montrent une réduction considérable des contraintes d'adhérence activées sur une distance d'environ 1 à 3 diamètres de barre à partir de la fissure principale. Dans cette région, la relation contrainte d'adhérence – glissement est similaire au reste de la barre pour des fables glissements mais montre une perte soudaine des contraintes d'adhérence.

L'influence des conditions de bétonnage a été confirmée pour tous les enrobages considérés et est en accord avec les recherches précédentes. Les barres situées dans des zones de mauvaises conditions de bétonnage (placées dans la partie supérieure de la masse de béton lors du bétonnage) ont la plus petite résistance d'ancrage. Les barres situées dans des zones de bonnes conditions de bétonnage (placées en bas, près du coffrage de fond) ont la plus grande résistance d'ancrage. Le comportement des barres orientées parallèlement à la direction de mise en place du béton se situe entre les mauvaises et les bonnes conditions de bétonnage.

L'influence de l'orientation des nervures sur la résistance à l'ancrage est faible et se situe dans la dispersion typique des essais d'adhérence. L'orientation semble avoir une influence sur la capacité de redistribution des efforts des barres dans de mauvaises conditions de bétonnage. Les barres dont les nervures sont perpendiculaires à la surface du béton (un côté des nervures se trouvant à l'endroit du tassement plastique et des vides de ressuage du béton) affichent des distributions de contraintes d'adhérence plus uniformes. Pour la même raison, ces barres ont montré des contraintes d'adhérence plus faibles pour les petits glissements, ce qui indique que cet effet pourrait avoir une plus grande influence dans les conditions de service.

L'influence de la géométrie des nervures pour les éprouvettes avec un enrobage de 1 diamètre a montré quelques différences qui peuvent être expliquées par l'orientation des nervures par rapport à la surface. Pour les éprouvettes avec un enrobage de 5 diamètres, on observe des différences qui ne correspondent pas aux différences d'indice d'adhérence des barres.

Les mesures détaillées effectuées à l'aide de la DIC et de la fibre optique ont montré que, pour des enrobages faibles et modérés et en ce qui concerne la rupture par arrachement, la réduction des contraintes locales d'adhérence et de glissement peut s'expliquer par le développement de fissures d'éclatement (parallèles à la barre et approximativement parallèles à la surface du béton), de fissures de fendage (parallèles à la barre et approximativement perpendiculaires à la surface du béton) et de fissures coniques conduisant à des ruptures de cônes de béton près de l'extrémité chargée de la barre (qui correspond généralement au plan de la fissure).

Amélioration de la relation analytique entre la contrainte dans la barre et la largeur de la fissure

La littérature fait état de recherches approfondies sur la relation analytique entre la contrainte dans l'armature et la largeur de la fissure. Cette question est généralement considérée dans les normes au travers des équations qui sont utilisées pour vérifier l'ouverture de fissure prévue à l'état limite de service en fonction de la contrainte calculée dans l'acier lors du projet d'une nouvelle structure. L'objectif de la présente recherche est l'inverse, en profitant du fait que, dans le cas d'une structure existante, des informations supplémentaires sont disponibles de sorte qu'il devrait être possible d'estimer la contrainte

de l'acier, par exemple pour une vérification à la fatigue, sur la base de la variation de l'ouverture mesurée de la fissure.

Le modèle mécanique qui sert de base aux équations dans les normes actuelles est examiné. Sur la base d'une analyse de sensibilité, la contrainte d'adhérence admise est l'un des principaux paramètres d'influence après l'espacement des fissures, qui est connu dans le cas d'une structure existante. Le retrait peut influencer considérablement l'effort de fissuration et les contraintes dans la barre. Toutefois, si l'on néglige cet effet, on obtient une estimation conservatrice des contraintes dans la barre. Ceci est favorable, car l'incertitude dans l'estimation des effets induits par le retrait dans les structures réelles est importante.

Une campagne expérimentale a été menée pour évaluer, à l'aide de mesures DIC et de capteurs optiques à fibres, l'activation des contraintes d'adhérence dans les éléments en béton armé. En outre, d'autres essais tirés de la littérature et utilisant les mêmes techniques de mesure ont été analysés. Les résultats expérimentaux montrent que, dans la plupart des cas, les contraintes d'adhérence activées sont inférieures aux valeurs admises dans les normes actuelles. Les contraintes d'adhérence activées dans les étriers sont une exception, car les résultats expérimentaux montrent des contraintes d'adhérence similaires ou supérieures aux valeurs admises par les normes. L'analyse des essais cycliques montre qu'une réduction considérable se produit dans les 10 à 15 premiers cycles, et une détérioration plus lente lors des cycles suivants.

Un modèle local plus raffiné pour caractériser l'activation de la contrainte d'adhérence est proposé. Ce modèle est basé sur des considérations mécaniques et sur les résultats expérimentaux des essais d'arrachement. À l'aide de ce modèle local, une expression permettant d'estimer les contraintes d'adhérence dans un élément fissuré est dérivée. Cette expression tient compte de la largeur de la fissure, des conditions de bétonnage, de la présence de fissures longitudinales et de l'action cyclique. Les résultats sont comparés aux valeurs expérimentales et donnent des résultats satisfaisants compte tenu de la variabilité inhérente aux résultats d'adhérence.

En utilisant l'espacement mesuré entre fissures, l'application de l'équation pour la vérification de l'ouverture des fissures améliore l'estimation de la contrainte dans l'acier par rapport aux formulations des normes. Les estimations utilisant les formulations des normes et les espacements moyens entre fissures calculés diffèrent considérablement des résultats expérimentaux. L'amélioration est plus pertinente pour les petites largeurs de fissure. Pour les grandes largeurs de fissure, l'erreur relative dans l'estimation des contraintes est plus faible. Cela est dû au fait que les contraintes dans la barre sont plus importantes. Par conséquent, l'erreur sur la contrainte calculée, résultant de la mauvaise estimation des contraintes d'adhérence, a un impact relatif plus faible.

Étude expérimentale de l'effet goujon dans les barres d'armature à l'aide de mesures affinées

Dans le calcul du béton armé, l'armature est généralement dimensionnée pour reprendre les forces normales, mais elle peut également résister à des forces transversales par l'effet goujon. Ce dernier se développe en cas de glissement des fissures perpendiculaires à la barre d'armature ou en cas d'ouverture de fissures inclinées par rapport à la barre. L'effet goujon est généralement négligé par souci de simplicité lors de la phase de dimensionnement, mais elle peut être pris en compte soit explicitement dans les modèles mécaniques, soit implicitement dans les relations empiriques. En outre, il existe des cas où la connexion entre divers éléments en béton dépend explicitement de l'effet goujon, comme par exemple dans les connexions entre des éléments préfabriqués ou entre deux parties en béton coulées à des moments différents. D'autre part, l'effet goujon peut avoir un impact négatif sur la résistance à la fatigue des barres d'armature soumises à des charges cycliques, en raison des concentrations locales de contraintes près des interfaces dues aux mouvements relatifs, soit par glissement, soit par l'ouverture de fissures non perpendiculaires à la barre. Pour évaluer la capacité restante des structures existantes, il

est nécessaire d'améliorer les modèles de comportement, y compris les modèles du comportement du béton, de l'acier et de leurs interfaces. À cette fin, il est présenté une contribution à une meilleure compréhension de l'effet goujon grâce à deux séries d'essais.

La première série d'essais s'est concentrée sur le comportement d'une barre d'armature soumise à l'effet goujon : les échantillons de béton avec les barres ont été placés dans un dispositif d'essai projeté sur mesure et soumis à des actions monotones ou cycliques à faible niveau de contrainte avec des composantes d'ouverture de fissure longitudinales et transversales, jusqu'à développer la pleine capacité plastique du goujon et la rupture de la barre après activation des effets de catenaire. Le système de mesure comprenait le suivi du champ de déplacement à la surface du béton et celui des déformations dans la barre d'armature par des fibres optiques collées dans des rainures longitudinales à sa surface. Ces dernières mesures permettent de déduire les efforts dans la barre d'armature et sa déformée, ainsi que la pression de contact entre la barre et le béton environnant. Les résultats montrent une forte dépendance aux variables d'essai : diamètre de la barre, cinématique de la fissure imposée et angle entre la barre et la fissure. La plus grande résistance à l'effort tranchant des armatures est associée à un diamètre de barre plus grand et à un angle plus grand entre la barre et la fissure. La résistance à l'effort tranchant de premier ordre est caractérisée par l'écrasement du béton sous la barre près de la fissure et par l'écoulement à la flexion de la barre. Au-delà de ce niveau, il est possible d'augmenter encore l'effort tranchant en activant l'effet de membrane associée à des déplacements transversaux importants. Les mesures par fibre optique indiquent que la section la plus sollicitée dans la barre en raison de la flexion liée à l'effet goujon se situe à une distance de la fissure d'environ 1,5 fois le diamètre de la barre. On observe que la rigidité du béton se dégrade considérablement à environ 40 à 60 % de la résistance à l'effort tranchant de premier ordre.

La deuxième série d'essais avait pour but d'examiner de plus près le comportement du béton sous la barre en présence d'une charge ponctuelle introduite à différents endroits. L'augmentation de la force maximale et de la rigidité initiale a été observée lorsque la charge ponctuelle était appliquée plus loin du bord du béton. Cette augmentation est due à la plus grande surface de béton supportant la force appliquée. Il a été observé que les essais proposés peuvent reproduire les essais comparables sur les barres d'armature soumises à l'effet goujon pour une position de la charge situé à une distance de 0,9 fois le diamètre de la barre par rapport à l'arête du béton. Ceci est dû au fait que cette position de la force correspond approximativement à l'emplacement de la résultante de la distribution de la pression le long de la barre observée dans les essais de goujons.

Modèles pour prédire la résistance à l'effort tranchant des barres et la relation entre le déplacement transversal et la contrainte dans la barre d'armature due à l'effet goujon

La modélisation de l'effet goujon pour la fatigue, l'aptitude au service et l'état limite ultime représente un défi en raison de la rareté des mesures détaillées concernant l'armature, le béton et l'interaction acier-béton sous des charges monotones et cycliques. Dans ce contexte, il est présenté une nouvelle formulation pour la rigidité du béton situé sous la barre d'armature, destinée à être utilisée dans le modèle de Winkler. Cette formulation prend en compte divers effets, est développée sur la base de considérations mécaniques et est calibrée sur les mesures réalisées avec les fibres optiques, telles que décrites dans le Chapitre 6. En ce qui concerne l'état limite ultime, les modèles mécaniques existants sont comparés aux nouveaux résultats de la résistance à l'effort tranchant des barres.

Il est proposé une nouvelle expression de la rigidité du béton situé sous la barre d'armature, à utiliser dans le modèle de Winkler (poutre sur fondation élastique). La rigidité initiale tient compte de l'effet des paramètres suivants : angle entre la fissure et la barre, diamètre de la barre, résistance du béton, conditions de bétonnage, enrobage des barres, nombre de cycles et fissures dans le béton dues à une éventuelle force normale. On a observé que de bonnes conditions de bétonnage donnaient une rigidité sous la barre d'armature environ 2 fois plus importante que de mauvaises conditions. La rigidité augmente avec l'enrobage,

atteignant son maximum pour un ratio enrobage/diamètre de barre d'environ 3. La rigidité initiale commence à diminuer progressivement lorsque le déplacement transversal augmente, en raison des fissures de fendage, de l'écrasement du béton et de l'écaillage à proximité de la fissure. Cette diminution est prise en compte dans une expression empirique calibrée sur la base de mesures par fibre optique. Le modèle amélioré prédit avec précision la réponse force de cisaillement-déplacement transversal observée dans les essais monotones. En outre, il fait preuve d'une bonne précision dans la prédiction de la contrainte longitudinale maximale, s'alignant bien sur les mesures de fibre optique des essais monotoniques et cycliques.

Pour l'état limite ultime, le modèle de Rasmussen basé sur l'analyse des limites est utilisé pour évaluer la résistance du goujon pour un angle de 90° entre la barre et la fissure, en incluant différentes valeurs du facteur de confinement. Pour les angles inférieurs à 90°, le modèle de Dulacska est employé. Les prédictions de ces modèles montrent une bonne concordance avec les essais considérés.

Zusammenfassung

Die Inspektion und Überwachung von Stahlbetonkonstruktionen ist von grundlegender Bedeutung für die Erkennung potenzieller Probleme, die die Trag- und Ermüdungssicherheit beeinträchtigen können. Die endgültige Entscheidung, ob Massnahmen erforderlich sind oder nicht, basiert immer auf der Interpretation der verfügbaren Daten. Jüngste technologische Entwicklungen wie die digitale Bildkorrelation (DIC) ermöglichen die Erfassung von Rissverschiebungen über grosse Flächen und liefern somit eine wesentlich grössere Datenmenge und detailliertere Informationen als die herkömmlichen In-situ-Messverfahren. Diese Art innovativer Messungen kann zum Beispiel wertvolle Informationen über die Folgen und Risiken liefern, die mit dem Vorhandensein anormaler Risse verbunden sein können.

Die Ziele dieser Forschung sind:
- Überprüfung der Möglichkeit, DIC für kurz- und langfristige In-situ-Messungen an Brücken und anderen Ingenieurbauwerken einzusetzen;
- Überprüfung der Zuverlässigkeit der DIC-Messung zur Quantifizierung der inneren Kräfte in einem Bauwerk (Normal- und Querkräfte in den Bewehrungsstäben und Kräfte, die vom Beton durch die Risse aufgrund der Rissuferverzahnung übertragen werden);
- Beitrag zur Abschätzung der Stahlspannungen in der Bewehrung auf der Grundlage der Messung von Rissverschiebungen, die für einen Ermüdungsnachweis verwendet werden sollen. Dies betrifft die Abschätzung der Normalkraft und der Biegemomente im Bewehrungsstab und ihrer entsprechenden Spannungen aufgrund der Rissverschiebungen. Die Abschätzung der Normalkraft wird indirekt in den Rissformulierungen behandelt, die eine Abschätzung der Rissbreite in Abhängigkeit von der berechneten Spannung im Stab ermöglichen. Die Abschätzung des Biegemoments basiert auf die Quantifizierung der Dübelwirkung.

Auf dieser Grundlage werden die folgenden Themen behandelt:
- Die Grenzen der Anwendbarkeit von DIC in bestehenden Tragwerken.
- Der Vergleich bestehender Messverfahren zur Überwindung einiger der Einschränkungen von DIC.
- Verbesserung der Beziehung zwischen der Rissöffnung in Richtung des Bewehrungsstabes und den erzeugten Stahlspannungen.
- Verbesserung der Beziehung zwischen der Rissverschiebung quer zum Bewehrungsstab und den erzeugten Stahlnormalspannungen.

Grenzen der Anwendbarkeit der digitalen Bildkorrelation in-situ

Die digitale Bildkorrelation (DIC) ist eine Technik, bei welcher, Untergruppen von Pixeln über eine Reihe von Bildern verfolgt werden. Die Lage der Untergruppen wird mit dem Referenzbild verglichen, um das Verschiebungsfeld des verfolgten Bereichs zu bestimmen. Das Messsystem besteht aus einer oder zwei Kameras, deren Halterungen, einem Beleuchtungssystem und einem Computer für die Datenerfassung. Für die Durchführung der Korrelation können verschiedene kommerzielle Softwareprogramme verwendet werden. DIC-Messungen können mit einer einzigen Kamera (die Verschiebungen auf der Ebene der Oberfläche liefert, 2D-DIC) oder mit zwei Kameras (die dreidimensionalen Verschiebungen liefern, 3D-DIC) durchgeführt werden. Heutzutage verwenden die meisten Anwendungen 3D-DIC-Messsysteme. Aus diesem Grund konzentriert sich die in diesem Bericht vorgestellte Forschung auf 3D-DIC und wird im Folgenden einfach als DIC bezeichnet.

Das aus DIC-Messungen gewonnene Verschiebungsfeld kann zur Bestimmung des Dehnungsfelds der untersuchten Zone verwendet werden. Im Falle von Stahlbetonkonstruktionen, sind die Zugverformungen im umgerissenen Bereich gering, da die Zugfestigkeit rasch erreicht wird, was zur Bildung von Rissen führt. Folglich hängen die

Dehnungsfeldmessungen in gerissenen Bereichen stark von den Rissverschiebungen ab. Aus diesem Grund kann das Dehnungsfeld verwendet werden, um das Rissbild und die Risskinematik (Öffnung und Schiebung) über grosse Flächen zu erkennen. Genau dies ist der Hauptvorteil von DIC im Vergleich zu den herkömmlichen Rissmesssystemen, die unidirektionale Informationen an diskreten Punkten liefern.

Es ist bekannt, dass DIC-Messungen durch mehrere Faktoren beeinflusst werden, darunter die relativen Bewegungen zwischen der Kamera und der Messfläche, die Beleuchtungsbedingungen oder die Luftströmungen zwischen den Kameras und der Messfläche. Diese Einflussparameter können unter Laborbedingungen recht gut kontrolliert werden. Dies spiegelt sich in der hohen Genauigkeit wider, die bei der Anwendung von DIC in Laborprüfungen von Stahlbetonbauteilen erzielt wird. Die Bedingungen, die bei der Durchführung solcher Messungen in bestehenden Bauwerken vorzufinden sind, können sich jedoch erheblich unterscheiden. Wind- und Verkehrslasten verursachen Schwingungen im Bauwerk, die sich dann auf die Kameraträger auswirken. Bei Messungen an den Aussenflächen von Bauwerken können leichte Schwankungen auftreten. Aus diesem Grund wurden zwei Versuchsreihen zur Quantifizierung des Einflusses der oben genannten Parameter auf die Messunsicherheit der absoluten Verschiebungen durchgeführt.

Zunächst wurde eine Reihe von Versuchen zur Charakterisierung des Einflusses der Beleuchtung durchgeführt, indem die Belichtungszeit der aufgenommenen Bilder variiert wurde. Dadurch ändert sich die Helligkeit der Bilder. Da es sich bei der variablen Beleuchtung um einen bekannten Effekt handelt, wurden spezielle Algorithmen entwickelt, welche dies berücksichtigen und welchein den meisten kommerziellen Korrelationsprogrammen verfügbar sind. Dies war bei den durchgeführten Messungen der Fall, die innerhalb einer Belichtungszeit von ±50 % der idealen Belichtungszeit nur einen geringen Einfluss auf die Helligkeit des Bildes zeigten. Es wurde jedoch festgestellt, dass Unterschiede in der Beleuchtung innerhalb des Bildes zu kleinen Schwankungen in der Messunsicherheit führen. Aus diesem Grund sollte die Unsicherheit im Messbereich vor der Durchführung der Messungen bewertet werden, um festzustellen, ob die erwartete Genauigkeit in allen wichtigen Bereichen der untersuchten Zone ausreichend ist.

Eine zweite Versuchsserie wurde durchgeführt, um den Einfluss von Schwingungen zu bewerten. Es wurden identische Messungen auf dem Boden unter Laborbedingungen, auf dem Boden im Aussenbereich und auf einer Fussgängerbrücke durchgeführt. Die Ergebnisse zeigen, dass die Messunsicherheit bei den ausserhalb des Labors durchgeführten Messungen zunimmt. Bei der Messung von Relativverschiebungen zwischen zwei Punkten sind die Unterschiede jedoch relativ klein.

Eine abschliessende Überprüfung dieser Ergebnisse erfolgte durch DIC-Messungen am Chillon-Viadukt auf der Autobahn A9. Es wurde ein Riss in der Nähe der Verankerung eines der Spannglieder in der Bodenplatte des Kastenträgers untersucht. Der Riss öffnete und schloss sich bei der Durchfahrt schwerer Lastwagen um etwa ±15 µm (0,015 mm). Zur Validierung der Messungen wurden zwei Omega-Dehnungsmesssensoren über dem Riss installiert. Die DIC-Ergebnisse zeigen eine gute Übereinstimmung mit den Kontrollmessungen mit einer gewissen Abweichung, die der geschätzten Messunsicherheit entspricht.

Ergänzende bildbasierte Techniken für die anfängliche und langfristige Riss-Charakterisierung

DIC-Messungen sind genau und vielseitig, da sie Informationen über einen gesamten dreidimensionalen Bereich des Tragwerks liefern können. Zu diesem Zweck wurde eine Reihe von Bildern mit einem Referenzbild verglichen. Eine notwendige Voraussetzung für die Korrelation ist, dass die Bilder mit der gleichen relativen Position zwischen den Kameras aufgenommen werden müssen. Diese Bedingung stellt zwei Einschränkungen für die Anwendung von DIC in bestehenden Tragwerken dar:

- Wenn im Referenzbild bereits ein Riss vorhanden ist, kann die gesamte Risskinematik nicht bestimmt werden, und die Rissgeometrie kann nur dann bestimmt werden, wenn sich die Öffnung (oder/und die Schiebung) zumindest geringfügig verändert hat, z. B. aufgrund von Verkehrsbelastung oder Temperaturschwankungen.
- Die Demontage und Montage des Messsystems zwischen den Inspektionen führt unweigerlich zu unterschiedlichen relativen Kamerapositionen bei den aufeinanderfolgenden Inspektionen. Folglich können die Bilder der neuen Inspektionen nicht mit denen der ersten Inspektion korreliert werden. Daher können keine Informationen über die Veränderung zwischen den Inspektionen gewonnen werden. Die einzige Möglichkeit, dies zu erreichen, wäre, das DIC-Messsystem an Ort und Stelle zu belassen. Dies ist äusserst ungünstig, da für jedes inspizierte Bauwerk ein DIC-Messsystem einschliesslich seiner Wartung erforderlich wäre.

Um diese Einschränkungen zu überwinden, werden zwei alternative Techniken vorgeschlagen. Die erste Technik zielt darauf ab, den ursprünglichen Riss auf der Grundlage von Algorithmen zur direkten Erkennung zu charakterisieren. In einem ersten Schritt werden die Risseigenschaften anhand der in einem einzigen Bild enthaltenen Informationen erkannt. In einem zweiten Schritt werden die erkannten Rissufer überlagert, um die Risskinematik zu bestimmen. Zu diesem Zweck wurden zwei frei zugängliche Programme verwendet. Es wurden Versuche durchgeführt, um die Messunsicherheit der Risskinematik unter Laborbedingungen zu quantifizieren. Die Ergebnisse zeigen, dass die Rissgeometrie mit einer Unsicherheit von ±1 Pixel für die Rissöffnung und ±2 Pixel für die Rissverschiebung gut charakterisiert werden kann. Die Messunsicherheit ist grösser als bei der Verwendung konventioneller DIC. Die einzigen erforderlichen Hilfsmittel sind eine Digitalkamera und ein Computer.

Die zweite Technik zielt darauf ab, die Rissverschiebungen für die Langzeitüberwachung zu bestimmen. Das Verfahren beruht auf der Verfolgung der Lage von Markern, die auf beiden Seiten des Risses angebracht sind. Durch den Vergleich der Lage der Marker bei aufeinanderfolgenden Inspektionen und die Betrachtung eines Rissufers als Referenz, bilden die Marker auf der anderen Seite die Verschiebungen des Risses ab. Folglich können sie zur Bestimmung der Risskinematik verwendet werden, die zwischen den Messungen stattgefunden hat. Die Temperaturschwankungen müssen angesichts des grösseren Abstands zwischen dem Zentrum der Marker und den Rissufern berücksichtigt werden. Es wird ein Modell zur Abschätzung der erwarteten Unsicherheit auf der Grundlage der Anzahl der Marker und ihrer Anordnung vorgeschlagen. Das System wurde unter Laborbedingungen mit einem Biegeversuch an einem kleinen Stahlbetonbalkengetestet. Die Technik erfasst die Risskinematik und liefert ähnliche Ergebnisse wie die mit herkömmlicher DIC gemessenen. Die Ergebnisse liegen innerhalb der durch das Unsicherheitsmodell geschätzten Toleranz.

Eine abschliessende Validierung dieser Techniken wurde an demselben Riss durchgeführt, der für die Validierung der Kurzzeitmessungen mit konventioneller DIC verwendet wurde. Die ursprüngliche Riss-Charakterisierungstechnik konnte den Riss genau erkennen. Die gemessenen Rissuferverschiebungen wurden mit den Ergebnissen verglichen, die mit einem Rissmikroskop und einem Risslineal erzielt wurden. Die Ergebnisse liegen in den meisten Punkten innerhalb der bei den Laborversuchen beobachteten Toleranzen. In einigen Fällen wurden jedoch grössere Unterschiede festgestellt. Dies ist verständlich, da in vielen Fällen das Ufer bestehender Risse leicht beschädigt oder erodiert sind. Ein Test der Technik wurde ebenfalls über einen halben Tag durchgeführt. Die Ergebnisse werden mit herkömmlichen Kurzzeit-DIC-Messungen verglichen und zeigen eine gute Übereinstimmung. Zusammenfassend kommt man zum Schluss, dass die vorgeschlagenen Techniken zur Überwindung der konventionellen DIC- Einschränkungen eingesetzt werden können, wobei sich die Messunsicherheit leicht erhöht.

Ausziehversuche zur Untersuchung der Verbunds Beton-Bewehrungsstab

Die Verbundkräfte zwischen den Bewehrungsstäben und dem Beton sind ein wesentlicher Bestandteil des Rissverhaltens von Stahlbetonbauteilen. Aus diesem Grund wurde ein Versuchsprogramm durchgeführt, um die Beziehung zwischen dem lokalen Verbundschlupfverhalten (basierend auf kurzen Ausziehversuchen) und dem Verhalten von Verankerungen mittlerer Länge zu verbessern. Untersucht wurde der Einfluss verschiedener Parameter, die bei üblichen Bauanwendungen typischerweise variieren können, darunter die Betonüberdeckung, die Lage des Bewehrungsstabs während des Betonierens (Betonierlage), die Rippengeometrie und die Ausrichtung der Rippen in Bezug auf die nächstgelegene Betonoberfläche. Die geprüften Stäbe wurden mit faseroptischen Sensoren instrumentiert und die Betonoberfläche mit DIC verfolgt. Ein speziell entwickelter Prüfrahmen wurde verwendet, um den Einfluss auf die Entwicklung sekundärer konischer Risse in der Nähe des belasteten Stabenden zu minimieren.

Der Einfluss der Betonüberdeckung stimmt mit früheren Untersuchungen überein. Eine Vergrösserung der Überdeckung erhöht die Betonumschnürung und damit die aktivierten Verbundspannungen bei kleinen Schiebungen und den Verbundwiderstand. Der Versagensmodus von Probekörpern mit einer Überdeckung von einem Stabdurchmesser wird durch das Abplatzen der Betonüberdeckung verursacht. Bei Überdeckungen von 3 und 5 Stabdurchmessern wurde das Versagen durch spaltbedingtes Ausreissen verursacht. Alle Ergebnisse zeigen eine erhebliche Verringerung der aktivierten Verbundspannungen in einem Abstand von etwa 1 bis 3 Stabdurchmessern vom Hauptriss. In diesem Bereich folgt die Last-Verformungskurve dem gleichen aufsteigenden Ast wie der Rest des Stabes mit einem plötzlichen Verlust der Verbundspannungen.

Der Einfluss der Betonierbedingungen wurde für alle betrachteten Betonüberdeckungen bestätigt und stimmt mit früheren Untersuchungen überein. Die Stäbe unter schlechten Betonierbedingungen (horizontale Bewehrungen im oberen Bereich des betonierten Bauteils) weisen den geringsten Verankerungswiderstand auf. Die Stäbe unter guten Betonierbedingungen (im unteren Bereich nah bei der Bodenschalung) weisen den grössten Verankerungswiderstand auf. Das Verhalten von Stäben, die parallel zur Betonierrichtung ausgerichtet sind, liegt zwischen den schlechten und guten Betonierbedingungen.

Der Einfluss der Rippenausrichtung auf den Verankerungswiderstand ist gering und liegt innerhalb der typischen Streuung bei Verbundprüfungen. Die Ausrichtung scheint einen Einfluss auf die Umlagerungsfähigkeit von Stäben unter schlechten Betonierbedingungen zu haben. Stäbe, bei denen die Rippen senkrecht zur Betonoberfläche angeordnet waren (eine Seite der Rippen befand sich an der Stelle der durch das plastische Setzen und das Betonbluten verursachten Hohlräume), zeigten eine gleichmässigere Verteilung der Verbundspannungen. Aus demselben Grund wiesen diese Stäbe geringere Verbundspannungen für kleine Schlupfwerte auf, was darauf hindeutet, dass dieser Effekt Im Gebrauchszustand einen grösseren Einfluss haben könnte.

Der Einfluss der Rippengeometrie bei Proben mit einer Betonüberdeckung von 1 Stabdurchmesser zeigte einige Unterschiede, die durch die Ausrichtung der Rippen in Bezug auf die Oberfläche erklärt werden können. Bei Proben mit einer Überdeckung von 5 Stabdurchmessern sind Unterschiede zu beobachten, die nicht mit den Unterschieden im Verbundindex der Stäbe übereinstimmen.

Die detaillierten Messungen mit DIC und faseroptischen Messungen haben gezeigt, dass die Verringerung der lokalen Verbund-Schlupf-Spannungen für kleine und mässige Betonüberdeckungen in Bezug auf das Auszugsversagen durch die Entwicklung von Abplatzungen (parallel zum Stab und annähernd parallel zur Betonoberfläche), Spaltrissen (parallel zum Stab und annähernd senkrecht zur Betonoberfläche) und konischen Rissen, die zu Betonkegelausbrüchen in der Nähe des belasteten Stabendes führen (was typischerweise der Rissebene entspricht), erklärt werden kann.

Verbesserung der Beziehung zwischen Stabspannung und Rissbreite

In der Literatur finden sich umfangreiche Untersuchungen über die Beziehung zwischen der Spannung in der Bewehrung und der Rissbreite. Dies wird in der Regel durch die Rissbreitenformulierungen in den Normen behandelt, die verwendet werden, um die vorhergesagte Rissöffnung im Grenzzustand der Gebrauchstauglichkeit in Abhängigkeit von der berechneten Stahlspannung beim Entwurf eines neuen Bauwerks zu überprüfen. Das Ziel dieser Forschung ist das Gegenteil, indem die Tatsache ausgenutzt wird, dass im Falle eines bestehenden Tragwerks zusätzliche Informationen verfügbar sind, so dass es möglich sein sollte, die Stahlspannung für einen Ermüdungsnachweis auf der Grundlage der Variation der gemessenen Rissöffnung zu schätzen.

Es wird das mechanische Modell betrachtet, das als Grundlage für Rissformulierungen in aktuellen Normen dient. Basierend auf einer Sensitivitätsanalyse ist die angenommene Verbundspannung nach dem Rissabstand, der bei einem bestehenden Tragwerk bekannt ist, einer der Haupteinflussparameter. Das Schwinden kann die Risslast und die Spannungen im Stab erheblich beeinflussen. Die Vernachlässigung dieses Effekts führt jedoch zu einer konservativen Schätzung der Stabspannungen. Dies ist vorteilhaft, da die Unsicherheit bei der Abschätzung der schwindbedingten Effekte in realen Bauwerken erheblich ist.

Es wurde eine Versuchsserie durchgeführt, um die Aktivierung von Verbundspannungen in Stahlbetonbauteilen mit Hilfe von DIC und verteilten, faseroptischen Sensoren zu bewerten. Darüber hinaus wurden weitere Versuche aus der Literatur analysiert, bei denen dieselben Messtechniken verwendet wurden. Die experimentellen Ergebnisse zeigen, dass die aktivierten Verbundspannungen in den meisten Fällen niedriger sind als die in den aktuellen Normen angenommenen Werte. Die aktivierten Verbundspannungen in den Bügeln bilden eine Ausnahme, da die experimentellen Ergebnisse Verbundspannungen zeigen, die ähnlich oder grösser sind als die vorgeschlagenen Werte der aktuellen Normen. Die Analyse der zyklischen Versuche zeigt, dass in den ersten 10 bis 15 Zyklen eine beträchtliche Verringerung und mit den folgenden Zyklen eine Stabilisierung eintritt.

Es wird ein verfeinertes lokales Modell zur Charakterisierung der Verbundaktivierung vorgeschlagen, das auf mechanischen Überlegungen und den experimentellen Ergebnissen der Ausziehversuche beruht. Unter Verwendung dieses lokalen Modells wird ein Ausdruck zur Abschätzung der Verbundspannungen in einem gerissenen Element abgeleitet. Dieser Ausdruck berücksichtigt die Rissbreite, die Betonierbedingungen, das Vorhandensein von Längsrissen und die zyklische Belastung. Die Ergebnisse werden mit den experimentellen Werten verglichen und liefern angesichts der Verbundergebnissen innewohnenden Variabilität zufriedenstellende Ergebnisse.

Unter Verwendung der gemessenen Rissabstände verbessert die Anwendung der betrachteten Rissöffnungsformulierung mit den vorgeschlagenen Verbundspannungen die Abschätzung der Stahlspannungen im Vergleich zu den aktuellen Norm-Formulierungen. Die Abschätzungen unter Verwendung der Norm-Formulierungen und der berechneten mittleren Rissabstände unterscheiden sich erheblich von den experimentellen Ergebnissen. Die Verbesserung ist vor allem für kleine Rissbreiten relevant. Bei grossen Rissbreiten ist der relative Fehler bei den Spannungsschätzungen geringer. Dies ist auf die Tatsache zurückzuführen, dass die Spannungen im Stab grösser sind. Daher hat der Fehler in der berechneten Stabspannung infolge einer falschen Schätzung der Verbundspannungen eine geringere relative Auswirkung.

Experimentelle Untersuchung der Dübelwirkung in Bewehrungsstäben durch verfeinerte Messungen

Bei typischen Stahlbetonkonstruktionen ist die Bewehrung für die Aufnahme von Normalkräften ausgelegt, sie kann jedoch auch Querkräften durch Dübelwirkung widerstehen. Letztere entsteht bei der Schiebung von Rissen, die quer zum Bewehrungsstab verlaufen, oder bei der Öffnung von Rissen, die in Bezug auf den Stab geneigt sind. Die Dübelwirkung wird in der Regel der Einfachheit halber bei der Bemessung vernachlässigt, kann aber entweder explizit in mechanischen Modellen oder implizit in empirischen Beziehungen berücksichtigt werden. Darüber hinaus gibt es Fälle, in denen die Kraftübertragung zwischen verschiedenen Betonelementen explizit von der Dübelwirkung abhängt, wie z. B. bei Verbindungen zwischen Fertigteilen oder zwischen zwei zu unterschiedlichen Zeiten gegossenen Betonteilen. Andererseits kann sich die Dübelwirkung negativ auf den Ermüdungswiderstand von Bewehrungsstäben auswirken, die einer zyklischen Belastung ausgesetzt sind, und zwar aufgrund lokaler Spannungskonzentrationen in der Nähe von Schnittstellen infolge von Relativbewegungen, entweder durch Gleiten oder durch Öffnen von Rissen, die nicht senkrecht zum Stab verlaufen. Für die Bewertung der verbleibenden Kapazität bestehender Bauwerke sind verbesserte Modelle erforderlich, einschliesslich realistischer Modelle für das Verhalten von Beton, Stahl und deren Schnittstellen. Zu diesem Zweck wird in Kapitel 6 ein Beitrag zum besseren Verständnis der Dübelwirkung anhand von zwei Versuchsserien vorgestellt.

Die erste Versuchsserie konzentrierte sich auf das Verhalten eines Bewehrungsstabs, der einer Dübelbeanspruchung ausgesetzt war: Die Betonproben mit den eingebetteten Stäben wurden in einem speziell angefertigten Versuchsaufbau platziert und mit monotonen oder zyklischen geringen Spannungen mit einer Längs- und einer Querrissöffnungskomponente ausgesetzt, bis zur Entwicklung der vollen plastischen Kapazität des Dübels und bis zum Bruch. Das Messsystem umfasste die Verfolgung des Verschiebungsfeldes an der Betonoberfläche und der Dehnungen im Bewehrungsstab mit Hilfe von optischen Fasern, die in Längsrillen auf der Oberfläche des Stabes eingeklebt waren. Aus letzteren Messungen lassen sich die inneren Kräfte im Bewehrungsstab und seine verformte Lage sowie der Kontaktdruck zwischen dem Stab und dem umgebenden Beton ableiten. Die Ergebnisse zeigen eine starke Abhängigkeit von den Prüfparametern: Stabdurchmesser, aufgezwungene Risskinematik und Winkel zwischen Stab und Riss. Der grössere Dübelwiderstand ist mit einem grösseren Stabdurchmesser und einem grösseren Winkel zwischen Stab und Riss verbunden. Der Dübelwiderstand erster Ordnung ist dadurch gekennzeichnet, dass der Beton in der Nähe des Risses unter dem Stab zerdrückt wird und der Stab aufgrund der Biegung plastisch fliesst. Eine weitere Erhöhung der Dübelkraft ist möglich, indem die Membranwirkung aktiviert wird, die mit erheblichen Querverschiebungen einhergeht. Messungen mit optischen Fasern zeigen, dass der am stärksten belasteten Querschnitt aufgrund der Biegung durch die Dübelwirkung etwa um das 1,5-fache des Stabdurchmessers vom Riss entfernt ist. Es wird beobachtet, dass die Betonsteifigkeit bei etwa 40 % bis 60 % des Dübelwiderstands erster Ordnung erheblich abnimmt.

In der zweiten Versuchsserie wurde das Verhalten des Betons unter dem Stab genauer untersucht, wenn eine Punktlast an verschiedenen Stellen durch einen Bewehrungsstab in den Beton eingeleitet wird. Der Anstieg sowohl der Maximalkraft als auch der anfänglichen Steifigkeit wurde beobachtet, wenn die Punktlast weiter von der Betonkante entfernt aufgebracht wurde. Dieser Anstieg ist auf die grössere Betonfläche zurückzuführen, die die aufgebrachte Kraft trägt. Es wurde festgestellt, dass die vorgeschlagenen Versuche die vergleichbaren Dübelversuche für die Lastposition in einer Distanz vom 0,9-fachen Stabdurchmesser vom Betonrand reproduzieren können. Diese Angleichung erfolgt, weil diese Kraftposition in etwa der Lage der Resultierenden der bei den Dübelversuchen beobachteten Druckverteilung entlang des Stabes entspricht.

Dübelmodelle zur Vorhersage des Widerstands und der Beziehung zwischen Querverschiebung und Spannung im Bewehrungsstab

Die genaue Modellierung der Dübelwirkung für Ermüdung, Gebrauchstauglichkeit und Grenzzustände der Tragfähigkeit stellt eine Herausforderung dar, da es kaum verfeinerte Messungen der Stahlbewehrung, des Betons und der Stahl-Beton-Interaktion unter zyklischen und monotonen Belastungen gibt. In diesem Zusammenhang wird in Kapitel 7 eine neue Formulierung für die Steifigkeit des Betons unter dem Bewehrungsstab vorgestellt, die im Winkler-Modell verwendet werden soll. Die Formulierung berücksichtigt verschiedene Effekte und ist auf der Grundlage von mechanischen Überlegungen entwickelt uns auf der im Kapitel 6 beschriebenen und Messungen mit optischen Fasern kalibriert worden. Im Hinblick auf den Grenzzustand der Tragfähigkeit werden die bestehenden Modelle zur Berechnung des Dübelwiderstands mit den neuen experimentellen Daten verglichen.

Es wird ein neuer Ausdruck für die Bettungssteifigkeit unter dem Bewehrungsstab vorgeschlagen, der im Winkler-Modell (Balken auf elastischem Fundament) zu verwenden ist. Die anfängliche Steifigkeit berücksichtigt die Auswirkungen folgender Parameter: Winkel zwischen dem Riss und dem Stab, Stabdurchmesser, Betonfestigkeit, Betonierbedingungen, Betonüberdeckung, Anzahl der Lastzyklen und Risse im Beton infolge einer Normalkraft. Es wurde festgestellt, dass bei guten Betonierbedingungen die Steifigkeit unter dem Bewehrungsstab etwa 2-mal grösser ist als bei schlechten Bedingungen. Die Steifigkeit nimmt mit der Betonüberdeckung zu und erreicht ihr Maximum bei einem Verhältnis von Betonüberdeckung zu Stabdurchmesser von etwa 3. Die anfängliche Steifigkeit nimmt allmählich ab, wenn die Querverschiebung zunimmt aufgrund von Spaltrissen, Betonquetschung und Abplatzungen in der Nähe des Risses. Diese Abnahme wird in einem empirischen Ausdruck berücksichtigt, der auf der Grundlage von Versuchsmessungen kalibriert wurde. Das verbesserte Modell sagt das in monotonen Versuchen beobachtete Verhalten von Querkraft und Querverschiebung genau voraus. Darüber hinaus zeigt es eine gute Übereinstimmung bei der Vorhersage der Spitzenspannung in Längsrichtung und stimmt gut mit den Versuchsmessungen aus monotonen und zyklischen Versuchen überein.

Für den Grenzzustand der Tragfähigkeit, wird das auf der Plastizitätstheorie basierende Modell von Rasmussen verwendet, um die Querkraftfestigkeit des Bewehrungsstabs für einen Winkel von 90° zwischen Stab und Riss unter Einbeziehung verschiedener Werte des Umschnürfaktors zu bewerten. Für Winkel kleiner als 90° wird das Modell von Dulacska verwendet. In beiden Fällen zeigen diese Modelle eine gute Übereinstimmung mit den betrachteten Versuchen.

1 Introduction and research objectives

The inspection and monitoring of existing reinforced concrete structures are fundamental to detect problems potentially affecting the structural safety. Cracks are often found in existing structures and they are often one of the indicators used in the periodical visual inspections for structural assessment [1, 2]. However, the evaluation of the safety of a structure based on the presence or absence of cracks is not straightforward. On the one hand, cracks do not necessarily indicate an insufficient level of safety if they are expected and accounted for based on the structural behaviour. At the same time, small cracks might not be an indicator of large resistance reserves in cases governed by fragile failure modes [1, 3].

Reinforced concrete structures can be affected by fatigue due to the variable nature of the loads acting on them (traffic, wind or waves). The long service life of existing structures in Europe [4, 5] combined with the increase in traffic volume and loads of the last years and their expected increase in the future [6, 7] are two factors that could contribute to the fatigue damage of existing infrastructure. In this context, structures such as railway bridges with a larger ratio of live to permanent load are more susceptible to fatigue. In other structures with relatively low variable loads, poorly conceived or executed details can increase the risk of fatigue. Fatigue damage in concrete structures is not easily identified [8] and fatigue is rarely identified as the sole reason for failure of a structure [9, 10, 8]. Nevertheless, experimental research with reinforced concrete elements has shown that the fatigue failure is possible with a lower number of cycles compared to fatigue tests of bare bars [11, 9, 8]. It must be noted that in typical reinforced concrete structures, the reinforcement is fairly distributed, thus the failure of a single bar might only increase the demand on the neighbouring bars. Moreover, a big part of the structural systems in existing structures are statically undetermined and have a certain redistribution capacity, which limits the effect of local damage.

The current approach for fatigue design is to compare the expected stress variations in the reinforcement (based on an elastic cracked sectional analysis) with fatigue resistance of the reinforcement obtained from the S-N curves based on the estimated number of cycles [12]. This procedure is practical and well-justified for the design of new structures. However, it can be cumbersome for existing structures when unusual cracks are detected in unexpected regions and where the acting loads are unknown. In such cases, a common approach is to monitor the crack width to see if there are permanent changes. Long-term measurements are generally required to capture the daily and seasonal variations. This is typically done using linear variable differential transformers (LVDTs, see Fig. 1b) or omega gauges (Fig. 1c); or, more recently, with Digital Image Correlation (DIC) (Fig. 1d).

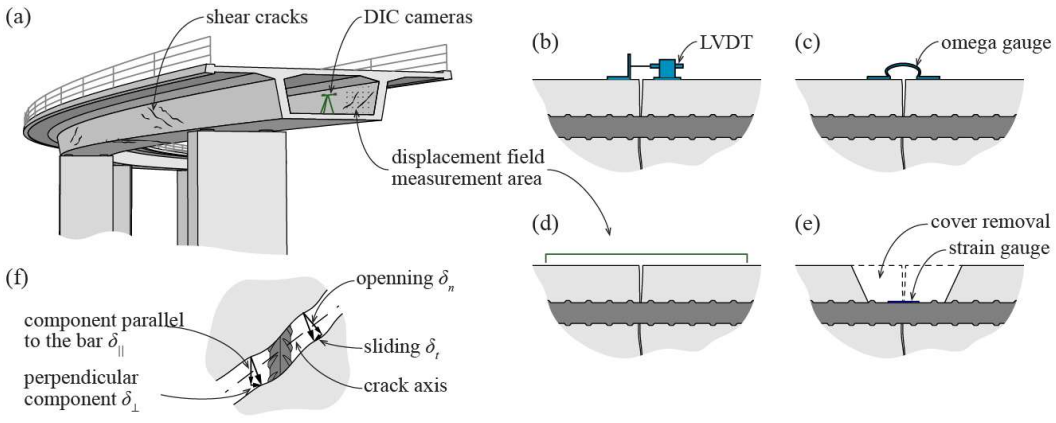

Fig. 1 *Schematic representation of typical measurement systems: (a) studied region; (b) LVDT; (c) omega gauge; (d) DIC; and (e) strain gauge.*

Another technique to evaluate the potential risk of fatigue in existing concrete structures is to directly measure the stress variations by gluing a strain gauge to the surface of the bar (Fig. 1e). This approach is more intrusive, as it requires the detection of the reinforcement and the removal of the concrete cover. Recent experimental studies using DIC and distributed fibre optical sensors in beams subjected to shear and bending have shown that significant local bending occurs at the reinforcement at the crack location due to dowel action, which might influence the strain measurements if only one gauge is installed [13, [14, 3].

From a phenomenological point of view, the stresses in the reinforcement are directly related to the kinematics of the crack at the bar location. Crack kinematics are typically characterized by two components: opening (component perpendicular to the crack axis) and sliding (relative displacement of the crack lips in the direction parallel to the crack axis), as shown in Fig. 1f. The crack lip displacement can also be decomposed in the directions parallel and perpendicular to the bar axis. The component parallel to the bar axis induces an axial force in the bar, typically considered in crack formulations. The component perpendicular to the bar axis induces bending in the bar, often referred to as dowel action. A better understanding of these phenomena and an accurate prediction of generated stress variations is crucial for the assessment of existing structures.

To that aim, this research is grounded on three main goals. The first goal is to determine the accuracy that can be expected for the determination of crack kinematics in existing structures. Extensive research has shown the feasibility of DIC measurements in laboratory conditions; however, less information is available for measurements in-situ. An experimental programme has been conducted to compare the accuracy of DIC measurements in different conditions. Furthermore, different techniques have been investigated to overcome some of the limitations of this technique. These techniques are validated in an existing bridge under traffic loads. This is addressed in Chapters 2 and 3.

The second goal is to improve the understanding of cracking and the activation of axial forces in the reinforcement. Recent developments using distributed fibre optical sensors has shown great potential to understand the activation of bond stresses along the reinforcement. An experimental programme using this technique in combination with DIC has been carried out to better characterize the parameters involved in the response of cracked elements. On this basis, new bond values are proposed in combination with a mechanical based formulation to improve the crack width-bar stress relationship. This is addressed in Chapters 4 and 5.

Finally, the third goal is to improve a prediction of the dowel resistance and the peak stress in the reinforcing bar due to dowel action. To that aim, a first test series was conducted focusing on the dowel subjected to monotonic and low-stress cyclic loads, using refined measurements (3D-DIC and optical fibres). The results show a strong dependency on the test variables: diameter of the bar, imposed crack kinematics and angle between the bar and the crack. A second test series looked more closely at the behaviour of concrete underneath the bar, in the presence of a point load introduced at various locations into concrete through a reinforcing bar. Based on these measurements, a new formulation of the bearing stiffness of concrete under the reinforcing bar to be used in the Winkler model is proposed. The formulation accounts for various effects, is based on mechanical considerations and is calibrated on the results of measurements with optical fibres. Regarding the ultimate limit state, the Rasmussen's and Dulacska's models are used to evaluate the dowel resistance for various cracks between the bar and the crack. This is addressed in Chapters 6 and 7.

The cracked response of reinforced concrete structures is fundamental for their functionality, as it influences the stiffness of the members (deflections and vibrations) and their water tightness. Furthermore, crack control is important for durability and aesthetic reasons. For this reason, construction standards often provide limits to the crack widths depending on the requirements of the structure. Crack width limits and its implications on the durability of structures are not in the scope of the present research.

2 Limits of applicability of Digital Image Correlation in-situ

2.1 Introduction

The increase in traffic volume and loads in the past and their anticipated growth [6], combined with the long service life of European structures [4, 5], call for efficient and accurate monitoring and assessment of existing infrastructures. During inspections of reinforced and prestressed concrete structures, cracks are often detected. However, the safety assessment of the structure based on the observed cracks is challenging since their presence does not necessarily indicate an insufficient level of safety. At the same time, small crack openings are not necessarily related to a sufficient margin of safety in cases where fragile failure modes govern [1, 3]. For these reasons, both accurate verification models and detailed measurement techniques are required to assess the condition of structures throughout their life and to plan appropriate interventions while minimizing the impact on the users.

During bridge inspections, cracks are typically characterized by visual comparison using crack width rulers (Fig. 2a) or microscopes (Fig. 2b), yielding the crack width at certain locations. This evaluation technique can be time consuming and subjective to the inspector's experience [15, 16]. Gauges or extensometers (Fig. 2c) can also be used to measure the relative displacement of the crack lips. Each sensor measures the displacement in one direction in one point, therefore multiple sensors are often necessary to obtain a clear understanding of the crack kinematics (opening and sliding). The number of sensors is however limited by the available space around the crack [17]. The use of a demountable mechanical strain gauge (DEMEC [18]) is also suitable for long-term monitoring. It makes use of metallic targets arranged around the crack. The relative distances of the targets are measured in the reference and deformed states and can be used to compute the relative crack lips displacement. This technique is convenient because it does not require permanent installation of sensors but it is inappropriate for monitoring short-term phenomena (such as the effect of passing traffic) and can be time-consuming if a large number of targets are used.

To overcome these limitations, extensive research has focused on automated crack detection using images. Various types of images can be used for this purpose. This section focuses on digital images in the visible spectrum, as they are the most commonly used [19]. Two main approaches can be distinguished: direct or indirect detection. Direct detection techniques use image processing tools to find the cracks based on the information contained in a single image. More information is provided in Section 3. Indirect detection techniques use data obtained by comparing subsequent images to a reference image.

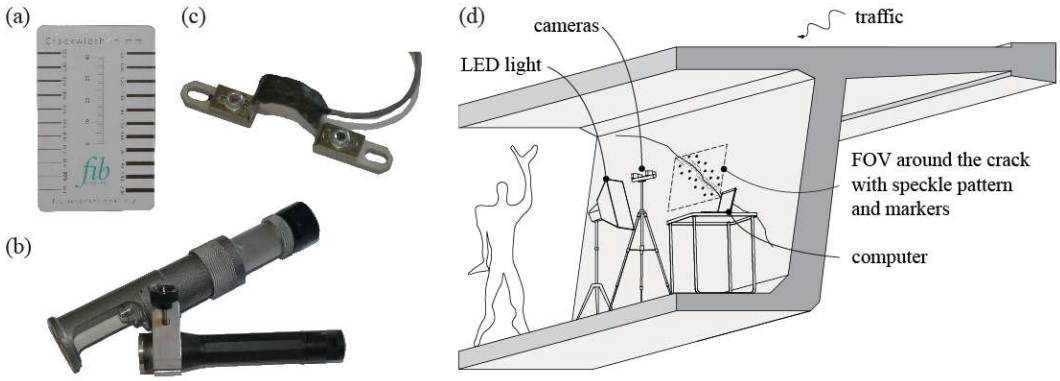

Fig. 2 *Crack width measurement tools: (a) crack width ruler; (b) crack width microscope, (c) omega gauge; and (d) DIC-3D set-up.*

Digital Image Correlation (DIC) is an indirect image-based technique that is well established in structural engineering [20, 21, 22]. Within the measurement surface or field of vision (FOV), the algorithm tracks groups of pixels (subsets) through a sequence of images and compares their position to the reference image. After interpolation between the subsets continuous displacement and strain fields are obtained. The accuracy is improved by maximising the number of high-contrast interfaces in the field of vision. For this reason, a “speckle pattern”, consisting of a random disposition of black dots on a white background, is typically used. By using one camera with the plane of the sensor (perpendicular to the objective axis) oriented parallel to the surface, the in-plane displacements can be measured (DIC-2D), but the addition of a second camera, which captures simultaneous images, allows the measurement of out-of-plane displacements using the principle of stereovision (DIC-3D, see Fig.2d).

Two main sources of uncertainty influence the measurement accuracy: the errors in the algorithm for the calculation of the displacements from the acquired images and the errors introduced by the imperfections of the optical system model. The former is influenced by the correlation algorithm and the quality of the pictures. The bias of modern algorithms is small (around 1/200 pixel [20]) and considerably lower than the uncertainty derived from the optical system model. The latter, is mainly caused by displacements of the cameras, ambient conditions (like air flow in the region between the camera and the studied area causing Schlieren effect) or deficient calibration [22, 23]. For this reason, the measurement uncertainty provided by the DIC system manufacturers (typically around 1/100 pixel) can only be obtained under extremely controlled laboratory conditions [23]. Typical measurement uncertainty in laboratory tests reported in the literature are around 1/30 to 1/50 pixel [24, 23, 3].

Since the early 2000s, the number of applications of DIC to monitor existing structures is increasing. Several authors have used DIC to measure bridge deflections under traffic [25, 26, 27, 28, 29] or displacements in other types of structures such as beams or retaining walls [30, 31]. Other applications aim directly at characterizing the behaviour of a crack [32, 33, 34]. Unfortunately, in most applications, the accuracy of the measurements is not mentioned. Generic values of around 1/50 pixel are occasionally provided [27, 32].

One well known limitation of DIC measurements also shared with the installation of omega gages or other types of displacement transducers is that only the relative movement from installation can be measured. Concerning long-term measurements, the use of DIC can be challenging due to the fact that the system requires the comparison of a set of images with the reference image. The relative position of the cameras cannot change between the reference image and the measurement images. Consequently, if the system is dismounted and installed in the next inspection, the new measurements cannot be correlated to the first inspection image. These two aspects will be further developed in Section 3.

In this section a systematic investigation of the influence of variable lighting conditions and vibrations on the DIC measurement uncertainty is presented. This includes tests in laboratory conditions and in-situ measurements on different structures.

2.2 Measurement uncertainty characterization

A clear characterization of the measurement uncertainty is required in order to determine the resolution of the performed measurements. Other terms such as noise-floor are often found in the literature. This is typically done performing a Zero Displacement Test (ZDT) that consists in the acquisition of several images of the measured region ensuring no displacements and no deformations of the measurement regions. Under these conditions, the results of the image correlation analysis should yield zero displacement and, therefore, zero strains. The measured displacements are errors and, therefore, any actual mechanical displacement smaller than the measured error cannot be distinguished from the noise of the measurement system [35].

The uncertainty is typically characterized by the standard deviation of the errors. At the same time, the error distributions vary spatially and in “time” (i.e. between different images).

Typically, both metrics are similar and both should be compared [35]. The guidelines of the Association of German Engineers performing (VDI 2626 [36]) propose a quantification method for the spatial standard deviation within one image by subdividing the measurement region in a grid of 20x20 subregions. Each subregion should include at least 9 data points [36].

Based on the experience of the authors, the temporal standard deviation in the different regions of the FOV is more useful for practical applications, because it allows to detect zones of the image where the expected uncertainty can be larger. Consequently, quantification of the measurement uncertainty in this report is done using the temporal standard deviation in a grid of 20x20 subregions. It is recommended to use between 10 and 50 images. Within this range the amount of generated data and the computation time remain reasonable. For each acquired image, the correlation analysis provides the movements for each subset. After subtracting the rigid body displacements (in this case zero) the average of the displacements of all the subsets (points) in each subregion can be calculated. For each subregion, the measurement uncertainty is quantified by the standard deviation of the in-plane displacements (Eq. 1) and out-of-plane displacements (Eq. 2):

$$NV_{uv} = \sqrt{\frac{1}{M}\sum_{q=1}^{M}\left(u_q^2 + v_q^2\right)} \tag{1}$$

$$NV_{w} = \sqrt{\frac{1}{M}\sum_{q=1}^{M} w_q^2} \tag{2}$$

where u_q, v_q or w_q are the average measured displacement from all the subsets in a subregion in the horizontal (u), vertical (v) and out-of-plane (w) direction; and M is the number of acquired images.

2.3 Influence of parameters affecting the optical system model

2.3.1 DIC measurement system

The different tests were carried out at the Structural Concrete Laboratory of École Polytechnique Fédérale de Lausanne or in-situ in structures in the Lausanne region. The optical setup used comprised of two digital cameras Manta G-419 4.2 Mpx arranged with a relative angle (stereo-angle) of 16° to maximize in-plane measurement precision. Recommended stereo-angles range between 15-35° depending on the used lenses [35]. The system was positioned 1.5 m away from the measurement surface. The image and pixel size were 2048×2048 pixels (620×620 mm) and 0.30 mm, respectively. Marker detection and image correlation analysis were performed using the software VIC3D 8 [37]. The measurement surface was composed of two steel plates of 30x30 cm mounted on 4 magnets. The steel surface was painted with two thin layers of white paint, on top of which a speckle pattern of random black dots with an approximate diameter of 1.5 mm was printed using a handheld printer. This size corresponding to approximately 5 pixels (within the typically recommended values 3-5 pixels [38]) was chosen because it is the smallest size that could be printed with the chosen printing device.

Before each application the DIC system was installed and calibrated for optimal performance [38, 23, 37]. The optimal parameters of the DIC measurement system and the calibration can vary depending on multiple factors, it is therefore recommended to follow general guidelines [35] and more the software and manufacturer guidelines [38].

2.3.2 Variable lighting

The effect of different lighting conditions on the measurement uncertainty was evaluated by a test in the laboratory, see Fig. 3a. The optimal exposure time for the tested conditions was 3.3 ms.

To represent the variable lighting conditions the exposure time was varied between 0.5 to 5.0 ms. The results over the measurement surface is shown in Fig. 3b. The measurement uncertainty for an exposure time of 3.3 ms near the centre of the field of vision is 5.5 µm (1/54 pixel). It can be observed that independently of the exposure time the noise levels are lower in the centre of the field of vision. This is due to the irregular lighting conditions within the same image. For this test two LED lamps were used and, consequently, the emitted light of the two sources overlap in the centre of the image. In consequence, the ideal choice of exposure time and aperture will not be uniform throughout the image, resulting in the observed noise variation.

Fig. 3c shows the maximum and the average value of all the subregions for each exposure time. The maximum values are approximately 2 µm larger for the tested conditions. The results show that for exposure times within 2 to 4 ms the measurement uncertainty is similar. This is achieved by using normalized interpolation methods in the correlation criteria [37].

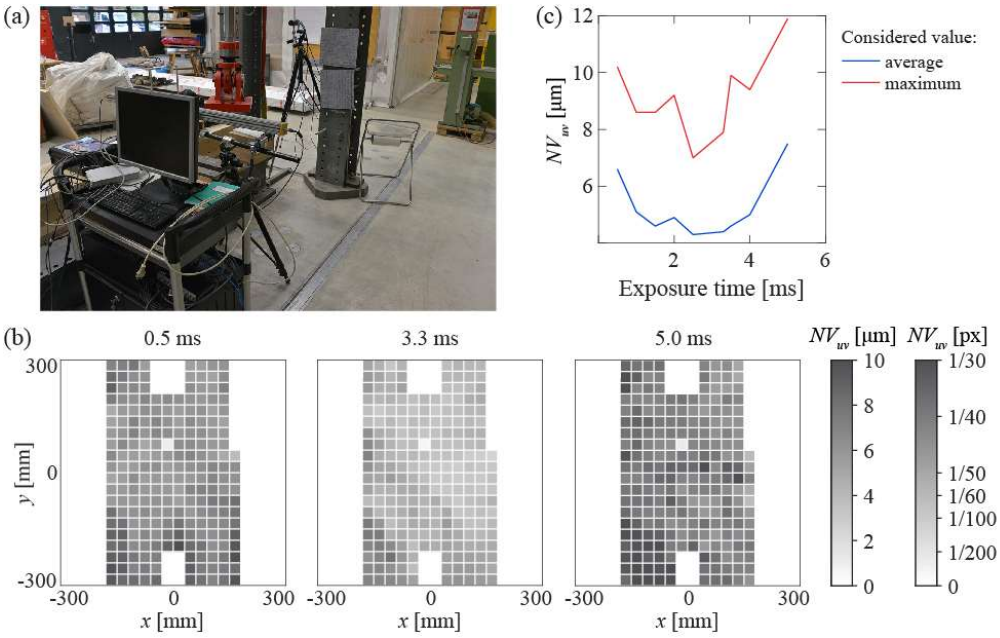

Fig. 3: *Influence of lighting conditions in the measurement uncertainty: (a) test set-up; (b) in-plane noise levels for exposure times of 0.5 ms, 3.3 ms and 5.0 ms; and (c) average and maximum in-plane noise levels for the measured surface.*

2.3.3 Influence of vibrations

The vibrations of the camera support (caused by the movement of the structure, wind or other perturbations in the camera support) will be observed as rigid body displacements on the measurement surface. Without any additional data, it is not possible to distinguish the movements of the camera from the movements of the measurement surface [39]. In order to quantify the influence on the measurement uncertainty three conditions have been compared:

- Laboratory: to serve as reference with no vibrations or lighting variations (Fig. 3a).
- Outdoor: the measurement system was exposed to the wind and outdoor light variations, but it was placed on stable ground (Fig. 4a).
- Footbridge (F): the measurement system was installed on a footbridge crossing the metro tracks. The structure vibrated under the excitation of pedestrians, passing trains and wind. Outdoor light variations were also expected (Fig. 4b).

The resulting measurement uncertainties for in-plane and out-of-plane displacements are presented in Fig.4c and Fig.4d respectively. The results in all conditions show that the accuracy decreases towards the edges of the FOV. The accuracy of the out-of-plane

displacements is around 2-3 times lower that for the in-plane measurements. This is a known consequence of choosing a rather small stereo-angle [35].

The homogeneity of the lighting has a large influence on the value of the error. In the spatial distribution of *NV* for laboratory conditions, the top part of the FOV shows a larger uncertainty coinciding with the region that was less lit. Additionally, the loss of accuracy in outdoors conditions is clear in the larger values of the uncertainty of both the outdoors and footbridge results. This can be due to the larger air movements than what can be expected inside the laboratory or to added difficulties in ensuring an optimal exposure during image capture because of changing light conditions. However, the effect of vibrations and associated camera movements, which should be visible when comparing the results obtained on the footbridge, do not seem to have a big influence as the results are comparable to the outdoor results. This might be due to the low amplitude of the vibrations in the considered case but might be different in roadway bridges where the range of displacements and accelerations can be larger.

In consequence, a clear reduction of the accuracy is to be expected when performing DIC measurements in in-situ conditions. Nevertheless, the effective uncertainty of around 5 µm in-plane and 12 µm out-of-plane is low and clearly comparable if not better than other measurement techniques.

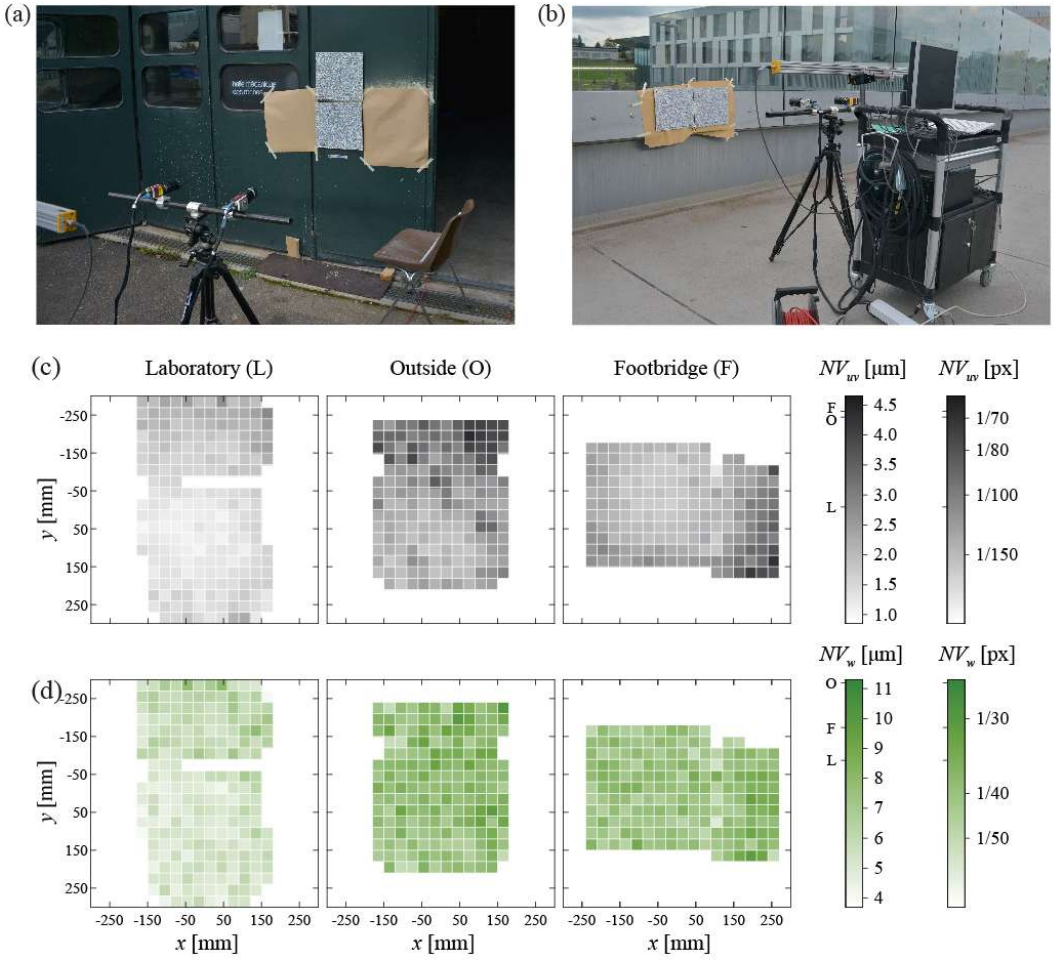

Fig. 4 *Influence of vibrations and light variations in different conditions: images of the test set-up in (a) outdoor and (b) footbridge conditions; (c) measurement uncertainty for in-plane displacements; and (d) measurement uncertainty for out-of-plane displacements.*

2.4 In-situ application

2.4.1 Structure description

The considered crack was detected in one of the Chillon Viaducts (Switzerland). These twin viaducts are post-tensioned reinforced concrete box-girder bridges with a total length 2150 m and average span of 95 m. They were built between 1968 and 1970 by the balanced cantilever method using precast segments produced on-site [40]. The investigated crack is located on the bottom slab of a segment at approximately one fifth of the span (see Fig. 5a,b) next to the anchorage of the prestressing cables that run along the bottom slab to carry positive bending moments. The crack is oriented at approximately 45° with the longitudinal axis of the bridge (see Fig. 5c) and is approximately 2 m long (combination of load introduction and shear between tendon and web). A segment of the crack of length 730 mm was studied within the field of vision of 600×600 mm (see Fig. 5e). After removing the dust, white paint and a speckle patter were applied. The measurement system described in Subsection 2.3.1 was used (see Fig. 5d).

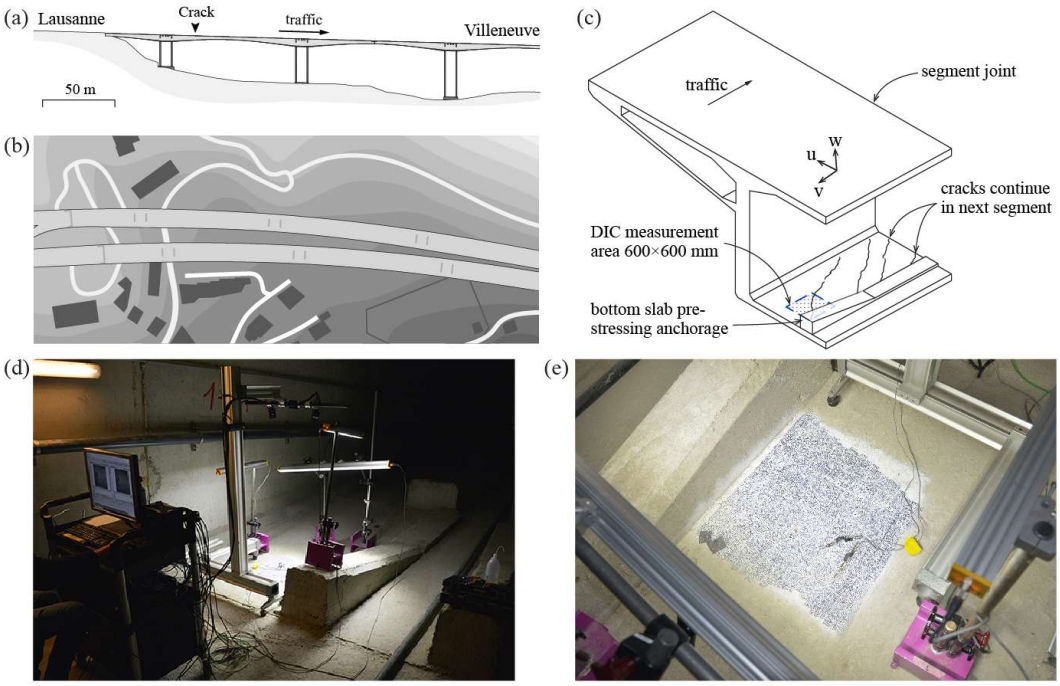

Fig. 5 *In-situ application: partial (a) elevation and (b) plan of the Chillon Viaducts; (c) segment of interest with investigated crack;(d) DIC set-up including cameras, light and the computer for data acquisition; and (e) studied region.*

2.4.2 Measurement uncertainty

Fig. 6 shows the in-plane measurement uncertainty for the results obtained in the Chillon Viaduct. The spatial distribution shown in Fig. 6a presents the same characteristics as the previously described conditions. Fig. 6b displays the average in-plane displacement NV_{uv} for all the subregions with the same x coordinate for the different compared conditions. The uncertainty clearly increases towards the edges of the FOV as mentioned earlier. Furthermore, it can be observed that the uncertainty in the viaduct is larger than in the laboratory conditions but lower than in the outdoor and footbridge measurements. Inside a box girder there is no natural light and the artificial light of the LED lamps has no light variations. The vibrations do not influence the results, as long as the reference images are obtained during periods with no trucks crossing the studied or the neighbouring spans.

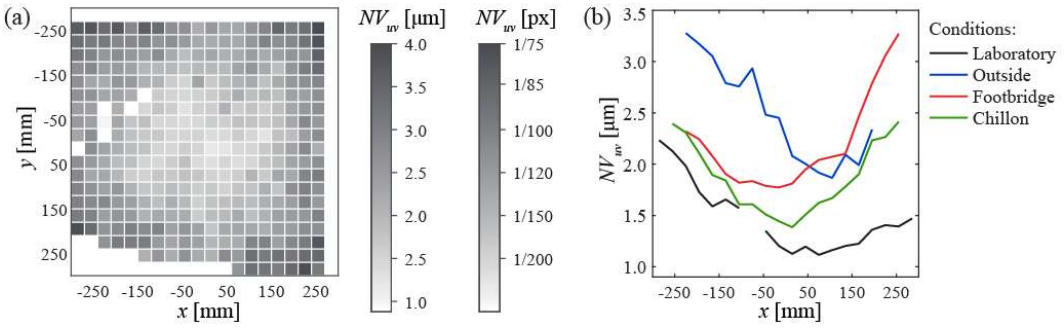

Fig. 6 *Measurement uncertainty for the measurements in the Chillon Viaduct: (a) in-plane measureme§nt uncertainty§§ over the FOV; and (b) comparison of the results along the x axis for all the tested conditions.*

2.4.3 Short-term crack movement characterization

The crack open and closes with the passage of trucks. A set of 375 images obtained during a 15 seconds cycle (acquisition frequency of 25 Hz) triggered by an accelerometer, was used for this purpose. The DIC analysis was performed with VIC-3D [37].

The validation of the results was done by installing two omega gages one in the longitudinal direction of the bridge and the other one perpendicularly to the crack axis, see Fig. 5e. As omega gauges only measure displacements along their longitudinal direction, only the correspondent component of the DIC measurements is plotted. The results of both methods are very similar (fig. 7a). It can be observed that the DIC measurements (blue) follow the omega gauge measurements (black) and fall approximately within the estimated measurement uncertainty from these measurements (black dashed lines).

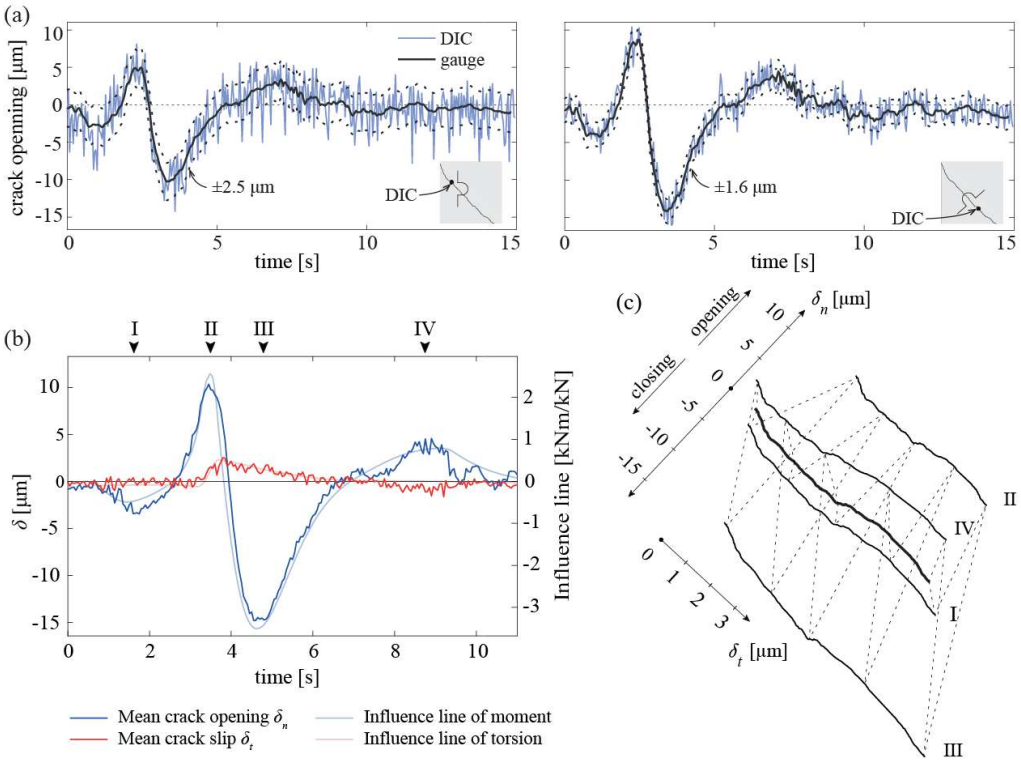

Fig. 7 *Short term measurement results during the passage of a truck: (a) comparison of the local measured crack width in the direction of the omega gauge with the DIC results; (b) comparison of the average opening and sliding over the full monitored length and the influence lines for longitudinal bending moment and torsion; and (c) crack kinematics for the selected instants.*

Fig. 7b presents the average crack opening and slip when a truck passes on the bridge. It must be noted that averaging the crack width over a certain length reduces significantly the uncertainty because of the random nature of the noise. These curves follow well the influence lines of the bending and torsional moments at the crack location. As the weight of the truck and its speed were unknown, the scale of the influence lines has been adjusted to fit the displacements in the graph.

Additionally, the crack geometry and kinematics were computed using the Automated Crack Detection and crack Measurement (ACDM) procedure [41, 42] (subset size: 23; step size: 4; filter size: 7). The results for the selected time steps are illustrated in Fig. 7c after smoothing of the results.

2.5 Conclusions

The limits of applicability of DIC for in-situ applications have been investigated by a series of tests in different conditions. The main findings of the section are the following:

1. DIC measurement systems are an excellent tool to characterize crack geometry and crack kinematics in laboratory conditions and in-situ applications.
2. The measurement uncertainty that can be achieved is influenced by the calibration, the light variations and the air flow between the camera and the measurement surface.
3. The vibrations or relative movements between the cameras and the measurement surface can have an influence on the results, particularly when measuring absolute displacements. For crack opening characterization the influence of vibrations is smaller due to the fact that only relative displacements are computed. Consequently, the rigid body displacements that will be measured due to camera movement will be similar on points close to the crack on both crack lips.
4. The measurement uncertainty for in-situ applications on roadway concrete bridges when the measurements are performed inside the box girder section can be expected to be similar to the uncertainty in laboratory conditions. This is due to the fact that no light variations are expected and air currents inside the bridge are small.
5. The measurement uncertainty for in-situ applications in less controlled conditions (e.g. on roadway concrete bridges when the measurements are performed outside the box girder section) can be expected to be at least two to three times larger than the uncertainty in laboratory conditions.
6. The opening and sliding of existing cracks (present in the reference image) can not be measured using DIC. The geometry and additional crack displacements (with respect to the reference image) can be measured.
7. Its application for long-term monitoring requires that the relative position of the cameras does not change between the inspections. This condition can not be guaranteed if the DIC measurement system is demounted between inspections.

DIC measurements can increase the accuracy and resolution of crack measurements with respect to the conventional measurement techniques. However, the installation of the equipment can be more laborious and time consuming than performing manual measurements. Therefore, the use of DIC measurements is interesting in regions with complex crack patterns where a deep understanding of the crack kinematics is required.

2.6 Outlook and future works

Some questions related to the topics studied in this section remain open. In the following, some of these future research lines are outlined:

- Based on the results presented in this section, the relative movement of the camera support does not have a big influence on the results when measuring the crack kinematics. Some authors have tried to used DIC mounted on drones. However, the results are typically limited to the measurement of the crack openings using markers. Further tests should be performed to determine the feasibility of measurements similar to the ones proposed in this section with an optical system mounted on a drone. This could be beneficial for inaccessible regions of existing structures.
- In addition, the validity of the system in cases where the system is stable but mounted on a different structure remains to be determined. This could be beneficial to assess the

feasibility of this type of measurements from an external support (scissor lift, scaffolding, etc.) in structures where internal inspection is not possible.

3 Complementary image-based techniques for initial and long-term crack characterization

3.1 Introduction

DIC is a high-resolution measurement system that can be used for refined crack characterization in laboratory conditions and in-situ applications. Nevertheless, this system presents two limitations due to the fact that it relies on the comparison to a reference image. Existing cracks cannot be measured if they are already present in the reference image. Furthermore, the implementation of DIC for long term monitoring is difficult, due to the fact that both the reference image and the measurement have to be captured with the same relative positions of the two cameras. Consequently, if the measurement system is removed between inspections this cannot be guaranteed because the camera position will change upon remounting the DIC set-up.

The characterization of the initial crack state can be done using direct detection techniques that use image processing tools to detect cracks using the information contained in a given image and, therefore, do not require a reference.

Direct detection algorithms typically consist of four steps: image acquisition, image pre-processing, crack detection and crack feature extraction [43, 19]. Detection tools targeting multiple defects require a fifth step of classification to distinguish the different types of defects as well as the non-defective features [44, 45, 46]. Several image processing techniques can be used for crack detection, including: thresholding or image binarization [47, 48, 49], edge-based detection (in spatial or frequency domain) [50, 51, 15, 44], morphological operations [52, 44, 43, 45], percolation methods [53] or route finder algorithms [54] amongst others. Machine learning algorithms are another popular approach for direct crack detection that require an extra step to train the algorithms. Numerous artificial neural networks can be found in the literature showing a good performance for defect detection and classification [55, 56, 57]. Recently, deep learning methods and in particular Deep Convolutional Neural Networks (DCNN) have been used for crack detection in concrete elements [46, 58, 59]. The need to train the neural network can be a time-consuming task; at the same time, it provides a big flexibility as these algorithms can be trained with different datasets to address specific user demands.

The performance of the various algorithms is typically evaluated through pixel-wise metrics where the detected pixels are compared with a known reference (often referred as ground truth) [53, 46, 58, 59]. Abdel-Qader et al. [15] compared the fast Fourier transform, the fast Haar transform, and the Canny and Sobel edge detectors on cracked concrete crack decks. According to their study, the fast Haar transform had the highest overall accuracy (86%), however the definition of the comparison criteria is not clear. Dorafshan et al. [46] compared four edge detection methods in the spatial domain, two in the frequency domain and an AlexNet-based DCNN in concrete elements. The results show that the most accurate edge detector was the Laplacian of Gaussian (79% of the cracked pixels and cracks larger than 0.1 mm); however, their performance was worse than the DCNN (86% of the cracked pixels and cracks larger than 0.04 mm). Other studies compare different methods but without providing a clear quantitative metrics [43, 45]. Another approach is the comparison by skeletonization, commonly used for linear structure detection [60, 61] but rarely used for crack detection. These two approaches can be used to validate and compare detection algorithms, and to assess whether a system is suitable for unsupervised use.

The next step is the extraction of the crack features, where various features can be relevant depending on the type of studied defect [19]. Various studies have shown that the crack geometry and kinematics (crack opening and sliding components) can be used to estimate the contribution of the various shear transfer mechanisms in reinforced concrete elements [62, 3]. Furthermore, the stress-state of reinforcement bars in existing structures, which is relevant for fatigue assessment, can be estimated using the crack kinematics and the bar characteristics with appropriate mechanical models. For this reason, this section focuses

on the crack width and crack kinematic measurement. The first required information to obtain crack widths is the pixel size. If multiple images or cameras are used, depth perception using 3D scene reconstruction [45] and stereovision [63] can be used to calculate the pixel size. Alternatively, a more common approach using one camera perpendicular to the surface is to install a visual reference of known dimensions to calculate the pixel size.

Several publications propose algorithms capable of detecting the crack widths. However, few of them provide clear information about the pixel and crack sizes, therefore lacking clear indications about the precision that can be achieved. Dare et al. [54] proposed a system based on the pixel intensity and a threshold to calculate the crack width in pixels in the direction perpendicular to the crack axis, reporting an error of 0.4 pixel. Zhu et al. [64] applied a thinning algorithm to skeletonize the crack and calculated the minimum distance to the crack boundary to estimate the width. The reported measurement error for the maximum crack width over the dimension of the element of 0.35%; however, the dimensions of the elements, cracks and pixel size are rather unclear. Lins et al. [65] proposed a system to measure the width in the direction perpendicular to the axis of single cracks with errors between 7% to 11% (for crack widths of 28.7 and 2.6 mm respectively) on buildings. Kim et al. [49] measured the horizontal crack width to compare different thresholding methods obtaining errors of 6 to 7% (for crack widths of 0.1 to 11.7 mm). Recently, Pantoja-Rosero et al. [66] proposed an algorithm that calculates the crack kinematics from a binary image resulting from the segmentation of a crack image. Using a non-linear least squares optimization algorithm, the two lips of the crack are matched to determine the two displacements and the rotation leading to the minimum error, reporting errors of less than 1 pixel (for crack widths of 6 to 20 mm) and errors of 2 to 14 pixels (for crack widths of 0.4 to 4 mm measured manually with a metric gauge).

Rezaie et al. [58] compared the performance of a DCNN with segmentation by applying a threshold on the principal strain calculated using DIC, concluding that the DCNN outperformed the thresholding approach in some of the considered pixel-wise metrics. The detailed geometry and kinematics (opening and sliding) of cracks within the region monitored with DIC can be extracted manually from these measurements [3] or automatically using the Automated Crack Detection and crack Measurement (ACDM) procedure proposed by Gehri et al. [41, 42]. Pantoja-Rosero et al. [66] compared their algorithm for crack kinematic estimation from imaged crack patterns to results using ACDM, showing comparable results to those in laboratory conditions (for crack widths between 1 to 11 mm).

Concerning the long-term monitoring of cracks, different methods can be found in the literature to compare measurements taken after removing and reinstalling the measurement system. Malesa et al. [67] attempted to solve this problem by fixing a plate around the crack containing markers that allow the deformation of the images after acquisition to simulate as if they were captured from the same location. Ruocci et al. [68] proposed a more sophisticated technique that uses reference points to correct the change of viewpoint. Both these techniques are difficult to implement and result in a drastic reduction of the measurement precision (around 1/20 pixel [67]).

The use of markers in the field of structural engineering was first proposed by Benning et al. [69] and later Valença et al. [17, 70]. They proposed to print a grid of markers on laboratory specimens whose displacements were tracked during the test and then interpolated to obtain the displacement field (same principle as DIC but with a rougher mesh of measurement points). More recently, several research groups proposed some applications for the monitoring of macroscopic cracks undergoing displacements of several millimetres of amplitude in concrete or masonry structures [71, 72, 73, 74]. In these applications, typically a single camera without calibration is used resulting in a measurement uncertainty of approximately ±1 pixel. The crack displacement is measured at discrete points by simply tracking the change of distance between pairs of points. For applications with microscopic cracks undergoing much smaller displacements, there is a need for a similar technique but of much higher precision and which can monitor the complete crack behaviour, including opening, sliding and rotating movements.

In this section, which is adapted from [75], two image-based techniques to characterize the initial state of a crack and for long-term monitoring of cracks are presented. The combination of these techniques with short-term DIC can be used to provide a complete characterization of cracks in existing structures. The literature presented in this subsection shows the large number of tools developed for crack detection; nevertheless, clear limits of application and recommendations for their application are rarely provided. Subsection 3.2 focuses on the initial crack characterization. Two open-source tools initially developed for masonry walls for crack segmentation [58] and crack kinematics estimation [66] are validated in laboratory and in-situ conditions on reinforced concrete structures. Subsection 3.3 focuses on the long-term monitoring of cracks. For this purpose, a complementary technique is proposed using the DIC measurement system and markers positioned around the crack. The accuracy of the technique is validated first in laboratory conditions and then in-situ Furthermore, clear guidelines for the application of these techniques in practice are provided based on the limits of applicability observed in the laboratory and in-situ applications.

3.2 Initial crack characterization

3.2.1 Objective

The technique described in this section aims to characterize the geometry and the initial crack kinematics of cracks that have been detected during inspections of existing structures. This cannot really be achieved by traditional human inspections that are limited to measurements of the crack opening at discrete locations and require a lot of time for the characterization of the crack geometry [15, 16].

3.2.2 Description of the technique

The first step is the crack segmentation of the crack images to generate the corresponding binary image (pixels categorized as cracked or uncracked). For this purpose, a deep learning network implemented by Rezaie et al. was used [76, 58]. The algorithm shows a good performance for crack segmentation of images with DIC speckles. In this subsection, crack images with and without speckles were analysed using the following algorithms:

- Images with DIC speckles: open-source Python code [77] trained with the publicly available dataset [78].
- Images without DIC speckles: open-source Python code [79] trained with the publicly available dataset [80].

The second step is the estimation of the crack kinematics based on the binary images using the algorithm proposed by Pantoja-Rosero et al. [66]. The open-source Python code is publicly available [81]. The code performs the analysis on a 256×256 pixels window. The assumption of rigid-body displacements of both lips of the crack is valid only for small regions surrounding the crack. When the window corresponds to a surface in the specimen small enough to satisfy this assumption, the full-edge approach can be used. In this case, the full length of the crack in the window is considered. Alternatively, in cases where the window corresponds to a large specimen surface where a rigid-body crack lip displacement is unlikely to occur, the algorithm can be run by comparing partial segments of the crack. Both approaches are compared in the following subsection.

3.2.3 Validation of the technique

The described technique was tested in laboratory conditions for validation in controlled conditions and to determine the accuracy under optimal conditions. For this purpose, two types of tests were used: a simplified fictitious crack and three-point bending tests of reinforced concrete beams. The tests were conducted in the Structural Concrete Laboratory of the École Polytechnique Fédérale de Lausanne (Switzerland).

The first type of tests is illustrated in Fig. 8a. A wooden formwork panel of 27 mm was cut using a Computer Numerical Control machine MACA BC170 to simulate the presence of a

crack. The geometry of the crack was extracted from an actual crack pattern of a concrete beam. The two panels where mounted on the fixed and moveable parts of a calibration bench (precision of ±5 µm). Once installed, the displacement was set to zero and two layers of white paint were applied to close the residual crack opening. The bench was progressively moved, imposing a horizontal crack opening. For each crack opening, pictures were captured from a distance ranging from 0.1 to 2.5 m using a professional digital camera and a smartphone. The camera was a Nikon D800 36.3 megapixels with an AF-S Nikkor 28-300mm f/3.5-5.6G ED VR objective [82] whereas the smartphone was a OnePlus 6 with a Sony IMX 519 sensor and a pixel count of 16 megapixels [83]. No additional sources of light other than the natural and artificial lighting of the laboratory were used. The analysis was performed using the compressed images (JPG).

As shown in Fig. 8b,c, for a given crack width (in this case 1 mm), the distance between the camera and the target determines the pixel resolution (size of the pixel in mm, mm/pixel) and the crack width in pixels (number of pixels inside the crack, 25 and 2.3 for resolutions of 0.04 and 0.43 mm/pixel respectively). Fig. 8d shows a comparison of the measured horizontal crack openings δ_x as a function of the pixel size for each camera. The horizontal lines represent the imposed displacement whereas the points correspond to the experimental results. The colours correspond to various crack widths. Additionally, the lightly coloured hatch represents a measurement error equal to the size of one pixel. The measurements fall within the tolerance of ±1 pixel in the left side of the graphs for crack widths larger than 3 pixels. This limit is represented by the dashed black line and the end of the hatch. For images with crack widths smaller than 3 pixels,, the results show larger measurement errors. This is easy to understand looking at Fig. 8c, having few pixels in the crack, the detection becomes more difficult due to lack of contrast. Furthermore, if the crack lips do not have sufficient features, the matching algorithm will not perform appropriately. Fig. 8e shows the same results for the imposed vertical crack opening δ_y, which was zero in all cases. The results show a measurement error of ±2 pixels. The results from the two cameras are comparable for similar pixel resolutions, the only difference being the distance between the camera and the crack needed to achieve the same pixel size.

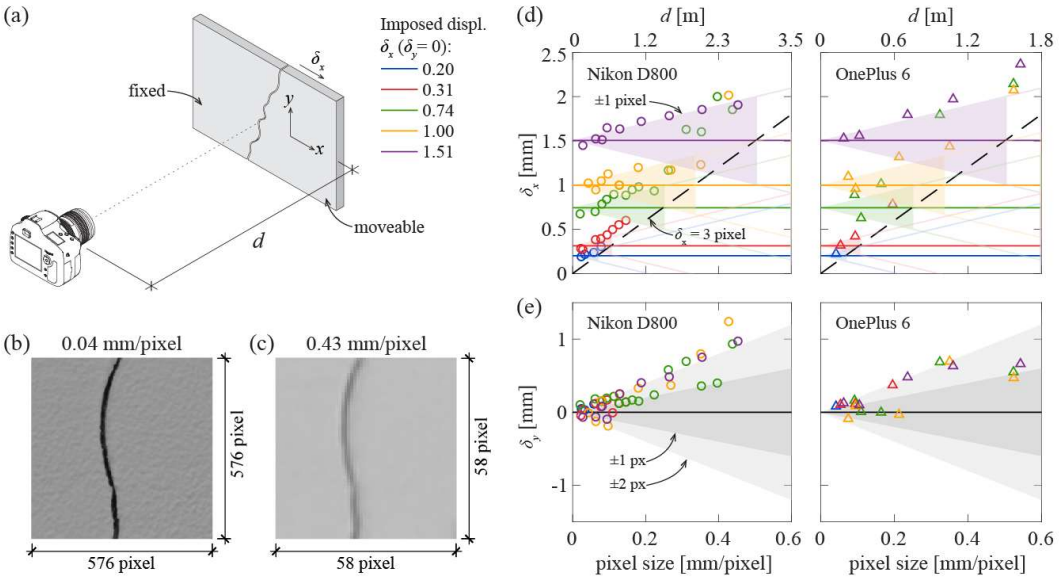

Fig. 8 *Concrete crack simulation: (a) schematic representation of the set-up; images from the studied crack with a crack width of 1 mm taken from distances of (b) 0.2 and (c) 2.5 m; (d) crack opening and (e) crack sliding as a function of the pixel size.*

A second validation test was performed using images from a three-point bending test on a reinforced concrete beam, as shown in Fig. 9a. The specimen SM15 had a shear reinforcement composed of 8 mm stirrups (shear reinforcement ratio ρ_w = 0.101%) and the central part of the specimen was reinforced with double 14 mm stirrups to prevent failure in that region (for additional details, see [3]). The lateral face of the specimen was monitored with DIC using a pair of cameras SVCam-hr29050 with a resolution of 29

megapixels and the correlation was done using the VIC-3D software [37] using a subset size of 23 pixels, a step of 7 and a filter for the strain calculation of 5. The average pixel resolution was 0.502 mm/pixel. The proposed technique is compared in this case with the crack kinematics detected using ACDM [42] from the DIC data.

Fig. 9b shows the image obtained with one of the cameras at the maximum force. The results of the detection technique presented in Subsection 2.2 are presented in Fig. 9c. The principal strain field obtained from VIC-3D and the detected cracks (black lines) using ACDM are presented in Fig. 9d. It can be observed that at the intersections of cracks or in regions with two closely spaced cracks, the neural network does a better detection. Some of the smaller cracks were not detected with the neural network, probably due their reduced openings compared to the pixel resolution.

Fig. 9e shows the kinematic estimation using ACDM and the proposed technique with the full-edge (k_β = 10) and with the finite-edge (k_β = 10, k = 50, μ = 1.5, λ = 4) approaches [66], both results are presented in Fig. 9e. For a load corresponding to 80% of the shear capacity, the crack opening in the direction normal to the crack δ_n was close to 0.8 mm. The proposed detection technique did not fully detect the crack and overestimated its opening, which is consistent with the previous tests as the crack opening corresponds to 1.5 pixels (under the limit of 3 pixels per crack). At the maximum load, both detection techniques provided crack openings within the tolerance of one pixel (±0.502 mm) and the sliding δ_t within the tolerance of two pixels (±0.104 mm). The crack axis detected by the neural network follows the crack in the image better. The stepped crack axis detected with ACDM is a consequence of the subset size used for the correlation, the results can be smoothed using a moving average [42]. It must be noted that the finite edge approach performed poorly at both load steps due to the lack of rugosity of the crack, particularly on the left side of the image.

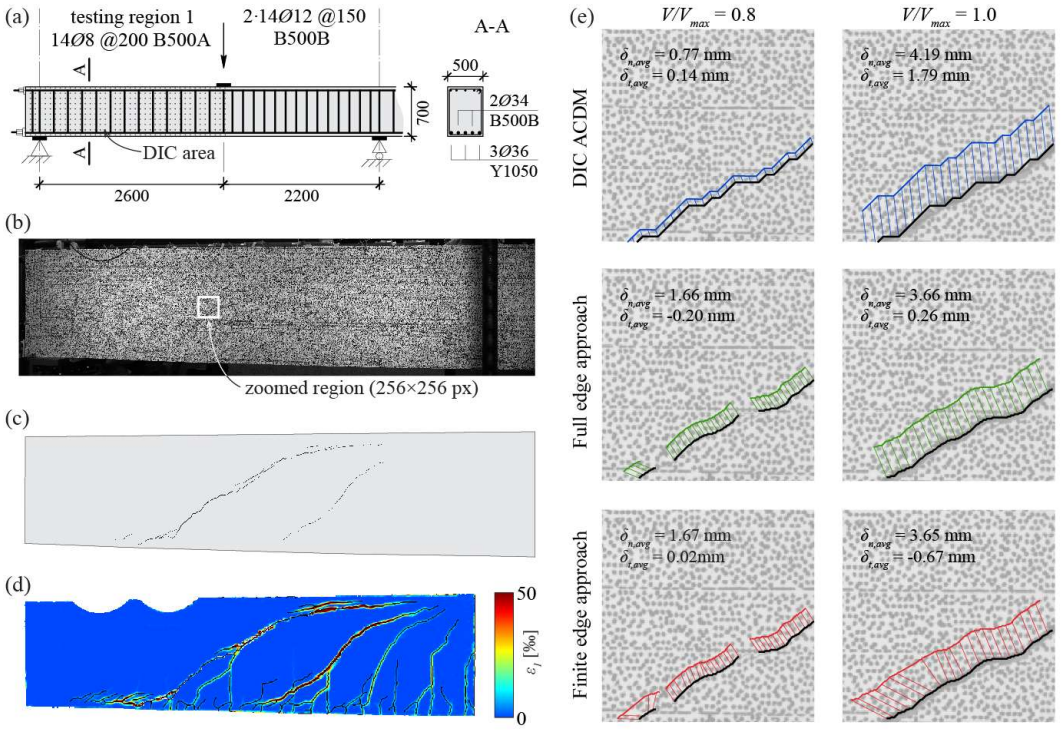

Fig. 9 *Specimen SM15 three-point bending test results: (a) test set-up and specimen description; (b) image at the maximum load; (c) crack detection using the proposed technique; (d) crack detection using DIC and ACDM; and (e) comparison of the crack kinematics using various techniques.*

3.2.4 Recommendations and limits of applicability

The proposed technique can be used to detect cracks and estimate the crack kinematics in concrete elements with and without DIC speckles. The following recommendations are proposed to maximize the quality of the results for in-situ applications:

- The resolution of the images (pixel size determined by the distance between the camera and the specimen) must be chosen to include at least 3 pixels in the crack. In such cases, the crack kinematic measurement resolution should be: ±1 pixel for the crack opening and ±2 pixels for the crack sliding. It must be noted that this would lead to an accuracy of ±30% for the crack opening. Consequently, a higher resolution of 6 to 8 pixels per crack is recommended for increased accuracy.
- The images should be taken with the camera oriented perpendicularly to the studied surface.
- For large surfaces, it is recommended to include multiple visual references for the pixel size detection as the pixel size is not uniform throughout the image.
- Depending on the rugosity of the surface, the use of flash or additional lighting can be beneficial. If the studied surface is very rough, the flash can increase the uniformity of the surface outside the crack leading to less false crack pixel detections. Consequently, it is recommended to acquire images with and without flash when possible as the needed time is almost the same and this could lead to better results.
- The full-edge approach should be used when the analysis window corresponds to approximately two times the maximum aggregate size. When the window size corresponds to a larger surface of the element, the finite-edge approach is recommended. A small window size can increase the measurement resolution but it requires a larger number of images and the added task of relative positioning of the different images.

3.3 Long-term crack monitoring

3.3.1 Objective

The technique described in this subsection aims to measure the long-term displacements of a crack by tracking and comparing the position of markers fixed on both sides of the crack between successive inspections. This could be alternatively done using conventional 3D-DIC, however it would require leaving the measurement equipment permanently in the bridge. The proposed technique does not require the correlation of the speckles with the reference image of the first inspection and, therefore, would allow the monitoring of multiple bridges with a single set of cameras.

3.3.2 Description of the technique

The crack geometry can be defined by a sequence of I points (C_I with coordinates $\underline{c_I}$) as shown in Fig. 10a. The crack defines to crack lips, one of which is considered fixed (used as reference between successive inspections) and the other is assumed to move. The n markers on the reference side are denoted A_n (with coordinates $\underline{a_n}$). The m markers on the moveable side are denoted as B_m (with coordinates $\underline{b_m}$). Upon the first inspection, the "reference position" of all these points is determined (the correspondent magnitudes are referred to with the subscript "ref"), see Fig. 10a. After the second inspection, the "deformed position" of points is determined (referred to with the subscript "def"), see Fig. 10b.

The markers in the reference and deformed states are photographed with a different position of the camera setup and therefore different coordinate systems. By superposing the markers on the reference side, the difference in the position of the markers in the moveable side can be used to estimate the crack displacements. The proposed technique is based on the following assumptions:

- Crack kinematics are bidimensional. This is typically the case in reinforced concrete structures. The technique proposed in this subsection uses bidimensional coordinates assuming planar displacements of the markers. A plane fitting operation is thus needed

to transform the 3D coordinates of the reference and deformed states into planar coordinates. Detailed expressions for this purpose can be found in Appendix I.

- Temperature variations result in uniform dilations of the crack lips. Significant temperature variations can occur between inspections, particularly when performing long-term monitoring. When the area close to the crack undergoes a difference of temperature between the two sets of images the thermal expansion of the crack lips falsely amplifies the computed crack displacements. This effect becomes more important when the centroids of the groups of markers are far away from the crack.
- After correction of the effect of temperature, the relative positions of the markers on a given crack lip are assumed fixed between the reference and deformed states. This assumption is valid as elastic deformations of the concrete next to the crack are usually one order of magnitude smaller than the displacement of the crack [41]. This means that a best-fit rigid-body displacement is a realistic simplification of reality to characterise the mapping operations needed.

Under these assumptions, the following steps are required to obtain the opening and sliding components ($\delta_{n,l}$ and $\delta_{t,l}$) at each crack point (detailed expressions for this purpose can be found in Appendix II):

1. The coordinates of the markers in the reference state are corrected for temperature using a uniform scaling transformation (S, $\underline{t}_s$) leading to the corrected marker points $A^s_{n,ref}$ and $B^s_{n,ref}$ represented in light blue Fig. 10c.
2. The best-fit in-plane rigid body motion (R_A, $\underline{t}_A$) to transform the group of markers $A_{n,def}$ into the scaled reference markers $A^s_{n,ref}$ is computed, see Fig. 10d. The coordinates of the markers in the deformed state after remapping of their position can then be computed $A^r_{n,ref}$ (pink in Fig. 10e).
3. The best-fit rigid-body displacement (R, $\underline{t}$) necessary to superimpose the group of markers $B^s_{m,ref}$ (light blue in Fig. 10e) to the group $B^r_{m,def}$ (pink in Fig. 10e) is calculated. This transformation corresponds to the relative displacement of the crack lips.
4. The deformed position of the crack points is computed by first applying the scaling operation (S, $\underline{t}_s$) which describes the effect of temperature and then the relative displacement of the crack lips (R, $\underline{t}$) to the coordinates of the crack points $\underline{c}_{l,ref}$. The translation between $\underline{c}_{l,ref}$ and the obtained coordinates $\underline{c}_{l,def}$ is the crack displacement $\underline{\delta}_l$ (see Fig. 10e).

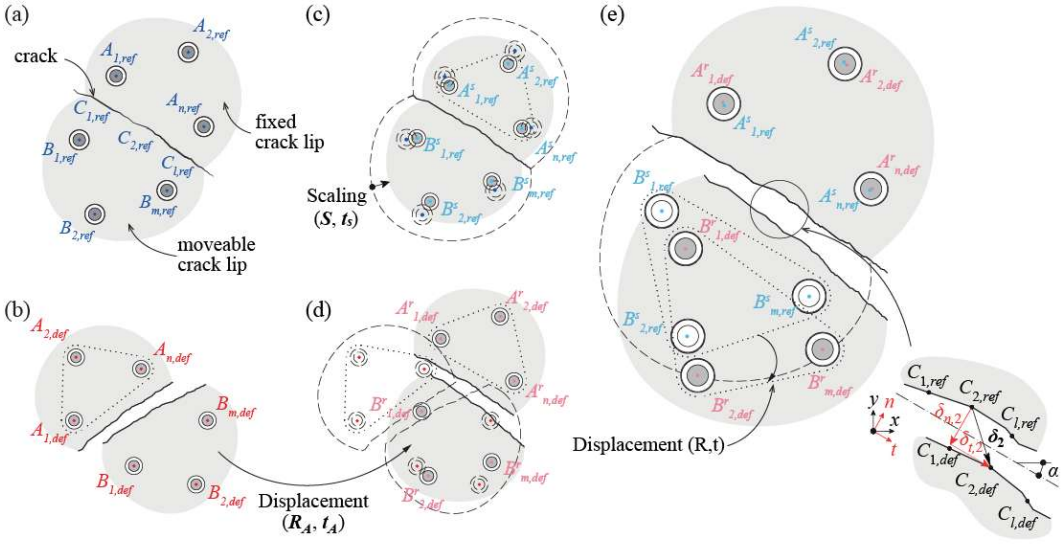

Fig. 10 *Processing of the marker coordinates: (a) reference marker positions; (b) deformed marker position; (c) scaling of the reference markers; (d) alignment of the deformed markers; and (e) relative displacement of the crack lips and detail of the crack kinematics.*

3.3.3 Measurement uncertainty

When performing long-term measurements, the camera setup is dismounted after photographing the initial state of the crack and repositioned when photographing the deformed state. A separate calibration of the cameras must be carried out each time. The measurement error resides in the detection of the centre of the markers which is reverberated in the crack displacement. A set of experiments were carried out at the Structural Concrete Laboratory of Ecole Polytechnique Fédérale de Lausanne to assess this error. The measurement system is described in Subsection 2.3.1. Marker detection was performed using the software VIC3D [37].

After testing different types of markers, it was found that bigger circular markers were detected with a higher accuracy. Circular black markers with a diameter of 15 mm (corresponding to 50 pixels) were used for these tests.

The uncertainty interval of conventional DIC measurements can either be quantified providing a minimum and a maximum value as typically in cases where the precision of the measurements is not critical and a conservative interval is sufficient [3]. However, the use of the standard deviation is advised by [36] because it gives a more realistic idea of the distribution of the measurement error. The standard deviation is therefore used in this subsection for the quantification of the uncertainties.

Uncertainty of the marker centre detection

The detection of the centre of round markers is obtained by computing the centre of an ellipse fitted to the black-white transition at the edge of the marker [85]. The centre of a given marker is detected on the two photographs captured simultaneously by the two cameras. A process called “triangulation” then transforms these two sets of 2D coordinates to the 3D coordinates of the marker. This operation necessitates the use of the optical model constructed during the calibration of the cameras (see [23] for additional information). The marker detection precision is influenced by a random error and a systematic error.

The first type is a random error or noise which is visible when comparing the position of a marker detected in a series of images captured without applying any displacement. The typical results of such a test are represented in red in Fig. 11. This error is due to the internal noise of the captors [22]. It results in small variations between similar photographs which are interpreted differently by the marker detection algorithm. These errors are highly dependent on the contrast of the marker edges and therefore on the quality of the exposure. The size of the markers also has an influence. Markers with larger diameters provide more precise measurements. The noise is easily reduced by averaging several measurements. It can be measured in a Zero Displacement Test (ZDT) and quantified through the standard deviation NV_N [36] (see Appendix III for more details).

The second type is a systematic error or bias. The result of this error is that the average of a large number of measurements, an operation that removes the noise, does not tend to the centre of the marker. The source of this error is due to imperfections of the optical model defined during the calibration of the cameras [23]. However, when applying small displacements to the marker inside the field of vision of the cameras, it was observed that the bias changes randomly as imprecisions in the optical model compensate each other. After subtraction of the applied displacement, the bias becomes visible in Fig. 11 where the three colours show measurements taken with different positions of the marker inside the field of vision. By averaging several measurements, the bias can be reduced similarly to the noise. The bias does not depend on the environmental conditions but rather on the lens and the quality of the calibration. It can be measured in a Zero Strain Test (ZST) and quantified through the standard deviation NV_B [36] (see Appendix III for more details).

The ZDT and ZST were performed by the authors in laboratory conditions using a stiff board presented in Fig. 12a with 36 printed markers, resulting in: NV_N = 3.3 μm = 1/90 pixel (corresponding to a margin of error ± 3.3 μm) and NV_B = 8.6 μm = 1/35 pixel.

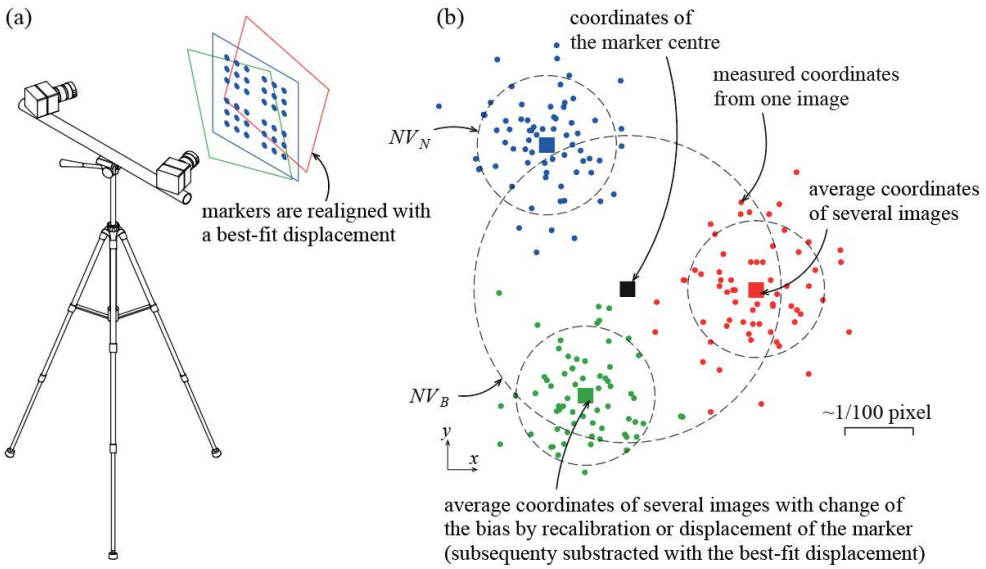

Fig. 11 *Uncertainty of the marker coordinates: (a) camera set-up and board used for the tests; and (b) schematic representation of the sources of error and the associated quantifications (NV)..*

Uncertainty of the crack lip displacements

The uncertainty of the relative crack lips displacement, characterised by a rotation θ about the origin and a translation vector $\underline{t} = [t_n \quad t_t]^T$, as defined in Fig. 12b, varies depending on NV_N, NV_B and the disposition of markers. In the equations shown below, the markers are assumed to be arranged symmetrically around the crack and the axis which runs through the centroids of both groups of markers is considered approximately perpendicular to the crack. The board previously used for the quantification of the marker detection error, represented in Fig. 12a, was used to provide experimental data. Symmetrical groups of markers were chosen randomly as illustrated in Fig. 12b and their apparent relative rigid-body displacement computed using the equations presented in Appendix II. The error margin is defined separately for the three parameters θ, t_n and t_t using the standard deviation.

The images captured for the Zero Displacement Test (ZDT) and Zero Strain Test (ZST) were used to quantify separately the effect of the noise and bias. It was found that the error due to both these sources were proportional to the respective values of *NV*. This means that the noise and bias can be treated with the same equations if they are normalised by *NV*. This aspect is validated in the experimental results. The measurements obtained using the images of the ZST present more scatter as less data was available than for the ZDT.

The relative translation normal to the crack t_n (see Fig. 12b) is not affected by small relative rotations of the group markers. Its uncertainty only depends on the reliability of the centroid of both groups of markers which is directly dependant on the number of markers *n*. Fig. 12d shows the relationship obtained experimentally between the number of markers and the standard deviation of t_n named $\sigma(t_n)$. This graph can be used to estimate the error margin of t_n produced by both noise and bias by multiplying the normalised value by either NV_N or NV_B.

The error margin of the rotation $\sigma(\theta)$ obtained experimentally in Fig. 12e shows that the expression of Eq. 3 is a good fit:

$$\sigma(\theta) = \frac{\sigma(t_n)}{d_1} \tag{3}$$

where $\sigma(t_n)$ indicates that the error margin depends on the number of markers and d_1, defined in Fig. 12c, characterises the proximity of the markers inside a group and indicates how precisely its rotation is evaluated. For large values of d_1, the markers are far apart and therefore small errors in the detection of their coordinates have a small impact on the rotation.

The error in the estimation of the relative translation parallel to the crack t_t is a combination of an error that depends on the number of markers $\sigma(t_t)_1 = \sigma(t_n)$ and an error due to the rotation of the crack lip $\sigma(t_t)_2 = \sigma(\theta)d_1/2 = \sigma(t_n)d_2/2d_1$. The combination of these two errors is not linear however. Indeed, when adding up two sets of data $\boldsymbol{a}$ and $\boldsymbol{b}$ with different standard deviations $\sigma(\boldsymbol{a}) < \sigma(\boldsymbol{b})$, $\sigma(\boldsymbol{a} + \boldsymbol{b})$ depends on the ratio $\sigma(\boldsymbol{a})/\sigma(\boldsymbol{b})$. If the ratio is close to 0, $\sigma(\boldsymbol{a} + \boldsymbol{b}) \sim \sigma(\boldsymbol{b})$ whereas if it is close to 1, the two sources of error have a similar scatter. In this case, a certain smoothing of the data occurs when summing them, which means that $\sigma(\boldsymbol{a} + \boldsymbol{b}) < \sigma(\boldsymbol{a}) + \sigma(\boldsymbol{b})$. To model this effect, tests were carried out in which the coordinates of the markers collected during the ZDT were used as $\boldsymbol{a}$ and $\boldsymbol{b}$. The reduction factor β which depends on the ratio $\sigma(\boldsymbol{a})/\sigma(\boldsymbol{b})$ describes this effect. It is defined in Eq. 4 and represented in Fig. 12h.

$$\sigma(\boldsymbol{a}+\boldsymbol{b}) = \beta\left(\frac{\sigma(\boldsymbol{a})}{\sigma(\boldsymbol{b})}\right)\left(\sigma(\boldsymbol{a})+\sigma(\boldsymbol{b})\right) \tag{4}$$

Therefore, $\sigma(t_t)$ can be estimated using Eq. 5:

$$\sigma\left(t_t\right) = \beta\left(\frac{\min\left(\sigma\left(t_t\right)_1, \sigma\left(t_t\right)_2\right)}{\max\left(\sigma\left(t_t\right)_1, \sigma\left(t_t\right)_2\right)}\right)\left(\sigma\left(t_t\right)_1 + \sigma\left(t_t\right)_2\right) = \beta\left(\frac{\min\left(d_2, 2d_1\right)}{\max\left(d_2, 2d_1\right)}\right)\sigma\left(t_n\right)\left(1+\frac{d_2}{2d_1}\right) \tag{5}$$

In most cases, a simplified analysis using a secant value of β = 0.72 is sufficient. This assumption yields Eq. 6:

$$\sigma\left(t_t\right) = 0.72\sigma\left(t_n\right)\left(1+\frac{d_2}{2d_1}\right) \tag{6}$$

The total error, which takes both noise and bias into account, can also be computed with Eq. 7 using the expression of the reduction factor β:

$$\sigma\left(t_n\right)_{tot} = \beta\left(\frac{\sigma\left(t_n\right)_N}{\sigma\left(t_n\right)_B}\right)\left(\sigma\left(t_n\right)_N + \sigma\left(t_n\right)_B\right) \tag{7}$$

Averaging

Averaging several measurements leads to a reduction of the measurement error and can be used to reduce the number of markers necessary to obtain the required precision. To reduce the noise, the coordinates of the markers obtained using several images taken with the same camera position are simply averaged before performing the processing described in Subsection 3.3.2. To reduce the bias, images with slight displacements need to be used. These can be obtained typically by carefully moving the camera setup several times while avoiding any relative displacement of the cameras which would lead to a de-calibration of the setup. The coordinates of the markers need to be mapped back to a similar position using the procedure described in Appendix II and then averaged.

The effect of averaging several measurements can be modelled by a reduction factor α which depends on the number of averaged images. This reduction factor was obtained experimentally and is presented in Fig. 12g. It can be applied to the standard deviations of t_n, t_t and θ obtained using the previously described procedure.

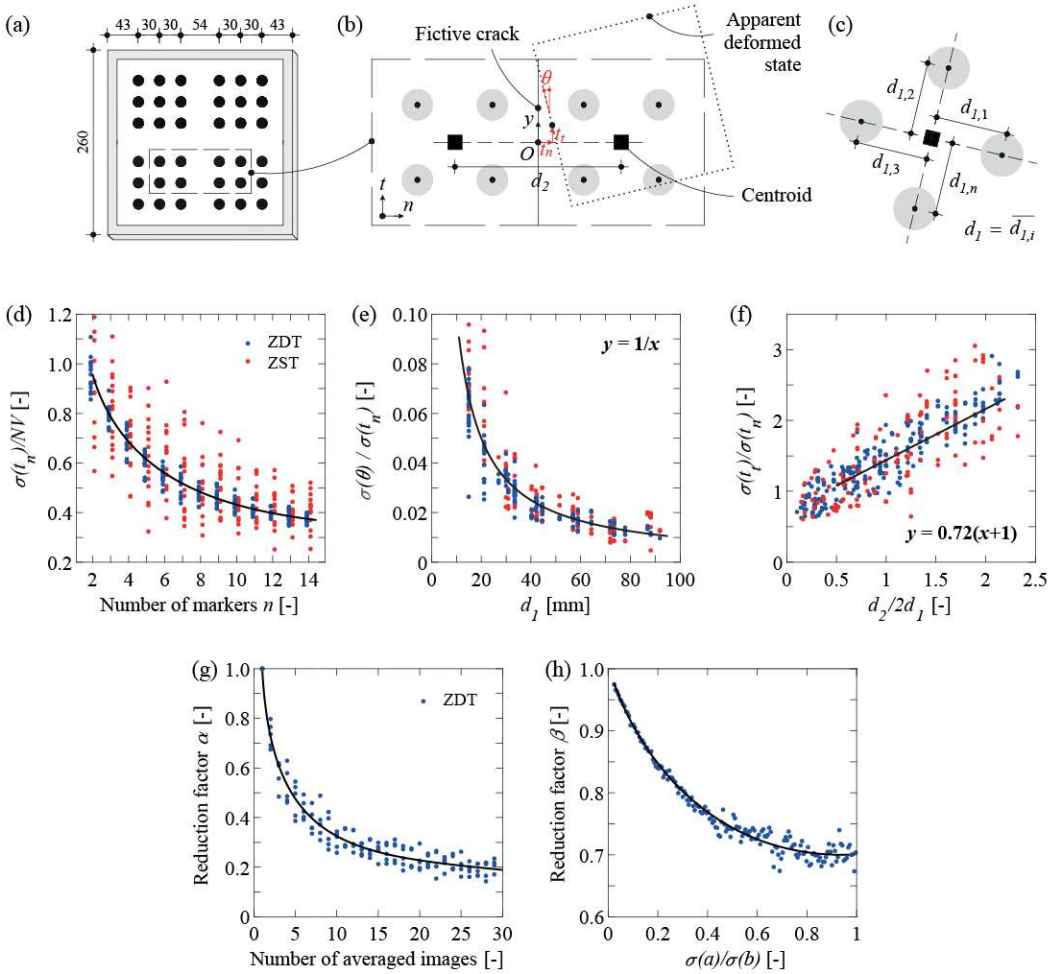

Fig. 12 *Model for the estimation of crack lip displacement measurement error: (a) board used for the tests; (b) principle of the tests with notations; (c) definition of distance d_1; (d) results for the quantification of the error for t_n; (e) results for the quantification of the error for θ; (f) results for the quantification of the error t_t; (g) effect of averaging several measurements; (h) effect of summing quantities with different standard deviations.*

Uncertainty of the crack kinematics

The uncertainty of the crack kinematics measurements depends on the error intervals of t_n, t_t and θ and on the position of the crack point. The kinematics of crack points close to the centroid of the markers are naturally more precise than those far away. As developed in Subsection 2.3.2, the crack displacements can be computed from t_n, t_t, θ and $[x\ y]^T$ the coordinates of any crack point (see Fig. 12b) using Eq. 8:

$$\begin{bmatrix}\delta_n\\ \delta_t\end{bmatrix}=\begin{bmatrix}\cos\theta & -\sin\theta\\ \sin\theta & \cos\theta\end{bmatrix}\begin{bmatrix}x\\ y\end{bmatrix}+\begin{bmatrix}\delta_n\\ \delta_t\end{bmatrix}-\begin{bmatrix}x\\ y\end{bmatrix} \tag{8}$$

By using the approximation of small angle and as $x \sim 0$ in the coordinate system defined above, the opening and sliding components can be expressed by Eq. 9:

$$\begin{aligned}\delta_n &= x - y\sin(\theta) + t_n - x \simeq -y\theta + t_n\\ \delta_t &= x\sin(\theta) + y\cos(\theta) + t_t - y \simeq t_t\end{aligned} \tag{9}$$

Using the reduction factor β described previously, the standard deviation of the opening and sliding components are expressed according to Eq. 10

$$\sigma(\delta_n) = \beta\left(\frac{\min(|y|,\, d_1)}{\max(|y|,\, d_1)}\right)\sigma(t_n)\left(1+\frac{|y|}{d_1}\right) \qquad (10)$$
$$\sigma(\delta_t) = \sigma(t_t)$$

3.3.4 Validation of the technique

The proposed technique was tested under laboratory conditions with the aim of validating the uncertainty model described in Subsection 3.3.3. The measurement system described in Subsection 2.3.1 was used to monitor a four-point bending test of a rectangular reinforced concrete beam, as shown in Fig. 13a. The beam was loaded up to the end of the cracking phase and then unloaded to place two groups of five markers on each side of one of the cracks (arranged according to Fig. 13b).

White paint and a speckle pattern (approximate size of 1.5 mm) where applied to the concrete surface to monitor it with DIC, thus providing a reliable reference for comparison with the marker measurements. The DIC analyses were performed using the software VIC3D. The software ACDM [42] was used for the automatic extraction of the crack geometry and the computation of the crack kinematics. The coordinate system used for the study is horizontally centred at the crack and vertically at the centroid of the markers, as shown in Fig. 13b.

Reference images were acquired in three distinct positions of the camera setup as represented in Fig. 13a. A displacement of the cameras was applied each time and a new calibration was performed to simulate a repositioning of the setup for long-term measurements. In the last, or “DIC position”, one reference image for DIC was acquired followed by images captured regularly during loading (see the loading curve in Fig. 13c). Each image of the loaded beam was used simultaneously to compute crack displacements using DIC (reference) and using the markers by comparing their state with the three reference states acquired before (see Fig. 13a).

Consequently, four sets of data were obtained at each load step: three marker measurements for the three camera positions and one measurement using DIC. The comparison of the four crack displacements for three loading stages is shown in Fig. 13d. The horizontal (δ_x) and vertical crack openings (δ_v) are represented as a function of the height of the beam. A secondary crack appeared, probably during the installation of the markers because one of them was too close to the crack (see Fig. 13b). Its kinematics were added to the kinematics of the main crack in the DIC results [84]. Along with the crack displacements, the error intervals computed according to Subsection 3.3.3 are presented (d_1 = 47 mm, d_2 = 108 mm, $\sigma(t_n)_{tot}$ = 5.4 μm, $\sigma(t_t)_{tot}$ = 8.1 μm, $\sigma(\theta)_{tot}$ = $1.1{\cdot}10^{-4}$ rad). A comparison of the DIC and marker measurements presented in Fig. 13d also shows that the approximation of a rigid-body displacement of the crack is valid (even with the appearance of a secondary crack). The kinematics obtained with DIC show a slight variability due to measurement uncertainties that can be smoothed using a moving average filter [42].

By comparing the different measurements, it can be observed that the repositioning of the camera setup between reference and deformed does not cause an increase of the error. This error is correctly described by the model of Subsection 3.3.3, which provides a value for the standard deviation of the measurements (the measurements can slightly exceed the interval). The crack opening measurements are more precise close to the centroid of the markers (y = 0), however the precision of the crack sliding is constant and satisfactory estimated by the model presented in Subsection 3.3.3, but only in cases where the camera setup is positioned perpendicularly to the surface. If the camera setup is positioned with a sharp angle relatively to the surface, the error interval can significantly differ from the model. In this case, the out-of-plane coordinates of the markers are put to contribution and as their precision is far lower than in-plane, the consequences on the precision of the crack kinematics can be significant.

These results indicate that the discrete measurements obtained with the markers allow a good description of the crack kinematics. This technique significantly reduces the computational effort compared with the full image correlation, however a smaller precision is achieved.

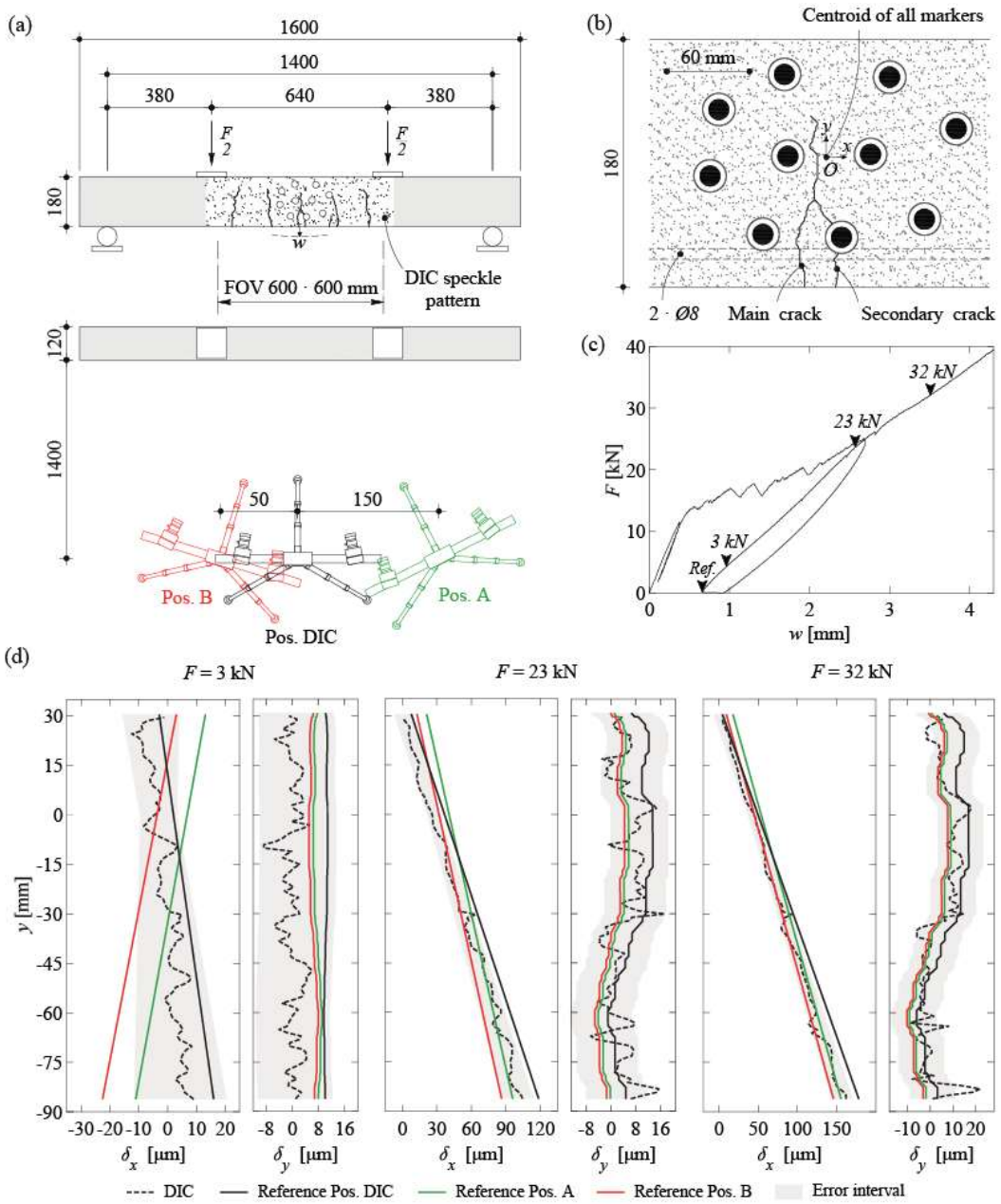

Fig. 13 *Results of the laboratory validation of the technique: (a) setup and camera positions (the positions of the cameras are not to scale); (b) detail of the crack instrumented with markers; (c) load deformation curve; (d) crack kinematics comparison for three load steps.*

3.3.5 Recommendations and limits of applicability

The marker technique is mainly limited by the inconvenience of the procedure: the need for illumination, the use of two cameras fixed on a tripod and the need to perform a calibration of the cameras before the measurements. It can be justified in cases where the crack kinematics need to be measured with a high precision at intervals and the use of gauge sensors is not practical (for example if a large region of an element with multiple cracks needs to be monitored).

In general, when using markers, the distance d_1 should be maximized and the distance d_2 minimized. Patterns of regularly spaced markers or two staggered lines of markers are usually the best solutions. Fig. 14 shows the error interval for both crack opening and sliding obtained experimentally and as predicted by the model of Subsection 3.3.3 for typical examples of disposition of markers as a function of the pixel size for the values of NV_N and NV_B. The procedure proposed for the choice of a disposition of markers for a given crack is detailed below:

1. The first step consists in the determination of the necessary framing of the crack, the pixel size and the minimum precision required for the crack kinematics.
2. As a first approximation, the values of NV_N and NV_B provided in Subsection 3.3.3 can be used. In further phases, the two tests of Appendix III can be carried out in-situ to consider the type of camera, lens and quality of the chosen illumination.
3. Fig. 14 can be used, by multiplying by the pixel size, to determine the number of markers required based on the desired precision. The noise can be ignored as it is easily removed by averaging at least 10 images.
4. If the number of markers is too large (e.g. the space around the crack is not sufficient), several measurements can be averaged to increase the precision. These measurements need to be taken from slightly different positions to reduce the bias. In cases where ambient vibrations are important, typically on a bridge, the induced movements of the cameras are sufficient to substitute manual displacements of the setup and therefore it is very easy to average a lot of measurements (however the gain is small over ten measurements). When ambient vibrations are negligible, the setup needs to be displaced by hand which often results in a “de-calibration” or a relative displacement of the cameras. A new calibration, which demands a large number of photographs, is therefore necessary for each camera displacement. In these cases, it is more efficient to increase the number of markers rather than to rely on the averaging of several images to increase the precision.
5. In more advanced iterations, the position of the markers can be refined, d_1 and d_2 computed and the procedure of Subsection 3.3.3 followed to evaluate the precision of the crack kinematics in a more refined manner until a suitable solution is found.

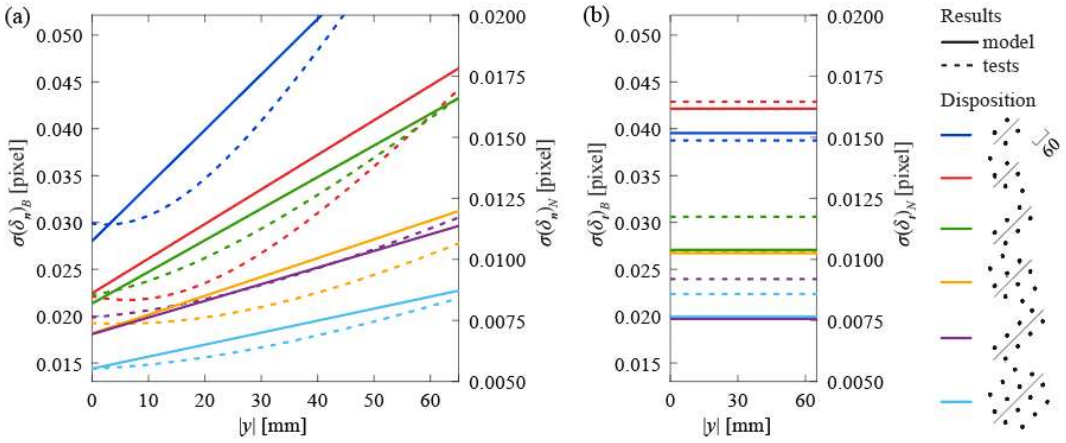

Fig. 14 *Measurement uncertainty of the crack kinematics for different marker dispositions considering β = 0.72 for: (a) the crack opening; and (b) the crack sliding.*

3.4 In-situ application

3.4.1 Existing crack characterization

The technique proposed in Subsection 3.2 is applied to estimate the kinematics of the existing crack. The crack detection is performed in an image after vacuuming the surface (Fig. 15a) and in an image after applying the white paint and speckles used for DIC measurements (Fig. 15b). The results are similar with the exception of the region around the centre of the image where two smaller cracks were observed. Fig. 15c presents the estimated crack kinematics that occurred in the past using the full-edge approach in images with speckles. The crack kinematics show an opening mostly perpendicular to the crack axis. This is reasonable if the studied region is considered as a shear panel reinforced in the two orthogonal directions, where an inclined stress field can develop with cracks parallel to the compression field that open perpendicularly to the compression field [86, 87].

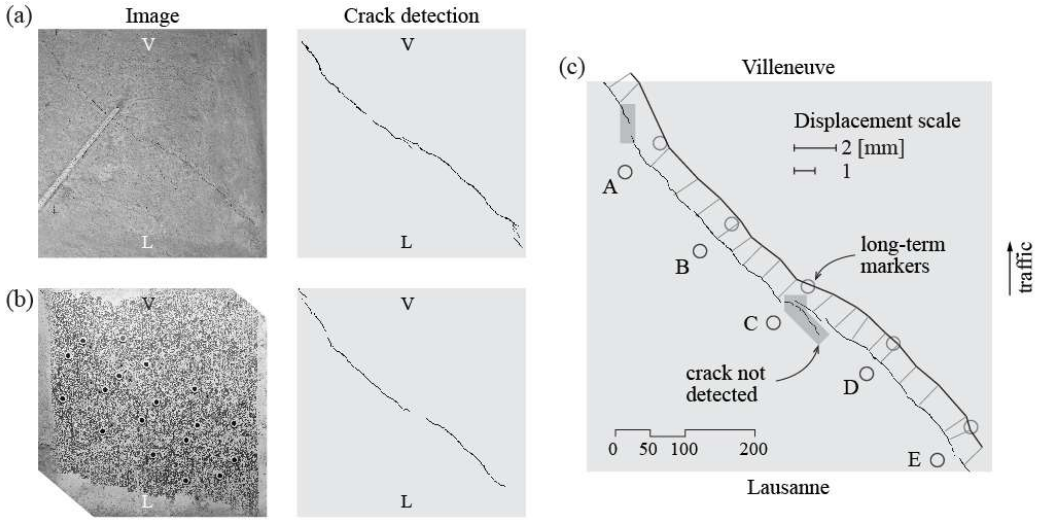

Fig. 15 *Existing crack detection and characterization: results of the crack detection for an image (a) without speckle pattern and (b) with applied speckle pattern; and (c) estimated crack kinematics.*

To validate the results, the crack width was measured at the points between the long-term markers. Three measurements were taken using a crack microscope and a crack width ruler. Tab. 1 includes the average of three manual measurements ($w_{M,avg}$) and the automatic crack detection results (w_D) at each point. The results fall within the tolerance of ±1 pixel with the exception of point D where the difference is slightly larger. It must be noted that the crack lips in existing structures are likely to be significantly less well-defined than in tests in laboratory conditions, due to the presence of dust and erosion of the crack lips at the surface amongst other reasons (the studied crack is probably more than 50 years old). Consequently, it is reasonable to expect a lower accuracy in such conditions.

Tab. 1 *Comparison of crack width measurements obtained using traditional measurements and the automatic crack detection algorithm*

Point	$w_{M,avg}$ [mm]	w_D [mm]	$w_{M,avg}$ - w_D [mm]	Pixel size [mm/pixel]
A	1.20	1.29	-0.09	0.323t
B	1.30	1.24	0.06	0.243
C	0.75	-	-	-
D	0.73	1.18	-0.45	0.322
E	0.80	1.07	-0.27	0.242

3.4.2 Long-term measurement simulation

Long-term monitoring of cracks requires several measurements collected at intervals for a period of several years. Given the daily and seasonal temperature variations (schematically represented with a black line in Fig. 16) the crack can be expected to open and close periodically. Consequently, a permanent crack displacement can only be detected if a sufficient number of measurements is available (red dots in Fig. 16). Due to time constraints and the lack of evidence that the studied crack presents any permanent crack displacement trend, the measurements presented in this subsection were limited to a duration of 19 hours. During this time span, the crack opens and closes due to deformations of the bridge under daily temperature variations (see detail in Fig. 16).

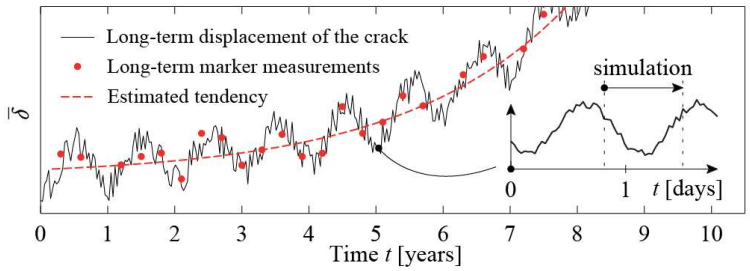

Fig. 16 *Schematic representation of the seasonal and daily crack opening evolution*

The investigated crack was equipped with 18 markers represented in Fig. 17a,b that were screwed into metallic anchors set inside the concrete. A set of reference images with slight displacements of the cameras was first captured. The camera setup was then modified and recalibrated to simulate it being brought back to the location after a time interval (this operation has a negligible impact on the measurement error as shown in Subsection 3.3.4). One image of the crack in the same state was captured for use as reference for the DIC. Images were then automatically captured at intervals of 200 seconds for 19 hours. Between each image, slight displacements of the camera setup due to the bridge vibrations occurred which means the bias of the measurements described in Subsection 3.3.3 changes randomly as would happen in the case of real long-term measurements.

Fig. 17c,d show the average opening and sliding components of the crack. Fig. 17f shows the amplified kinematics for five timesteps. For each image, the results of the DIC analysis (black curves) and of the marker analysis performed on the same image for comparison are presented simultaneously. In green, a single image was used in reference and deformed states for the marker measurements and in red, ten reference images were averaged and ten deformed images were averaged using a moving filter.

The uncertainty of the marker measurements, observable by comparing them to the DIC measurements, is characterised by a systematic offset (similar to a bias) and a certain variability (noise). Both these errors are reduced when more images are averaged. These two characteristics of the uncertainty can be decoupled: the offset is caused by the reference image and the variability by the deformed images. As described in Subsection 3.3.3, the uncertainty of the measurements is due to slight errors in the detection of the centre of the markers. Therefore, each image (reference or deformed) carries an intrinsic error in the detection of its markers. These errors are more or less summed or compensated when two images are compared (resulting in the error quantified in Subsection 3.3.3). As the reference image is always the same, the error appears regardless of the deformed image which it is compared to, resulting in a systematic error in the measurements (the offset of Fig. 17c,d). The deformed images change at each timestep; therefore, their individual error varies randomly, only resulting in a variability of the measurements around an average value.

Zero Displacement and Zero Strain Tests yield NV_N = 4.4 μm and NV_B = 8.6 μm. The noise is more important because it depends on the illumination which was not optimal but the bias, which depends on the lens and calibration, remains the same as in the laboratory tests.

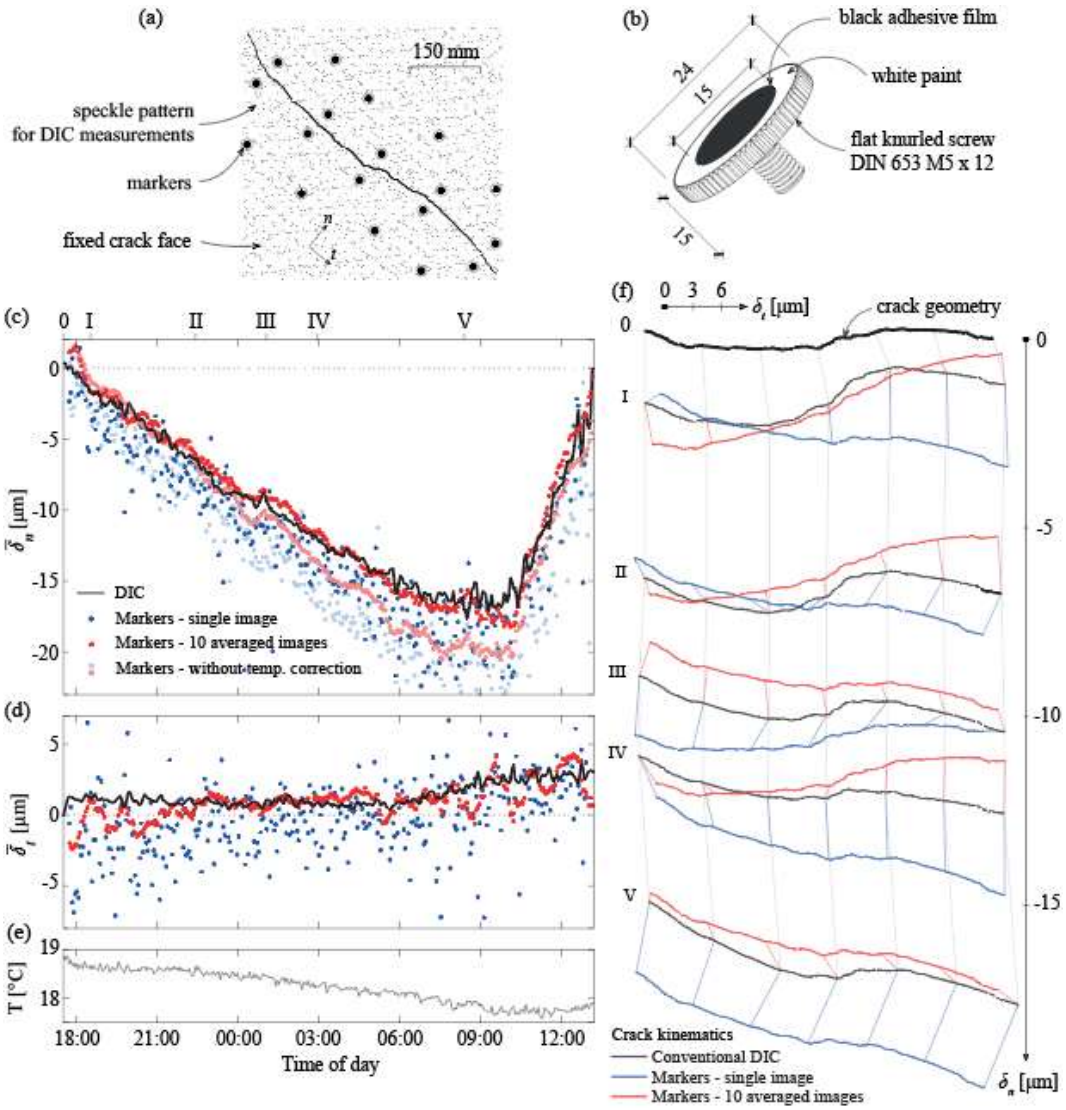

Fig. 17 *Results of the on-site validation of the marker technique: (a) disposition of markers around the crack; (b) detail of one marker; (c) mean crack opening; (d) mean crack slip; (e) temperature; (f) crack kinematics at selected time steps.*

The values for the precision of the measurements according to the procedure described in Subsection 3.3.3 are:

- For one image: $\sigma(\delta_n)$ = 4.8 μm to 10.0 μm respectively at the marker centroid and at the extremities of the field of vision and $\sigma(\delta_t)$ = 5.4 μm.
- For ten averaged images (reduction factor α = 0.3 according to Fig. 12g): $\sigma(\delta_n)$ = 1.5 μm to 3.0 μm and $\sigma(\delta_t)$ = 1.6 μm.

These values are in good agreement with the results. They show that the averaging of ten measurements significantly increases the precision. When taking measurements on a bridge, ambient vibrations are sufficient to cause enough displacements of the camera setup to modify the bias between similar images. This means that averaging can be used in practical applications to reduce the number of necessary markers around a crack.

In Fig. 17c,d, the measurements obtained without using the correction for temperature described in Subsection 3.3.2 are shown in light red and light green. As expected, the value of the correction increases with the change of temperature. The corrected measurements are in close agreement with the DIC measurements, which shows the validity of considering a uniform dilatation of the crack lips. DIC measurements are not affected by temperature because the points used to compute the kinematics are very close to the crack and

therefore insensitive to dilatations of the crack lips. The correction to the crack opening has a value of approximately 2.5 μm at the coldest temperature which is in good agreement with the expected dilatation of the crack lips between the centroids of both of markers assuming a thermal expansion coefficient for concrete of $\alpha_c = 10 \cdot 10^{-6}$ ($d\delta_n \sim \alpha_c \cdot dT \cdot d_2 = 10 \cdot 10^{-6} \cdot 1.5 \cdot 180 = 2.7$ μm).

3.5 Conclusions

This section presents the principles and application of an automated crack detection algorithm to characterize of the existing crack and a marker-based technique to monitor the crack over long periods of time with high precision in concrete structures. The steps to apply these techniques, along with validations and limits of application are presented. The main conclusions are:

1. The tested algorithms for direct detection of crack geometry and kinematics have proven to be an effective technique to characterize the crack geometry and crack kinematics. They achieved precision is ±1 pixel for the crack opening and ±2 pixels for the crack sliding, for the evaluated conditions.
2. The automated detection results have been validated and compared with traditional measurements showing similar results with the clear advantage of being able to compute crack kinematics and not only crack openings. Furthermore, the resolution of the measurements is far greater that the point measurements that can be obtained using traditional measurements.
3. DIC can be used for long-term monitoring of cracks only if the system is left permanently on the structure.
4. The DIC setup can be used in subsequent inspections using markers fixed around the crack. In this case, the position of the markers recorded before and after a deformation can be compared and used to calculate the crack displacements that occurred between inspections.
5. The measurements obtained with the markers have a degree of redundancy that is far lower. Therefore, the precision of the measurements is governed by the number of markers and how they are positioned around the crack and can vary between ±1/20 to ±1/150 of a pixel. The precision can sometimes be improved by averaging several measurements.

The conclusions indicated above are applicable for the algorithms described in this section. Nevertheless, other algorithms can be used for such purposes. The approach presented in this chapter can be used to characterize the expected measurement uncertainty. The following aspects were considered in the selection of the algorithms:

- The algorithm for crack detection was selected based on its good performance shown scientific publications and its availability as an open-source Python program [77].
- The algorithm to estimate of the crack kinematics based on the binary images was selected because, to the best knowledge of the authors, it is the only open-source available for this purpose [81].

The measurement uncertainty is expressed in pixels and depends on the algorithms. It remains constant if certain conditions are respected, Subsection 3.2.4 provides these conditions for the considered algorithms. Taking this into consideration, the camera used for image acquisition is less important, as discussed in Subsection 3.2.3 where similar results can be obtained using a professional digital camera and a commercial mobile phone. If a camera with lower resolution is used the accuracy can be improved by capturing the image from a smaller distance from the studied region. This leads to a smaller pixel size (mm/pixel), which results in a smaller measurement uncertainty, as it is proportional to the pixel size. For this reason, the measurement uncertainty discussed in this chapter are provided in pixels. However, a larger camera resolution can be beneficial to characterize a larger surface with one single image avoiding the relative repositioning process.

3.6 Outlook and future works

Some questions related to the topics studied in this section remain open. In the following, some of these future research lines are outlined:

- Further validation of the proposed technique for the characterization of the initial crack in more adverse conditions are required. In existing structures, other signs of deterioration (such as corrosion traces, water, sediment marks or moss amongst others) can often be found around the cracks. The influence of these signs should be evaluated.
- The proposed technique for long-term monitoring of cracks was only validated over the duration of a day due to time constraints. Further tests to validate the technique over a long period of time are required.
- The influence of thermal deformations not resulting in uniform dilations can be assessed measuring the deformations in unrestrained plates in the same conditions as the monitored region. Tests combining both techniques could be useful to characterize thermal induced stresses.
- The two approaches presented in this section require the access and mastery of three different computer software. The implementation of both approaches in a single open-access program could be useful for the engineers in the practice.

4 Pull-out tests to investigate the bond stress development

4.1 Introduction

The transmission of longitudinal forces between straight reinforcement bars and the surrounding concrete is made possible by the bond forces. Consequently, bar-to-concrete bond is a key parameter in the structural behaviour of reinforced concrete structures at the Serviceability Limit State (SLS) as well as at the Ultimate Limit State (ULS). However, the complexity of the physical phenomena involved in this interaction hinders its characterization.

At a local level, the response is related to the relative displacement between the bar δ_s and the concrete δ_c (slip δ_{sc}, Fig. 18a,c), which is inherently associated with the interaction of the rib lugs with the concrete and its internal cracking. For this reason, the interface response is typically characterized by the relationship between the slip and the bond stress (τ_b, Fig. 18d), which is often assumed to be uniformly distributed over the nominal surface of the bar [88].

In structural members, the bond behaviour of the bar is a consequence of the different conditions along the bonded length (Fig. 18b). In a cracked member, it is sometimes assumed that the point of the bar halfway between cracks has no slip, due to compatibility, and that the point at the crack slips by approximately half of the crack width. The reality is more complex, the point between cracks can slip due to the crack sequence and different effects cause a variation of the crack width along the cover [88], as shown in Fig. 18a. Nevertheless, bond stresses remain relatively small and have a direct influence on the crack width and the so-called tension stiffening (reduction of steel strains due to activation of concrete in tension between two cracks). In an anchorage or in a lap splice, the bond is necessary to transfer the force in the reinforcement to the concrete or to another bar through the concrete. In these cases, the unloaded end of the bar can slip leading to the activation of larger bond stresses, particularly at ULS, as illustrated in Fig. 18c.

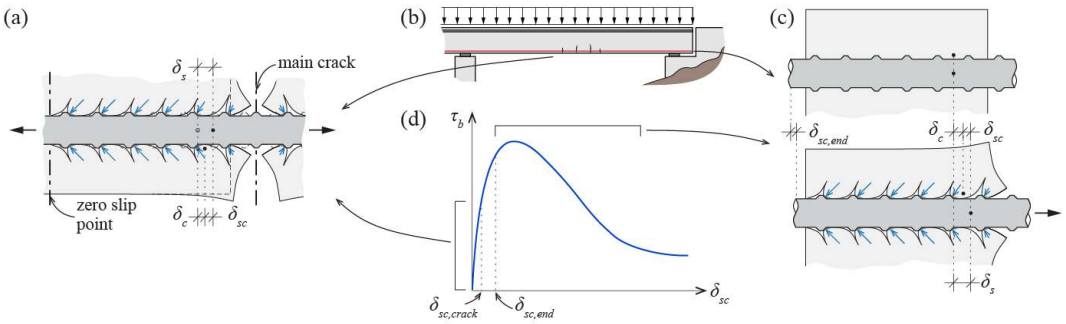

Fig. 18 *Bond in structural members; schematic representation of (a) a cracked region, (b) a reinforced concrete beam and (c) an end anchorage; and (d) general bond-slip relationship.*

Extensive research on the topic has shown that bond is affected by numerous parameters, including the concrete properties, the bar properties and geometry, the stress-state of both materials, the confinement (provided by the concrete cover, by transverse reinforcement, or by transverse pressure), the relative position of the bar with respect to the casting direction, the type of loading and the test conditions amongst others [88, 89]. This complexity is reflected in the broad range of local bond-slip relationships that can be found in literature [90, 91, 92, 93, 94].

Current standards account for this complex mechanism and some of the aforementioned parameters in a simplified manner. For instance, in the calculation of the anchorage and

lap lengths, a constant bond strength is often assumed as in *fib* Model Code 2010 [94] (MC2010), Eurocode 2 [12] (EC2:2004), or SIA 262:2013 [95]. The drafts for the new generation of standards have opted for another approach, providing the bond length directly on the basis of the steel stress to be activated [96, 97, 98]. These provisions are based on the expression of *fib* Bulletin 72 [99], where the stress that can be activated in an anchored bar is derived semi-empirically from a statistical study of a large test database. The nonlinearity in the relationship between the steel stress that can be activated and the bond length accounts indirectly for a non-constant distribution of the bond stresses along the bond length. With respect to the crack width formulations at SLS, the code provisions usually consider a rigid-plastic bond-slip relationship where the bond strength is explicitly or implicitly considered in the calculation of the crack spacing and the tension stiffening effect [94, 12].

MC2010 provides a local bond-slip relationship for ribbed bars subjected to monotonic loading that accounts for the effect of concrete compressive strength, bar diameter, casting conditions (also called bond conditions), concrete cover and confinement. Additional expressions are provided to consider the effect of bar yielding, transverse and longitudinal cracking and other types of loading [94]. The relationship is based on experimental results from pull-out tests in well-confined conditions with short embedment lengths (typically five times the nominal diameter of the bar Ø) and a certain unbonded length at the loaded end of the bar to prevent the development of conical cracks [100, 101]. These relationships are based on the work of Eligehausen et al. [90] and adapted on the basis of the expressions from *fib* Bulletin 72 for low and moderate confinement (so-called splitting failures) [99]. They are applicable to ribbed bars respecting the bond index or relative rib area (f_R) requirements of current standards to ensure a good bond performance (EC2:2004 requires a minimum value of 0.056 for bars with a nominal diameter larger than 12 mm [12]). Metelli et al. [102] conducted an experimental programme with 151 pull-out tests to evaluate the effect of the bond index, showing that bars with the minimum bond index can reach higher bond strengths and stiffer responses than the MC2010 relationships. Recent studies using detailed measurement techniques have shown the strain gradients generated in the vicinity of the ribs due to the introduction of the bond forces [13], the nonuniform bond stress distribution and its evolution in tests with short bonded lengths between 2 and 5Ø [103, 104].

The pertinence of the pull-out test has been questioned, as the stress-state in the materials and the cover may not be representative of structural applications [105]. Another test commonly used for bond research is the beam-end test that provides more flexibility for the concrete cover and bonded length [106]. A recent experimental campaign compared the results of pull-out and beam-end tests with a bonded length of 2Ø observing no influence of the test set-up for slip values below 0.1 mm and a 3 to 5% increase of the bond strength for pull-out specimens with comparable confinement [107]. It must be noted that, being a phenomenon of local nature, the variability observed in experimental results of theoretically identical specimens can be in the range of 1 to 18%, as summarized in Tab. 2.

***Tab. 2** Main experimental programme characteristics and coefficient of variation for the maximum bond stress ($\tau_{b,max}$) and its corresponding slip ($\delta_{sc}(\tau_{b,max})$) of identical tests from the literature.*

Reference	Test type	Series	Specimens	Ø [mm]	l_b/Ø [-]	CoV $\tau_{b,max}$	CoV $\delta_{sc}(\tau_{b,max})$
Eligehausen et al. [90]	Pull-out	1.1-1.5	2 or 3	25.4	5	1-12%	2-14%
Tepfers et al. [108]	Ring test	4	5	16	3	7%	23%
Metelli et al. [102]	Pull-out	13	7	12	5	15%	
		14	7	20	5	18%	
Moccia et al. [109]	Pull-out	BL5D12-S5	3	12	5	7-10%	8-18%
		BL5D20-S5	3	20	5	2-8%	3-10%

For typical bonded lengths in structural applications, the assumption of a uniform bond distribution is unrealistic. This was experimentally observed already in the 1950's using bars instrumented with strain gauges placed near their axes with various test set-ups [110, 111], providing information about the local bond-slip at different positions along the bond length [112, 91]. However, the measurement resolution was limited by the minimum spacing between gages.

The improvements in the recent years of fibre optic sensing (FOS) and Digital Image Correlation (DIC) have shown great potential to better understand the bond phenomenon. FOS provides pseudo-continuous strain measurements along the bars with high spatial resolutions and acquisition frequencies. DIC systems allow for detailed measurements of the displacement field over large regions of the specimen's surfaces. Recent works have used this technique to gain better understanding of the local bond-slip relationship and the distribution along bars in different structural members [13, 104, 113].

Several efforts have been done in order to establish a correlation between the local phenomenon and the bond performance in structural members. Balázs [114] proposed a crack width model based on the integration of the local bond-slip relationship proposed in the *fib* Model Code 1990 [115] assumed to be valid over the bar. This model justifies the variation of the average bond strength for different crack widths. Nevertheless, it ignores the effect of proximity to the crack face which leads to lower bond forces due to the development of conical cracks at the rib lugs [101]. This effect is often considered by a reduction factor multiplying the local bond stresses with a linear [94] or exponential decrease [116] towards the loaded end of the bar. Furthermore, longitudinal cracking along the bar has been shown to significantly reduce the bond stresses and several models have been proposed to account for this effect [92, 93, 117, 118, 119, 94].

The approximations with constant bond stress along the bond length are reasonable and practical for many design purposes. Nevertheless, a better understanding of the underlying mechanisms is required to verify the limits of applicability of current expressions, to develop mechanical models that can more easily be extended to new materials and to refine the design models. This is necessary to build efficient new structures and to better assess the state of existing ones (e.g., for a more refined fatigue verification accounting for the bar-concrete interaction or to estimate the residual resistance of anchorages affected by longitudinal cracks due to corrosion). Furthermore, local bond-slip relationships are used in finite element models.

In this context, the aim of the present research is to investigate the bond behaviour in specimens with medium anchorage lengths where conical and longitudinal cracks can develop to establish a better understanding of the effect of visible deteriorations on the concrete surface on the local bond stresses. The influence of some parameters commonly found in structural applications such as concrete cover, casting direction and rib geometry is considered in an experimental programme consisting of 29 pull-out tests instrumented with DIC and FOS. The experimental results show the interaction between the crack development and the local bond stresses that can be activated.

4.2 Experimental programme

An experimental programme was conducted in the Structural Concrete Laboratory of the École Polytechnique Fédérale de Lausanne (Switzerland) to investigate the effect of different parameters on the behaviour of steel reinforcement bars anchored in concrete and the influence of the cracks visible in the surface of the concrete on the local bond-slip relationship. The results of three tests performed by Moccia et al. [120] (series CM11) are included as well.

4.2.1 Series PC01 and PC02

Specimens

Two series of pull-out tests were conducted using bars with a nominal diameter (Ø) of 20 mm: series PC01 with 4 specimens and an anchorage length (l_b) of 10Ø and series PC02 with 22 specimens and an anchorage length of 15Ø. In all specimens, the bonded length corresponds to the full anchorage length, with the aim of representing realistic anchorage conditions where conical cracks can develop near the loaded end of the bar. The effect of the following parameters were investigated in these series:

- Clear concrete cover c: $1Ø \leq c \leq 5Ø$.
- Casting position: bars placed horizontally in the formwork were located at the top and bottom position, and bars placed vertically in the formwork were pulled in the same or opposite direction of casting (Fig. 19b).
- Rib geometry: three types of bars with ribs composed of two and four lugs were tested.
- Lug orientation: for bars with ribs composed of two lugs, tests were conducted with the lugs oriented parallelly (//) or perpendicularly (⊥) to the concrete free surface; the bars with four lugs were placed with the lugs in a 45° disposition with respect to the concrete surface (×), see Fig. 19c.

The bars to be tested were embedded in a concrete prism with one dimension corresponding to the anchorage length and the other being 400 mm. The concrete prisms were reinforced in the longitudinal direction with three 18-mm bars to control cracking during the tests. The spacing between test bars on the same side of the specimen was 800 mm and their position within opposite sides was shifted by 400 mm. Fig. 19a shows the geometry of the specimens and the main investigated parameters of the series. Details about the test parameters of each specimen are provided in Tab. 3.

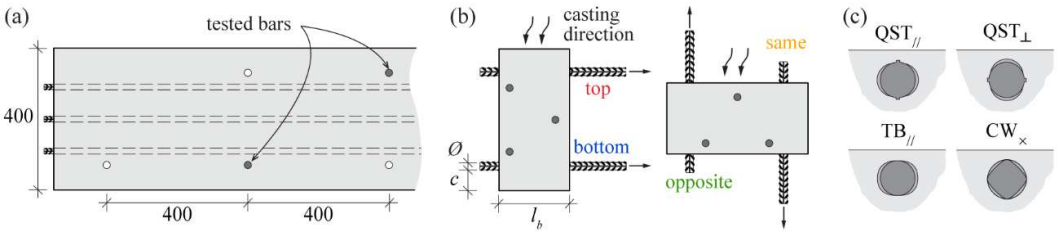

Fig. 19 *Specimen geometry and main investigated parameters of series PC01 and PC02: (a) front elevation of a typical concrete prism containing the test bars; (b) investigated casting positions; and (c) investigated rib geometries and lug orientations (refer to Fig. 20 for the used symbols describing the rib geometries).*

Tab. 3 *Series PC01 and PC02 main parameters and experimental results (see Notation for the definition of the parameters)*

Specimen	Ø [mm]	l_b/Ø	c/Ø	Casting	Bar type	Rib orientation	f_c [MPa]	F_{max} [kN]	σ_{sR} [MPa]	$\tau_{b,max}$ [MPa]	$\tau_{b0.1}$ [MPa]	Failure mode
PC0106	20	10	1	top	CW	×	39.5	76.3	243	6.1	4.1	S
PC0108	20	10	1	bottom	CW	×	39.5	87.9	280	7.0	6.4	S
PC0101	20	10	3	top	CW	×	40.6	93.7	298	7.5	6.6	SPO
PC0103	20	10	3	bottom	CW	×	39.5	115.5	368	9.2	7.0	SPO
PC0201	20	15	1	top	QST	//	40.6	96.1	306	5.1	3.4	S
PC0202	20	15	1	top	QST	⊥	40.5	88.5	282	4.7	3.2	S
PC0203	20	15	1	bottom	QST	//	40.7	115.6	368	6.1	5.1	S
PC0204	20	15	1	bottom	QST	⊥	40.7	119.6	381	6.3	5.9	S
PC0205	20	15	3	top	QST	//	40.9	114.8	365	6.1	4.8	SPO
PC0206	20	15	3	top	QST	⊥	40.9	125.5	400	6.7	2.4	SPO
PC0207	20	15	3	bottom	QST	//	41.0	163.5	521	8.7	7.0	SPOy
PC0208	20	15	3	bottom	QST	⊥	40.9	167.3	533	8.9	7.1	SPOy
PC0209	20	15	5	top	QST	//	41.1	158.5	504	8.4	5.8	SPOy
PC0210	20	15	5	top	QST	⊥	41.1	160.5	511	8.5	3.0	SPOy
PC0211	20	15	5	bottom	QST	//	41.2	>171	>545	>9.1	8.3	-
PC0212	20	15	5	bottom	QST	⊥	41.2	>175	>557	>9.3	7.1	-
PC0213	20	15	1	opposite	QST	//	41.3	106.0	337	5.6	5.6	S
PC0214	20	15	3	opposite	QST	//	41.4	157.1	500	8.3	6.6	SPO
PC0215	20	15	5	opposite	QST	//	41.4	163.0	519	8.6	8.1	SPOy
PC0216	20	15	1	same	QST	//	41.5	107.8	343	5.7	5.1	S
PC0217	20	15	3	same	QST	//	41.5	133.9	426	7.1	4.9	SPO
PC0218	20	15	5	same	QST	//	41.5	163.7	521	8.7	7.2	SPOy
PC0220	20	15	5	top	CW	×	41.3	133.5	425	7.1	4.6	SPO
PC0221	20	15	5	bottom	CW	×	41.3	149.8	477	7.9	6.7	SPO
PC0222	20	15	5	top	TB	//	41.2	140.1	446	7.4	5.9	SPO
PC0223	20	15	5	bottom	TB	//	41.3	176.0	560	9.3	8.0	SPO

$\sigma_{sR} = F_{max} / (\pi \cdot Ø^2/4)$.
$\tau_{b,max} = F_{max} / (\pi \cdot l_b \cdot Ø)$.
S = spalling before yielding of the reinforcement.
SPO = splitting induced pull-out before yielding.
SPOy = splitting induced pull-out after yielding.
- = test stopped after extensive yielding without anchorage failure.

Material properties

All specimens from each series were produced from one batch of normal-strength ready-mixed concrete provided by a local supplier with a maximum aggregate size of 16 mm. The concrete was poured in two layers of approximately 200 mm. The compressive strength f_c of the concrete measured on cylinders (height×diameter = 320×160 mm) is indicated in Tab. 3. The tensile strength measured at 28 day by direct tensile tests with the same type of cylinders was 2.6 MPa for series PC01 and 2.5 MPa for series PC02.

Three types of 20-mm diameter steel bars with rib profiles commonly found nowadays in Switzerland were used in the pull-out tests. The stress-strain diagrams are shown in Fig.20a. The bars display different characteristics:

- Quenched and self-tempered (QST) bars: hot rolled, quenched and self-tempered bars with a well-defined yield plateau. The ribs are composed of 2 lugs with a non-symmetrical distribution, see Fig. 20b.
- Cold-worked (CW) bars: cold-worked bars with no clear yield plateau (nominal yield strength determined at 0.2% residual strain). The ribs are composed of 4 lugs disposed symmetrically along the axis of the bar, see Fig. 20c.
- Threaded bars for reinforced concrete (TB): cold-worked steel bars with no clear yield plateau (nominal yield strength determined at 0.2% residual strain). The ribs are composed of 2 lugs disposed in continuous threads along the axis of the bar, see Fig. 20d.

The geometrical characteristics of the bar, including the bond index f_R, the maximum rib height $h_{R,max}$, the transverse rib angle β, the transverse rib flank inclination α_R and the transverse rib spacing s_R are obtained from a laser scan of the surface of the bars according to their definition [121]. The average rib height $h_{R,avg}$ is calculated by dividing the projected rib area over the nominal bar perimeter. The clear spacing between ribs c_{clear} is considered as the spacing between consecutive rib flanks at mid-height of the ribs based on the laser scans. The main properties of the bars are summarized in Tab. 4.

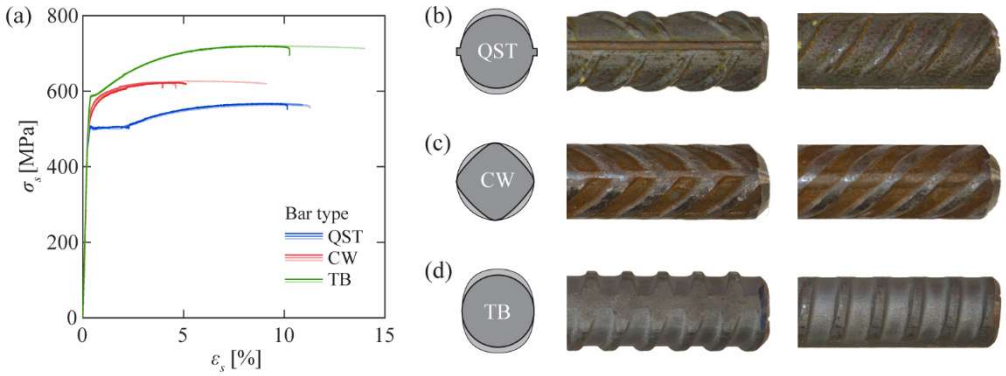

Fig. 20 *Bar characteristics: (a) stress–strain curves; and cross section and pictures of (b) QST bars, (c) CW bars and (d) TB bars.*

Tab. 4 *Bar mechanical and geometrical properties (see Notation for the definition of the parameters)*

Type	Ø [mm]	f_y [MPa]	f_t [MPa]	Lugs	f_R [-]	$h_{R,avg}$ [mm]	$h_{R,max}$ [mm]	s_R [mm]	c_{clear} [mm]	β [°]	αR [°]
QST	20	504	567	2	0.075	0.94	1.46	12.63	8.17	52.6	33.9
CW	20	558	625	4	0.079	0.94	1.42	11.91	6.83	42.4	37.5
TB	20	587	726	2	0.089	0.88	1.43	9.90	6.38	80	46.8

Test set-up and test development

All specimens where tested with the bar oriented in the vertical direction as illustrated in Fig. 21a,b. The bar was clamped with a steel wedge and the pull-out force was exerted through a hinge to minimize bending in the bar. The reaction on the concrete specimens was applied trough a steel frame to minimize the influence on the development of concrete cone breakouts. The frame was composed of two UPN 120 profiles and the frame legs were SHS 50×50×5 mm with 70×70×20 mm steel plates welded at the extremities. In each test, the frame was aligned with the axis of the bar. The frame was hinged at the position of the bar to minimize the bending moment in the concrete prism in the bar region. Two 16-mm threaded bars were used to counterbalance the applied force. The tests were conducted by applying the load at constant loading rate reaching the maximum load in 4 to 5 minutes. After the maximum force was reached, the test continued at a constant displacement rate to capture the post-peak response.

Measurements

The force applied to the bar and the reactions on the threaded bars were measured using load cells. The slip between the bar and the concrete at the unloaded end was measured with two LVDTs. The concrete surface parallel to the bar was tracked with DIC (see “DIC area” in Fig. 21a) using a pair of cameras SVS EVO4070 with a resolution of 4.2 Mpix. The correlation was done using the VIC-3D software [37], with a pixel size of 235 µm for series PC01 and 255 µm for series PC02. The displacement error was 1/75 pixels for in-plane displacements and 1/30 for out-of-plane displacements. The data acquisition frequency was 1 Hz.

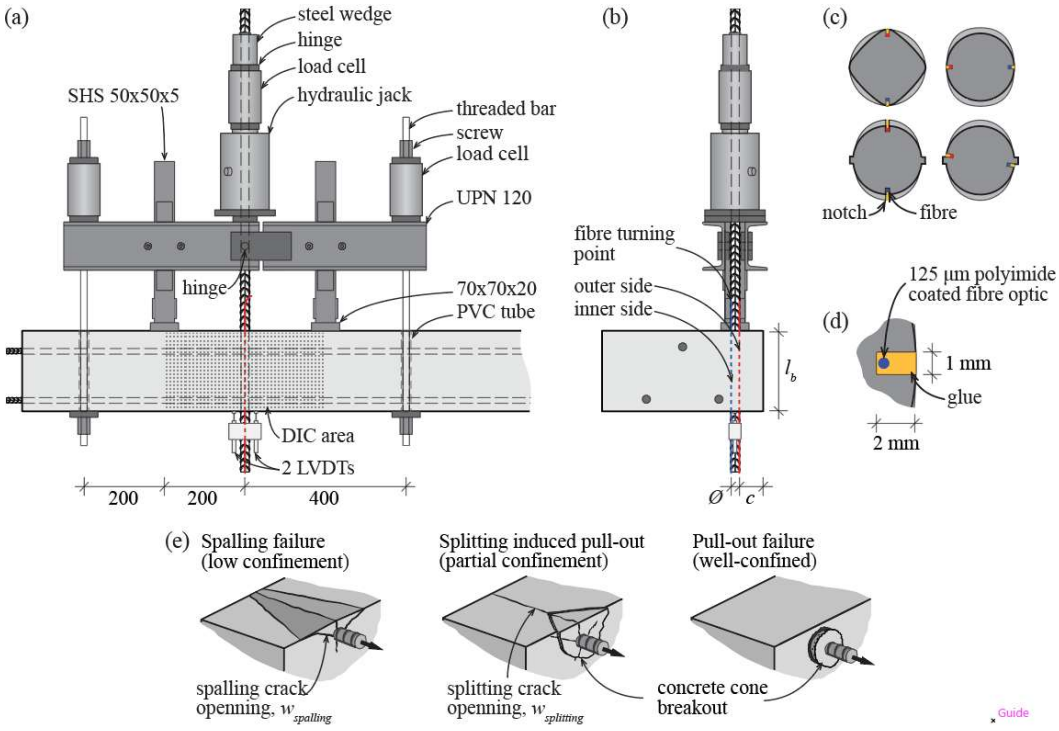

Fig. 21 *Test set-up, measurement systems and typical failure modes in the pull-out tests: (a) front and (b) side elevation of the test set-up; (c) position of fibre optic sensors in the different types of bars; (d) optical fibre detail; and (e) typical failure modes in pull-out tests. Polyimide I figure*

The reinforcement bars where instrumented using a single fibre optic installed along two opposite sides of the specimen, as illustrated in Fig. 21b. Polyimide-coated fibres with a diameter of 125 µm were used (Fig. 21d). The fibres were placed in a groove 1 mm wide and 2 mm deep that runs along the opposite faces of the bars. The position of the grooves was chosen to keep the fibres in a plane perpendicular to the concrete surface, independently of the rib orientation, see Fig. 21c. The strains were measured using Optical Distributed Sensor Interrogator ODiSI-6100 by Luna Innovations with a strain measurement range of ±12000 µε and a measurement accuracy of ±25 µε [122]. The spatial resolution of the strain measurements was 0.65 mm and the acquisition frequency varied between 40 and 62.5 Hz. It must be noted that for QST bars with a clear yield plateau, the yielding of the bar leads to strains larger than the measurement range and, therefore, to the loss of the fibre measurements.

4.2.2 Series CM11

Specimens of the pull-out test series CM11 conducted by Moccia et al. [120] had the same geometry as specimens from series PC01. The steel bars with a nominal diameter of 20 mm were embedded in a concrete prism 200×400 mm, corresponding to a bonded length of 10Ø. The evaluated parameters in the test series were the concrete cover and the casting conditions. The main properties of the specimens are summarized in Tab. 5.

The average concrete strength at the time of the tests was 42.3 MPa. The hot-rolled, quenched and self-tempered steel bars had a distinct yielding plateau, an average yield strength of 521 MPa and a tensile strength of 620 MPa. The ribs were composed of two lugs with a non-symmetric disposition and a bond index f_R = 0.072. The tests have been conducted in a similar manner as for series PC (more details can be found in Moccia et al. [120]).

***Tab. 5** Series CM11 main parameters and experimental results (see Notation for the definition of the parameters)*

Specimen	Ø [mm]	l_b/Ø	c/Ø	Casting	Bar type	Rib orientation	f_c [MPa]	F_{max} [kN]	σ_{sR} [MPa]	$\tau_{b,max}$ [MPa]	$\tau_{b0.1}$ [MPa]	Failure mode
CM1120	20	10	1	top	QST	⊥	42.3	64.0	204	5.1	2.3	S
CM1128	20	10	1	bottom	QST	⊥	42.3	70.8	225	5.6	5.2	S
CM1124	20	10	3	top	QST	⊥	42.3	94.7	302	7.5	5.4	SPO

$\sigma_{sR} = F_{max}/(\pi \cdot Ø^2/4)$.
$\tau_{b,max} = F_{max}/(\pi \cdot l_b \cdot Ø)$.
S = spalling before yielding of the reinforcement.
SPO = splitting induced pull-out before yielding.

4.2.3 Data post-processing

The strain measurements along the bonded length show local variations due to the variable cross section of ribbed bars, the potential variable material properties within the cross section, the noise in the measurement system and the transmission of bond forces at the ribs [13, 123]. These local strain oscillations have to be removed to calculate nominal bond stresses. A moving average filter over a length corresponding to 3 times the rib spacing (around 2 bar diameters) was applied to the raw strain measurements for the analysis of the test results. This distance is similar to the disturbed length observed in pull-out tests of bars with one and two ribs performed by Cantone et al. [13]. For the measurement of the strain due to shrinkage, a distance of 10 rib spacings was used. The average strain was computed from the smoothed measurements of the two fibres. The stresses were calculated considering the stress-strain relationship obtained from tensile tests of grooved bare bars with fibres. The pertinence of this assumption was verified with the average strain measurements over a length of 4 rib spacings from the loaded end of the bar outside the concrete (Fig. 21a). Bond stresses are derived from the smoothed stress profiles using Eq. 11, which can be obtained from the equilibrium of a differential bar element.

$$\frac{d\sigma_s}{dx} = \frac{4\tau_b}{Ø} \tag{11}$$

4.2.4 Failure modes

The typical failure modes in pull-out tests and the definitions used in this section are illustrated in Fig. 21e. Regardless of the test conditions, all specimens developed a splitting crack (parallel to the bar and approximately perpendicular to the concrete surface). Specimens with a cover of 1Ø failed by spalling of the concrete cover (failure mode “S” in Tab. 3 and 5) with the propagation of two longitudinal cracks along the bar with a small angle with respect to the concrete surface. Specimens with a cover of 3 and 5Ø displayed a splitting-induced pull-out failure (“SPO”). Some bars with an anchorage length of 15Ø yielded (“SPOy”) and two tests with QST bars at the bottom of the formwork (good casting conditions) were stopped when the stresses approached the tensile strength of the bar.

4.3 Experimental results

4.3.1 Shrinkage

Strain measurements from the fibre optic sensors were recorded 6 hours after the casting (day 0 measurements) and before testing. The measurements from the bar outside the concrete were used to remove the effect of temperature variation, assuming a uniform temperature distribution along the bar. Fig. 22a,b show the results for specimens PC0206 and 08, including the raw strain measurements (ε_s) from the external (closest to the concrete surface, red curves) and internal fibres (located in the opposite face of the bar, blue curves), the smoothed average stress (σ_s) and the bond stress. In specimen PC0206 (poor casting conditions), the signal presents large strain variations reaching strains over 1.5‰ for the external fibre and regular low amplitude variations for the internal fibre. In specimen PC0208 (good casting conditions), both signals show strain variations reaching approximately 1‰, similar to the measurements by Lemcherreq et al. [104]. The difference can be explained by the presence of plastic settlement voids under bar PC0206, which limit the capacity of the concrete to transfer forces to the bar [109]. The bar in good casting conditions is surrounded by the concrete on all sides, thus causing a similar strain profile on both sides of the bar. Similar trends could be observed in other specimens with the ribs oriented perpendicularly to the concrete surface.

The fibre measurements were smoothed using a moving average filter over a distance of 10 rib spacings (126 mm). The resulting stress profiles are coherent with those found in literature [104, 124]. The bar in poor casting conditions displays a minimum stress of -5.6 MPa and an average bond stress of 0.2 MPa (average value at each side of the maximum steel stress, see Fig. 22a) with maximum local values close to 0.5 MPa. For the bar in poor casting conditions, the minimum steel stress was -10.9 MPa with an average bond stress of 0.4 MPa, see Fig. 22b. The results indicate that smaller shrinkage axial and bond stresses are induced in the bar in poor casting conditions due to plastic settlement voids. Nevertheless, these results must be considered with care as the peak raw strain measurements are two orders of magnitude larger than the shrinkage strains. Consequently, the results are highly dependent on the smoothing. Further tests are required to confirm these findings.

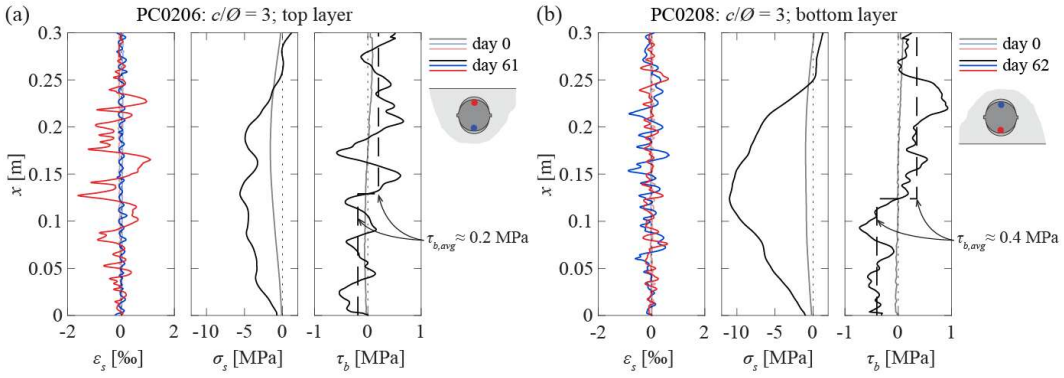

Fig. 22 *Shrinkage-induced effects: distribution along the bonded length of raw strain measurements, axial stresses and bond stresses in the bars for specimens (a) PC0206 and (b) PC0208 (red and blue colours refer to each fibre optic sensor, see sketch, black and grey curves refer to the mean values).*

4.3.2 Anchorage resistance

The anchorage resistance expressed in terms of the maximum stress activated in the bar (σ_{sR}) is represented as a function of the anchorage length in Fig. 23a-c. The experimental results are compared with the tensile stress that can be developed in the anchorage according to the expression for mean values proposed in the Background Document for

the final draft of Eurocode 2 (BD FprEC2:2023) [97, 98]. In all specimens, the experimental anchorage resistance was larger than the proposed values.

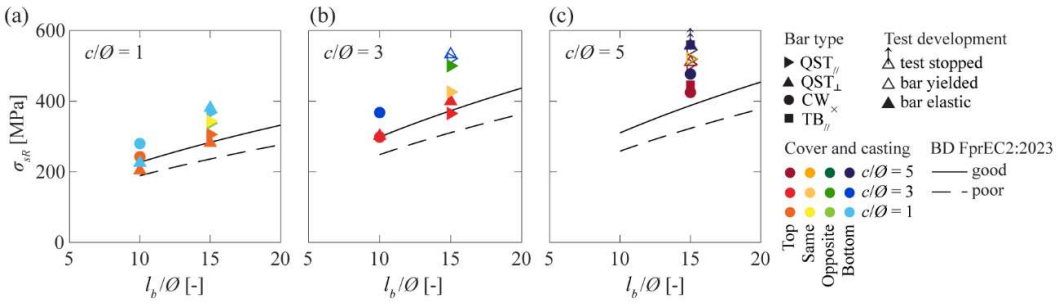

Fig. 23 *Anchorage resistance as a function of the anchorage length for specimens with covers of: (a) 1Ø; (b) 3Ø; and (c) 5Ø.*

4.3.3 Effect of the concrete cover and casting conditions

Fig. 24a shows the average bond stress over the anchorage length ($\tau_{b,avg}$) as a function of the unloaded end slip ($\delta_{sc,end}$) for specimens with an anchorage length of 15Ø in all the considered casting conditions. The maximum anchorage resistance is reached for good casting conditions (blue), followed by the bars loaded in the opposite direction of casting (green), then by the bars loaded in the casting direction (yellow), and finally the bars in poor casting conditions (red). Specimens with a cover of 1Ø present a relatively brittle failure with a sudden drop in the force and the consequent lack of experimental data (dotted lines).

The influence of the concrete cover and the casting position on the maximum stress activated in the bar is shown in Fig. 24b. This difference is caused by the cracks and the voids under the bars due to the plastic settlement of the fresh concrete and the higher porosity of the concrete under the bars [125, 126, 127, 109]. The effect of the confinement and casting position on the anchorage length is included in current standards; however, its effect on cracking at SLS is not [12, 94].

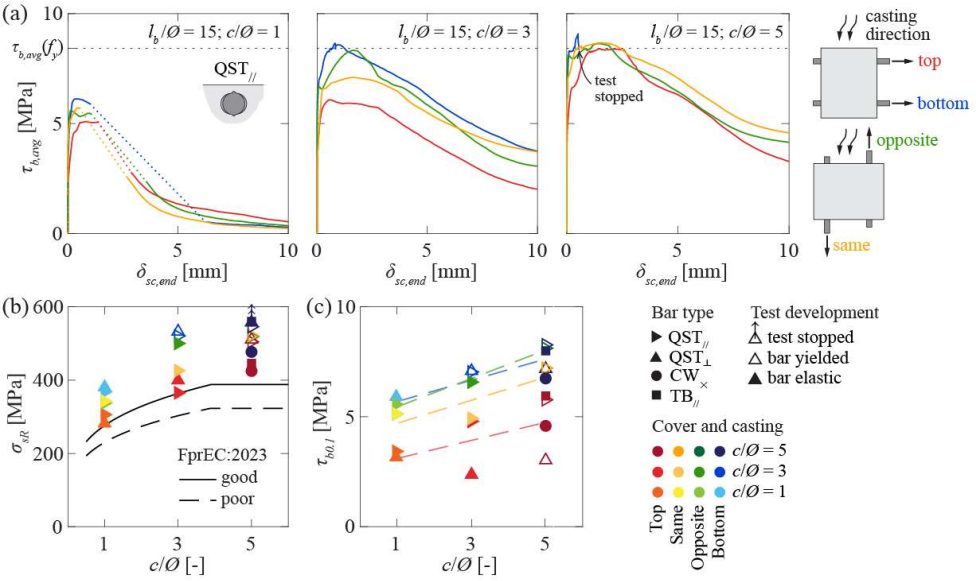

Fig. 24 *Effect of concrete cover and casting conditions: (a) average bond stress-slip relationships for specimens with covers of 1Ø (PC0201, 03, 13 and 16), 3Ø (PC0205, 07, 14 and 17) and 5Ø (PC0209, 11, 15 and 18); (b) anchorage resistance as a function of concrete cover; and (c) average bond stress corresponding to a slip at the unloaded end of 0.1 mm as a function of concrete cover.*

Fig. 24c presents the average bond stress corresponding to a slip at the unloaded end of 0.1 mm ($\tau_{b0.1}$) for the considered covers. Significant variations can be observed due to the other parameters; however, the linear regression (dashed lines) shows an increasing trend for all casting conditions. Therefore, the effect of confinement and casting conditions can be relevant for serviceability verifications. Pérez Caldentey et al. [128] recently proposed an empirical factor for the crack spacing formulation based on the experimental results of four-point bending tests to account for the effect of casting conditions and the effect of cover in poor casting conditions. The results in Fig. 24c confirm that the cover can influence the bond stresses at SLS in all casting conditions. The new generation of standards includes the effect of casting conditions on the crack width formulation [97].

Fig. 25 shows the detailed measurements obtained with DIC and FOS along the anchorage length for specimens PC0201, 05 and 09 with $QST_{//}$ bars in poor casting conditions. For each specimen, the crack opening at the maximum load (F_{max}) is represented in red and the cracks developed during the post-peak phase are shown in grey in Fig. 25 a,c,e. This information was extracted from the DIC data using the Automatic Crack Detection and Measurement software (ACDM) [42]. Fig. 25b,d,f display the distribution of raw (light grey curves) and smoothed strains ε_s (red, purple and dark grey curves), smoothed axial stress σ_s, bond stress τ_b, steel δ_s (dotted curves) and concrete displacements δ_c (dashed curves), relative slip δ_{sc} (solid curves) and crack width w for different load levels. The concrete displacement is calculated from the displacement field on the concrete surface measured with DIC. The bar displacement is calculated by adding the slip at the unloaded-end measured with the LVDTs and the integrated strains along the bar. The relative slip is the difference between these two values. The opening of the spalling crack $w_{spalling}$ (solid curves) is assumed to be equal to the out-of-plane displacement of the concrete cover along the bar axis. The opening of the splitting crack $w_{splitting}$ (dashed curves) is measured using the DIC displacements from the concrete surface (for the definition of splitting and spalling cracks used in this section, see Fig. 21e and 26d).

For all specimens, the splitting crack appeared first at the loaded end of the bar and propagated towards the unloaded end. Typically, as the load increased, one or more cracks with a “V” shape developed on the concrete surface along the length of the specimen. These cracks probably correspond to the intersection of conical cracks originating at the ribs [101] with the concrete surface. The development of these cracks can also be observed in the stepped distribution of concrete displacements. Near the loaded end of the bar, the propagation of these cracks caused the breakout of a conical concrete block (dark grey area in Fig. 25c,e) causing large displacements and a reduction of the bond stresses. Specimen PC0201 failed by spalling of the cover, the spalled region is indicated with a dark grey hatch in Fig. 25a.

The axial steel stress distribution shows that for small load levels, larger bond stresses are activated at the loaded end of the bar. As the load increases, the distribution flattens near the loaded end, indicating lower bond stresses in that region. A redistribution of the bond stresses occurs and larger bond stresses are activated near the unloaded end, as observed by other authors [110]. After the maximum load is reached, the concrete cone detachment causes bond stresses to vanish within the corresponding length as can be clearly observed in Fig. 25d. In specimen PC0209, whose reinforcement yielded at around 95% of the anchorage capacity, the length of the concrete cone breakout along the bar is similar to the region where yielding was detected (Fig. 25f). The slip plots indicate that the displacement of the concrete can be neglected until the propagation of the conical cracks reaches the concrete surface. The crack opening plots show that the spalling crack width reaches considerably larger values for the bars with a cover of 1Ø. For specimens with larger covers, the splitting crack widths tend to be larger. An interaction between the concrete cone breakout and the splitting and spalling cracks is observed. Within the region affected by conical cracks, larger spalling crack widths occur due to the displacement of the concrete cover. Concerning the splitting crack, as the bar slides, the partially detached concrete blocks composing the cone are pulled. This causes their rotation in opposite directions in the plane of the concrete surface, reducing the splitting crack width near the intersection of the two cracks. Similar crack patterns and stress distributions were observed in other specimens. The results for all tested specimens can be found in Appendix IV.

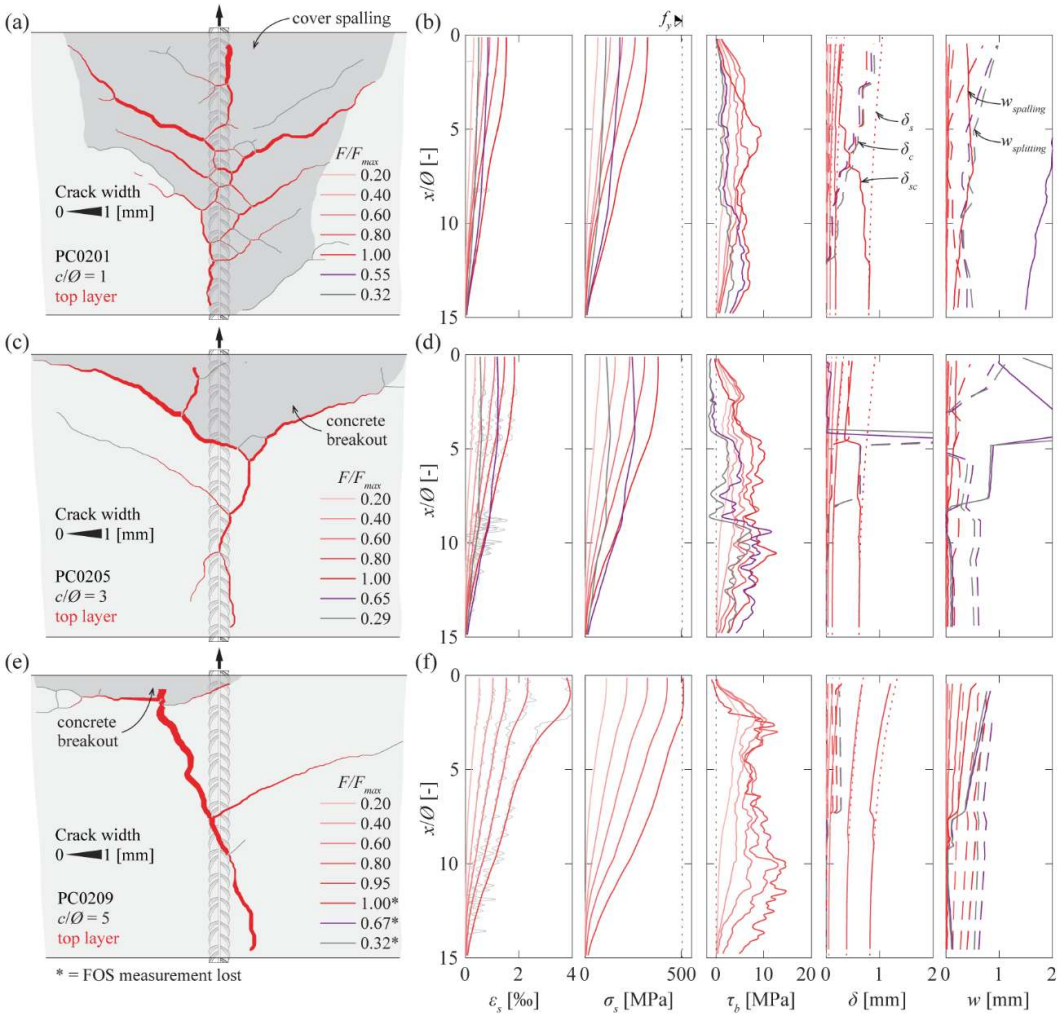

Fig. 25 *Pull-out test detailed measurements: crack pattern and distribution along the anchorage length of axial steel strains, axial steel stresses, bond stresses, slip and crack widths for specimens (a)-(b) PC0201, (c)-(d) PC0205 and (e)-(f) PC0209.*

More detailed information about the local response at various positions along the bar can be obtained from the measurements presented in Fig. 25 by plotting the different values as a function of the local slip. The local bond stress-slip distribution and the evolution of the crack widths at different locations are illustrated in Fig. 26. The average bond stress as a function of the unloaded and loaded end slips (grey hatch) and the MC2010 local bond-slip relationship (red curves) are represented for comparison. As it can be observed in Fig. 26a,b, the average response for specimens with a cover of 1 and 3Ø displays a lower peak bond strength than the MC2010 provisions, which is logical as the MC2010 expressions were calibrated with short pull-out tests with a more uniform bond stress distribution. The local bond stress measurements display similar peak values or even higher for the points not affected by the cone breakout. The local measurements display a less brittle post-peak response than the corresponding relationship according to MC2010 (unconfined splitting failure). This is also probably related to the longer bonded length and the stress redistribution capacity. For the specimen with a cover of 5Ø (Fig. 26c), the average response reaches a peak stress close to the MC2010 provision with higher local bond stresses. Points outside the concrete cone breakout display a fairly uniform behaviour. Within the breakout region, the local bond stresses reach lower values and have a more brittle response. The response does not seem to correspond to a uniform reduction of the bond stresses as proposed by MC2010, but rather a similar ascending branch with different maximum bond stresses and post-peak responses [90, 129]. In all specimens, the measured response displays higher stiffness in the ascending branch than the MC2010 expressions. These results agree with other recent studies using pull-out tests [102], beam-end tests [103] and concrete ties [113].

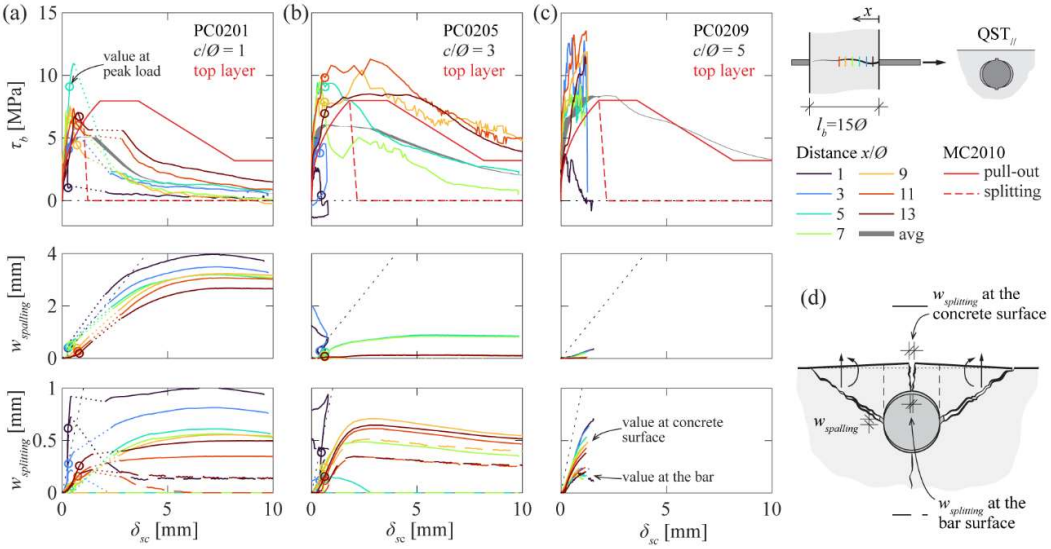

Fig. 26 *Local measurements along the bonded length: local bond-slip, spalling crack opening-slip and splitting crack opening-slip relationships for specimens (a) PC0201, (b) PC0205 and (c) PC0209; and (d) schematic representation of the crack development mechanism.*

It must be noted that the crack patterns represented in Fig. 25 correspond to the measurements on the concrete surface. The activation of bond forces is directly related to the internal cracking of the concrete around the bar, which can differ from the measurements on the concrete surface. The spalling of the cover causes the rotation of the concrete segments delimited by the splitting and the spalling cracks in a plane perpendicular to the bar, as illustrated in Fig. 26d. This rotation increases the crack with of the splitting crack on the concrete surface and reduces it at the bar surface. The variation of the crack opening can be estimated by multiplying the rotation at both sides of the crack by the cover. Therefore, the estimated crack width at the bar can be obtained by subtracting the estimated variation from the measurement on the visible concrete face. The pertinence of this estimation was verified and compared with DIC measurements on the surface perpendicular to the bar on the loaded end [130]. The estimated splitting crack width at the bar is shown with dashed lines in Fig. 26a-c.

The crack width plots for specimen PC0201 show large spalling crack openings reaching values close to two times the maximum rib height. As the out-of-plane displacements of the cover take place, the width of the splitting crack at the bar is reduced (Fig. 26a). Specimens with larger covers show smaller spalling openings, particularly for points outside the cone breakout. Specimen PC0205 shows the largest splitting crack widths at the bar surface (close to 0.5 mm) that remain stable during the post-peak phase, see Fig. 26b. The specimen with a cover of 5Ø shows the smallest crack openings, see Fig. 26c.

Fig. 27a shows the local bond stress corresponding to a local slip of 0.1 mm ($\tau_{b0.1}$) along the anchorage length for specimens with a cover of 3Ø in different casting conditions. The average value for each specimen is represented with a dashed line. The points closer to the loaded end (x = 0), which are affected by the concrete cone breakout, typically display lower secant stiffness, with the exception of the bar loaded along the casting direction (yellow curve), which shows a similar stiffness along most of the bonded length and even higher values near the loaded end. In this case, the loaded end is close to the bottom of the formwork (good casting conditions). Outside the cone breakout region, the specimen in the bottom of the formwork (blue curve) and the specimen loaded against the casting direction (green curve) show similar secant stiffnesses larger than for the other conditions. The local response of the specimen at the top of the formwork (poor casting conditions, red curve) is slightly stiffer than the specimen loaded along the casting direction. This seems reasonable because for the bar at the top of the formwork, the voids caused by the plastic settlement of concrete will be located under the bar; whereas for the vertical bar, they will appear under the ribs along the full perimeter of the bar. Nevertheless, the average

response yields similar values as the voids will get smaller in the regions close to the bottom of the reinforcement. The difference between these two conditions can differ depending on the distance to the bottom of the formwork [109].

The local bond-slip responses for the four considered casting conditions at three locations are shown in Fig. 27b,c. The results at a distance of 2Ø from the loaded are within the concrete cone breakout and show a brittle response (Fig. 27b). The results at 7 and 13Ø from the loaded end reach larger bond stresses and have a less brittle softening response (Fig. 27c,d). At each location, the experimental curves show similar behaviours for the different conditions besides the differences in stiffness and peak values. In all cases, the responses are stiffer than the MC2010 relationships.

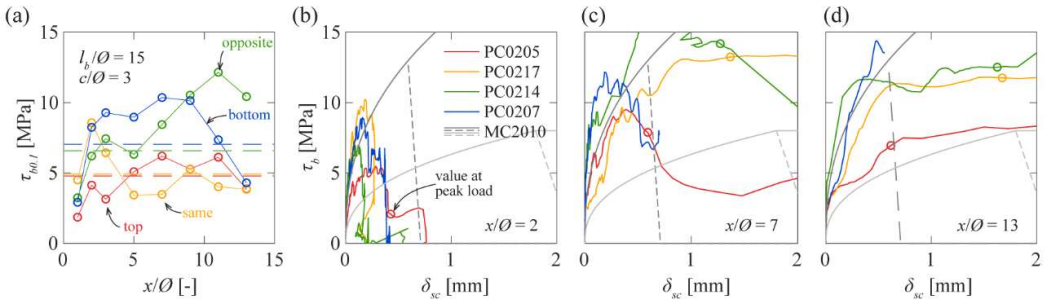

Fig. 27 *Effect of casting position for specimens PC0205, 07, 14 and 17: (a) local bond stress corresponding to a local slip of 0.1 mm along the anchorage length; and local bond-slip relationships at (b) x/Ø = 2, (c) x/Ø = 7 and (d) x/Ø = 13.*

4.3.4 Rib orientation

The measured average bond stresses as a function of the unloaded end slip for specimens with an anchorage length of 15Ø and different concrete covers are illustrated in Fig. 28a. The QST bars were placed with two orientations: bars with the ribs oriented parallel to the concrete surface ($QST_{//}$, solid curves) and bars with the ribs oriented perpendicularly to the surface ($QST_{\perp}$, dashed curves). The same general response and failure mode is observed independently of the rib orientation for good (blue curves) and poor casting conditions (red curves). Fig. 28b shows the influence of the rib orientation on the maximum stress activated in the bar. The results for specimens in good casting conditions show little influence of the rib orientation. For specimens in poor casting conditions with a cover of 1Ø (spalling failure), the $QST_{//}$ specimen reached an anchorage resistance 9% larger than the $QST_{\perp}$. For specimens in poor casting conditions with covers of 3 and 5Ø, the anchorage resistance for $QST_{//}$ bars is, on average, 5% lower. Fig. 28c shows that the $\tau_{b0.1}$ is, on average, 67% lower for $QST_{\perp}$ specimens in poor casting conditions. The response in good casting conditions shows no difference on average (values of ±15%). This can be explained by the presence of plastic settlement voids and the porous concrete layer that, in the case of perpendicular orientation, directly affect the rib placed towards the bottom of the formwork. For specimens with ribs oriented parallelly to the concrete, only a lower portion of the lugs is affected by the voids. This effect is not present in bars in good casting conditions, which justifies the lack of uniform tendency and values within typical bond test scatter.

Fig. 28d illustrates the bond stress distribution along the bar for 5 load levels for specimens with covers of 3Ø. The results show that for loads close to 20% of the anchorage resistance, bars in poor casting conditions activate lower bond stresses but over a longer portion of the bar, particularly for the $QST_{\perp}$ bar. This is in good agreement with the differences in stiffness (Fig. 28c), and can indicate a higher redistribution capacity when the bond-slip relationship is less stiff. Moreover, it can be observed that higher bond stresses are activated near the unloaded end in specimen PC0206 which explains the higher anchorage resistance. The difference in the activation for low load levels can also be observed for specimens with covers of 1 and 5Ø (see Appendix IV).

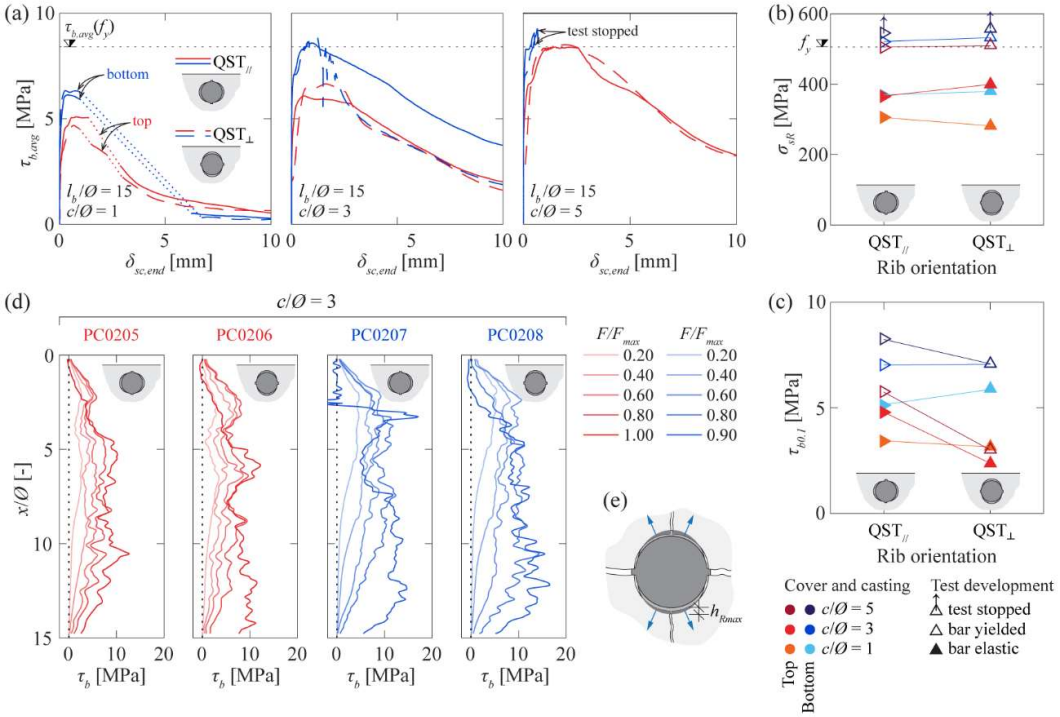

Fig. 28 *Effect of rib orientation: (a) average bond stress-slip relationships for specimens with covers of 1Ø (PC0201 to 04), 3Ø (PC0205 to 08) and 5Ø (PC0209 to 12); (b) anchorage resistance as a function of the rib orientation; (c) average bond stress corresponding to a slip at the unloaded end of 0.1 mm as a function of the rib orientation; (d) local bond stress distribution along the anchorage length for specimens with a cover of 3Ø (PC0205 to 08); and (e) schematic representation of the rib orientation effect.*

The results seem coherent with the fact that bars with the ribs oriented perpendicularly to the concrete surface will develop a larger component of bursting forces, whereas if the rib lugs are oriented parallelly, there will be a larger component of splitting forces (Fig. 28e). Consequently, specimens with a failure mode governed by spalling (low confinement) can have a lower anchorage resistance if the ribs are placed perpendicularly to the concrete surface. In good casting conditions, the sudden crack development limits the influence of this effect.

Cairns et al. [131] reported that there is a high probability that rib orientation influences the bond strength, based on an analytical formulation and an experimental programme with lap-splices that favoured splitting failure. Koschemann et al. [107] conducted an experimental campaign with beam-end tests with bond lengths of 2Ø investigating the effect of rib orientation on bars with a nominal diameter of 16 mm and rib pattern similar to the QST bars in this publication. The lowest anchorage resistance (around 5%) was observed for specimens with ribs oriented parallel to the concrete surface and the lugs leading to compression struts towards the concrete surface. The experimental results presented in this section indicate that, for specimens with pull-out or splitting-induced pull-out failures, the influence of the rib orientation is larger in the redistribution of bond stresses than in the crack development. Recent studies on lap-splices [132] and anchorages [133] have shown that local bond-slip relationships with lower peak values and stiffness can lead to higher strengths in poor conditions for long anchorage lengths.

It must be noted that the difference in anchorage resistance due to the rib orientation reported in this study and in the literature lies within the typical scatter observed in bond tests. However, the differences in the secant stiffness for small slip values are significant and indicate that the effect of rib orientation is potentially relevant for SLS conditions.

4.3.5 Rib geometry

Fig. 29a presents the average bond stress as a function of the unloaded end slip for specimens with an anchorage length of 10Ø and a cover of 1Ø. The results indicate that the anchorage resistance of the $QST_{\perp}$ bars is lower than for CW bars: 19% for good (blue curves) and 16% for poor casting conditions (red curves). The stiffness follows the same trend, being lower for $QST_{\perp}$ specimens: 18% for good and 44% for poor casting conditions. This could be explained by the difference in orientation, given the similar geometrical characteristics of these bars. CW bars were placed with the lugs in a 45° disposition with respect to the direction of the concrete surface, therefore generating a lower bursting force component and being less susceptible to the effect of plastic settlement voids. The results for specimens with a cover of 3Ø in poor casting conditions show similar peak bond stresses and lower secant stiffness, see Fig. 29b.

Fig. 29c shows the average bond stress as a function of the unloaded end slip for specimens with an anchorage length of 15Ø and cover of 5Ø. For good and poor casting conditions, the QST bars developed the largest anchorage resistance (around 19% higher in poor casting conditions), followed by the TB bars (5% and 17% higher in poor and good casting conditions respectively) and the CW bars. The difference in the bond indices of the bars does not correlate with the results, as the bar with the lowest bond index (QST) activates the highest bond stresses. In well-confined conditions, the pull-out failure occurs by shearing off the concrete keys between the ribs and increasing the rib spacing leads to larger bond strengths, as observed by other authors that tested bars with the same rib geometry and different spacings [108, 102]. As indicated in Tab. 4, QST bars have the largest clear spacing amongst the considered bars, followed by CW and TB bars (8.17, 6.83 and 6.38 mm, respectively). This explains the highest results for QST bars. The width of the rib can influence the results as the ratio of c_{clear}/s_R determines the proportion of the perimeter per unit of length occupied by concrete keys: 0.65 for QST bars, 0.57 for CW bars and 0.64 for TB. Another factor influencing the bond behaviour is the transverse rib angle (β), as previously observed by Soretz et al. [134], who reported a small increase in the bond performance with increasing inclination of the lugs using pull-out tests on cubes. The higher transverse rib angle for TB bars can increase the bond strength. Consequently, the differences in the measured responses are likely the result of the combination of the aforementioned effects.

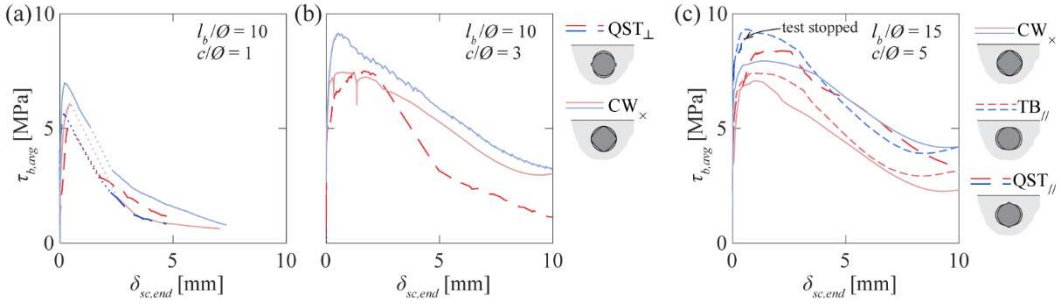

Fig. 29 *Effect of rib geometry: average bond stress-slip relationships for specimens with covers of (a) 1Ø (CM1120, 28, PC0106 and 08), (b) 3Ø (CM1124, PC0101 and 03) and (c) 5Ø (PC0209, 11, 20, 21, 22 and 23). Blue curves: good casting conditions, red curves: poor conditions.*

4.4 Result discussion

Fig. 30 shows the evolution of the spalling crack opening (solid curves) and of the splitting crack opening at the bar surface (dashed curves) as a function of the local slip at different locations along the bar for different specimens. As shown in Fig. 30a,b, specimens with low confinement display similar trends regardless of the type of bar, anchorage length and casting conditions. For small slip values (around 0 to 0.1 mm), both crack openings remain small and comparable. For larger slip values, the spalling crack becomes significantly larger in most specimens, particularly after the peak load is reached (circles). The crack widths are comparable to the local slip values within a distance of around 7Ø from the loaded end

and gradually decrease for locations closer to the unloaded end. However, the values at the peak load are considerably larger for the specimens in poor casting conditions. This indicates a lower stiffness in the spalling mechanism, which can be explained by the presence of plastic settlement cracks [109]. In good casting conditions, the cracks develop and propagate suddenly close to the peak load, which explains the more brittle behaviour. Only small differences can be observed due to the rib orientation. Specimens with $QST_{//}$ bars (PC0201 and 03) display slightly larger splitting crack widths than $QST_{\perp}$ specimens (PC0202 and 04).

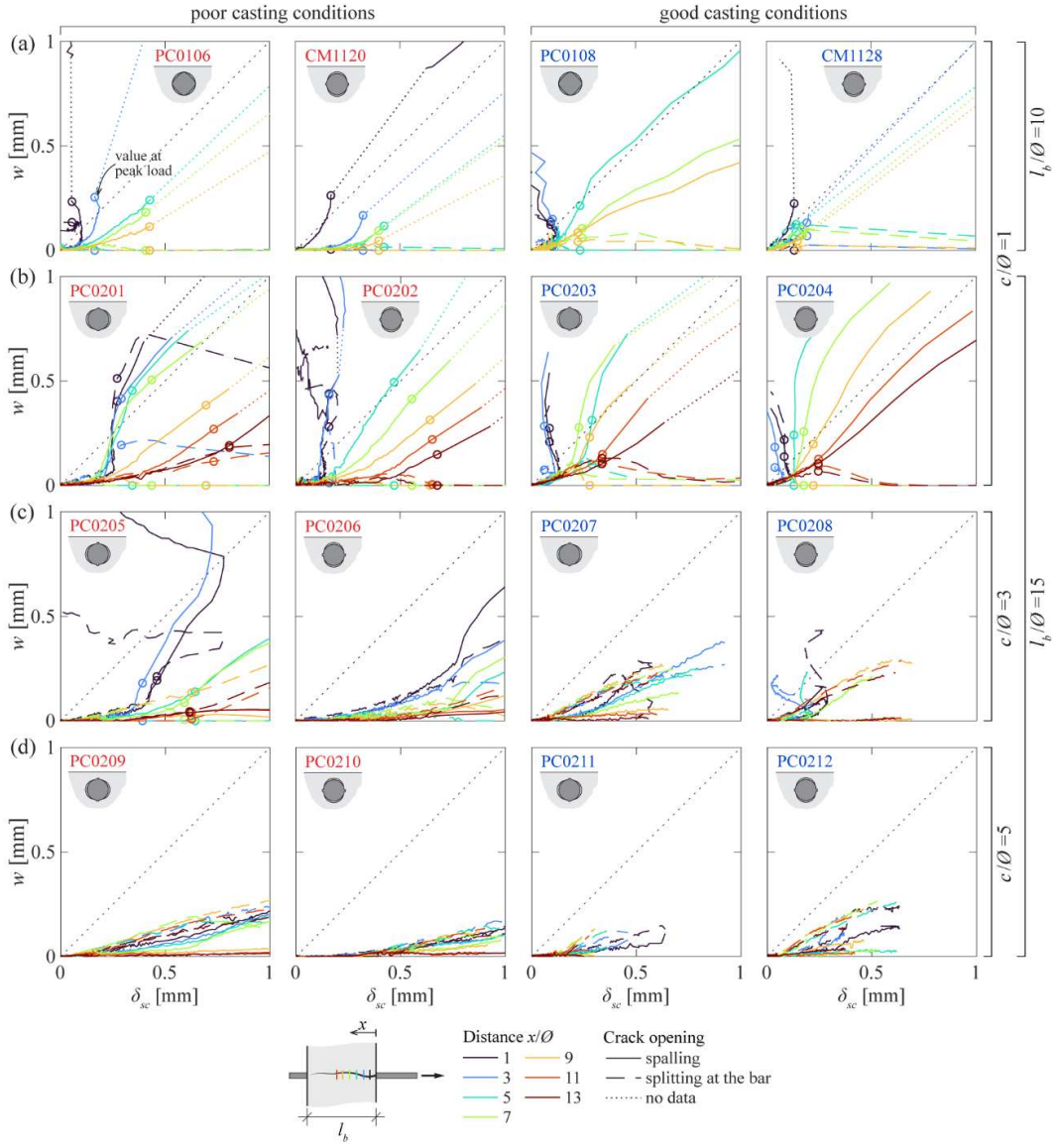

Fig. 30 *Spalling crack opening and splitting crack opening at the bar surface as a function of the local slip for specimens with covers of: (a) 1Ø and l_b/Ø = 10 (CM1120, 28, PC0106 and 08), (b) 1Ø and l_b/Ø = 15 (PC0201 to 04), 3Ø and l_b/Ø = 15 (PC0205 to 08) and 5Ø and l_b/Ø = 15 (PC0209 to 12)*

Fig. 30c presents the results for specimens with a cover of 3Ø and show a clear effect of the conical cracks noticeable in the sudden change of tendency of the spalling crack propagation. For example, in specimen PC0205, the concrete cone breakout causes large spalling cracks at 1 and 3Ø from the loaded end and a second conical crack causes an increase in the spalling crack width after the peak load for locations at 5 and 7Ø (see Fig. 25c,d). For the rest of the locations, the splitting crack increases almost linearly with the slip and very small spalling openings are measured. The fibre signal is lost before the maximum force for specimens PC0207 to 12. Fig. 30d shows the results for specimens

with a cover of 5Ø. For most locations, both splitting and spalling cracks follow a fairly uniform tendency and with smaller crack widths than specimens with a cover of 3Ø. It must be noted that for similar slip values, specimens with larger covers reach higher bond stresses, as shown in Fig. 24a. No clear trend can be observed due to the rib orientation.

4.5 Conclusions

This section presents the results of an experimental programme to investigate the influence of different parameters on the local bond-slip relationship along anchored bars of medium length, with the aim of understanding the relationship between the cracks visible in the concrete surface and the bond stresses. The main findings of this research are summarized below:

1. The bond behaviour in structural elements is complex and the study of elements with medium and long anchorages is necessary to complement the experiments with short bonded lengths.
2. Fibre optical sensors in combination with DIC have proven to be useful to study the distribution of steel stresses and bond stresses along the anchorage length, the local bond-slip response and the influence of the cracks visible on the concrete surface. The experimental results show that cracking has an unfavourable effect on the bond performance of anchored bars.
3. The effect of concrete cover and casting direction on the bond strength agrees with previous research. The anchorage resistance increases for larger covers. The largest anchorage resistance is obtained for bars placed in good casting conditions (lower position), followed by bars loaded in the opposite direction of casting, and then by the bars loaded in the casting direction. The lowest resistance is obtained for bars placed in poor casting conditions (upper position).
4. The effect of the rib orientation with respect to the concrete surface is more relevant for anchorages with low covers governed by spalling of the concrete cover. In well-confined conditions, the anchorage resistance of bars with similar bond indexes but different rib geometries can differ by more than 15%. In such conditions, the anchorage response is not sufficiently well characterized accounting only for the bond index.
5. In specimens with medium anchorage lengths and moderate or well-confined conditions, the behaviour is less brittle, and the effect of the redistribution of bond forces due to a lower stiffness of the local bond response can lead to a higher anchorage resistance, even if lower local bond stresses are activated.
6. The measured local bond-slip relationships show higher stiffness than the MC2010 expressions for all the tested conditions and parameters. Specimens with a cover of 3Ø do not display such a brittle post-peak response as the corresponding unconfined splitting failure proposed in MC2010. They failed by splitting induced pull-out developing bond stresses even for slip values similar to the rib spacing.
7. The differences in the local bond-slip responses for low and moderate confinements, with respect to the pull-out failure, can be explained by the development of spalling cracks (parallel to the bar and approximately parallel to the concrete surface), splitting cracks (parallel to the bar and approximately perpendicular to the concrete surface) and conical cracks leading to concrete cone breakouts near the loaded end of the bar.

4.6 Outlook and future works

Some questions related to the topics studied in this section remain open. In the following, some of these future research lines are outlined:

- The optical fibre measurements have shown great potential for the understanding of bar-to-concrete bond. In particular, they have shown the differences in the bond distributions of bond stresses along the bonded length for bars in good and poor casting conditions. The bond length in this research correspond to moderate lengths. However, these findings should be confirmed in real anchorage lengths (around 40 times the bar diameter).
- The influence of the casting conditions is dependent on the distance to the bottom of the formwork. In many structures such as bridges or walls this depth can be of several meters. Pull-out tests in elements cast in such conditions could be performed to determine the bond performance.

- Tests to study the redistribution of bond stresses under sustained loading using fibre optical measurements could be performed.
- The influence of certain parameters is still unknown. The type of aggregate is known to affect the elastic modulus of concrete and could have an influence on the bond response.

5 Enhancement of the bar stress - crack width relationship

5.1 Introduction

The cracked response of reinforced concrete structures is fundamental for their functionality, as it influences the stiffness of the members (deflections and vibrations) and their water tightness. Furthermore, crack control is important for durability and aesthetic reasons. Accordingly, current design standards such as Eurocode 2 (EC2:2004) [135] or *fib* Model Code 2010 (MC2010) [94] include expressions to estimate the crack width and impose limits based on the environmental exposure and other criteria. However, crack formulations have the opposite goal to that of the present research, that is to estimate the crack width from the calculated reinforcement stress. This often includes simplifying assumptions that might not be pertinent if the formula is used in reverse for bar stress estimation. Moreover, in the case of an existing structure, additional information such as crack spacing, which is an essential parameter in the crack width formulations, or the existence of secondary or splitting cracks can be measured or visually verified.

The first proposed crack width formulae were based on the slip defined as the relative displacement between the steel and the concrete. When the crack appears, compatibility of deformations between the steel and the concrete is lost. The slip activates bond stresses which determine the crack spacing and the tensile stress distributions in the bar and the concrete.

Starting in 1936, Saliger [136] proposed a formulation based on this principle to calculate the crack spacing and width in flexural elements with smooth bars assuming a linear bond stress distribution with a maximum at the crack location. Thomas [137] proposed analytical expressions including the effect of shrinkage assuming a parabolic bond stress distribution. A different approach was adopted by Brooms [138], assuming that no slip occurs between the bar and the concrete and that plane sections do not remain plane. In these conditions, tensile stresses develop linearly from the cracks leading to the generation of principal or secondary cracks, depending on whether they reach the surface of the concrete. The resulting crack spacing is proportional to the cover [139]. Ferry-Borges [140] proposed a formulation accounting for both effects that is the base of some of the current code formulae [135] [94]. Several crack formulations can be found in the literature using different approaches (thorough reviews of the available models can be found in [141, 142, 143]). The comparison of 30 formulations performed by Lapi et al. [142] shows that the semi-analytical models of Eurocode 2 [135] and Model Code 10 [94] are amongst the most accurate.

Concerning the bond stresses, Balazs [114] proposed an analytical model based on the integration of the ascending branch of the bond-slip relationship for well-confined conditions from the *fib* Model Code 1990 [115]. A closed form solution can be found for the crack propagation stage, and a numerical integration was used for the stabilized cracking phase. Based on the analytical integration of a bond-slip relationship [144], Sigrist [145] proposed a rigid plastic bond-slip law with the bonds stress equal to $2f_{ctm}$ and f_{ctm} before and after bar yielding, respectively. The considered bond-slip laws [144] [115] were derived from a small number of tests. Recent experimental programmes have shown that the bond performance of bars is not accurately represented by bond-slip relationship from MC2010 [102, 113, 146].

Some attempts have been made to estimate the bar stress from surface crack measurements. Campana et al. [147] used the model by Sigrist [145] to estimate the stresses in the stirrups of beam tests based on crack width measurements; however, the results could not be compared as the stirrups were not instrumented. Calvi [148] proposed a model for the assessment of elements with shear cracks, where the estimation of the bar strains based on the crack width measurement is based on the expressions for the slip proposed by Shima et al. [149] and the considerations of Maekawa et al. [150] for the

estimation of the crack width. Brault et al. [151] used this model to predict the strains measured in small beams subjected to bending instrumented with Digital Image Correlation (DIC) and distributed fibre optical sensors glued to the reinforcing bars. The estimated strains have the same order of magnitude as the measurements; however, the trends of the experimental results and the predictions show significant differences. Carmo et al. [152] estimated the average steel strain based on the results of ties with internally strain gauged bars and marker photogrammetry on the surface. They concluded that this approach is feasible but the accuracy was limited by the camera resolution.

Recent experimental studies using DIC and distributed fibre optical sensors in ties [13, 113, 153, 154] and beams [155, 13, [14, 3] have shown great potential to improve the understanding of the cracking process and the bar-to-concrete interaction. Some of these results show average bond stress values significantly lower than the code formulations [[14] [153]. Fibre optic sensors have proven to be useful to characterise shrinkage induced strains in the reinforcement [156, 124, 153, 154].

Based on these observations and the fact that bond plays a critical role in the response of cracked members, this section, which is adapted from [157], investigates the development of bond stresses through analytical and experimental work, with the aim of improving the existing crack formulations to estimate the reinforcement stress based on crack width measurements. Given its mechanical basis, the slip approach is considered in this publication. First, the slip-based model is presented and the influence of the different parameters is evaluated. Secondly, experimental results from tie and beam tests instrumented with DIC and fibre optical sensors on the reinforcement are analysed to better understand the cracking phenomenon and bond development. Lastly, new values for the bond stresses are proposed on the basis of a local bond stress-slip model adapted from [158]. The slip-based model with the proposed bond values is used to estimate the stresses in the experimental results, showing good agreement.

It must be noted that the term “crack width” used in current standards and other publications concerning cracking refers to the crack displacement component in the direction of the reinforcement. This is due to the fact that in most regions prone to cracking, the reinforcement is placed in the direction of the principal tensile stresses. Consequently, the crack width corresponds to the crack displacement component in the direction of the reinforcement. One exception is the shear reinforcement that is typically placed vertically; whereas shear cracks have generally a certain inclination.

For conciseness and clarity purposes, in this section the term “crack width” is used to designate the “crack displacement component in the direction of the reinforcement” and denoted with the symbol $\delta_{||}$ (see Fig. 1). The calculated uniform longitudinal stress in the bar due to the axial force is denoted with the symbol σ_s.

5.2 Cracking in structural members

5.2.1 Slip-based model

The mechanical behaviour of a cracked element in tension is typically characterized by the force-average strain response, as shown in Fig. 31a. The response can be divided in three phases. First, the uncracked response is characterized by compatibility of strains between the bar and the concrete. The crack formation stage begins with the first crack, that appears when the tensile strength of the weakest concrete section is reached, leading to the strain distribution shown in Fig. 31c. Bond stresses progressively transfer the force from the bar to the surrounding concrete that will eventually reach the cracking strain again at a distance which cannot be shorter than l_{cr} from the 1st crack. When all crack distances are not larger than $2l_{cr}$, new cracks cannot develop (end of the crack formation phase). The minimum and maximum crack spacings (s_{cr}) are thus l_{cr} and $2l_{cr}$, respectively. At this point, the stabilized cracking phase starts, characterized by an increase of the streel strains when the force is further augmented, see Fig. 31c. This publication focuses on the stabilized cracking stage as it is the most relevant for structural members subjected to external loads.

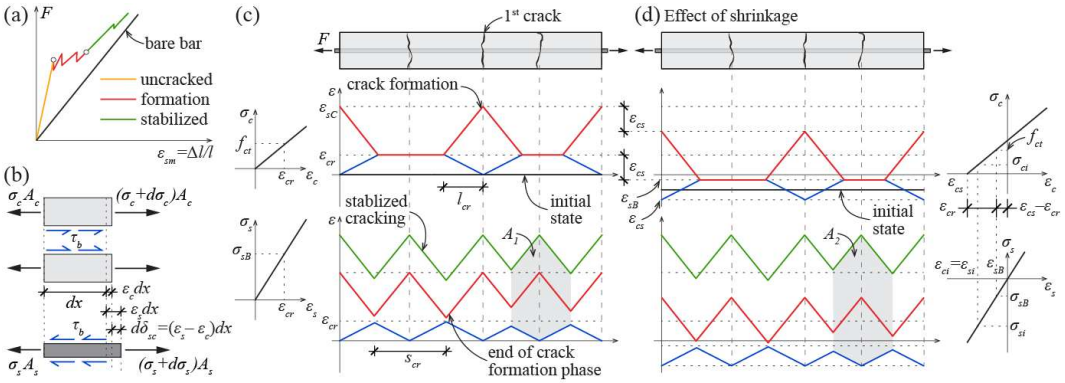

Fig. 31 *Response of a concrete tie: (a) force – average strain diagram; (b) differential tie element; strain distribution in the crack formation phase and the stabilized cracking phase (c) without the effect of shrinkage and (d) accounting for shrinkage.*

The slip δ_{sc} corresponds to the difference between the displacements of the steel and the concrete. The slip in the differential element shown in Fig. 31b can be calculated from the steel (ε_s) and concrete strains (ε_c) using Eq. 12. The crack width results from the slip at each side of the crack (i.e. the crack spacing s_{cr}) as per Eq. 13.

$$d\delta_{sc} = (\varepsilon_s - \varepsilon_c)dx \tag{12}$$

$$\delta_{||} = \int_{s_{cr}} (\varepsilon_s - \varepsilon_c)dx = s_{cr}(\varepsilon_{sm} - \varepsilon_{cm}) \tag{13}$$

The stress and strain distributions in the two materials are determined by the external loads and the bond forces. A common approach in numerous crack models is to use a constant bond stress corresponding to the average over the bonded length ($\tau_{b,avg}$). This leads to the diagrams presented in Fig. 31c where the strain profiles vary linearly. The residual tensile strength of the concrete [159] is neglected.

Shrinkage influences the initial stress and strain distributions (Fig. 31d) and can reduce the cracking force [160, 161]. According to Eq. 13, the crack width corresponds to the area between the strain profiles of the bar and the concrete (areas A_1 and A_2 in Figs. 31c,d). The consequence of shrinkage can clearly be observed: for a given stress in the bar, the crack width is larger compared with the case neglecting shrinkage ($A_1 < A_2$). This is reflected in Eq. 14 that allows to calculate the resulting crack width for a given bar stress in the stabilized cracking phase.

$$\delta_{||} = \frac{s_{cr}}{E_s}\left[\sigma_{sC} - \frac{s_{cr}\tau_{b,avg}}{\varnothing}\frac{1+(n-1)\rho_t}{1-\rho_t} - E_s\varepsilon_{cs}\right] \tag{14}$$

where, E_s is the elastic modulus of the reinforcement, σ_{sC} is the stress in the reinforcement at the crack location, $\varnothing$ is the bar diameter, $n = E_s/E_c$, ρ_t is the reinforcement ratio of the tie and ε_{cs} is the unrestrained shrinkage strain (considered as a negative value, see Fig. 31d). The development of this expression can be found in Appendix V.

This expression is the basis of the maximum crack width formulations in the current codes. MC2010 specifies the average bond strength in the calculation of the length over which slip between concrete and steel occurs. The proposed values for the average bond strength are $1.8f_{ctm}$ for short term loading and $1.35f_{ctm}$ for other types of loading. EC2:2004 does not explicitly mention the average bond stress. A factor to account for the casting position has been proposed [128, 162] for the *fib* Model Code 2020 and the new generation of Eurocode 2 [163], which leads to average bond stresses of $2f_{ctm}$ and $1.5f_{ctm}$ in good and poor casting conditions respectively. The proposed expressions for the relative mean strain are similar with a factor which accounts for short or long-term loading.

The Tension Chord Model (TCM) [164] uses the same approach assuming a rigid plastic bond-slip relationship with bond stresses of $2f_{ctm}$ and $1f_{ctm}$ before and after yielding of the reinforcement.

A sensitivity analysis for a tie with a section of 100×100 mm and a reinforcement bar of Ø18 is presented in Fig. 32. Fig. 32a shows the bar stress-crack width diagram according to EC:2004 (dashed black line), MC2010 (solid grey line) and Eq. 14 (solid black line) for the reference value of the influencing parameters. For a given stress, the code formulations underestimate the crack width compared with Eq. 14, because the stress variation is calculated assuming the maximum spacing. Fig. 32b shows the influence of the different parameters. It can be observed that the crack spacing is a crucial parameter. For an existing structure, it can be measured with a certain precision. The effect of shrinkage is non-negligible. Estimating the shrinkage effects is difficult in simple specimens in laboratory conditions [165], and even more so in real structures. However, as shrinkage strains induce compressive stresses in the reinforcement, by neglecting this effect a conservative estimate of the stress is obtained. Bond stresses have a relevant contribution particularly for small crack widths. The influence of the other parameters is relatively small.

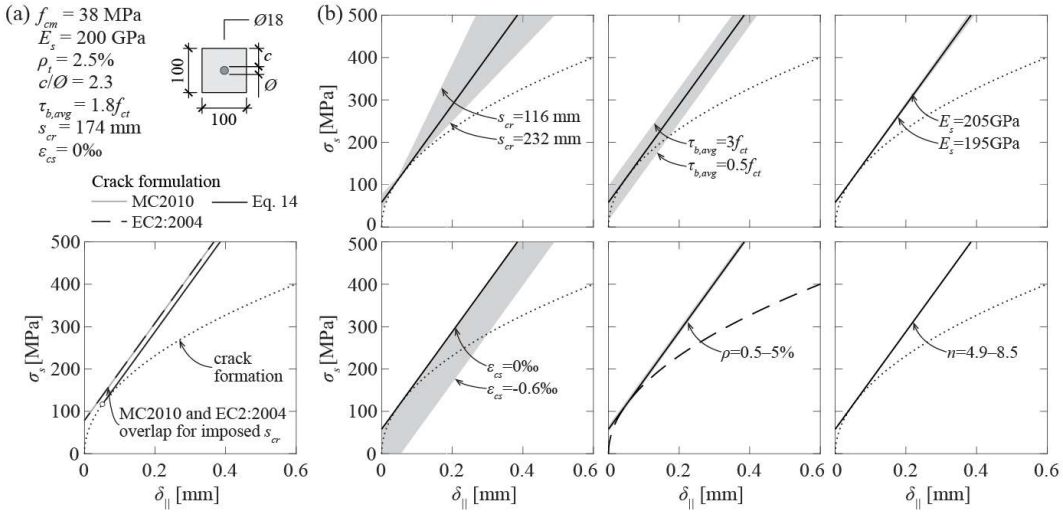

Fig. 32 *Sensitivity analysis of the influencing parameters in the bar stress – crack width relationship: (a) reference parameters and model comparison; and (b) effect of crack spacing, average bond stress, elastic modulus of steel, unrestrained shrinkage strain, reinforcement ratio and elastic moduli ratio.*

The stress difference with respect to the stress for the reference values is summarized in Tab. 6.

Tab. 6 *Sensitivity analysis results (see Notation for the definition of the parameters)*

$\delta_{\|}$ [mm]	**Bar stress variation due to the variation of the parameter**					
	s_r	$\tau_{b,avg}$	E_s	ε_{cs}	ρ	n
0.1	-5 / +22%	-24 / +23%	± 2%	-69 / +0%	-3 / +6%	-1 / +2%
0.2	-13 / +33%	-15 / +14%	± 2%	-42 / +0%	-2 / +3%	± 1%
0.3	-16 / +38%	-11 / +10%	± 2%	-30 / +0%	-1 / +2%	± 0.5%
0.4	-18 / +41%	-7 / +8%	± 2%	-23 / +0%	-1 / +2%	± 0.5%

5.2.2 Detailed experimental results

The reality is slightly more complex than the response of the idealized concrete ties described above. First of all, the bond distribution is not uniform. Due to the propagation of secondary conical cracks developing from the ribs [101] which can reach the main crack,

bond stresses are significantly reduced near the crack. This is typically accounted for by considering a different bond-slip response near the crack [90, 129] or by applying a reduction factor over a certain length [115, 116, 94]. Due to compatibility of displacements, the slip at the mid-point between cracks has to be zero and, therefore, bond stresses in that region are small.

Several authors have observed that the crack width at the level of the reinforcement is smaller than at the concrete surface [166, 167, 168]. The difference is often attributed to the secondary conical cracks [168, 169]. Moreover, in cases with relatively small covers, secondary conical cracks can reach the concrete cover during the stabilized cracking phase and eventually propagate across the section, modifying the stress distribution. In such conditions, splitting and spalling cracks can significantly reduce the bond performance of the bar near the crack as described in Section 4.

5.3 Experimental programme

An experimental programme was conducted in the Structural Concrete Laboratory of the École Polytechnique Fédérale de Lausanne (Switzerland) to investigate the relationship between the crack width and the stress in the reinforcement, and the development of bond stresses in structural elements. Furthermore, results from beam tests from series SM10 by Monney et al. [3] and SC70 by Cantone et al. [13] performed in the same laboratory and instrumented with similar techniques are included in this section.

5.3.1 Tension test series TC10

Main parameters and test set-up

Two tension tests were performed on reinforced concrete ties with a square cross section and a length of 1250 mm, see Fig. 33a. Specimen TC11 had a cross section of 214×214 mm and was reinforced with 4 bars with nominal diameter (Ø) of 18 mm, as shown in Fig. 33b. Specimen TC12 had a single Ø18 centred in a cross section of 100×100 mm. All the details including the clear cover (c) are provided in Tab. 7. The tests were performed using a Trebel Testing Machine with 5 MN capacity in tension at a displacement rate of 0.1 mm/min. Specimen TC11 was loaded monotonically until failure. TC12 was loaded monotonically until $\sigma_{cyc,max}$ = 275 MPa, then unloaded until $\sigma_{cyc,min}$ = 27.5 MPa. After that, 35 cycles with the same stress range were applied before the tie was loaded until the bar yielded.

The specimens were cast horizontally, as illustrated in Fig. 33c, from a single batch of normal-strength ready-mixed concrete provided by a local supplier with a maximum aggregate size of 16 mm. The compressive strength f_{cm} and the tensile strength f_{ctm} of the concrete measured on cylinders (height×diameter = 320×160 mm, direct tensile tests for f_{ctm}) are indicated in Tab. 7.

Tab. 7 *Series TC10 main parameters (see Notation for the definition of the parameters)*

Specimen	Ø [mm]	Bars [-]	ρ [%]	c/Ø [-]	Loading	Age at testing [days]	f_{cm} [a] [MPa]	f_{ctm} [b] [MPa]
TC11	18	4	2.22	1	monotonic	244	43.1	2.5
TC12	18	1	2.54	2.3	cyclic	239	43.1	2.5

[a] measured at testing age
[b] measured at 28 days

The longitudinal reinforcement bars were hot rolled high-strength threaded bars with a nominal diameter of 18 mm. As shown in Fig. 33d, they had no clear yield plateau. The mean value of the yield strength at 0.2% residual strain was 731 MPa. The ribs were composed of two lugs disposed in continuous threads along the axis of the bar, see Fig. 33e. They were oriented parallelly to the concrete surface, see Fig. 33c. The geometrical characteristics of the bar were obtained from a laser scan of the surface of the bars [121]:

bond index f_R 0.088, maximum rib height 1.13 mm, transverse rib angle 82°, transverse rib flank inclination 46.4° and transverse rib spacing 8.02 mm. The clear rib spacing c_{clear} measured at the top of the lugs was 6.34 mm.

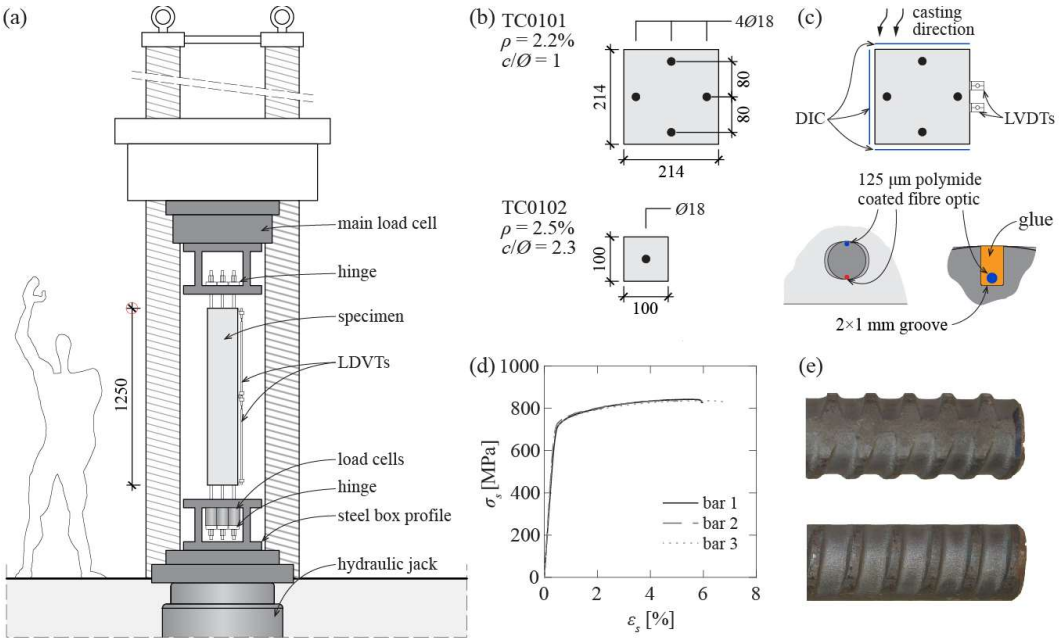

Fig. 33 *Test series TC10: (a) elevation of the test set-up; (b) specimen cross section; (c) measurement systems on the concrete surface and fibre installation for strain measurement; (d) reinforcement bar tensile tests results; and (e) rib profile.*

Measurements

Three faces of the ties were tracked using DIC: at the bottom face of the formwork (resolution 20 megapixels and resulting pixel size 277 µm/pixel), at the top face (29 megapixels and 215 µm/pixel) and for a lateral face (5 megapixels, 544 µm/pixel), see Fig. 33c. The correlation was done using the VIC-3D software [37]. The maximum in plane displacement error was 1/60 pixels. In the face with no DIC measurements, two LVDT's were installed to follow the total elongation.

The reinforcement bars were instrumented by Polyimide-coated optical fibres with a diameter of 125 µm running along two opposite sides of the bar, as shown in Fig. 33c. A single fibre per bar was placed in grooves 1-mm wide and 2-mm deep running along opposite faces of the bar. The fibres were oriented in a plane perpendicular to the nearest concrete surface, Fig. 33c. The strains were measured using Optical Distributed Sensor Interrogator ODiSI-6100 by Luna Innovations with a strain measurement range of ±12,000 µε and a measurement accuracy of ±25 µε [122]. The spatial resolution of the strain measurements was 0.65 mm, and the acquisition frequency was 10 Hz.

5.3.2 Beam test series SM10

Six three-point bending tests conducted by Monney et al. [3] and the authors of this publication were used to characterize the cracking response of large-scale elements. Three beam specimens with constant height h of 700 mm and various widths b_w were tested as shown in Fig. 34b. Each beam had two test regions with the same shear reinforcement consisting of Ø8 stirrups placed with a spacing of 200 mm, one with ductility class A and the other with ductility class C according to EC2:2004 [135]. To prevent a failure in the central part, it was reinforced with double Ø14 stirrups with a spacing of 150 mm, see Fig. 34a. The flexural reinforcement was composed of two B500C Ø34 bars (f_{ym} = 561 MPa) and three to six Y1050 Ø36 bars (f_{ym}=1014 MPa) to provide an approximatively constant flexural reinforcement ratio (ρ_f ~ 1.5%, see Tab. 8). With an effective depth d of 650 mm, the nominal clear cover c_f of the flexural reinforcement was 33 mm (~1$Ø_f$), while the nominal

clear cover c_w for the stirrups was 25 mm (3.1$Ø_w$) as shown in Fig. 34d. The beams were loaded monotonically until failure using two hydraulic jacks anchored to the strong floor at a loading rate of 10 kN/min. Further details are provided in Tab. 8.

The two lateral faces were tracked with DIC. In each beam, the two longitudinal Ø34 bars were instrumented with a single fibre optic installed along two opposite sides of the specimen, as illustrated in Fig. 34d. The 125 µm polyimide-coated fibres were placed in a groove 2mm deep in the longitudinal reinforcement and 1 mm deep in the stirrups. The stirrups ST2 to 13 were instrumented with fibres, as shown Fig. 34c. Stirrups ST5, 8 and 11 had one fibre running along the opposite faces of the stirrup, see Fig. 34d. The rest had only one fibre running along the perimeter of the stirrup, see Fig. 34e. For additional details, see Monney et al. [3].

Tab. 8 *Monotonic test series SM10 main parameters (see Notation for the definition of the parameters)*

Test	Shear reinf. ductility class	b_w [mm]	h [mm]	ρ_f [%]	ρ_w [%]	f_{cm} [MPa]	f_{ctm} [MPa]	f_{ywm} [MPa]	V_{max}[a] [kN]
SM11	A	800	700	1.52	0.063	50.7	3.2	505	603
SM12	C	800	700	1.52	0.063	50.6	3.2	538	610
SM13	A	600	700	1.51	0.084	50.4	3.2	505	540
SM14	C	600	700	1.51	0.084	50.4	3.1	538	639
SM15	A	500	700	1.50	0.101	50.2	3.1	505	454
SM16	C	500	700	1.50	0.101	50.0	3.1	538	515

[a] measured shear strength without self-weight

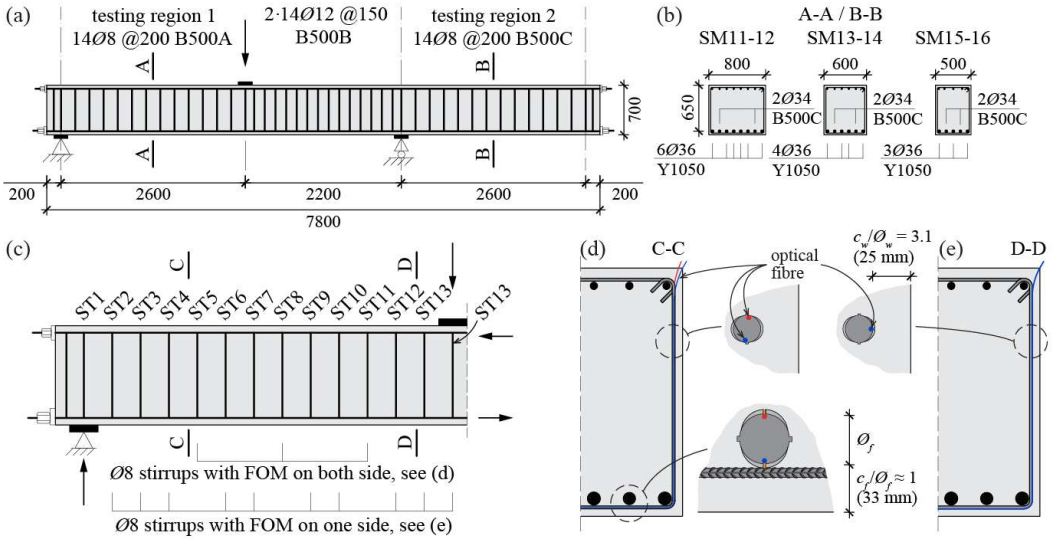

Fig. 34 *Monotonic test series SM10: (a) elevation of the test set-up; (b) cross section of the test specimens; (c) fibre instrumentation within the tested region; and details of the fibre installation in the longitudinal reinforcement and in the stirrups with (d) two sensors or (e) one sensor (for additional details, see [3]).*

5.3.3 Beam test series SC70

Three four-point bending tests conducted by Cantone et al. [13] were analysed to characterize the cracking response under cyclic loading. Fig. 35a shows the main dimensions of the test set-up. The beams had a height of 320 mm, a width of 300 mm and a longitudinal reinforcement consisting of two high-strength Ø22 bars, see Fig. 35b. The

effective depth d was 274 mm, leading to a nominal clear cover c_f of 35 mm (1.6$Ø_f$), see Fig. 35c. No shear reinforcement was disposed.

The beams were loaded cyclically with three different shear force ranges. SC75 was loaded up to a maximum shear correspondent to the theoretical cracking force. SC76 was loaded up to a shear force of 55% of the shear strength V_{max}. SC77 was loaded up to the formation of the sub-horizontal branch of the shear crack. After 50 cycles, the specimens were loaded until failure, except for specimen SC77 where the propagation of the shear crack due to cyclic loading led to a premature failure after 21 cycles. The main parameters of the tests are given in Tab. 9. Fig. 35d shows the shear force as a function of the mid-span deflection for the three tests.

Tab. 9 *Cyclic test series SC70 main parameters (see Notation for the definition of the parameters)*

Specimen	b_w [mm]	h [mm]	ρ_f [%]	ρ_w [%]	f_{cm} [MPa]	f_{ym} [MPa]	Cycles [-]	$V_{cyc,min}$ [kN]	$V_{cyc,max}$ [kN]	V_{max}[a] [kN]
SC75	300	320	0.92	-	33.3	701	60	27.8	5.3	95.4
SC76	300	320	0.92	-	36.0	701	50	54.0	7.3	97.1
SC77	300	320	0.92	-	36.3	701	21	86.4	10.2	80.7

[a] shear strength including self-weight

The front face of the specimen was tracked with DIC. In each beam, the longitudinal Ø22 bar closest to the front face was instrumented with a single optical fibre installed in a 2 mm deep groove running along two opposite sides of the bar, as shown in Fig. 35c. For additional details, see Cantone et al. [13]).

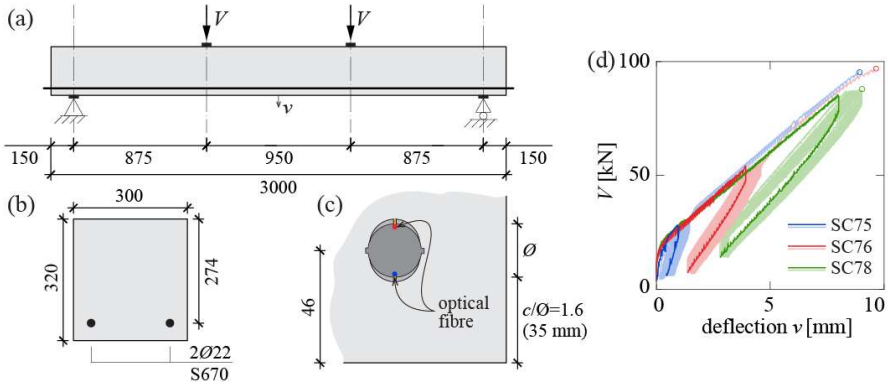

Fig. 35 *Cyclic test series SC70: (a) elevation of the test set-up; (b) cross section of the specimens; (c) fibre instrumentation within the tested region; and (d) applied shear as a function of the mid-span deflection for specimens SC75, SC76 and SC77 (for additional details, see [13]).*

5.3.4 Measurement post-processing

The DIC results were used to detect the crack patterns and estimate crack kinematics using the Automated Crack Detection and Crack Measurement (ACDM) procedure proposed by Gehri et al. [42]. The fibre strain measurements were post-processed to remove noise and the large variations due to the variable cross section and the introduction of bond stresses at the ribs [13, 123, 104]. For this purpose, a moving average filter over a length of two bar diameters was used. The bar strains are calculated by averaging the results from the two sides of the bar. The stresses are calculated assuming a bilinear stress-strain constitutive law assuming an elastic modulus of E_s = 200 GPa and a strain hardening modulus according to the respective tensile tests. Local bond stresses (τ_b) are derived from the equilibrium considerations of a finite bar element [13] only in the elastic range of the bar.

Average bond stresses ($\tau_{b,avg}$) are computed based on the average of the local bond stresses over the relevant length. The curvature of the bar (χ_s) is calculated assuming a distance between fibres equal to the nominal bar diameter minus 4 mm, assuming that the fibre is at the bottom of the groove.

The slip considered for the estimation of the local bond-slip response is estimated from the steel strains measured with the fibres. The steel strains are integrated from the point where strains where negligible (point at approximately l_{cr} from the crack) during the crack formation phase, or from the inflection point of the strain profiles (similar to the mid-point between cracks) during the stabilized cracking stage. The cracking sequence is considered. The concrete strains are neglected.

5.4 Experimental results and discussion

5.4.1 Tensile tests

The results of the tension test series TC10 are presented in Fig. 36. The relationship between average stress in the reinforcement (calculated as the applied force divided by the nominal steel surface) and the average strain (calculated as the average of the fibre measurements divided by the tie length, namely 1250 mm) is shown in Fig. 36a. For each specimen, the measured response (including the initial shrinkage strains) is shown with a black solid line and the bar tensile tests (grey hatch) are shown. The response after removing the initial shrinkage strains (black dashed line) is shown for visual reference. The initial shrinkage strains were around -0.14‰ and -0.25‰ for specimens TC11 and TC12, respectively. These results are in the same order of magnitude as those found in the literature [156, 154]. Furthermore, the difference between them is probably related to the different ratio between the element cross section and its perimeter (often referred to as notional size in standards [94], 107 and 50 mm for specimens TC11 and TC12, respectively). Elements with smaller ratios have a larger specific surface and therefore a faster drying shrinkage, in this case TC12.

Figs. 36b,c show the crack patterns for the North and South faces of specimen TC11 at two load steps. The two faces correspond respectively to the bottom and the top faces during casting. Due to the relatively small cover, several secondary cracks originating from the conical cracks at the ribs [101] are visible. Some of them eventually propagated to become traversing cracks. The average crack spacings are 102 and 105 mm for the North and South faces, respectively. The corresponding value for specimen TC12 was 131 mm (similar values for both faces). The figures include also the steel strain ε_s, the axial stress σ_s (calculated form the strains with the assumed stress-strain relationship) and the bond stress τ_b distributions for 6 load steps along the tie length. The strain and stress profiles show good correlation with the observed cracks. The stress distribution near the crack location and the point between cracks vary smoothly, indicating low bond stresses. This can also be observed in the bond stress distribution. Smaller bond stresses are developed for the bar at the top of the formwork (poor casting conditions). This is a well-known effect due to the plastic settlement and bleeding voids that form under the bars [125, 128, 109].

The results of the DIC and fibre optical measurements allow analysing in detail each crack with a precision which was not possible with classical measurement and observation methods. Fig. 37a shows the contribution of the secondary cracks to the total crack width $\delta_{||}$ for the case of crack 2 of the bottom face of specimen TC11 (TC11 North). It can be observed that the width at the initial crack (point A) does not increase after a stress of around 300 MPa. After that, a second and a third crack develop (points B and C), that concentrate additional components of the crack width. At a larger stress level, another secondary crack develops (point D) with a negligible contribution (w ≈ 0.01 mm). The total crack width measured at the concrete surface near the bar is smaller than the corresponding width near the corners of the specimen (points E and W). This is consistent with experimental measurements that show the variation of the crack with over the concrete cover [170, 168]. It indicates that the crack width at the bar location is likely smaller that the crack width observed on the concrete surface, particularly for large covers. For this reason, the crack widths in this section include the neighbouring secondary cracks if present.

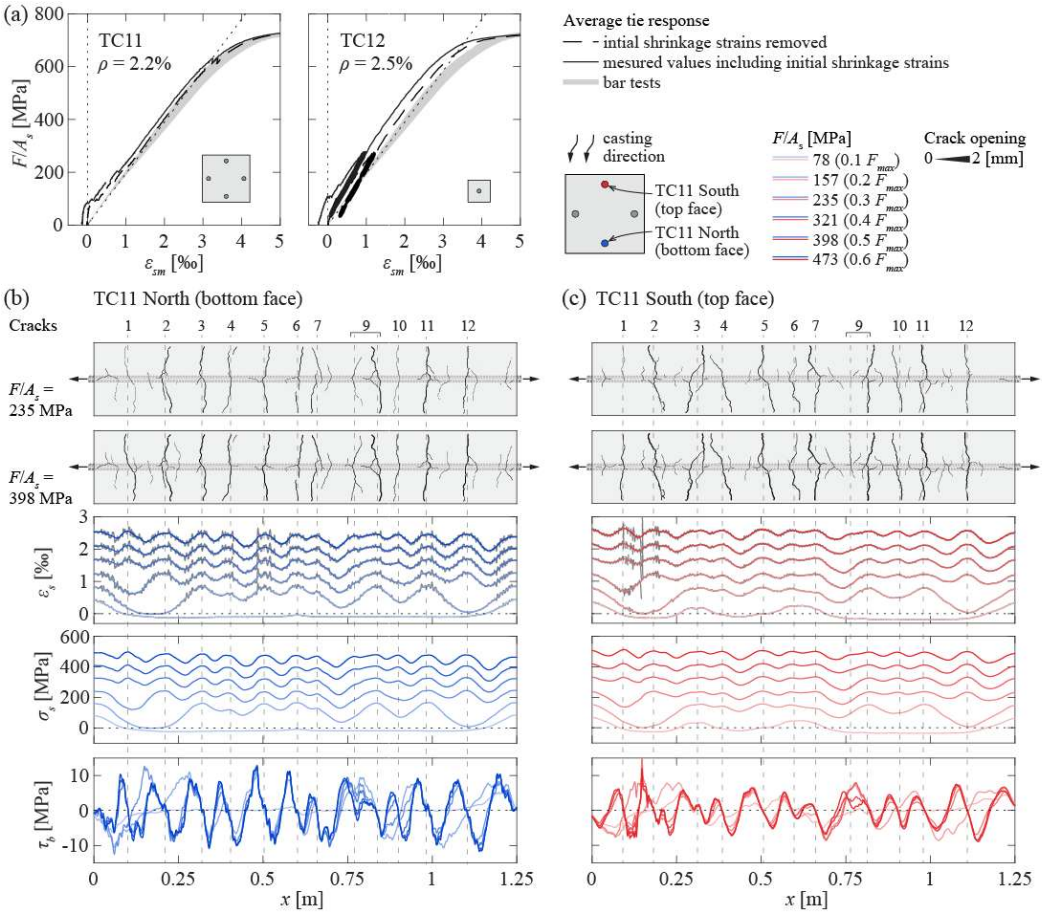

Fig. 36 *TC10 series main results: (a) steel average stress – strain diagrams for specimens TC11 and TC12; and crack patterns, steel strain, steel stress and bond stress distributions along the bonded lengths for the (b) North face and (c) South face of specimen TC11 (corresponding to good and poor casting conditions respectively, see sketch in the top right part of the figure).*

The bar stress (estimated from the fibre measurements) as a function of the crack width is shown in Fig. 37b for some cracks on the bottom face of specimen TC11. Using the bond stress distributions from Figs. 36b and c, the average bond stress at both sides of the crack (spanning between the mid-points between the studied crack and the adjacent cracks) can be calculated for each load step. Fig. 37c shows the average bond stress as a function of the steel stress in the bar. Two cases can be observed: for crack 10 (which was a secondary crack that eventually propagated across the full section), the bond stress tends to increase with increasing steel stress and crack width; whereas in the case of cracks 2 and 6 (which developed earlier as principal cracks) the average bond stress undergoes sudden variations. These variations occur when principal or secondary cracks develop. This can be understood by looking at the bond stress diagrams in Fig. 36b. The distribution changes significantly before and after the development of cracks 1 and 2, which explains how the average bond on the left side of crack 3 can vary. Similar changes were observed by Cantone et al. [13].

Fig. 37d shows the bar stress – crack width relationships for all the cracks on the bottom face TC11. In general, the results show rather linear trends as predicted by the stabilized crack model presented in Subsection 5.2.2. Some cracks show some trend variations, for example crack 6 (Fig. 37b). This could be due to the residual tensile strength of concrete given the small crack widths or due to the fact that crack 6 did not fully propagate initially as it can be observed in Fig. 36c. The design crack width formulations according to EC2:2004 (grey dashed line) and MC2010 (black dashed line) show that both formulations overestimate the crack width for a given stress. This can be explained by the fact that both

predicted maximum crack spacings (336 and 261 mm) are larger than the experimental values.

Figs. 37e,f show the average bond stress in the range with $\delta_{||} \geq 0.1$ mm and $\sigma_s < 500$ MPa for each crack. Two values are presented: the mean value within the range (solid circular markers) and the maximum value in the range (empty circular marker). It can be observed that both values are below the values proposed by the codes. Furthermore, the values in poor casting conditions (Fig. 37f) correspond to approximately 65% of the value in good casting conditions (Fig. 37e). This value is close to the factor typically assumed for design anchorage lengths in poor casting conditions (η_2 = 0.7) [135] [94] and to the recently proposed factor of 0.75 for the crack width calculation [162].

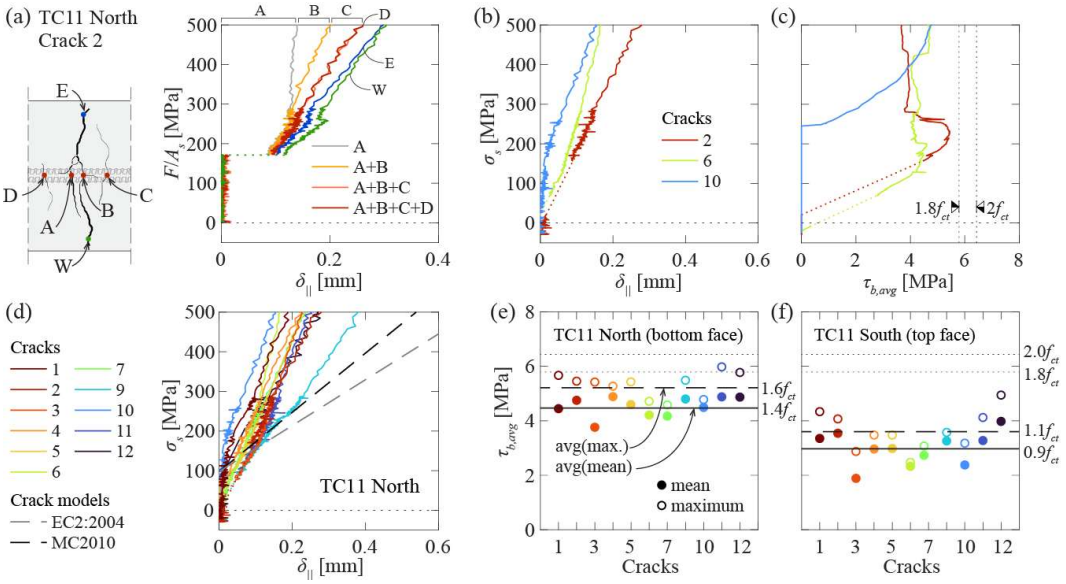

Fig. 37 *Detailed crack results from specimen TC11: (a) contributions of the secondary cracks to the crack width of crack 2 on the North face (see Fig. 36b); (b) rebar stress – crack width and (c) rebar stress – average bond stress diagrams for selected cracks on the North face; (d) rebar stress – crack width diagrams for all cracks on the North face; and mean and maximum values of the average bond stress on both sides of the crack (in the range between $\delta_{||} \geq 0.1$ mm and $\sigma_s < 500$ MPa) for (e) bottom face (North), and (f) top face (South).*

5.4.2 Monotonic beam tests

Fig. 38a shows the crack pattern obtained from the DIC strain field at 90% of the maximum load for the North face of specimen SM15 (the width of the black lines is proportional to the crack width). The shear failure crack can be easily identified. It can also be observed that most of the flexural cracks occur at the location of the stirrups. In such case, the presence of transverse reinforcement does not act as confinement for the bond development between cracks. Fig. 38b shows the results of the fibre measurements including the measured steel strain, the calculated bond stress and the normalized curvature in the bar $\chi_s \cdot Ø/2$ (strain in bar related to local bending due to dowel action and other effects [13]). A good agreement between the strain peaks and the crack positions can be observed. The strains calculated assuming an elastic cracked response of the section (lever arm $z = d - h_c/3$, h_c being the depth of the compression zone assuming a linear elastic behaviour of concrete, neglecting the residual tensile strength of concrete after cracking and not considering the effect of the shear force) are indicated with a dashed line. The corresponding calculated stresses are smaller than the values derived from fibre measurements, as consistently observed in specimens subjected to shear [171, 13]. This can be explained by the inclination of the cracks (the bending moment should be calculated at the tip of the crack and accounting for the force in the stirrups) [13]. For shear forces closer to the shear strength, the propagation of the delamination crack due to dowel action

in the flexural reinforcement [84] leads to a considerable increase in the strains and stresses in the reinforcement in that region [172, 13].

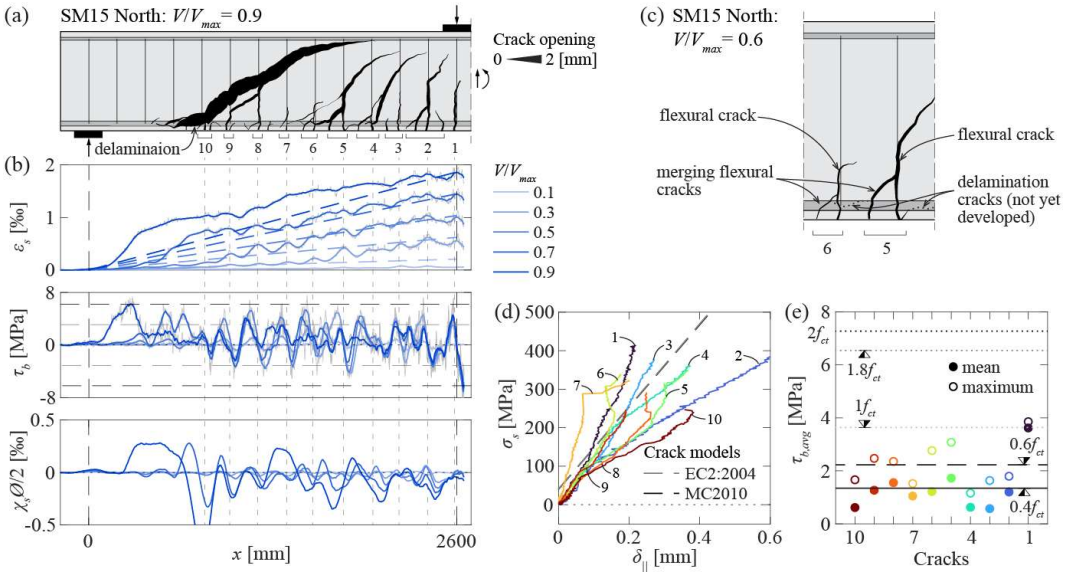

Fig. 38 *Detailed crack results of the flexural reinforcement from the North face of specimen SM15: (a) crack pattern for V/V_{max} = 0.9; (b) steel strain, bond stress and normalized curvature distributions for five load levels; (c) contribution of the secondary cracks to the crack width for cracks 5 and 6; (d)) rebar stress – crack width diagrams for all cracks; and (e) mean and maximum values of the average bond stress at both sides of the crack (in the range between $\delta_{||} \geq 0.1$ mm and $\sigma_s < 500$ MPa).*

The bond stress profiles in the longitudinal reinforcement presented in Fig. 38b have the same appearance as in the ties; however, notably smaller values are observed even though the concrete strength was higher in the beam tests. The curvature profiles show that significant local bending occurs in the bars, particularly as the delamination crack develops. This bending can significantly increase the maximum stress at the surface of the bar. At the same time, stress concentrations occur in that region due to the introduction of the bond stresses [88, 13]. This can have a negative effect on the fatigue resistance as the ribs are known to cause stress concentrations leading to the initiation of fatigue cracks [9, 173].

Tests in reinforced concrete beams have shown that the fatigue resistance of the reinforcement bars is lower than that of bare bars [11]. In regions subjected to bending, the maximum axial stress at the surface of the bar might occur at the crack location due the axial force and the local curvature of the bar. In regions subjected to bending and shear (more common in structural elements), the maximum is not necessarily at the location of the crack due to dowel action as shown in Sections 6 and 7. The stress concentrations induced by the bar-to-concrete interaction will occur somewhere within the concrete between cracks as shown by the bond profiles. Some considerations are described in last section of this report, but further research is required to determine which of the two effects has a bigger influence on the fatigue resistance of the bar.

The bar stress as a function of the crack width is shown in Fig. 38d. As explained in the previous section, neighbouring cracks can concentrate part of the total crack width. In most of the flexural cracks, another flexural crack developed and merged in the lower part of the beam as shown in Fig. 38c [84]. Both crack widths at the level of the reinforcement are considered. The curves also show a fairly linear response in most cases with a larger slope which is consistent with the larger crack spacings according to Subsection 5.2.2. In this case, the average experimental crack spacing (206 mm) is similar to the maximum crack spacing according to EC2:2004 (186 mm) and MC2010 (187 mm). Some of the experimental curves show sudden trend changes for large stresses (near the shear capacity of the specimen). This is probably related to the propagation of several small delamination and secondary cracks at the bottom of the specimen (see Fig. 38a) that cross

the other cracks, disturbing the DIC results in the points considered for the crack kinematic calculation. The average bond stress results for all the cracks presented in Fig. 38e confirm the extremely low values of bond stresses (around $0.5f_{ct}$) compared with code formulations. Similar values were obtained for the other specimens of the series. This can be explained by the large diameter of the bars, the small cover of the longitudinal bars, the small spacing between bars and the development of splitting cracks along the bars (visible in the bottom face of the specimens). The effect of these parameters, which are not accounted for in current crack formulations, will be discussed in the following.

Figs. 39a,b show the crack patterns and the stress profiles of the stirrups from specimens SM13 and 14. The stress profiles show the occurrence of peaks at the crack locations, leading to the yielding (red lines) in some stirrups close to the maxim load (shear strength). In most cases, the fibre measurements were lost soon after yielding (regions without measurements in the profiles).

Based on the stress distribution, the average bond stresses were calculated for crack points that were not too close to the bends of the stirrup (see Fig. 34e) where only a single crack was traversing the stirrup. The average stress was computed for the maximum load (solid marker) or before yielding of the reinforcement (empty marker), if this was reached before the maximum load. Therefore, the average bond stresses were not calculated when the signal was lost, which was typically the case after yielding.

The results presented in Figs. 39c,d show that two cases can be distinguished: stirrups activated by an inclined crack (blue and red markers for the top and bottom parts respectively, see sketch in Fig. 39d) and stirrups where besides the inclined crack, a flexural crack developed creating a longitudinal crack along the stirrup (green and yellow markers for the top and bottom parts respectively). The results show that the average bond stresses are generally smaller for the stirrups that did not reach yielding. The results also indicate that the regions affected by the longitudinal cracks along the stirrups have lower average bond stresses. This can be explained on the one hand because the inclined cracks in these regions have typically smaller openings (compared with the stirrups that yielded) and because of the reduction of the contact area between the ribs and the concrete due to the crack development [119, 146]. Similar results were found in the other specimens.

It can be observed that in most cases for the bars that reached yielding, the average bond stresses just before yielding reach values close or larger than the proposed values of current codes. The values for the bars that did not yield were lower.

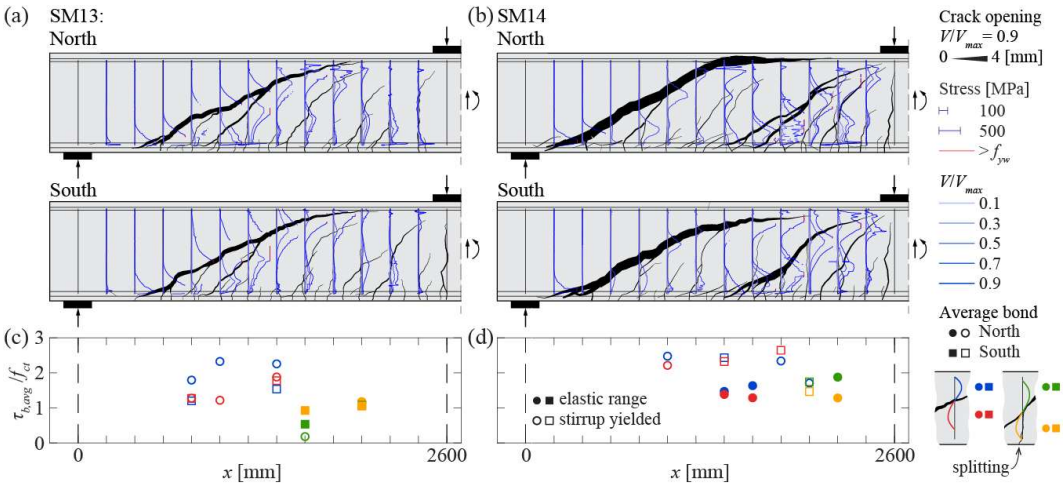

Fig. 39 *Detailed crack results of the stirrups: (a) (b) crack pattern at V/V_{max} = 0.9 and stirrup stress distributions for five load steps; and (c) (d) average bond stress (at V_{max} or before yielding of the stirrup) for specimens (a) (c) SM13 and (b) (d) SM14.*

5.4.3 Cyclic beam tests

Figs. 40a,b show the crack patterns and fibre measurement results for specimens SC75 (maximum load reaching the cracking load) and SC77 (maximum load reaching $0.9V_{max}$), respectively. For specimen SC75, peaks in the steel stresses in the longitudinal bars can be observed at the crack locations since the first cycle. However, not all the cracks could be detected with the DIC measurements (this is perhaps related to the fact that nonlinear concrete strains in tension can appear before reaching the tensile strength and the development of cracks [174, 175]). In Fig. 40a, the crack pattern for the first cycle is shown in blue (shifted to the right for clarity) and for the last cycle is shown in black. Cracks 2 and 4 did not extend beyond the reinforcement positions at 1st cycle, and cracks 3 and 5 reached only half of their final length with widths of around 0.03 mm. For specimen SC77, all the cracks were present since the first cycle and only a slight increase in the width and small propagations of some secondary cracks were observed. The bond stress distributions at $V_{max,cyc}$ indicate that bond stresses increase with the cycles in specimen SC75 and decrease for SC77.

This is more evident in the results presented in Fig. 40c, that shows the evolution of the average bond stress over the cycles. The difference can be explained by the fact that in SC75, the increase of crack width is mostly related to a propagation of the crack in the zone with residual tensile strength under the neutral axis and a reduction of the uncracked zone which leads to an increase of the tensile stress in the reinforcement and an increase of the bond stresses. For specimen SC77, the crack development is very small and the decrease of the bond is due to the load cycles that deteriorate the interface as observed by other researchers [13, 154].

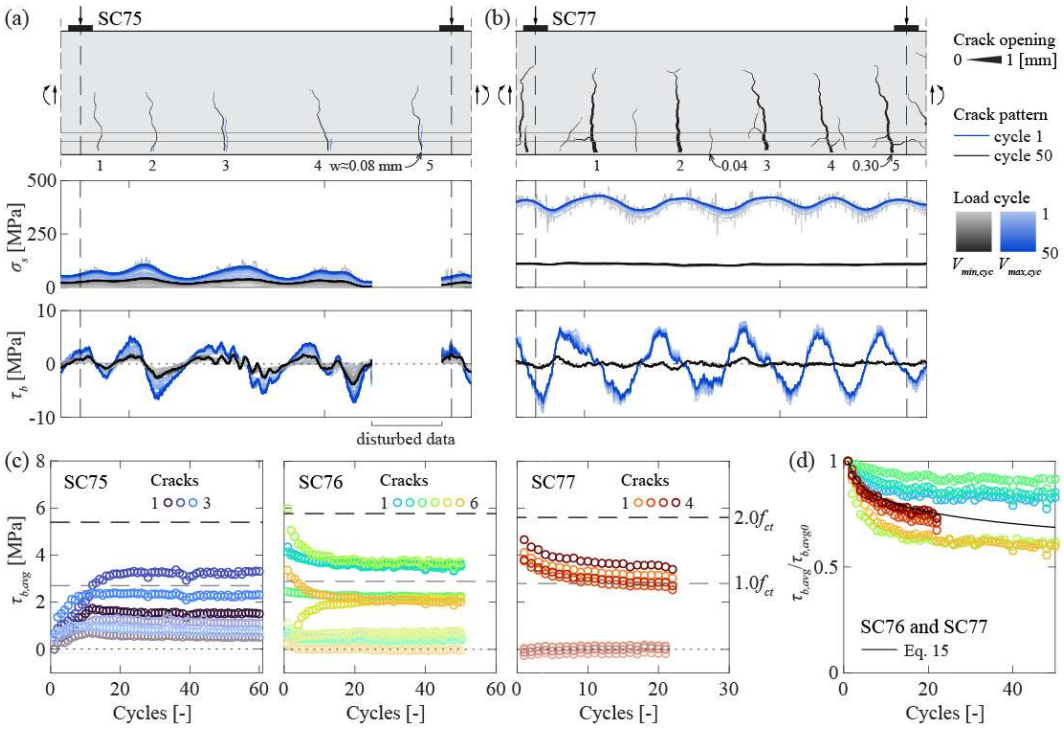

Fig. 40 *Detailed crack results of the flexural reinforcement from series SC70: crack pattern at maximum load; steel strain and bond stress distributions for all cycles for specimens (a) SC75 and (b) 77; (c) average bond stress as a function of the number of cycles for specimens SC75, 76 and 77; and (d) relative reduction of the average bond stresses with the number of cycles.*

As shown in Fig. 40c, the steepest variations occur in the first 10 to 15 cycles. At the end of the cyclic loading, the bond stresses remain fairly stable for SC75. For SC76 and SC77 a slight decreasing trend remains after the applied cycles, particularly in SC77. Bond stresses increase with the cycles in crack 5 of SC76, this is because the crack propagated

from a secondary crack in the first cycles. No clear trend regarding the average bond stress and the presence or absence of splitting and secondary cracks can be observed. It must be noted that the bond stresses are in all cases lower than the values proposed by the codes. At $V_{min,cyc}$, the variations are considerably smaller.

Fig. 40d shows the relative reduction of average bond stresses at $V_{max,cyc}$ compared with the value correspondent to the first cycle ($\tau_{b,avg0}$). The general trend is well captured by the reduction factor proposed by Lemcherreq et al. [154] defined by Eq. 15.

$$k_{cyc} = 1 - 0.08 \log N \tag{15}$$

5.5 Improvement of the bond-slip relationship

Based on the principle that the underlying mechanisms in the bond response in anchorages and near cracks are the same, the local bond-slip relationship can be used to determine the bond in service conditions. A clear difference between both phenomena is the range of slips. In a cracked element, due to compatibility conditions, the mid-point between cracks should have no displacement. At the same time, near the crack (if the influence of the secondary cracks is neglected), the slip should correspond to half of the crack width. This yields maximum slips in service conditions of around 0.1 to 0.3 mm.

Another significant difference, particularly for relatively small crack spacings, is that the influence of the secondary cracks and the resulting reduction of bond near the crack is not negligible. Debernardi et al. [176] adapted the model proposed by Balazs [114] to account for the loss of bond near the loaded area, establishing that the average bond should remain constant. However, recent experimental results from ties and beam tests show that average bond increases with the load in monotonic tests [14, 153].

In a recent publication [158], the authors proposed a bond-slip relationship based on mechanical considerations that shows good agreement with the results of a large test database. The relationship depends on the confinement provided by the concrete cover and the transverse reinforcement. As explained in Subsection 5.4.2, the confinement provided by the stirrups is not considered in this case, due fact that most of the flexural cracks appeared at the stirrup locations. Fig. 41a shows the general formulation for each segment of the curve and the resulting bond-slip law for good casting conditions and three concrete covers. The largest bond stresses are reached for well-confined conditions ($c/Ø \geq 5$); and lowest for unconfined conditions ($c/Ø \leq 1$). Intermediate cases are considered moderately-confined conditions. More details are provided in Appendix VI.

The ascending branch is controlled by the pull-out bond stress ($\tau_{bu,po}$) and the peak bond slip ($\delta_{sc1,po}$) in well-confined conditions that depend on the concrete compressive strength, the bar diameter and the bond index, as described in Eq. 16 and 17.

$$\tau_{bu,po} = 0.5 f_{cm} \left(\frac{30}{f_{cm}} \right)^{1/6} \left(\frac{20}{Ø} \right)^{1/8} \tag{16}$$

$$\delta_{sc1,po} = 1.0 \cdot \frac{Ø}{20} \cdot \left(\frac{30}{f_{cm}} \right)^{1/3} \left(\frac{0.08}{f_R} \right)^{1/5} \tag{17}$$

Fig. 41b shows the local bond-slip relationship at distances of 0.5, 1 and 2Ø from crack 5 in the North face of specimen TC11 obtained from the fibre optical measurements. The proposed relationship (blue curve) follows the general trend of the experimental results at 1 and 2Ø from the crack; however, the initial stiffness is slightly underestimated. The measurements show a reduction of the bond stresses at 0.5Ø from the crack. Consequently, a linear bond reduction factor (λ) acting over a distance of 1Ø from the crack is considered, as shown in Fig. 41c.

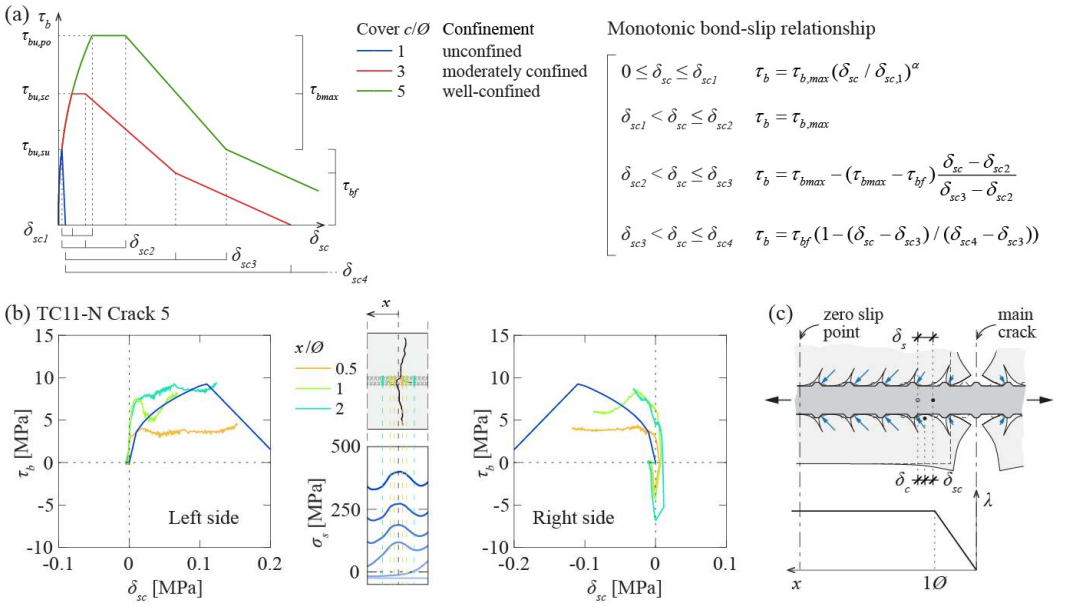

Fig. 41 *Local bond-slip response: (a) considered local bond-slip response for monotonic loading; (b) local bond-slip measurements on both sides of crack 5 of the North face of TC11; and (c) proposed reduction factor for the bond stress near the crack.*

Using the proposed bond-slip relationship (Fig. 42a) and reduction factor to account for secondary cracks (Fig. 41c), a numerical integration was performed as proposed by Balazs [114]. The results in terms of the average bond stress as a function of the crack width are illustrated in Figs. 42b,c,d for Ø8, Ø18 and Ø34 bars. The colours correspond to different confinements. For each crack spacing (curves with different colour shades), the average bond stress before yielding of the reinforcement is represented with a solid line and the yielding point with a circular marker. The favourable effect of the confinement and the size effect are clearly visible in Figs. 42b,c,d.

The response in well-confined conditions (sufficient cover) is governed mostly by the ascending branch. In these conditions, the average bond stress can be estimated using Eq. 18 (dashed curve in Figs. 42b,c,d). This expression is derived using the analytical solution for the average bond stress as a function of the crack width in homogeneous conditions, multiplied by an adjustment factor k_{sr} depending on the crack spacing (a constant value of 1.3 is proposed):

$$\tau_{b,avg} = k_{sr} \cdot \tau_{bu,po} \frac{1-\alpha}{1+\alpha} \left(\frac{\delta_{||}}{2 \cdot \delta_{sc1,po}} \right)^{\alpha} \tag{18}$$

where α is the exponent of the ascending branch of the local bond-slip relationship (a value of 0.4 as proposed in MC2010 is considered). Eq. 18 refers to the case with good bond conditions and without the development of splitting/spalling cracks along the reinforcement bar [146]. The improvements of Eq. 18 to account for other effects are described in the following paragraphs.

As observed by Moccia et al. [109], the bond performance of bars is influenced by the plastic settlement voids and cracks. The effect is directly related to the height of the bar above the formwork. In this section, only results from one relatively shallow specimen are available. Based on these results, the factor of η_2 = 0.7, typically considered for short anchorages, seems to give a good estimation of the bond stress reduction. Further, research is needed to confirm these results.

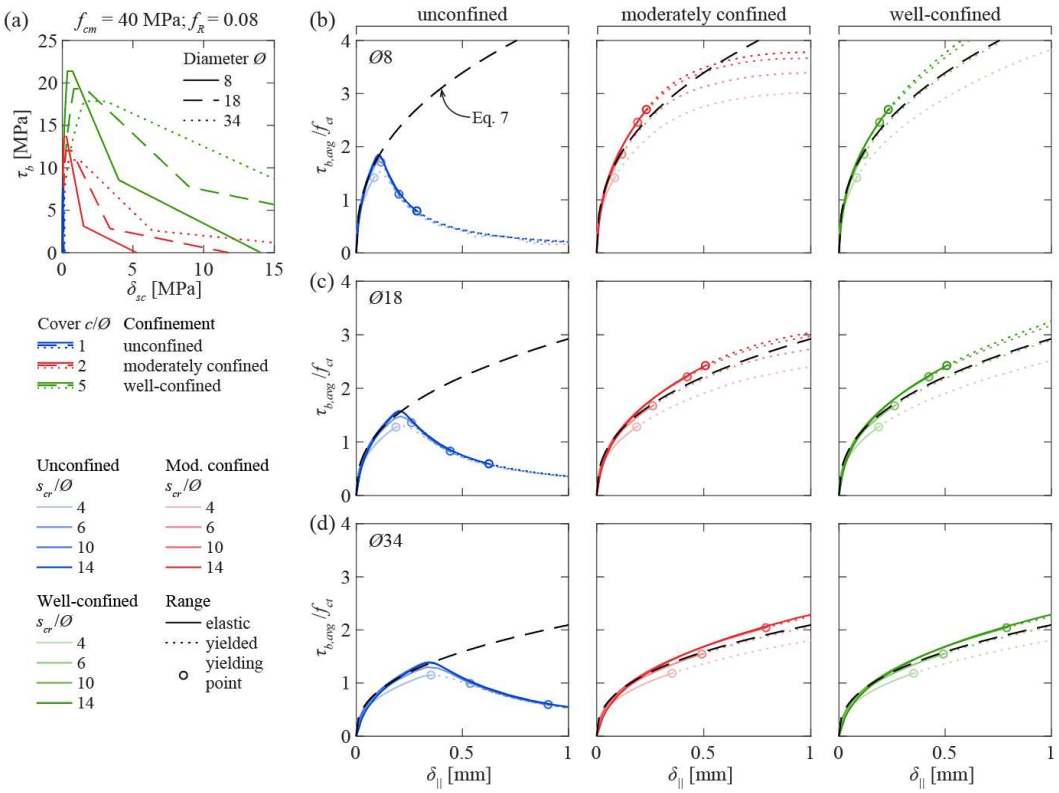

Fig. 42 *Bond in the stabilized cracking phase: (a) considered local bond-slip relationships; (b) bond reduction factor according to MC2010; and average bond stress as a function of the crack width for (c) Ø8, (d) Ø18 and (e) Ø34 bars.*

Based on the work of Brantschen et al. [119], the authors recently showed that the development of local bond stresses along the anchorage length is affected by the development of splitting and spalling cracks along the bar due to the reduction of contact surface between the ribs and the concrete [146]. Using as reference the bond-slip relationship for well-confined conditions, the local bond stresses can be determined using a reduction factor based on the splitting and spalling crack widths. Consequently, the integration of the different local bond-slip relationships (shown in Figs. 42b,c,d) inherently accounts for the splitting and spalling crack development. However, as Eq. 18 accounts mostly for the ascending branch and the secondary cracks, the effects of splitting are not considered. In most cases, in existing structures, the splitting cracks can be measured. Furthermore, longitudinal cracks along the reinforcement can appear for other reasons (such as the flexural cracks along the stirrups shown in Figs. 39a,b). Consequently, the factor proposed by Brantschen et al. [119] defined by Eq. 19 can be adopted as a reduction factor for cases where cracks along the reinforcement bar are observed on the concrete surface.

$$k_{lc} = \frac{\tau_b}{\tau_{b0}} = \frac{1}{1 + \frac{\kappa_f}{f_R}\frac{w_{lc}}{\varnothing}} \tag{19}$$

where κ_f is a factor proportional to the number of lugs composing the ribs ($\kappa_f = 0.75 n_l$) and w_{lc} is the crack width of the longitudinal cracks along the reinforcement. If this information is not available, the value corresponding to two rib lugs ($\kappa_f = 1.5$) and a bond index of 0.08 (average value from the database [158]) are recommended.

Considering these two factors and the cyclic reduction factor of Eq. 15, the expression to estimate the bond stresses is defined by Eq. 20:

$$\tau_{b,avg} = \eta_2 \cdot k_{sr} \cdot k_{lc} \cdot k_{cyc} \cdot \tau_{bu,po} \frac{1-\alpha}{1+\alpha} \left(\frac{\delta_{||}}{2 \cdot \delta_{sc1,po}} \right)^{\alpha} \tag{20}$$

After yielding, the bond stresses reduce significantly [149, 116, 177]. This is out of the scope of this section, especially as in such case, the stress in the bar is less uncertain.

5.6 Comparison of the proposed model with the experimental results

5.6.1 Average bond stresses

Fig. 43a shows the experimental results (coloured lines) and the proposed analytical expression (black dashed line) in terms of the average bond stress as a function of the crack width. Additionally, the results of the numerical integration of the local bond-slip relationships are shown with a grey hatch. The increase in the bond stresses with the crack width is well captured. However, stresses are slightly underestimated. Fig. 43b shows the mean (filled marker) and maximum values (empty marker) of the average bond stresses for the flexural reinforcement of all specimens of series SM10. The corresponding predicted values are shown with black markers. The size effect and the influence of the longitudinal cracks along the bars reduce considerably the bond stresses. Nevertheless, the proposed values overestimate the experimental ones by a factor close to 2. This overestimation is likely due to the fact that the width of the delamination cracks in the lateral faces of the specimen are smaller than in the middle of the specimen due to the presence of the stirrups. The values proposed by the codes (1.8 to 2f_{ct}) overestimate experimental results by a factor of 3 to 4. Figs. 43c,d show the results from the stirrups not affected and from the stirrups affected by the presence of cracks along the bars (flexural cracks or splitting cracks), as explained in the previous section (see Fig. 43e). The proposed expression captures well the evolution of bond stresses with the crack width. The average bond stress is slightly overestimated for B500A stirrups (Fig. 43c). This can be explained by the lower bond index of the bars and could indicate that the influence of this parameter in the proposed bond-slip relationship is underestimated. These results are coherent with the smaller crack spacings for larger bond indices observed by Galkovski et al. [153]. The influence of splitting is satisfactorily considered by the splitting factor (black triangular results).

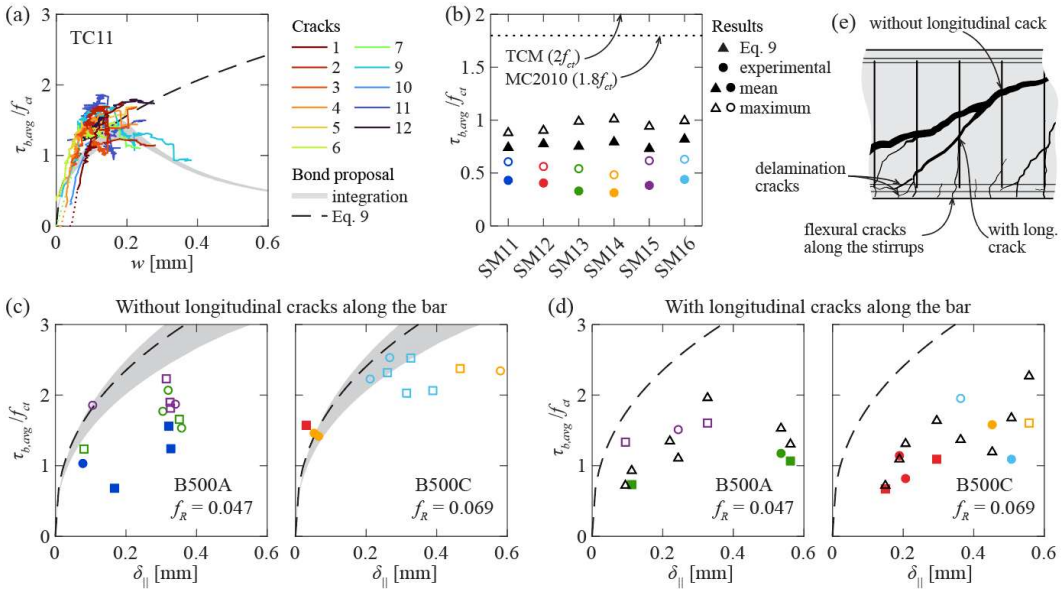

Fig. 43 *Comparison of the proposed average bond stresses and the experimental values: (a) specimen TC11; (b) flexural reinforcement of series SM10; (c) shear reinforcement without and (d) with cracks along the bar; and (e) schematic representation of stirrups with and without cracks along the bars.*

5.6.2 Steel stress estimation based on the crack width for short term monotonic loading

Three estimations are compared with the experimental values:

- Using the proposed model for the crack width estimation (Eqs. 14 and 20) and the measured crack spacing (distance between mid-points of consecutive cracks measured from the DIC).
- Using the relative mean strain according to EC2:2004 and the measured crack spacing.
- Using the relative mean strain and the calculated crack spacing according to EC2:2004.

In all three cases, the measured shrinkage strains are included in the relative mean strain calculation.

Fig. 44a shows the ratio of experimental over calculated stresses for tie TC11. The results indicate that the proposed model slightly underestimates the stress in the bar. This can be explained by the underestimation of the bond stresses (see Fig. 43a). The code formulation slightly overestimates the stress. As explained in Subsection 5.2.1, for a given crack spacing and width, the code estimation yields larger bar stresses (see Fig. 32a). Consequently, the code formulation tends to overestimate the stresses. Fig. 44b shows the results for the flexural reinforcement of beams of series SM10. The proposed model performs better than the code formulation for small crack widths. This is due to the bond activation expression, that gives a good estimation of the average bond stresses for smaller crack widths. For larger crack widths, both models underestimate the steel strain reduction which leads to the overestimation of the stress. The reduction of the dispersion for larger crack widths can be explained by the fact that the bond stress has a constant influence on the crack width in terms of absolute values (see Fig. 32b) and has thus a smaller relative impact for large crack widths. As a consequence, the relative error is lower for larger stresses. The importance of an accurate estimation of the crack spacing is reflected in the poor performance of the estimations using the calculated crack spacing.

The assumption of a constant bond stress used in current code formulations is reasonable and practical given the inherent uncertainty and variability of the cracking phenomenon. However, the lower experimental bond stresses could have an influence in the crack spacing estimation. This is visible in the results from series SM10 where the calculated maximum crack spacing is actually close to the average of the experimental results (see Fig. 38d). This explains the average results for series SM10 which is around 0.85. Further research is required to confirm this potential effect.

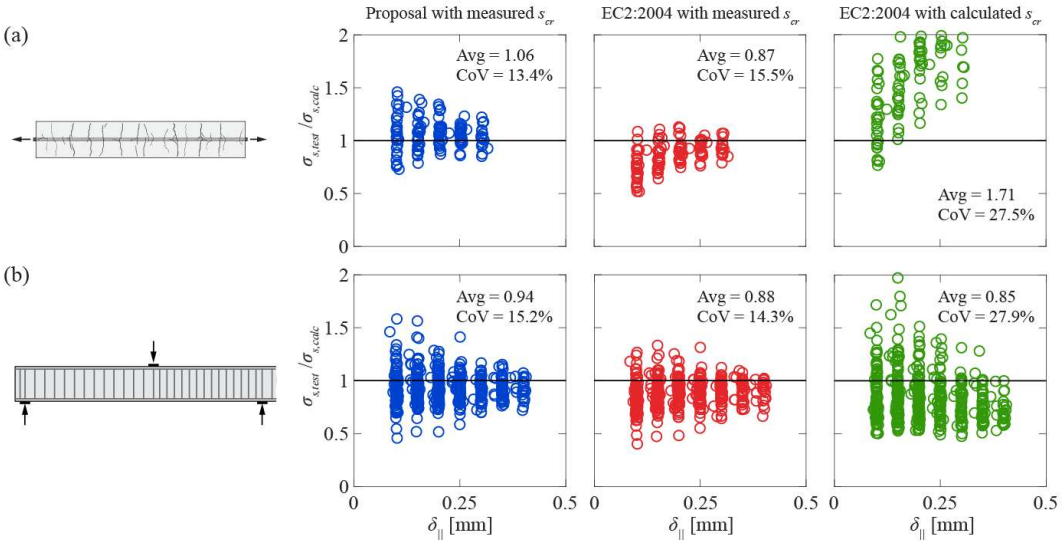

Fig. 44 *Ratio of experimental over calculated steel stress as a function of the crack width: (a) tension specimen TC11; and (b) all beam specimens of series SM10.*

5.7 Conclusions

This section presents the results of an experimental programme and an analytical investigation to improve the current understanding of cracking in structural elements, with the aim of estimating the stress in the reinforcement based on crack width measurements. The main findings of this research are:

1. The measured average bond stresses are in most cases lower than the values proposed by current standards, with the exception of the stirrups in the beam tests that showed in some cases larger values. This could have a relevant influence in the estimation of the crack spacing.
2. The decrease of bond stresses for cyclic loading concentrates in the first 10 to 15 cycles. After that, the decrease progresses at a slower pace. This seems to depend on the stress variation range. Further research is required to confirm these findings.
3. In cases where the flexural cracks develop at the transverse reinforcement location, the presence of transverse reinforcement does not guarantee its activation as confinement for bond stress development between cracks along the longitudinal reinforcement.
4. An expression to estimate the average bond stresses considering the crack width, the casting conditions, the type of loading (monotonic or cyclic) and the presence of splitting cracks is proposed. The expression is derived from the integration of the local bond-slip relationship, accounting for the presence of secondary cracks. The estimated values show good agreement with the experimental values for short-term monotonic loading.
5. The slip-based model gives good results for the bar stress-crack width response, provided that the average bond stresses are adjusted. Using this model, a reasonable estimation of the bar stress as a function of the measured crack width can be obtained.
6. Shrinkage induced strains have a significant influence on cracking and the estimated bar stresses. However, neglecting its influence leads to an overestimation of the bar stress.
7. The estimated bar stresses using the slip-based model and the proposed expression for the average bond stresses perform better than current code formulations. The code formulations tend to overestimate the bar stress due to the inherent assumptions for the calculation of the relative mean strain.

5.8 Outlook and future works

Some questions related to the topics studied in this section remain open. In the following, some of these future research lines are outlined:

- The number of tests used for the validation of the model remains limited. Additional tests covering a wider range of the parameters considered in the model should be performed for validation.
- Additional tests are required to validate the average bond stress estimation in cyclic conditions. Different stress variations should be considered to confirm the proposed factor.
- Additional tests are required with bars in poor casting conditions the bars placed at representative heights over the formwork to represent full-scale structures.
- Additional tests are required to validate current values of average bond stresses for long-term loading.
- It is well known that the rib lugs lead to stress concentrations and to the initiation of fatigue cracks. The average longitudinal steel stresses peak at the crack location where bond stresses are zero. Due to bond stresses, the steel stress diminishes with the increase of the distance from the crack. Therefore, the bar sections within the concrete have lower steel stress. However, bond stresses are introduced in the bar through the rib lugs which increases the stress concentrations in that region. Additional research is required to determine the role of bond stresses (transferred through the lugs) in the initiation of fatigue cracks.

6 Experimental investigation of dowel action in reinforcing bars using refined measurements

6.1 Introduction

The steel reinforcement in reinforced concrete (RC) structures is commonly designed to carry longitudinal forces only. Its ability to resist transverse forces by dowel action is usually neglected to simplify the structural design and the assessment of existing structures. Dowel action is the transmission of transverse forces in a reinforcing bar on either side of cracks (Fig. 45a), in connections of precast elements (Fig. 45c), at the interface between two concretes cast at different times, etc. (Fig. 45b), where a relative displacement component perpendicular to the bar axis occurs. Reinforcing bars can also be designed to carry transverse forces at the ultimate limit state (Fig. 45c,d), provided the concrete embedment is strong enough. If cracks or joints are subjected to cyclic loadings, for instance due to traffic loads, stress concentrations due to dowel action can lead to fatigue failures of the reinforcing bars.

Simplified design formulae in codes of practice [12, 94, 95] are typically conservative, underestimating the actual structural resistance for most cases. This can become problematic for the assessment of existing structures, because underestimating the actual strength can lead to unnecessary retrofitting measures, with the associated costs. This is why more refined models are needed, allowing to accurately estimate the actual resistance. In some cases, the analytical verification can be complemented with in-situ measurements. This is typically the case for the fatigue verification, where the stress variations in the steel reinforcement can be estimated on the basis of detailed measurements on the concrete surface. Directly gluing strain gages on reinforcing bars is impractical as it implies a significant disturbance of the bond behaviour and the dowel action. This is why more refined models of dowel action are needed to reliably evaluate the resistance of the existing structures at the ultimate and fatigue limit states.

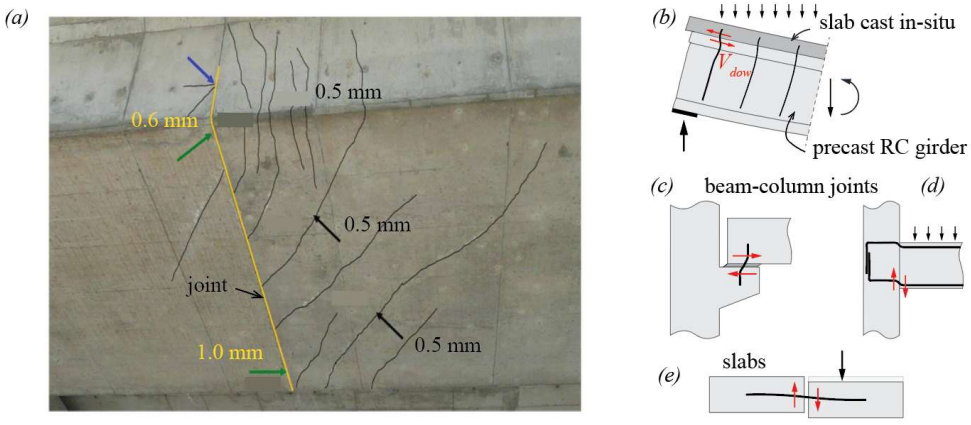

Fig. 45 *(a) Cracks due to torsion in the Weyermannshaus Viaduct (Bern, Switzerland) and (b-e) other cases where dowel action can occur.*

Previous investigations have often focused on dowel action at the ultimate limit state under monotonic or cyclic loads (e.g. due to seismic actions). Three failure modes are generally distinguished (Fig. 46): (1) splitting of the concrete cover for dowel forces parallel to the free surface, (2) spalling of concrete perpendicular to the free surface and (3) local crushing of concrete in combination with yielding of the dowel bar in bending.

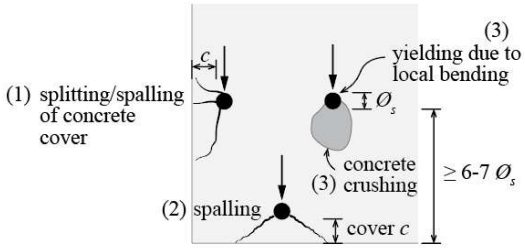

Fig. 46 *Failure modes due to dowel action.*

The first two failure modes typically occur for concrete covers smaller than 6-7 times the bar diameter [178]. In this case, the dowel resistance was observed to depend on the bar diameter, the concrete strength, the thickness of the cover, the crack kinematics (crack opening and relative displacement parallel or perpendicular to the free surface), etc. [179, 180, 181, 182, 183, 184]

If the concrete cover is larger than 6-7 times the bar diameter, splitting and spalling failures are prevented. In this case, relatively large imposed transverse displacements can be reached leading to plastic hinges in the steel bar due to local bending. At the same time, local crushing of the concrete occurs under the bar, near the crack (or the interface between concretes cast at different times) [185, 186, 187, 188, 189, 190, 191, 192, 193, 194, 195, 196]. In this case, most of the concrete reaction is provided over a length of approximately two bar diameters from the crack, where the plastic hinge is located [197]. If the dowel is not perpendicular to the crack, its resistance decreases [187]. Significant concrete strains associated to concrete crushing can be observed, up to a depth of around half a bar diameter from the crack [190]. The effect of an axial force in the bar on its dowel response has also been examined: in addition to concrete crushing, larger tensile axial forces also degrade the dowel response, as they reduce the stiffness of the concrete embedment due to the development of micro cracks around the bar associated to the bond stresses [101, 198, 199]. In addition, the bending resistance of the bar which contributes to the dowel resistance is reduced by the presence of an axial tensile force [200, 201, 202, 198, 199]. The activation of the second-order catenary action in a dowel bar has also been observed for large transverse displacements. If the axial tensile force in the bar reaches the plastic axial force, the bending capacity of the dowel disappears. Under these conditions, the catenary action is the only remaining contribution to the dowel resistance [188]. If the bar is subjected to large cyclic stresses, the dowel response is notably degraded after only a couple of cycles, because of yielding of the dowel and local concrete crushing [178, 195, 202].

The stiffness and the strength of the concrete embedment have also been investigated and their values exhibit a large scatter. They were observed to depend on multiple parameters including the bar diameter, the compressive concrete strength, the confinement level, the magnitude of the imposed displacements, etc. [203].

With respect to its phenomenology, further in-depth understanding of dowel action in the confined concrete embedment is still required. This particularly concerns the contribution of the dowel action to carry shear forces and its influence on steel stress variations, which can potentially lead to a fatigue failure.

To that purpose, this section, which is adapted from [204], presents the results of an experimental investigation of dowel action in a confined concrete embedment (with sufficient concrete cover) subjected to monotonic loading up to failure and low-stress cyclic loading. This includes cutting-edge measurement techniques: Three-Dimensional Digital Image Correlation (DIC-3D) [205] and optical fibre sensors [13, 113, 104]. They allow for precise measurements of, respectively, the complete 3D-displacement field of the cracked concrete surface and the continuous strain distribution in the steel reinforcement. The dowel test series consisted of bars embedded in concrete blocks designed to prevent concrete spalling and to limit the risk of concrete splitting. They were subjected to low-stress level cycles and/or monotonic loading up to the bar rupture due to excessive

catenary action. Imposed axial and shear forces were selected in the cyclic tests to match typical service load scenarios. The results of an additional test series, aimed at investigating the local concrete behaviour and resistance under the bar, are also reported in this section.

6.2 Experimental programme

The experimental programme was carried out at the Structural Concrete Laboratory of the École Polytechnique Fédérale de Lausanne in Switzerland. It consisted of two different test campaigns: the first investigated the dowel action (DP series) and the second studied the stiffness and strength of concrete under a rebar (CP series).

6.2.1 Specimens and test set-ups

The main design idea for the specimens of both series was to reproduce the behaviour of confined structural details at cracks or member interfaces, as shown in Fig. 45. The laboratory tests of DP series (dowel action) were performed using 11 concrete block specimens (Fig. 47b-e). Each specimen contained a single ribbed reinforcing bar of diameters $Ø_s$ = 20 mm or 14 mm subjected to dowel action. Each bar was 500 mm long and was symmetrically embedded in a 300 mm concrete block. The reinforcing bars subjected to dowel action had threaded ends which allowed anchoring them to the testing machine (Fig. 47a). Each concrete block (Fig. 47c-e) was in two parts, separated by a smooth pre-made notch with a thin concrete layer around the bar to simulate the crack. The notch was created by placing steel sheets in the formwork during the casting of concrete, and removing them after hardening of the concrete. This ensured that there was no transfer of stresses by the aggregate interlock. The angle between axis of the bar and the crack (θ, Fig. 47a) was 45°, 70° or 90°. The casting direction of the specimens is shown in Fig. 47c. To prevent a global splitting failure of the concrete, each half of the specimen was reinforced by four stirrups (Ø10 mm, Fig. 47c-e). To align the applied shear force with its horizontal reaction, the specimens were confined using steel plates fixed by threaded steel bars (Fig. 47a), which allowed controlling the global rotation of the specimens. The external confining bars were fixed sufficiently far from the pre-made crack that they did not affect the dowel response. The properties of the specimens are summarised in Table 10.

The specimens were tested in a test setup (Fig. 47a) that was derived from that previously used to investigate aggregate interlocking and local bond behaviour [206]. The testing machine has a stiff steel frame with three vertical columns, rigidly connected by the steel caps. Two perpendicular hydraulic jacks were fixed to the machine frame and enabled to apply displacements in two independent directions. A set of rollers prevented unwanted rotations. The vertical jack was attached to the bottom steel cap. Its tensile capacity was close to 1 MN for static loading. The vertical jack allowed applying the axial force by pulling on the vertical reinforcing bar. The bar was fixed to two steel anchoring plates (Fig. 47a) using small steel plates and nuts screwed on both threaded bar ends. The anchoring steel plates (500 x 500 x 50 mm) had slits to enable the placement of the specimens on the test machine. The horizontal jack used to impose the transverse displacement had a 0.3 MN compression capacity for the static loading (no tensile force was applied). It was fixed to two frame columns of the test machine while the third frame column was used as a horizontal support.

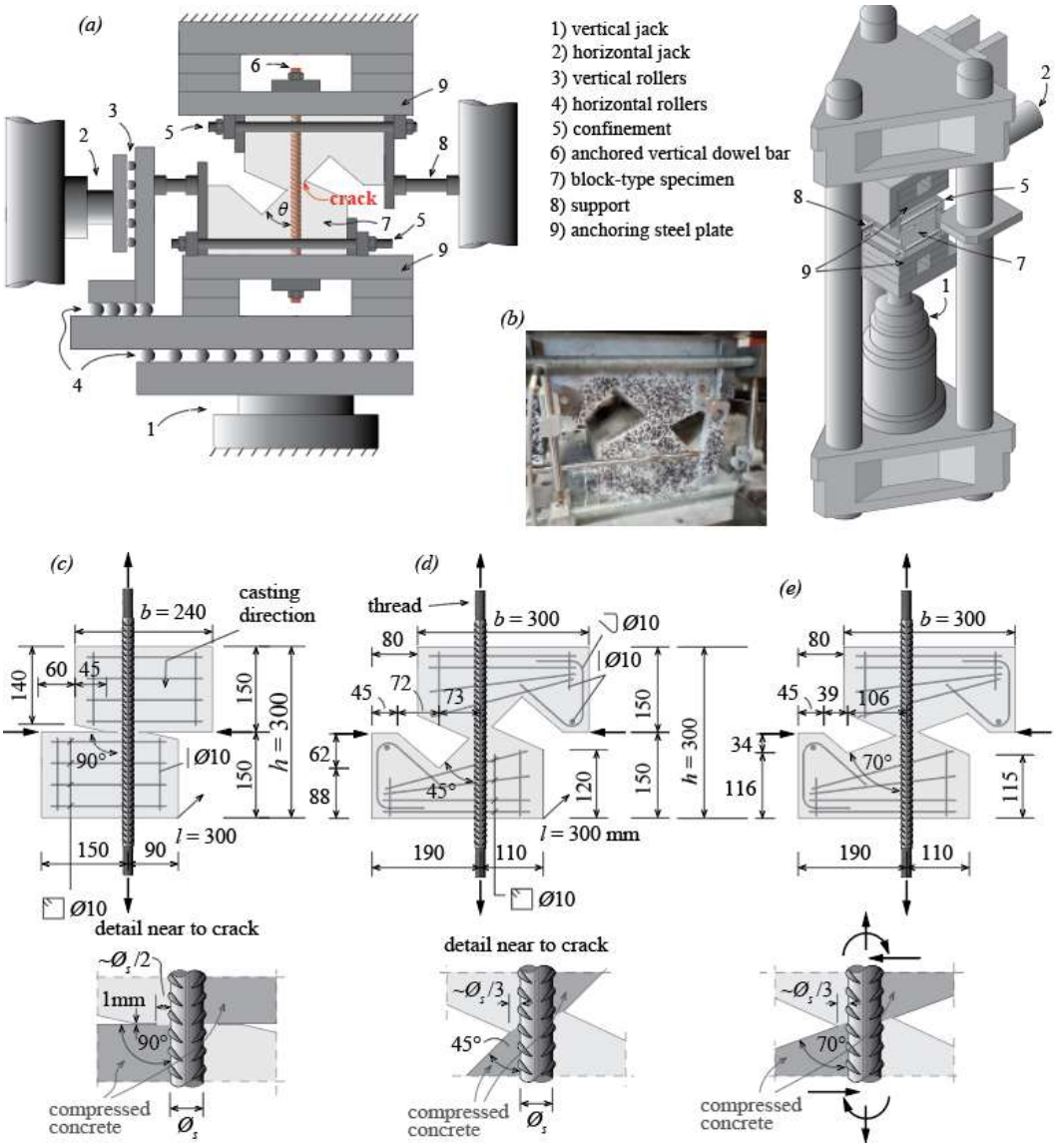

Fig. 47 *Test set-up and specimens for dowel DP tests: (a) test set-up; (b) photo of a specimen; and geometry of specimens, reinforcement and applied forces for (c) 90°; (d) 45° and (e) 70° specimens (dimensions in mm).*

The second experimental campaign (CP series), aimed at investigating the concrete behaviour under a steel reinforcing bar, consisted of 9 specimens. Each specimen contained a single reinforcing bar ($Ø_s$ = 20 mm, length: 120 mm) horizontally embedded on top of the concrete block (Fig. 48). The concrete blocks were shaped so that the acting and reacting forces were vertically aligned. The embedded bar was welded to a steel profile with a rectangular cross-section (120 x 30 x20 mm, Fig. 48a). This allowed applying the point load along the bar causing small bending deformations. It also provided a vertical surface for DIC measurements of the bar kinematics as the bar itself was hidden in concrete. The concentrated force was applied at various locations along the axis of the bar (distance *a* from its end, Fig. 48a). In all tests of this series, the concrete surface representing the crack surface was perpendicular to the bar (θ = 90°) and was aligned with the end of the bar. The specimens were confined by horizontal reinforcing bars and stirrups (Ø8 mm) to prevent a brittle global splitting failure. The specimens were cast from the side and turned by 90° to be tested (casting direction shown in Fig. 48a). Relatively small casting height with respect to the bar ensured good concrete conditions around the bar, preventing notable voids due to bleeding and fresh concrete settlement [109]. The specimens of the CP series were tested using a Schenck test machine with a compression capacity of 2.5 MN. The point load on the investigated bar was applied under displacement control.

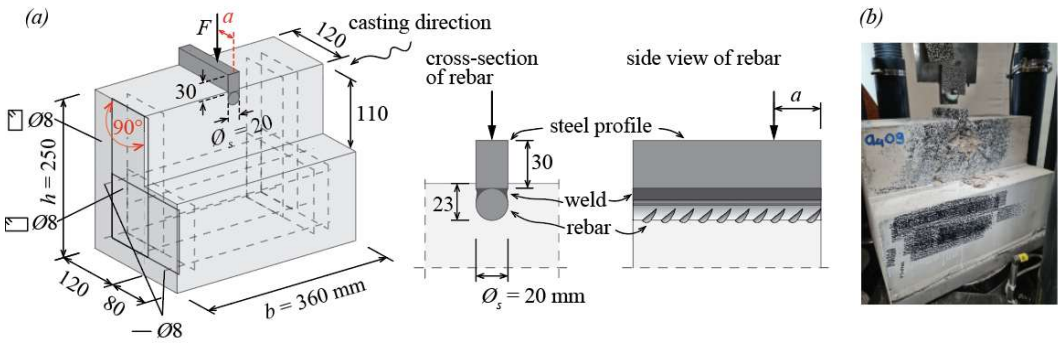

Fig. 48 *Specimens for CP tests: (a) geometry, reinforcement and applied force and (b) photo of a specimen.*

6.2.2 Material properties

Normal strength concrete with crushed aggregates with the maximum size of 16 mm was used for all specimens. The uniaxial compressive concrete strength f_{cm} was measured on cylinders (Ø160 x 320 mm). Their mean values at the time of testing were 36.3 MPa and 27.5 MPa for the DP and the CP series, respectively (details are given in Tables 10 and 11).

Conventional ribbed steel rebars were used for both test series. Figure 49a shows the experimental stress-strain relationships for the two used diameters.

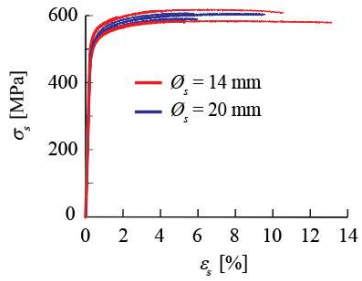

Fig. 49 *Stress-strain relationships of the reinforcement.*

Table 10 summarises the main test variables and properties of the DP test series: angle θ between the bar and the crack, bar diameter $Ø_s$, mean concrete compressive strength f_{cm}, yield strength of the dowel bar f_y, tensile strength of the dowel bar f_u, ultimate first-order dowel force $V_{dow\,l,u}$ (without the contribution of catenary action), test type, angle α defining the applied crack kinematics in monotonic tests (see Section 6.3 and Fig. 53), initial crack opening component in the direction of the reinforcement $\delta_{||,\,init}$ and initial global axial force N_{init}. The first two digits in the name of the specimens refer to the bar diameter while the last two are the serial number.

Table 11 summarises all relevant properties related to the CP test series including the position of the point load a, the compressive concrete strength f_{cm} and the peak load F_u.

Tab. 10 *Properties of dowel tests (series DP).*

Test	θ [°]	$\varnothing_s$ [mm]	f_{cm} [MPa]	f_y [1)] [MPa]	f_u [MPa]	test type	α [°]	$\delta_{\|\|,\,init}$ [mm]	N_{init} [kN]	$V_{dow\,l,u}$ [kN]
DP2001	90	20	33.6	524	606	monotonic	0	0.08	47.1	76.1 [2)]
DP2002			33.9				15	0.20	78.8	63.8
DP2007	70		37.3				0	0.20	122	51.5 [2)]
DP2008	45		38.3					0.20	120	32.8
DP2022	90		34.9	520	590	cyclic / monotonic		0.15	98.1	52.5 [2)]
DP2027	45		36.2					0.10	51.1	35.5
DP1403	90	14	35.6	510	584	monotonic	30	0.20	42.6	18.6 [2)]
DP1404			35.5				0	0.20	40.2	30.2 [2)]
DP1411	45		38.9					0.20	51.4	19.0
DP1437	45		38.4	547	618	cyclic / monotonic		0.20	38.7	18.1
DP1440	90		36.8					0.10	21.5	25.1 [2)]

[1)] The yield strength is taken at 0.2% residual strain.

[2)] Based on the shear force without catenary action (see Fig. 52 for tests without clearly defined plateau).

Tab. 11 *Properties of tests of concrete behaviour under a rebar (series CP).*

Test	$\varnothing_s$ [mm]	a [mm]	f_{cm} [MPa]	F_u [kN]
CPa101	20	18	26.7	87.0
CPa102		18	26.7	78.5
CPa104		18	27.9	87.1
CPa205		31	27.3	146.5
CPa206		30	27.9	150.4
CPa307		44	27.9	213.9
CPa308		45	27.3	193.1
CPa409		60	28.5	270.5
CPa410		60	27.3	254.1

6.2.3 Measurements

For the DP series, the applied forces were measured by load cells while 3D Digital Image Correlation was used to measure the displacement field in three perpendicular directions [23, 13]. The DIC was used to track displacements of the concrete surface around the crack (Fig. 50b). A pair of digital cameras SVCam-hr29050 (29 megapixels) were used. The black speckle dots had the diameter of around 2-3 mm. The pixel size of the images was in the range from 0.155 mm to 0.220 mm. The acquisition rate of the cameras was in the range of 1-2 Hz up to the ultimate dowel force. Thereafter, when the catenary action started to increase, it was decreased to 0.5 Hz up to the final bar rupture. The VIC-3D software was used to analyse and post-process the acquired images [207]. Before each test, a sufficient number of images of the unloaded specimens was taken to verify the noise level of the measurement. The mean noise value of maximum and minimum displacements was around 1/70 and 1/20 of a pixel size for in-plane and out-of-plane displacements, respectively.

In addition, optical fibres were used to continuously follow the longitudinal strains in the dowel (Fig. 50a,b). The software Odisi-B by Luna Innovations [208] was used to analyse

the results. This software is based on Optical Frequency Domain Reflectometry which treats optical light paths and reflection characteristics. This allows for the refined measurements with the high frequency and the sufficiently large spatial resolutions [13, 209, 113, 210]. In this work, the spatial resolution was chosen as the gage pitch of 0.65 mm for all the specimens. Optical fibres (125 µm diameter) were glued inside grooves milled on two opposite sides of the reinforcing bar (Fig. 50a,b, see green and blue colours). The grooves were 1 mm wide and 2 mm deep. The fibres were placed using a two-component glue. In some specimens, the fibres were additionally protected by a soft silicon layer along the groove. This allowed reducing the perturbation of the optical fibre measurement due to the stress concentrations at the ribs. More information about the adopted fibre installation process can be found in [13].

Four vertical LVDTs were used to control the imposed crack opening component $\delta_{||}$ (relative displacement between the two crack faces in the direction of the bar axis, Fig. 50b). Two of them were fixed on the front and two on the back side of the specimen. A pair of horizontal LVDTs were used to control and measure the transverse displacement ($\delta_{\perp}$, relative displacement between the two sides of the crack perpendicular to the bar axis).

For the CP series (Fig. 50c), in the DIC measurement pixel size was somewhat less than 0.1 mm for all specimens. The rest of the DIC properties were similar to those of the DP series. The speckle pattern for the measurement was applied: on the front vertical concrete surface below the end of the bar, on the front cross-section of the bar and on the vertical side of the welded steel piece along the bar axis. This enabled the DIC measurements to follow the in-plane and out-of-plane displacements of the concrete surface, the penetration of the bar end into the concrete δ and the kinematics of the bar welded to the steel profile.

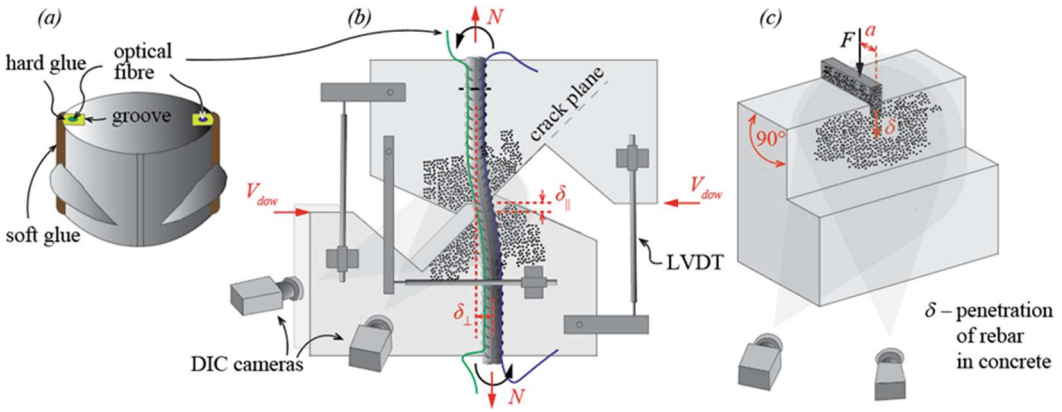

Fig. 50 *Measurements: (a) optical fibres glued on the reinforcing bar; (b) DIC and LVDTs measuring $\delta_{||}$ / $\delta_{\perp}$ ratios in DP series and (c) DIC measurement in CP series.*

6.3 Experimental results

The results of the dowel tests (DP) are divided in two groups, depending on their loading regime: monotonic and cyclic tests. The test results of the concrete behaviour under the bar (CP) are presented in another subsection.

6.3.1 Monotonic dowel tests

The monotonic dowel tests were conducted under controlled displacement to follow the full dowel response up to the bar rupture. The monotonic tests were carried out in two phases. In the first phase (called MI for Mode I), the bar was pulled to impose a specified initial crack opening component $\delta_{\parallel, init}$ in the direction of the reinforcement. In the second phase, a gradually increased transverse displacement $\delta_{\perp}$ (crack opening component perpendicular to the reinforcement) was applied. The opening component $\delta_{\parallel}$ was either simultaneously incremented proportionally with $\delta_{\perp}$ in Mixed-Mode (MM) or kept approximately constant in Mode II (MII).

Figure 51 shows the results of the monotonic dowel tests in terms of the shear force V_{dow} and the global axial force N, as a function of the transverse displacement $\delta_{\perp}$. The results are shown for the specimens with various crack-bar angles θ and bar diameters $\varnothing_s$. Figure 51a,c shows the response up to a transverse displacement $\delta_{\perp}$ = 3 mm, whereas Fig. 51b,d shows the full dowel response up to the bar rupture.

It can be observed that the dowel response is linear-elastic for small imposed transverse displacements (small shear forces). As the force increases, the bar reaches its yield strength and the concrete embedment starts crushing locally under the bar, close to the crack. These two phenomena reduce the initial stiffness of the dowel response (Fig. 51a). An almost horizontal plateau in the shear force – transverse displacement relationship is reached when a plastic hinge develops in the reinforcement and the concrete strength is reached (in accordance with Rasmussen's model [185]). The plateau is clearly visible for tests with cracks inclined with respect to the bar, whereas for cracks perpendicular to the bar, the shear forces slightly increased. The load defined by the plateau, which is characterized by a negligible second-order catenary action is defined as first-order resistance $V_{dow\,I,u}$. Figure 51b shows that after reaching this plateau, the dowel force can be further increased by activating the catenary action related to a significant displacement (transverse displacement larger than approximately one bar diameter). This is enabled by the fixed bar ends which reproduce the typical boundary conditions in most structural RC cracked members (sufficient anchorage away from the crack). The tests typically finished with the bar rupture close to the crack. This occurs at the cross-section with the maximum combination of local axial strains due to bending and the local axial force. The axial force measured at the edges of the specimen (in the direction of the undeformed bar) was observed to decrease up to the transverse displacement $\delta_{\perp}$ reached approximately $\varnothing_s/2$ and increased thereafter showing the activation of the catenary action (Fig. 51c,d). This decrease of the axial force can be explained by the loss of the bond between the concrete and the bar as the transverse displacement increases ($\delta_{\parallel}$ was an imposed displacement). In addition to that, when the bar's most stressed cross-section is fully plasticized (refer to the plastic domain in Fig. 52g), the axial force reduces due to the plastic deformation associated to the local bending of the bar. For the transverse displacement $\delta_{\perp}$ larger than approximately half of the bar diameter, the axial force increases again due to the local elongation associated with the catenary action.

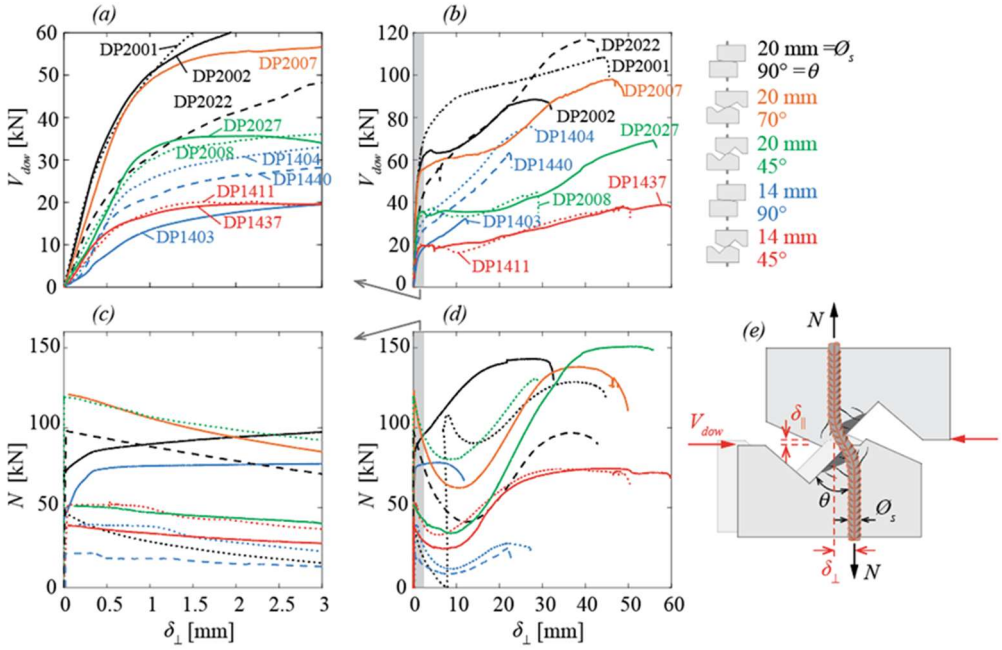

Fig. 51 *Monotonic test results - dowel force V_{dow} and global axial force N as a function of the transverse displacement for: (a,c) elastic and plastic response up to a displacement $\delta_\perp = 3$ mm and (b,d) complete response up to failure; (e) main crack kinematic parameters and forces.*

For large transverse displacements, the dowel resistance results from two components. The first-order component ($V_{dow\,I}$), is related to a shear force in the reinforcing bar while the catenary action ($V_{dow,cat}$) corresponds to the transverse component of the inclined local axial force in the rotated bar in the plane of the crack (N', Fig. 52f). It can be calculated using the equilibrium of forces on the deformed bar configuration (rotation ψ, Fig. 52f). It can be observed that the local axial force in the bar frequently reaches the axial yield strength ($N_p = \pi\, Ø_s^2\, f_y/4$) between the plastic hinges. This occurs due to the elongation related to the large transverse displacement of the catenary action. Consequently, in this configuration, the cross-section of the bar is not able to resist any bending moment (Fig. 52c) and the dowel resistance is provided by the sole catenary action.

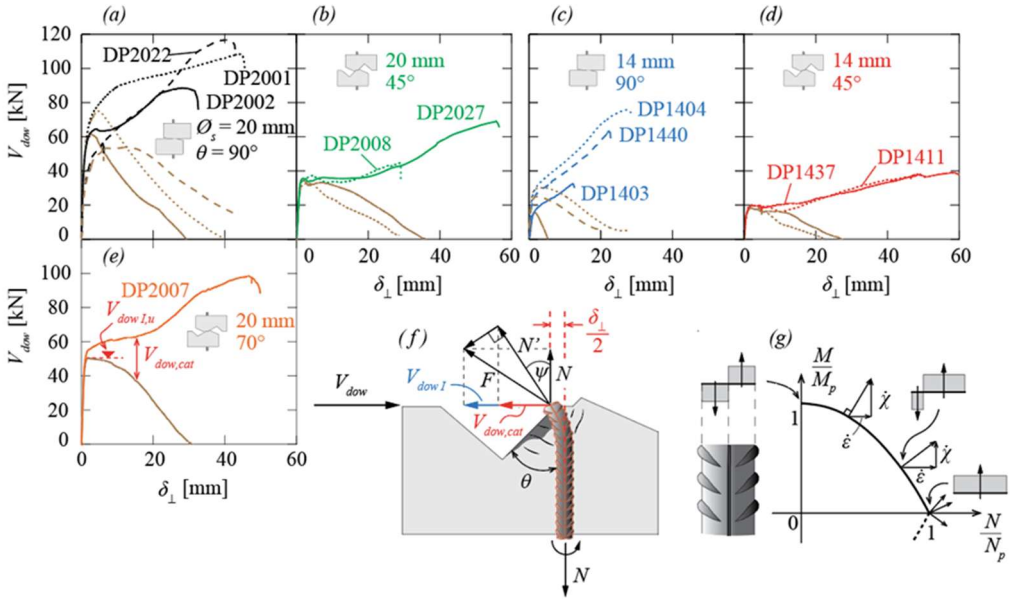

Fig. 52 *(a-f) Catenary action in monotonic tests as a function of transverse displacement and (g) yield domain of a round cross-section of a reinforcing bar.*

Effect of the angle between the bar and the crack

To underline the influence of the angle between the bar and the crack, the responses of three specimens with the same bar diameter (20 mm), displacement protocol ($\alpha \approx 0$), but variable angles (θ = 45°, 70° and 90°) are shown in Fig. 53. The results are shown in terms of the average shear stress as a function of the normalized transverse displacement. Tests DP2001 and DP2007 experienced a rupture of the bar due to catenary action whereas the test DP2008 experienced a premature failure triggered by the rupture of the anchorage at the end of the bar. These experiments show that the angle of the crack has a significant influence on the initial stiffness and on the final dowel resistance. Cracks perpendicular to the bar correspond to a stronger and stiffer concrete embedment under the bar, which limits concrete cracking and crushing. On the contrary, smaller angles cause a decrease in both dowel resistance and initial stiffness.

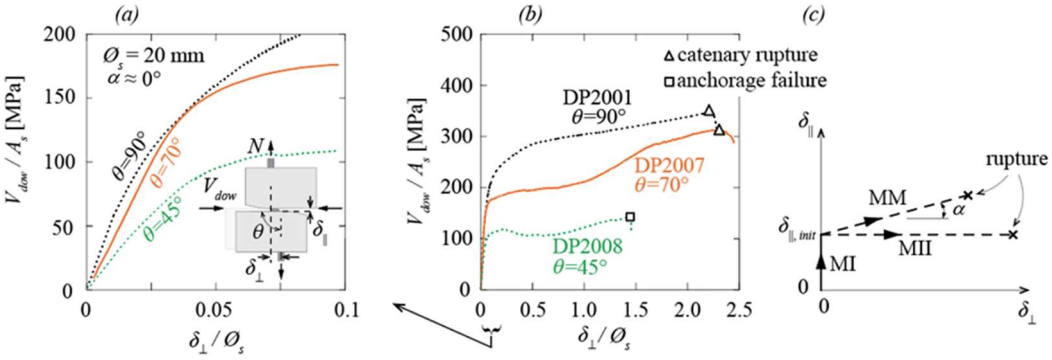

Fig. 53 *Monotonic tests: shear stress in the reinforcing bar as a function of the normalized transverse displacement for three specimens with various angles between the bar and the crack: (a) initial stiffness; (b) complete behaviour up to failure and (c) displacement protocol for monotonic tests.*

Effect of the bar diameter

Figure 54 shows a comparison between two comparable specimens with different bar diameters ($Ø_s$ = 14 mm, 20 mm). It appears that the 20 mm and the 14 mm bar exhibit a similar behaviour for small displacements in the normalized representation of Fig. 54a (the difference for small transverse displacements may be due to measurement inaccuracies), but the normalized resistance of the 14 mm bar is larger, showing a clear size effect.

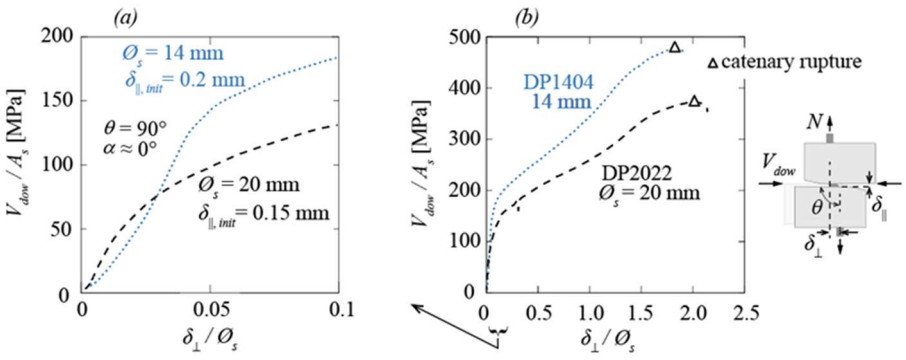

Fig. 54 *Monotonic tests: shear stress in the reinforcing bar as a function of the normalized transverse displacement for two specimens with various bar diameters ($Ø_s$ = 14 mm and 20 mm); (a) initial stiffness and (b) complete behaviour.*

Optical fibre measurements

Optical fibres glued on both sides of the bar (Fig. 50a and 55a) allowed for the continuous monitoring of the longitudinal strains in the monotonic tests. Figure 55 shows the measurement of the DP2027 test ($Ø_s$ = 20 mm, θ = 45°), while the results of the other tests are shown in Appendix VIII. Optical fibre measurements allow calculating the distribution of internal forces in the bar (assuming a bilinear stress-strain relationship for steel according to Fig. 55j, see results in Fig. 55c,d,e), the contact pressure on the concrete embedment exerted by the bar (by double derivation of the moment in the bar, see results in Fig. 55f), the curvature (difference of the strains on both sides divided by the distance between fibres, see results in Fig. 55g), the rotation (by integrating the curvature, see Fig. 55h) and the deformed shape of the reinforcing bar (by integrating the curvature, Fig. 55i). The results are shown for five different load levels including the ultimate dowel force $V_{dow\,l,u}$. In some graphs, the raw data is presented together with smoothed values over a length of around 0.5 to 2 bar diameters [13, 146].

In the presented test, the local axial force remains approximately constant for all the considered load stages (average tensile stress around 190 MPa). The normalized axial stress due to bending (Fig. 55d assuming elastic behaviour) reaches a peak value in tension larger than 500 MPa, indicating yielding of the bar. The distribution of the concrete pressure is calculated as the first-order derivative of the shear force and assumed to be constant over the bar diameter (Fig. 55f). The peak pressure is located at a distance of approximately one bar diameter from the crack plane and has a value of around 62 MPa (~ 1.70 f_{cm}).

Figure 55i shows the transverse displacement $\delta_\perp$ calculated by double integration of the curvature assuming zero rotation at bottom extremity and neglecting the shear deformation of the bar (solid line). The calculated transverse displacement is compared with the DIC measurements (dashed lines, Fig. 55i) for various load levels. The agreement between the two measurements is fairly good, showing that the procedure is reliable and that the shear deformation of the bar is negligible.

The results clearly show the two critical cross-sections with the largest bending moments in the bar (Fig. 55b). They are observed to be symmetrical with respect to the crack for the same concrete properties on both crack sides. The distance between the crack and the critical cross-section is approximately 1.5$Ø_s$. This distance appears to be slightly smaller for perpendicular cracks than for inclined ones (Fig. 55l), due to the stiffer and stronger concrete embedment under the bar. Figure 55k shows that there is no evident size effect with respect to the bar diameter.

Large local axial forces in the reinforcing bar lead to reaching the yielding strain for smaller transverse displacements. On the other hand, larger local axial forces cause second-order effects for a larger imposed transverse displacement, which slightly reduce the longitudinal stresses due to the bending in the bar.

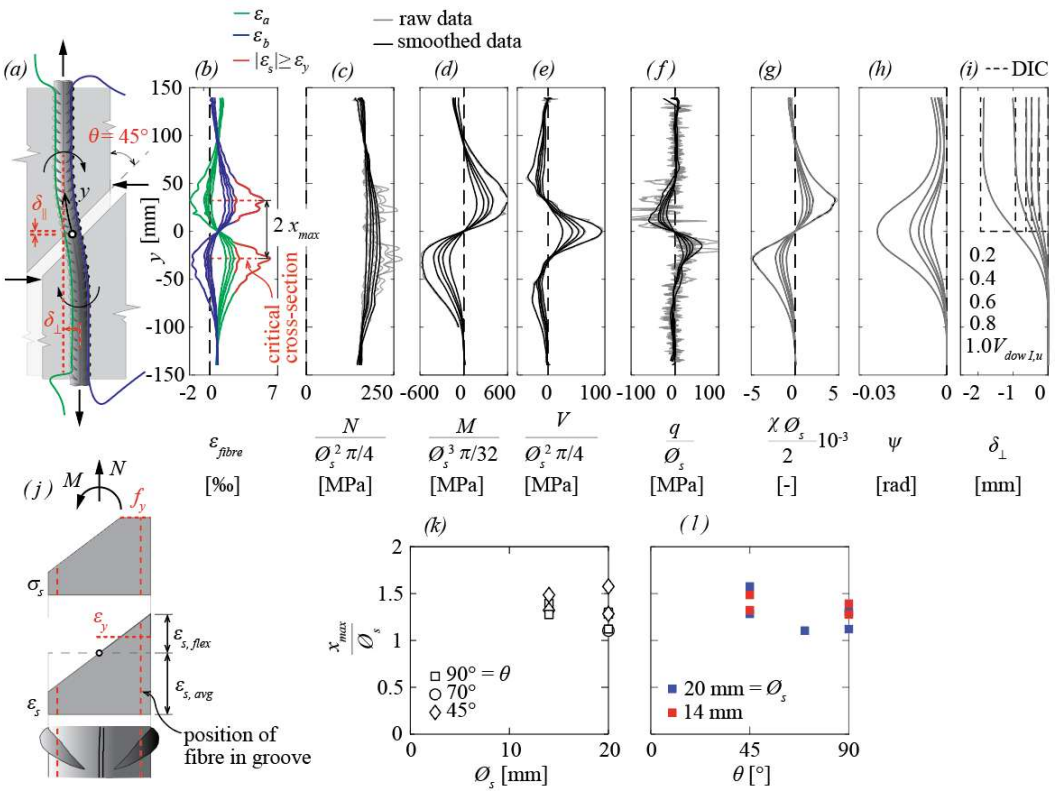

Fig. 55 *Optical fibre measurements: (a) bar deformation and parameter definitions; (b) measured strains; (c) normalized local axial force; (d) normalized moment (stress assuming an elastic behaviour); (e) average shear stress; (f) pressure between bar and concrete (averaged over the bar diameter); (g) normalized curvature; (h) bar rotation; (i) transverse displacement (dashed lines show the results of the DIC measurement); (j) assumption for calculating the internal forces; (k) distance between the crack and the critical cross-section as a function of the bar diameter and (l) as a function of angle between the crack and the bar (test DP2027 with* $\varnothing_s$ *= 20 mm,* θ *= 45°, see Appendix VIII for the other tests).*

Figure 56 shows the interaction diagram of the normalized bending moment and the normalized local axial force at the critical bar cross-section (position of the maximum bending moment, derived from the optical fibre measurements). The plastic bending moment of the bar with a circular cross-section can be calculated as $M_p = \varnothing_s^3 f_y /6$. The dots refer to the calculated values for steps of 0.2 $V_{dow\,l,u}$, the last one referring to the first-order ultimate force $V_{dow\,l,u}$ (except for DP2007 for which optical fibres measured up to 0.9 $V_{dow\,l,u}$). The local axial force tends to increase or to be approximately constant for small transverse displacements while it appears to slightly decrease when the critical cross-section is almost fully plasticized. It can be observed that regardless of the specimen configuration, for $V=V_{dow\,l,u}$, the most stressed cross-section reaches or is relatively close to the plasticity domain at the first-order ultimate shear force. For larger imposed transverse displacement ($V > V_{dow\,l,u}$), the fibre measurement were lost, but one can assume that the local axial force increased again (see increase of the global axial force in Fig. 51d), so that the local internal forces had to follow the plasticity domain of Fig. 56 toward the limit $N = N_p$; $M = 0$.

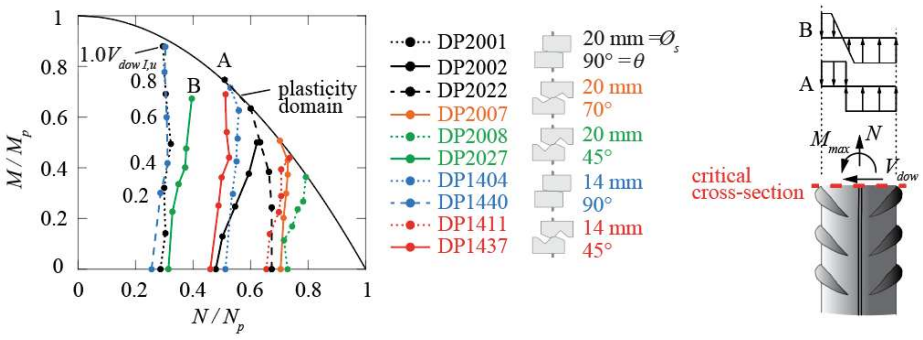

Fig. 56 *M-N interaction diagram of the critical cross-section.*

Figure 57a shows the peak values of the contact pressure between the bar and the concrete (q_{max} / $Ø_s$) along the bar, calculated by double derivation of the bending moments from the optical fibre measurements as a function of the normalized transverse displacement for various load levels up to the first-order ultimate force $V_{dow\ I,u}$ (0.9 $V_{dow\ I,u}$ DP2007). Figure 57b displays their normalized values q_{max} / ($Ø_s \cdot f_{cm}$). It is important to note that the specimens with θ = 90° have the largest peak values of the concrete pressure. The specimen with the slightly inclined crack (θ = 70°) shows almost the same peak pressure values along the bar, except at the ultimate load, for which the pressure is smaller. More inclined cracks (θ = 45°) exhibit reduced values of the normalized pressure, approximately half of those observed in specimens with θ = 90°.

Figure 57c shows the normalized stiffness, calculated as the secant slope of the pressure curves normalized with the ratio of the bar diameter to modulus of elasticity of the concrete $Ø_s$ / E_c. The specimens with θ = 90° have on average the largest normalized stiffness for initial load stages. However, this stiffness reduces as concrete begins to crack (due to splitting) and crush under the bar. The degradation of concrete becomes more pronounced at around 0.4 - 0.6 $V_{dow\ I,u}$. Interestingly, the degradation rate of the normalized stiffness is similar for all considered specimens. Figure 57c shows that both bar diameters exhibit, on average, similar normalized stiffnesses.

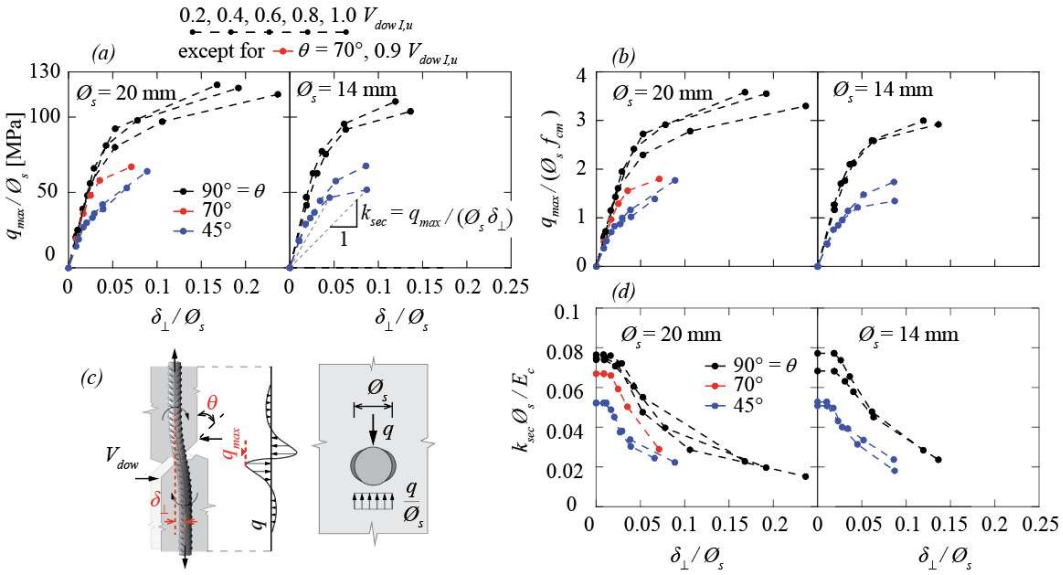

Fig. 57 *Local pressure and local stiffness of concrete derived from optical fibre measurements: (a) peak pressure; (b) pressure normalized with respect to the uniaxial concrete strength; (c) scheme with definitions; and (d) normalized secant stiffness of peak pressure curves.*

6.3.2 Cyclic dowel tests

The cyclic dowel tests were conducted under force control. The majority of the tests were performed through three phases (Fig. 58a). In the first phase, the initial axial force N was imposed (mode I). After that, the initial shear force V_{dow} was applied (mode II). Eventually, the third phase included various combinations of the shear forces V_{dow} and axial forces N (with the minimum and maximum values $V_{dow,\,min/max}$ and $N_{min/max}$ within each cycle combination, Fig. 58a,b). In some cases, instead of the three phases, only mode II (V_{dow}) was imposed, without applying any initial axial force N (Fig. 58b). In this case, the bar was not attached to the test machine, ensuring no axial force was applied. The magnitudes of the forces were chosen to cause only elastic stresses in the reinforcement steel. After the application of initial forces, several groups of typically 5 to 10 cycles with a small stress amplitude were imposed to each test specimen.

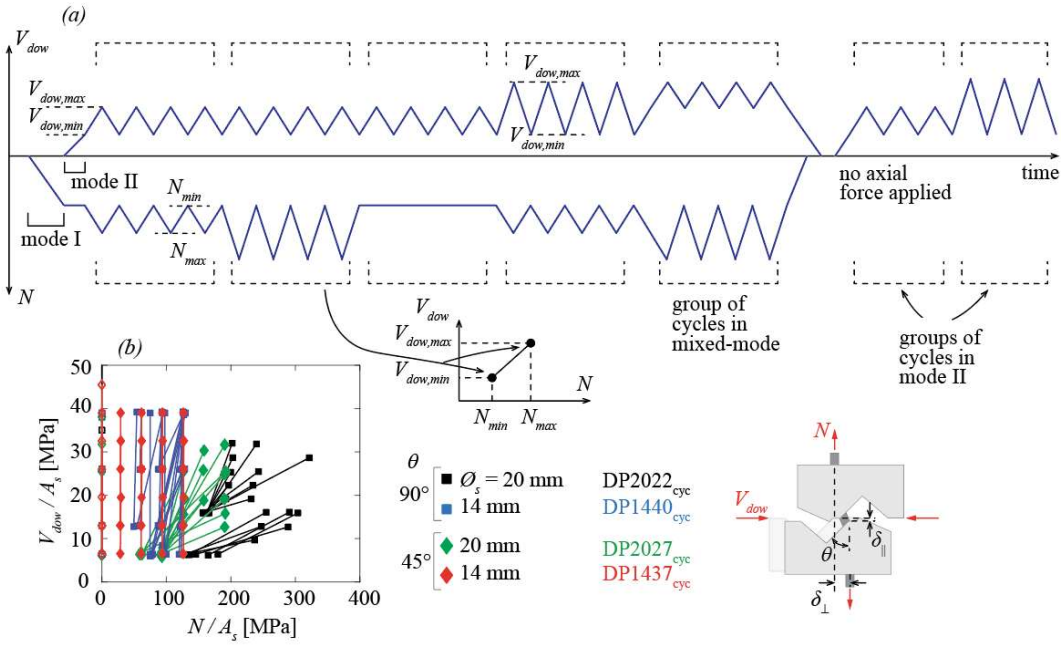

Fig. 58 *Cyclic tests: (a) protocol principle (rectangles indicate groups of typically 5-10 cycles with constant V_{dow} / N ratios) and (b) maximum and minimum values within performed V_{dow} / N cycle groups (each group of cycles as presented in (a) is shown in (b) by a segment connecting two points).*

Figure 59 shows the optical fibre measurements of a cyclic test performed on the specimen DP2027$_{cyc}$ due to the cycle combination with the minimum / maximum shear force $V_{dow,\,min/max}$ = 2 / 8 kN and the axial force $N_{min/max}$ = 20 / 40 kN (specimen with identical geometry and materials as DP2027 used for the monotonic test). For small stress amplitude cycles, the reinforcing bars typically remain elastic. The strains are composed of the average axial stress ($\sigma_{s,\,avg}$, Fig. 59c) and the nominal longitudinal bending stress at the edge of the bar cross-section ($\sigma_{s,\,flex}$ Fig. 59d). The critical cross-section (Fig. 59b) sustains average axial stresses of 63 / 135 MPa due to the minimum and maximum axial force $N_{min/max}$ within the cycle combination. The nominal axial stresses due to bending reach the values of 82 / 186 MPa due to the minimum and maximum shear force $V_{dow,\,min/max}$. Due to the same shear forces, the peak pressure on the concrete (Fig. 59f) along the bar is 9 / 24 MPa (~0.25 / 0.66 f_{cm}). Again, the bar deformation derived from the optical fibre measurements (Fig. 59i) corresponds well to the DIC measurement on the concrete surface.

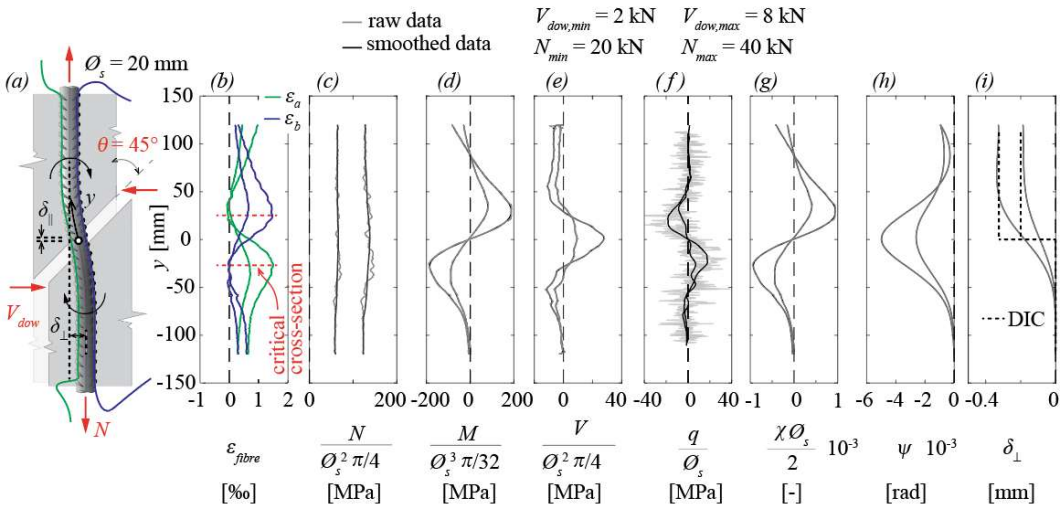

Fig. 59 *Optical fibre measurements: (a) main parameters and installed optical fibres; (b) measured strains and (c-i) derived results (specimen DP2027$_{cyc}$, see Fig. 55 for description).*

The peak longitudinal stresses at the critical cross-section ($\sigma_{s,flex}$ due to bending and $\sigma_{s,avg}$ due to local axial force, Fig. 59) are shown as a function of the two components of the displacement ($\delta_\parallel$ and $\delta_\perp$) in Fig. 60a. The figure identifies the three phases of the test protocol: pure tension (MI) in which the axial force N is imposed, pure shear (MII) in which the dowel force V_{dow} is imposed and a group of cycles in mixed-mode (MM).

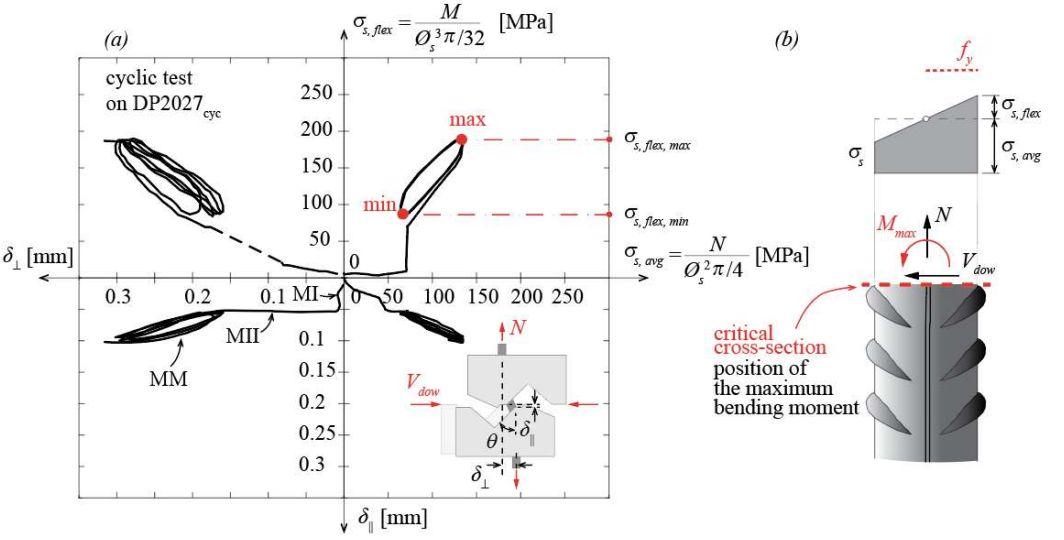

Fig. 60 *Cyclic test results for specimen DP2027$_{cyc}$: (a) relationship between stress and kinematic components in mode I, mode II and mixed-mode and (b) internal forces at the critical cross-section.*

Figure 61 shows the optical fibre measurements at the critical cross-section for all cyclic tests. Only values corresponding to the minimum and maximum shear force $V_{dow,\,min/max}$ and the axial force $N_{min/max}$ within cycle groups are presented (see Fig. 58). Again, the measured longitudinal stresses are decomposed into the average stress $\sigma_{s,avg}$ and the bending stress $\sigma_{s,flex}$. Figure 61a-c show the nominal elastic stresses due to bending (associated to $V_{dow,\,min/max}$) and due to the axial force $N_{min/max}$ as a function of the normalized transverse displacement for all cyclic tests (tests in which both shear force V_{dow} and axial force N are applied are identified by solid markers and tests in mode II only, with N = 0, are identified by empty markers). Figure 61a shows that the longitudinal stress due to bending (associated to $V_{dow,\,min/max}$) increases approximatively linearly with the transverse

displacement. The stiffness of this response increases with the bar diameter and with the crack-bar angle. In addition, there appears to be a slightly larger measured transverse displacement associated with smaller average local axial stresses. Figure 61c shows that the reinforcing bars subjected to the pure shear (MII with no initial axial force) do not sustain any average axial stresses at the critical cross-section. However, these stresses increase for the somewhat larger shear force (this occurs because the bar elongates as it is anchored by the concrete embedment). Figure 61d shows the average elastic stresses due to the minimum and maximum axial force $N_{min/max}$ within each group of cycles at the critical cross-section as a function of the normalized longitudinal displacement $\delta_{||}$ for two different bar diameters. These results encompass both pure tension tests (mode I, empty markers) and tests in which both shear force V_{dow} and axial force N are applied (full markers). The relationship between longitudinal stress due to axial force and longitudinal displacement is approximately linear.

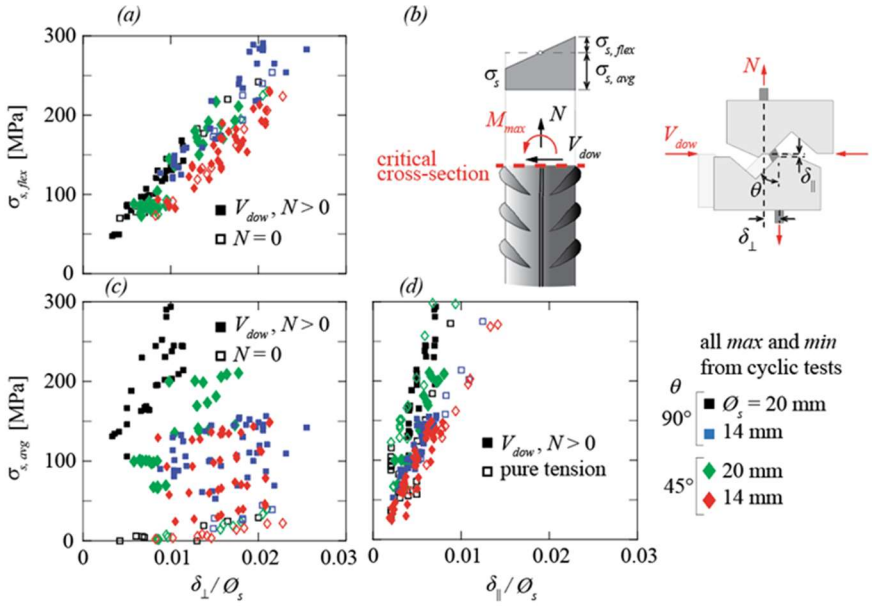

Fig. 61 *Calculated longitudinal stresses of all cyclic tests corresponding to the minimum and maximum shear force $V_{dow,\ min/max}$ and axial force $N_{min/max}$ within group of cycles at the critical cross-section based on optical fibre measurements: (a) axial stress due to bending as a function of the normalized transverse displacement, (b) definitions; average axial stress as a function of (c) the normalized transverse displacement; and (d) of the normalized longitudinal displacement component $\delta_{||}$.*

6.3.3 CP test series

The CP test series examined the concrete stiffness and strength underneath a rebar subjected to a concentrated load perpendicular to the bar axis. The position of the force is denoted as distance *a* from the concrete edge (representing the crack surface in dowel tests, Fig. 62). In Fig. 62a, the relationship between the applied force *F* and the penetration δ of the bar at concrete edge is shown (colours indicating various distances *a*). Both the initial stiffness and the peak force increase with the distance *a* between the concrete edge and the point load, due to the larger concrete area carrying the applied force. However, the post-peak branches exhibit similar rates of decrease for all load positions.

For comparison, Fig. 62b shows the local shear force in the bar for three corresponding dowel tests (DP series, black curves, all of them with bar diameter $\varnothing_s$ = 20 mm and θ = 90°, δ assumed to correspond to $\delta_\perp/2$). It can be observed that the CP tests can reproduce the behaviour of the comparable dowel tests for the load position $a = 0.9\ \varnothing_s$ = 18 mm (red curves). This match occurs because this force position approximately corresponds to the position of the resultant of the pressure distribution along the bar in the dowel tests. It is interesting to note that in the CP tests, after reaching the peak load, a softening behaviour associated with the development of splitting cracks perpendicular to the concrete surface

and spalling cracks associated with concrete crushing can be observed. A similar softening behaviour can also be observed in the considered dowel tests if the contribution of the catenary action is removed (Fig. 62b, brown curves). On the contrary, when the catenary action is accounted for, the dowel tests exhibit a hardening behaviour in the depicted range. This observation seems to indicate that the shear force contribution of the catenary action is transferred to concrete at larger distances from the crack surface. Moreover, the spalling patterns at the free surface are similar in the CP tests and the DP tests (see Appendices VII and IX).

DIC measurements on the lateral surface of the welded steel piece allowed to determine the displacement profiles of the bar which are shown in Fig. 62c at the peak load F_u for various load positions a. In most cases, the bars do not bend and only rotate because they are stiffened by the welded steel profile. However, bars subjected to a centric load (orange curves) exhibit slight bending underneath the point load due to the larger forces and lever arms involved.

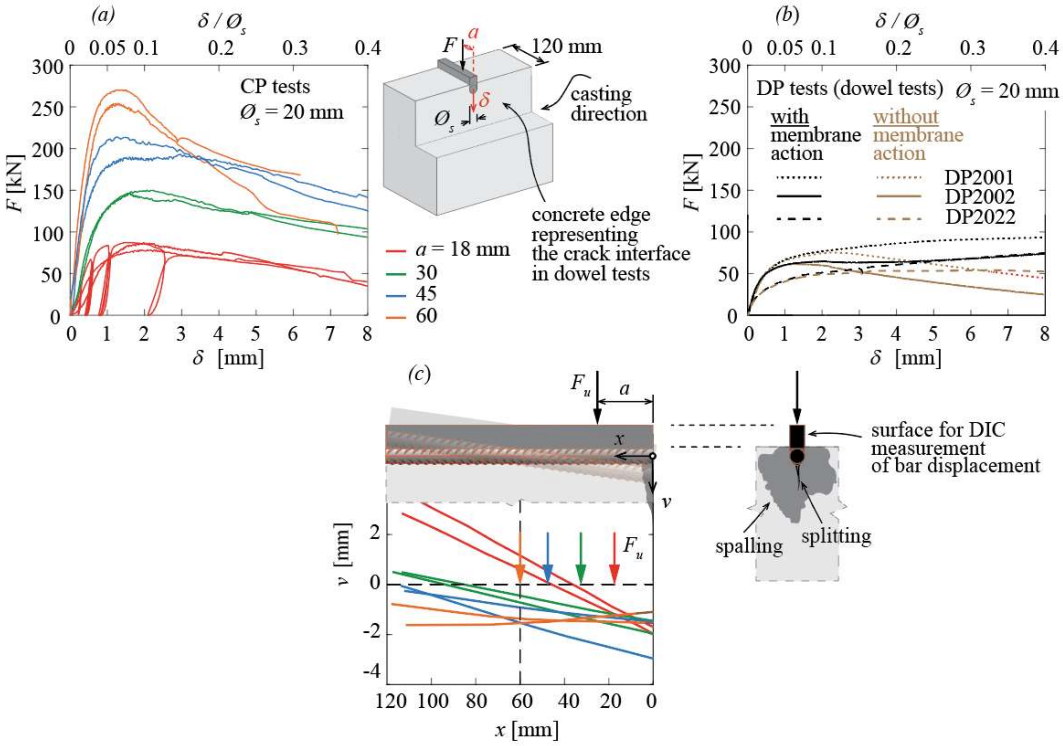

Fig. 62 *CP test results: force-penetration relationships for (a) CP tests; (b) DP tests and (c) deformed shape of the bar at peak load for different load positions (same colours as in (a)).*

Figure 63a shows the relationship between the measured peak force F_u and the distance a. The peak force increases approximately linearly with its distance from the edge of the bar.

If the compressive stress in concrete under the bar is assumed to be uniformly distributed and symmetrical with respect to the point of application of the load, a nominal concrete plastic stress can be calculated: $\sigma_{c,pl} = F_u / (Ø_s \cdot 2a)$. Figure 63b shows the values of the plastic stress normalized by the uniaxial concrete strength as a function of the normalized force distance. All the values are close to four due to the confinement effect of the concrete embedment. It must be noted that the stress $\sigma_{c,pl}$ shown in Fig. 63b is affected by several assumptions which are a rough simplification of the reality. In addition, the load introduction device did not allow for sufficiently exact definition of the position of the force. These two effects can explain the larger normalized strengths for small distances a which is counterintuitive (for very small distances a, the biaxial stress state at the surface should become governing).

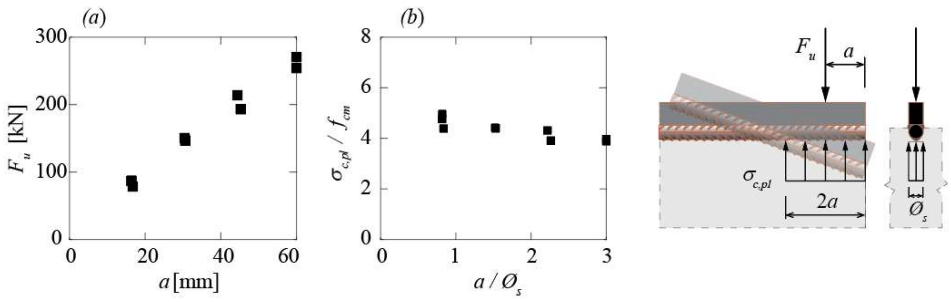

Fig. 63 *CP test results: (a) peak force as a function of the distance from the bar end to the load and (b) plastic concrete stress normalized by uniaxial concrete strength as a function of the load position.*

The concrete near the edge crushes and gradually spalls due to the penetration of the bar. Figure 64 shows the values of concrete spalling (out-of-plane displacement, *w*) at discrete points along the vertical axis under the bar end. Significant spalling commonly occurs within a depth of two to three bar diameters (spalling failure patterns at peak load are given in Appendix IX). The depth of spalling is an indicator of the stiffness degradation, which starts at approximately half a peak force. The amplitude of the measured spalling displacement *w* (several mm at peak load) suggests that in the dowel tests of series DP, where the imposed longitudinal displacements were significantly smaller, spalling is partially prevented, which leads to a larger strength and/or a less brittle behaviour (this effect could also explain the different behaviour of the DP and CP tests shown in Fig. 62).

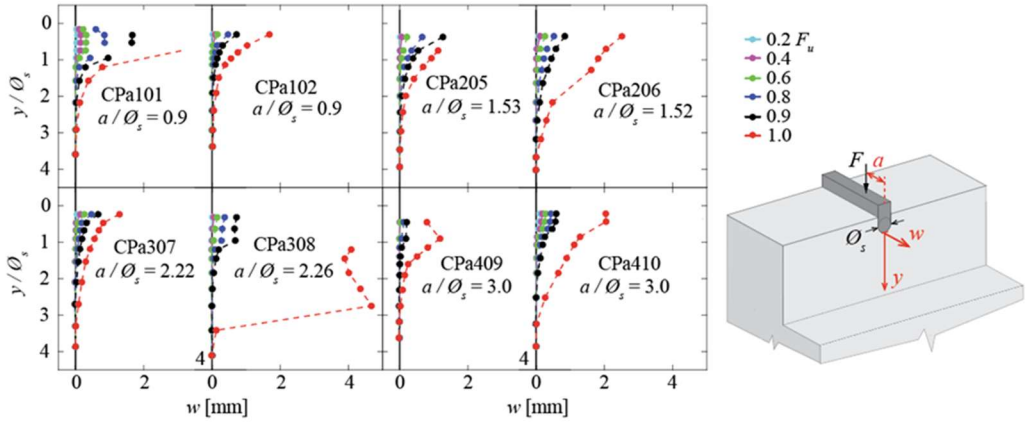

Fig. 64 *Out-of-plane displacement (spalling, w) of the concrete face under the bar for various specimens at various load stages measured by DIC.*

6.4 Conclusions

This section presents an experimental investigation of the dowel action in steel reinforcing bars using refined measurements: digital image correlation and distributed optical fibres. Dowel action (DP test series) was studied for various angles between the crack and the bar, bar diameters and imposed crack kinematics with monotonic or cyclic loadings. The section also investigates the behaviour of concrete under a rebar (CP test series). The majority of the findings observed in this study align closely with or provide further support for the conclusions from previous research. The main conclusions are:

1. The observed dowel response is significantly influenced by the angle between the bar and the crack, the bar diameter and the applied crack kinematics. A bar nearly perpendicular to the crack and a larger bar diameter correspond to a stiffer dowel response and a larger first-order ultimate load. The imposed crack kinematics determine both the linear and non-linear regime of the dowel response.

2. Large shear forces in the bar associated to large imposed transverse displacements result in concrete crushing under the bar near the crack. Yielding of the bar is caused by the combination of bending and axial force in the bar.
3. The dowel resistance under large transverse displacements consists of two components: the first-order ultimate dowel force associated with a shear force in the bar and the second-order catenary force associated with the axial force and the rotation of the bar in the crack region.
4. According to optical fibre measurements, the section of the bar with maximum longitudinal stresses (combined local axial force and bending) is located approximately at 1.5 times the bar diameter $Ø_s$ from the crack.
5. The angle between crack and reinforcement has a significant influence on the behaviour.
6. A substantial degradation of the concrete stiffness under the bar occurs at approximately 40% to 60% of the first-order ultimate load (shear resistance before activating the catenary action). The degradation rate remains approximately constant across all specimen configurations with respect to the normalized transverse displacement.
7. The dowel response remains comparable under monotonic and low-stress amplitude cyclic loading within the studied service-load domain. Furthermore, several low-stress cycles do not reduce significantly the stiffness.

6.5 Outlook and future works

Several questions regarding the dowel resistance and stiffness still remain open. In the following, some aspects that could be further studied are outlined:

- This research has shown that the measurement technique using distributed optical fibres is very efficient in studying experimentally the dowel action is small specimens designed to investigate this effect. However, similar investigations could be conducted on large-scale concrete members. Such an investigation could include various parameters such as the bar diameter, the angle between the concrete and the bar, the crack kinematics, the casting conditions, and the concrete cover.
- Tests of the compressed concrete under the uniformly loaded reinforcing bar show a strong dependence on the concrete cover and casting conditions. However, these effects could be studied directly in dowel tests. This would allow further investigation of their influence on both the dowel resistance and stiffness.
- The effect of the angle between the concrete and the bar could be further investigated. Additional dowel tests could also include the angles larger than 90°.
- Low-stress cyclic tests could be extended to large-stress cyclic tests. Refined measurements could provide the important information on the stiffness deterioration due to the non-linear behaviour of both concrete and the reinforcement.
- Additional dowel tests could be conducted, including visible crack faces for DIC measurements. This could enable the detailed investigation of concrete crushing and spalling, as well as splitting cracks under the bar.

7 Dowel models to predict the resistance and the relationship between transverse displacement and stress in the reinforcing bar

7.1 Introduction

The dowel action in reinforcing bars embedded in concrete is due to a transverse component of the relative displacement of the two lips of a crack (or an interface between two parts of concrete cast at different times) which intercept the bar. Such a displacement component can be related to the slip of a crack perpendicular to the bar and/or to the opening of a crack inclined with respect to the bar.

The dowel force can be limited by spalling of the concrete cover, primarily occurring when the concrete cover (net distance between concrete surface and bar) is thin compared to the bar diameter [178]. Alternatively, in cases with sufficient cover, the dowel force can be limited by localized concrete crushing near the interface combined with yielding of the bar in bending (development of a plastic hinge in the bar). Focusing to the case with sufficient cover, failure is characterized by a relatively ductile behaviour due to the potentially significant steel plastic strains. Consequently, many authors have evaluated the dowelling resistance of a steel bar using the limit analysis approach (see Rasmussen [185] and [186, 187, 189, 190, 192, 193, 194, 195]). This approach assumes that the plastic hinge develops in the bar at a certain distance from the crack which intercepts the bar. In the limit analysis approach, the contact pressure between the bar and concrete activated by dowel action is assumed to be constant. This pressure can reach a value which can be significantly higher than the uniaxial concrete strength due to the local tri-axial stress state. The ratio between the confined concrete strength and the uniaxial concrete strength (measured on cylinders) is often referred to as a confinement factor. Its values were typically determined from dowel tests with interfaces perpendicular to the bar, with a range between approximately 3 and 5 [192, 211, 185]. For angles between the bar and the crack smaller than 90°, the dowel resistance was observed to decrease [187]. The resistance was also observed to decrease due to an axial force in the reinforcing bars [186, 94].

The behaviour of dowels under cyclic loads has also been experimentally investigated in the past [212, 213, 214]. These experiments commonly indicated an increased shear displacement with cycles, a considerable stiffness degradation, and a reduction in hysteresis loop areas over cycles. Vintzeleou et al. [195] conducted an extensive parametric experimental investigation of dowels under cyclic loads, emphasizing the influence of the concrete cover. They observed the significant stiffness degradation in cases involving fully reversed deformations. Using these findings, they proposed a model addressing the failure due to steel yielding and concrete crushing [178]. Soltani et al. [215] developed a path-dependent mechanical model for deformed reinforcing bars at the concrete interface under the coupled cyclic shear and axial force. This model considered the bond-slip strain relation, the three-dimensional yield criterion, and the cyclic stiffness deterioration. Tests by Kato et al. [216] showed no substantial response degradation in the reinforcing steel due to cyclic loads. Consequently, the degradation in the dowel response is primarily associated with the degradation of concrete. Li et al. [217] conducted dowel tests to investigate the response deterioration due to fatigue and identify fatigue failure modes. Their study highlighted that the accumulated fatigue damage significantly reduced the dowel resistance measured under monotonic loads. Based on these findings, they proposed a nonlinear bond model for numerical applications, accounting for the effect of the fatigue damage.

Regarding service loads, the model developed by Winkler [218] and Zimmermann [219] already in the 19th century with the elastic analysis solution of slender members resting on a cohesionless foundation can be adapted to describe the interaction between the reinforcing bar and the surrounding concrete for moderate dowel forces. In this case, the concrete can be modelled as linear springs smeared along the bar. The mathematical

solution for a bar with an infinite length was reported by Timoshenko et al. [220], subsequently applied by Friberg [221] for the case of dowel bars between concrete pavement segments. The uncertainty in the prediction relies on estimating the concrete stiffness under the bar, which remains a challenge due to the complexity of the problem related to the development of local cracking. Many authors have attempted to estimate the stiffness through empirical expressions, typically accounting for the bar diameter and concrete strength [211, 203]. These expressions were usually calibrated to fit the load-displacement curves using the shear force or the transversal displacement as indicators of the concrete degradation [222, 190, 215, 223], particularly for larger loads. However, the stiffness is significantly influenced by other factors such as casting conditions due to the plastic settlement and bleeding of the fresh concrete [224], thickness of the concrete cover [225], angle between the crack and the bar, number of cyclic loadings, and secondary cracks induced by the axial force [101].

The following subsection introduces a new formulation for the concrete bearing stiffness under the reinforcing bar to be used in Winkler model. The formulation accounts for the aforementioned phenomena and is calibrated based on mechanical considerations and measurements with optical fibres described in Section 6. Regarding the dowel resistance, existing models are validated against the collected tests. Rasmussen's model is used to evaluate the dowel resistance for the 90°-angle between the bar and the crack, including different values of the confinement factor. For the angles smaller than 90°, Dulacska's model is used.

7.2 Steel stress variations for a fatigue verification

7.2.1 Winkler's model

Winkler's model [220, 221], which describes the behaviour of an elastic beam continuously supported by elastic springs, can be used to investigate in the elastic domain a reinforcing bar embedded in concrete which is submitted at its end by an imposed transverse displacement which corresponds to half of the crack slip $\delta_\perp$ (Fig. 65a, or transverse component of the crack opening in case of cracks not perpendicular to the bar).

For this purpose, one can assume that (1) at interface between reinforcing bar and concrete, no tensile forces can be carried and that (2) on the compression side, the contact pressure between bar and concrete can be smeared over the bar diameter $\varnothing_s$ (Fig. 65c), so that the average value of the pressure can be calculated from the distributed bearing force q (in N/mm) between the bar and the concrete: $q/\varnothing_s$ (in MPa).

According to Winkler's assumption, the pressure $q/\varnothing_s$ is proportional to the local relative transverse displacement $\tilde{\delta}_\perp$: $q/\varnothing_s = k_c\,\tilde{\delta}_\perp$, where k_c is the bearing stiffness (in MPa/mm). The differential equation of Winkler's model for our case without external action on the bar becomes thus:

$$E_s I_s \frac{d^4\tilde{\delta}_\perp}{dx^4} + k_c \varnothing_s \tilde{\delta}_\perp = 0 \tag{21}$$

where x is the bar's axis, E_s is the elastic modulus of the reinforcing bar and $I_s = \pi\varnothing_s^4/64$ is the moment of inertia of the rebar.

The solution for the case of a semi-infinite rebar [220, 221] subjected to a concentrated dowel force V_{dow} at its end is given by:

$$\tilde{\delta}_\perp = \frac{V_{dow} e^{-\beta x} \cos \beta x}{2\beta^3 E_s I_s} \tag{22}$$

where $\beta = \sqrt[4]{\frac{k_c \varnothing_s}{4 E_s I_s}}$ (in mm^{-1}) is a parameter which expresses the relative stiffness between the bar and the surrounding concrete. The definition of the bearing stiffness will be treated in the following subsection. The transverse displacement at the crack interface ($\delta_\perp$ / 2, Fig.65a) can be calculated for x = 0:

$$\frac{\delta_\perp}{2} = \frac{V_{dow}}{2\beta^3 E_s I_s} \tag{23}$$

The bending moment in the bar M is calculated as a function of V_{dow}, or as a function of $\delta_\perp$ (see Eq. 23):

$$M = -\frac{V_{dow}}{\beta} e^{-\beta x} \sin \beta x = -\delta_\perp \beta^2 E_s I_s e^{-\beta x} \sin \beta x \tag{24}$$

The position of the maximum bending moment along the bar (Fig.65d) can be calculated as:

$$x_{\max} \approx 0.52 \varnothing_s \left(\frac{E_s}{\overline{k}_c E_c} \right)^{\frac{1}{4}} \tag{25}$$

where $\overline{k}_c = k_c \varnothing_s / E_c$, with E_c being the elastic modulus of concrete. After replacing the position of the peak moment into Eq. 24, the maximum bending moment can be calculated as:

$$M_{\max} = -\frac{V_{dow}}{\sqrt{2}\beta} e^{-\beta x_{\max}} = -\frac{\delta_\perp \beta^2 E_s I_s}{\sqrt{2}} e^{-\beta x_{\max}} \tag{26}$$

so that the maximum stress in the bar (Fig.65e) becomes:

$$\sigma_{s,flex} \approx 0.37 \sqrt{\overline{k}_c E_c E_s} \frac{\delta_\perp}{\varnothing_s} \tag{27}$$

When the bar is subjected to the variation of the transverse displacement $\Delta\delta_\perp$ at the crack interface, assuming linear elastic behaviour, the longitudinal stress variation $\Delta\sigma_{s,flex}$ at the critical cross-section can be estimated as:

$$\Delta\sigma_{s,flex} \approx 0.37 \sqrt{\overline{k}_c E_c E_s} \frac{\Delta\delta_\perp}{\varnothing_s} \tag{28}$$

which can be used, in case of cyclic actions, to verify the fatigue resistance of the bar.

The measured transverse displacement $\delta_\perp$ at the crack interface is also an input to compute the shear force V_{dow}, which is limited by the ultimate shear force $V_{dow\,I,u}$ in accordance with Rasmussen's model [185] (see also Subsection 7.3 for an improvement of Rasmussen's model):

$$V_{dow} = \beta^3 E_s I_s \delta_\perp \le V_{dow\,I,u} \tag{29}$$

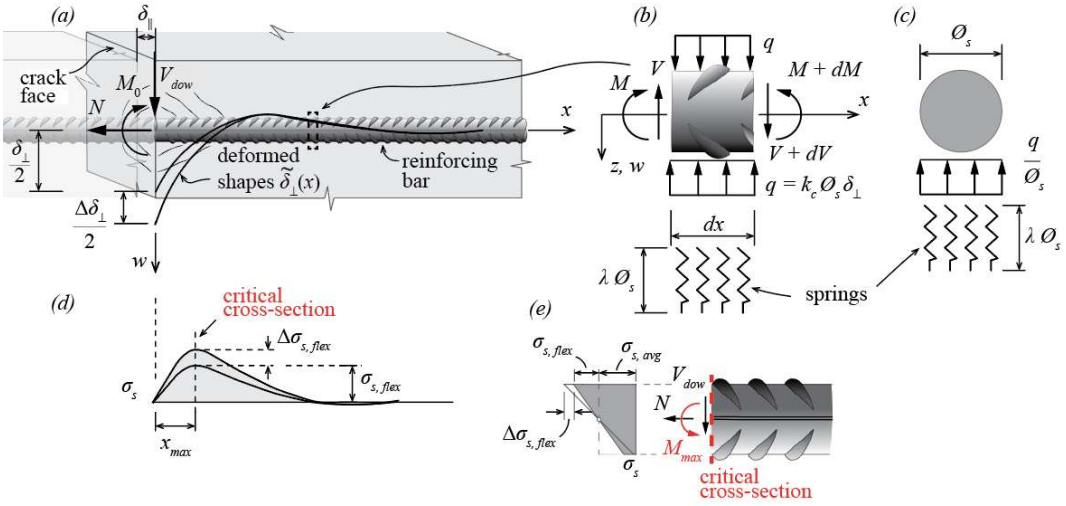

Fig. 65 *(a) Reinforcing bar subjected to the crack opening components $\delta_\perp$ and $\delta_\parallel$; (b) forces on a portion of the bar; (c) cross-section; (d) longitudinal stress $\sigma_{s,flex}$ and its variation $\Delta\sigma_{s,flex}$ due to bending along the bar's axis and (e) stress $\sigma_{s,flex}$ and its variation $\Delta\sigma_{s,flex}$ at the critical cross-section.*

The bearing stiffness k_c is a crucial parameter for the accuracy of the model's prediction. Several empirical formulations for k_c were proposed in the past (see Subsection 7.2.2), typically accounting for the bar diameter and the concrete strength. In the following, a new expression for the bearing stiffness k_c is proposed, based on mechanical considerations and measurements with optical fibres (Subsection 7.2.3). Besides the bar diameter and the concrete strength, the proposed expression for the bearing stiffness k_c accounts for the angle between the crack and the bar θ, the casting conditions, the concrete cover and the stiffness reduction due to cycling loading, as well as due to local secondary cracks caused by an axial force.

7.2.2 Existing models for the bearing stiffness of concrete

The existing formulae that predict the concrete bearing stiffness under the bar were typically derived empirically. In this section, two analytical expressions are compared to the experimental results presented in this work. The first is the formula by Soroushian et al. [203] which was fitted on numerous tests involving compressed concrete under the bar (similar to the series CP described above). The expression defines the bearing stiffness k_c as a function of the bar diameter $\varnothing_s$ and the uniaxial compressive concrete strength f_c:

$$k_c = \frac{127\sqrt{f_c}}{\varnothing_s^{\frac{2}{3}}} \tag{30}$$

where k_c is expressed in MPa/mm, f_c in MPa and $\varnothing_s$ in mm (the exponent 2/3 on the bar diameters relates to a size effect). This expression solely predicts the initial concrete stiffness under the bar.

The second considered expression by Brenna et al. [222] is also empirical. It was fitted on multiple dowel tests on the basis of the Winkler's model. This expression accounts for the degradation of the concrete stiffness with increasing transverse displacement, but has no size effect:

$$k_c = 400\frac{f_c^{0.7}}{\varnothing_s}\left[\left(0.66-\frac{f_c}{80.5}\right)+0.487\left(1+\frac{f_c}{116}\right)\sqrt{1+0.023\left(\frac{2+f_c/116}{1+f_c/116}\right)^2\left(1-\frac{f_c}{30.7}+174\frac{\delta_\perp}{\varnothing_s}\right)^2}\right]^{-\frac{4}{3}} \tag{31}$$

In Fig. 66, a comparison is presented between the two predictions and the bearing stiffness derived from the optical fibre measurements of test series DP (see Section 6). These results (a representative test is shown in Fig. 67a-d) allow to calculate the local values of the bearing stiffness k_c by dividing the measured concrete pressure $q/Ø_s$ (Fig. 67b) by the corresponding transverse displacement of the bar (Fig. 67c). In Fig. 67d, the distribution of the calculated values of k_c (normalized by the ratio $Ø_s / E_c$) is presented along the bar. It can be observed that the derived local bearing stiffness increases farther from the crack interface, reaching a plateau approximately half a diameter away from the crack. The average stiffness values taken from the plateau are presented for several tests in Fig. 66 as a function of the transverse displacement $\delta_\perp$. One can observe that for small transverse displacements $\delta_\perp$, the normalised value of k_c is almost constant. In Fig. 66, the predictions are shown by envelopes, accounting for the variability of governing test parameters. Soroushian's expression generally underestimates the concrete stiffness except for large transverse displacements, where the initial underestimation is compensated by the neglected concrete degradation. This discrepancy arises because Soroushian's expression was calibrated on tests involving relatively long bars laterally loaded against concrete, which is different from dowels that transmit stresses to concrete over a smaller area, resulting in a larger stiffness. The concrete stiffness predicted by Brenna et al. [222] corresponds well with the results of the tests with $\theta = 90°$, while it tends to overestimate the stiffness for $\theta = 45°$. However, this prediction effectively captures the degradation rate of the concrete stiffness. This means that current expressions, and particularly Brenna's relationship, can be improved accounting for parameters and effects which have not been considered in the empirical evaluation.

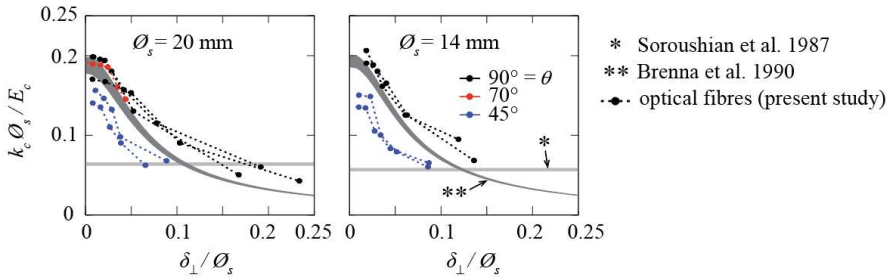

Fig. 66 *Comparison of the existing empirical expressions with the derived stiffness based on optical fibres measurements in dowel tests (see Section 6).*

7.2.3 Improved expression for the bearing stiffness

With respect to the bearing stiffness which is defined in Winkler's model as ratio between pressure and local displacement ($k_c = q/(Ø_s \cdot \tilde{\delta}_\perp)$ as described above), it can be calculated assuming in a first approximation the case of a strip load applied to a concrete half-space according to Boussinesq [226]. For a strip with the width $Ø_s$ (Fig. 65c), the bearing stiffness is thus related to the concrete elastic modulus and the bar diameter:

$$k_c = \frac{E_c}{\lambda Ø_s} \tag{32}$$

where the product $\lambda\, Ø_s$ expresses the length of an idealized spring (see Fig. 65b and c).

Since the case of the reinforcing bar submitted to dowel action is significantly different compared to the strip load according to Boussinesq (half-space limited vertically by the crack, circular shape of the bar), the factor λ can be calibrated on the basis of the bearing stiffness calculated from the optical fibre measurements, as previously explained.

With respect to the angle θ between the crack and the reinforcing bar, it can be accounted for by applying to the bearing stiffness according to Eq. 32 a coefficient η_θ defined in Eq. 33:

$$\eta_\theta = \left(\frac{\theta}{90°}\right)^{\frac{3}{5}} \tag{33}$$

As shown in Fig. 67e, the normalised bearing stiffness is correctly corrected with coefficient η_θ defined in Eq. 33. For all cases, the normalised value of k_c for small transverse displacements $\delta_\perp$ is approximately 0.2, which means that factor λ = 5 can be assumed. Interestingly, as shown in Figure 68, similar results can be obtained from the compression tests (series CP) described in Section 6.

Fig. 67e also shows that the bearing stiffness k_c starts to gradually decrease when the transverse displacement $\delta_\perp$ reaches a critical value due to the development of splitting cracks, local concrete crushing and spalling near the crack. This reduction can be accounted for by applying a reduction factor η_δ fitted on the available data as a function of the transverse displacement $\delta_\perp$ according to Eq. 34:

$$\eta_\delta = \frac{1.5}{1+25\dfrac{\delta_\perp}{\varnothing_s}} \le 1.0 \tag{34}$$

The transverse displacement $\delta_\perp$ for which the stiffness starts to decrease is therefore $\delta_\perp = \dfrac{1.5-1}{25}\varnothing_s = 0.02\varnothing_s$.

Figure 67e shows the comparison with the tests results accounting for both coefficients η_θ and η_δ showing fine agreement.

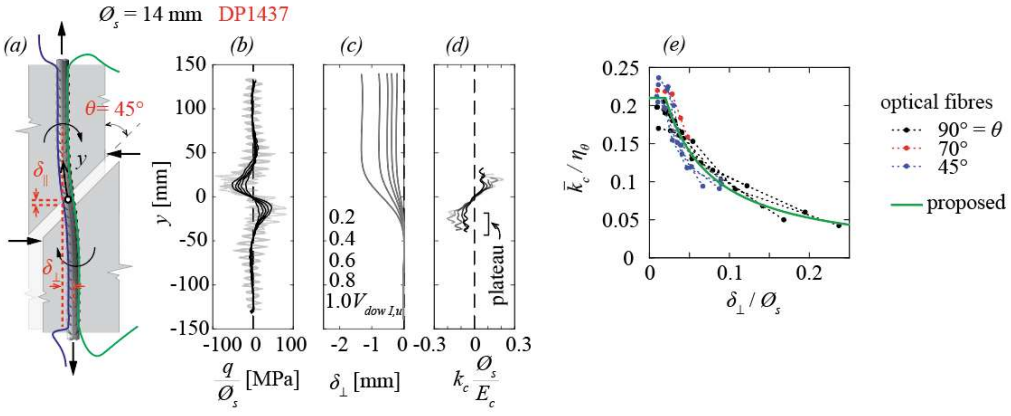

Fig. 67 *Calibration of the concrete stiffness under the reinforcing bar based on optical fibre measurements: (a) representative specimen with main parameters; (b) pressure between concrete and the bar; (c) transverse displacement of the bar; (d) normalized concrete stiffness and (e) comparison between the measured and the calculated bearing stiffness accounting for coefficients η_θ and η_δ (data from Section 6).*

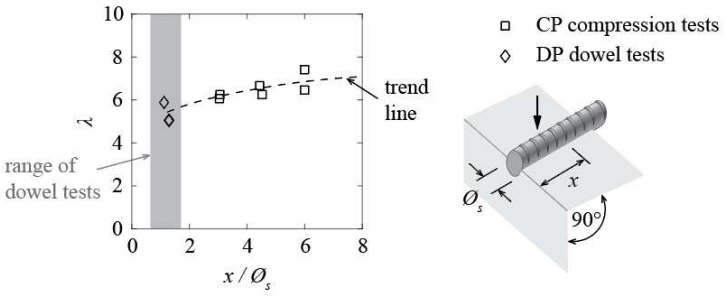

***Fig. 68** Coefficient λ as a function of the $x / Ø_s$ ratio for the dowel (DP series) and compression (CP series) tests (see Section 6).*

To account for other effects, Eq. 32 is adapted by introducing additional coefficients as shown in Eq. 35:

$$k_c = 0.2 \frac{E_c}{Ø_s} \eta_\theta \cdot \eta_\delta \cdot \eta_c \cdot \eta_{cast} \cdot \eta_{fc} \cdot \eta_{bond} \cdot \eta_{cyc} \tag{35}$$

where η_c accounts for the presence of a free surface near to the bar; η_{cast} accounts for presence of pores and cracks due to the bleeding and settlement of fresh concrete (Monney et al. [225], Moccia et al. ([224]); η_{fc} accounts for the concrete strength; η_{bond} accounts for the presence of local cracks induced by bond activated by a longitudinal component of the crack opening and η_{cyc} accounts for cyclic loading. Each of these factors is calibrated based on various test results (all the details are presented in following subsections).

7.2.4 Influence of the casting conditions, concrete cover and direction of the dowel force

It is well known from other researches (see for instance Moccia et al. [224]) that fresh concrete behaves just after casting in a similar manner as a saturated soil with resulting settlements and bleeding (migration of mixing water toward the top part of the concrete element). These phenomena can cause settlement cracks near to the top reinforcement bars as well as voids (due to settlement) and pores (once the bleeding water is evaporated) under the bars as shown in Fig. 69a. These cracks, voids and pores have typically a detrimental effect on the bond behaviour of reinforcing bars located in the top parts of the concrete element (so-called top-bar effect, or poor casting conditions, see for instance Moccia et al. [120]) which is accounted for in most codes of practice in calculating the anchorage and laps lengths. With respect to the dowel action, this effect has not been investigated yet, but some results of tests carried out to investigate the bond and other problems can be used to estimate the bearing stiffness to be used in the Winkler's formulation. Figure 4b shows the 8 cases which need to be distinguished and the covers c_x and c_y which can have an influence on the behaviour. Since in actual structures, different cases occur at the two sides of a crack (namely A with D, B with C, E with H and F with G), the bearing stiffness on both sides of the crack can be different. This effect is treated in Subsection 7.2.9 below.

For the cases A, B, E and F, the results of the tests conducted by Monney et al. ([225], Fig. 70) can be used to calibrate the coefficients η_c and η_{cast} . In these tests, a reinforcing bar was pressed into concrete prisms in a similar manner as the tests of series CP described in Section 6. The cover c_x (Fig. 70c) was varied from $c_x / Ø_s = 0$ to 3 and two bar diameters were used ($Ø_s$ = 14 mm and 20 mm). In a series, the reinforcing bar was supported on the lateral formworks during casting and the specimen was tested in the same direction (poor casting conditions). In a second series, the reinforcing bar was placed on the bottom formwork during casting and tested upside-down (good casting conditions). Figure 70a shows the uniform pressure under the bar ($\sigma_{c,avg}$, averaged across the bar's width and length) normalized by the uniaxial concrete strength f_c as a function of the bar's penetration δ in the concrete normalized with the bar diameter $Ø_s$. The blue and red curves

correspond to good and poor casting conditions, respectively, while different shades represent various cover-to-bar diameter ratios $c_x / Ø_s$. As expected, the stiffness is smaller for poor casting conditions than for good conditions.

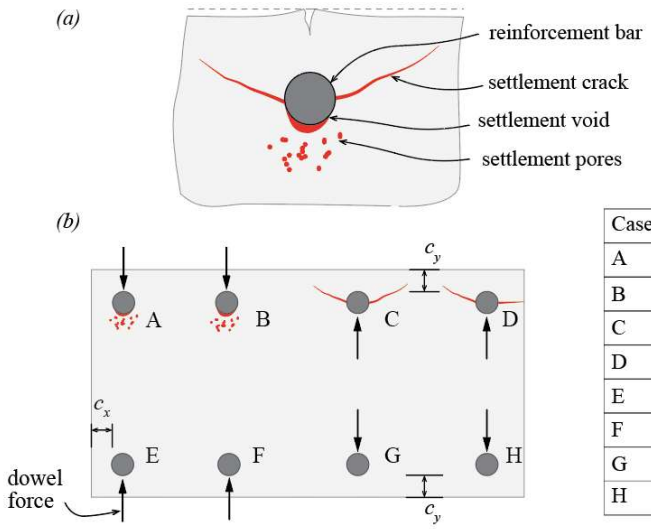

Case	η_{cast}	η_c
A	0.45	Eq. 38
B	0.45	1.0
C	0.45	Eq. 39
D	–	–
E	1.0	Eq. 37
F	1.0	1.0
G	1.0	Eq. 39
H	1.0	–

Fig. 69 *(a) Consequences of settlement and bleeding of fresh concrete around top bars (adapted from Moccia et al. [224]); and (b) investigated cases and proposed coefficients η_c (influence of cover) and η_{cast} (influence of casting condition).*

Figure 70b shows the initial slope of the stress-bar penetration curves, as a function of the cover-to-diameter $c_x / Ø_s$ ratio. The results, which can be associated to bearing stiffness k_c, are normalized by the values for good casting conditions and large cover c_x, so that they can be associated to the product $\eta_c \cdot \eta_{cast}$. The results show that the normalized stiffness increases with the $c_x / Ø_s$ ratio, gradually reaching its maximum value for approximately $c_x / Ø_s = 3$. One can observe a similar increasing trend for both casting conditions and bar diameters, but the reduction for thin covers is larger for poor bond conditions than for good ones. Based on these results, empirical expressions for coefficients η_c (influence of cover) and η_{cast} (influence of casting condition) are proposed (Fig. 70b, dashed curves):

$$\eta_{cast} = 1.0 \quad \text{for good and} \quad \eta_{cast} = 0.45 \quad \text{for poor casting conditions} \tag{36}$$

$$\eta_c = 1 - \frac{0.2}{1 + \left(c_x / Ø_s\right)^2} \quad \text{for good casting conditions} \tag{37}$$

$$\eta_c = 1 - \frac{0.45}{1 + \left(c_x / Ø_s\right)^2} \quad \text{for poor casting conditions} \tag{38}$$

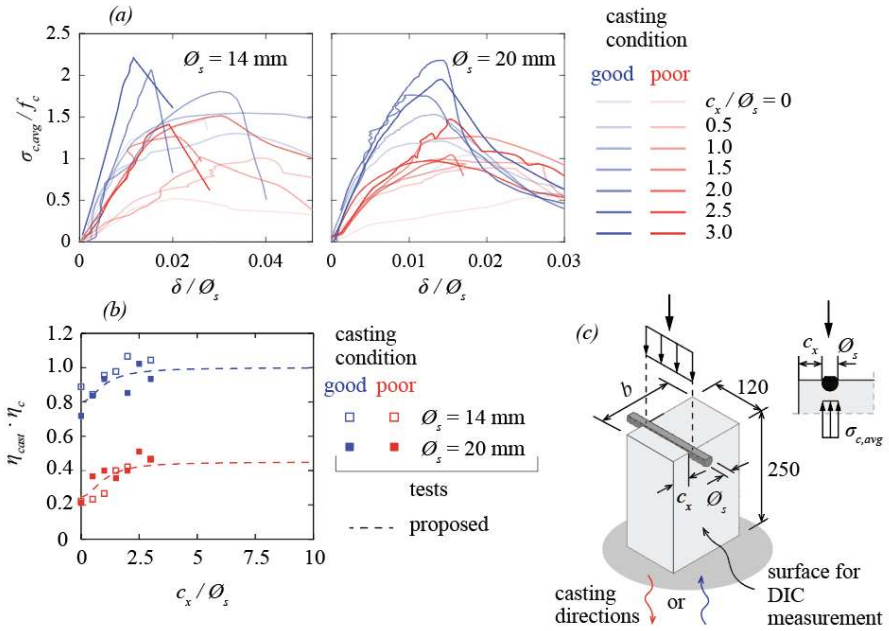

Fig. 70 *(a) Normalized average stress under a bar as a function of the bar penetration-to-diameter ratio; (b) coefficients η_c (influence of cover) and η_{cast} (influence of casting condition) for cases A, B, E and F in Figure 69b; and (c) specimen (adapted from [225]).*

The tests conducted by Moccia et al. ([120], Fig. 71) can be used to investigate the influence of the cast conditions and the cover for the cases C and G shown in Figure 69b (dowel force pushing perpendicularly against a free surface). The cases of corner bars D and H are not considered due to the lack of experimental evidence. In these tests by Moccia et al., a pressure was applied in cylindrical openings (diameter 20 mm) located at various distances c_y from the free surface (ratios $c_y / \varnothing_s$ ranging from 0.25 to 2.5). Casting with the opening on top of the formwork was associated with poor conditions, while casting with the opening at the bottom corresponded to good conditions.

Figures 71a,b show the internal pressure p in the opening as a function of the displacement δ measured on the free concrete surface for both poor and good casting conditions. The shades correspond to various $c_y / \varnothing_s$ ratios. The initial slope of the curves (bearing stiffness k_c) shown in Fig. 71c is normalized by the value for good casting conditions and relatively large cover, so that it represents in fact the product $\eta_c \cdot \eta_{cast}$. Based on these results, the same coefficient η_{cast} as for the other cases can be used (namely 1.0 and 0.45 for good and poor casting conditions, respectively), whereas for coefficient η_c, the following empirical expression can be proposed (Fig 71c, dashed curves):

$$\eta_c = \frac{1}{1+\left(c_y/\varnothing_s\right)^{-2}} \tag{39}$$

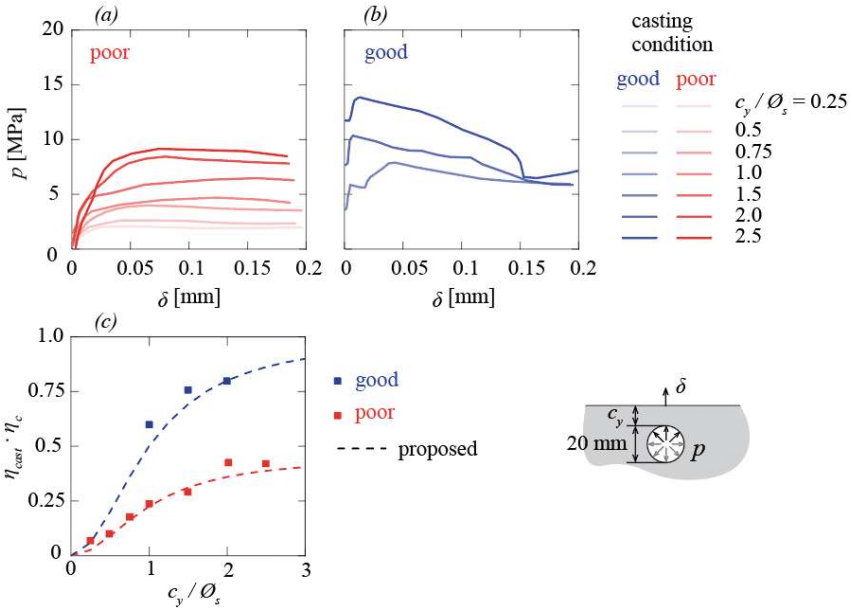

Fig. 71 *(a) Internal pressure as a function of the cover-to-diameter ratio c_y / $Ø_s$ from tests conducted by Moccia et al. [120] for poor and (b) good casting conditions; and (c) coefficients η_c (influence of cover) and η_{cast} (influence of casting condition) for cases C and G in Figure 69b.*

7.2.5 Influence of the concrete strength

The influence of the concrete strength should be theoretically accounted for with its elastic modulus which, if not measured on specific tests, can be derived from the concrete strength using the relationships defined in codes of practice. In this work, the comparisons are conducted with an average value of:

$$E_c = 10'000 f_c^{1/3} \tag{40}$$

Nevertheless, the expressions proposed by Soroushian et al. [203] and Brenna et al. [222] described in subsection 7.2.2 which were fitted on their tests provide larger values of the bearing stiffness for higher strength concrete (see comparison in Figure 72). This is also confirmed by the results of the tests by Monney et al. [225] described above (two series with concrete strengths of about 34 and 76 MPa have been conducted). In Figure 72, the bearing stiffness by Monney et al. corrected with the coefficients η_c and η_{cast} defined above are compared with the analytical solutions by Soroushian et al. [203] and Brenna et al. [222]. The results by Monney et al. lie between the two analytical solutions, so that the following expression for the correction factor η_{fc} to account for the influence of the concrete strength can be proposed:

$$\eta_{fc} = \left(\frac{f_c}{30} \right)^{2/5} \tag{41}$$

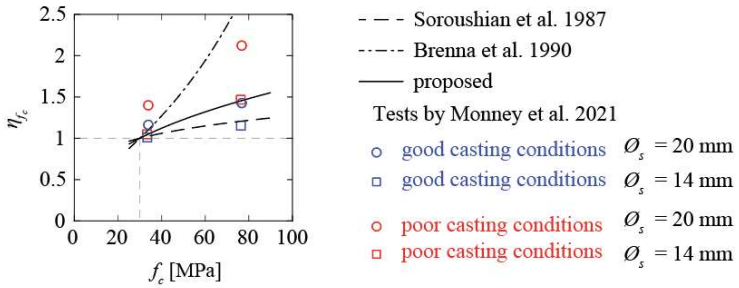

Fig. 72 *Concrete stiffness as a function of the concrete strength, tests by Monney et al. [225] compared to the analytical solutions by Soroushian et al. [203] and Brenna et al. [222] (normalized to provide identical results for f_c = 30 MPa, analytical solution by Brenna et al. shown for initial stiffness with $\delta_\perp$ = 0).*

It has to be noted that this expression is based on a small number of tests and a phenomenological explanation is still missing. For this reason, this effect deserves to be investigated more in detail in the future.

7.2.6 Interaction with bond

From a phenomenological point of view, the development of secondary cracks near to the ribs of reinforcing bars due to bond (Figure 73a, see also Goto [101]), can reduce the bearing stiffness related to the dowel action. To investigate this effect, a cyclic test reported in Section 6 ($\varnothing_s$ = 14 mm and θ = 90°) has been repeated using plain bars. Figure 73b shows the maximum and minimum shear force $V_{dow,\,min/max}$ as a function of the corresponding transverse displacement $\delta_\perp$ for constant V_{dow} / N cycle groups for approximately constant crack opening components parallel to the bar ($\delta_\parallel \approx$ 0.08 mm and 0.1 mm). One can observe that the response of the ribbed bar (red markers) is slightly less stiff than for smooth bar (blue markers). Based on this comparison, the following coefficient η_{bond} to reduce the bearing stiffness in Winkler's model to account for the interaction with bond can be proposed:

$$\eta_{bond} = \left(\frac{1}{1+\delta_\parallel / 0.2} \right)^{\frac{1}{6}} \tag{42}$$

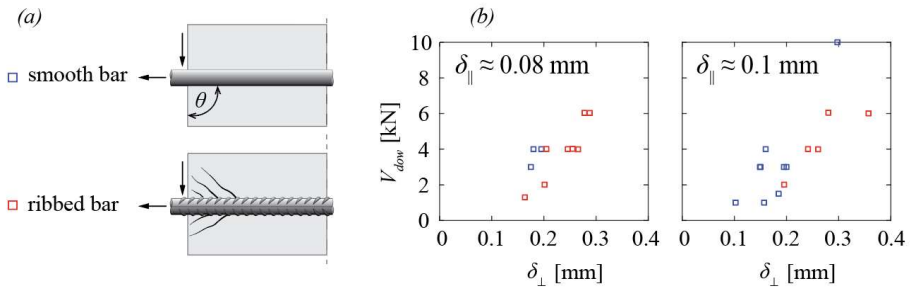

Fig. 73 *(a) Presence of secondary cracks due to bond around ribs in reinforcing bars compared to plain bars and (b) shear force as a function of the transverse displacement $\delta_\perp$ for constant $\delta_\parallel$ in cyclic tests ($\varnothing_s$ = 14 mm and θ = 90°, see also Section 6).*

Here again, this coefficient is fitted on a too small number of tests, so that an additional investigation in the future is needed to enhance this relationship.

7.2.7 Influence of the number of cycles

In case of cyclic loading, a stiffness degradation in the dowel response can also be observed as a function of the number of cycles and the amplitude of cyclic loads. Since the cyclic tests described in Section 6 have been conducted with a relatively small number of cycles, the dowel tests conducted by Li et al. [217] ($Ø_s$ = 12, 20 and 25 mm and θ = 90°) are analysed to investigate this effect. Figure 74a shows the dowel force as a function of the half a transverse displacement $\delta_\perp$ for two identical specimens, one tested under the monotonic load and the other under cyclic loading (colours correspond to the response after the various numbers of cycles N). In all considered tests, the minimum and maximum cyclic load was 0.5% and 55% of the dowel resistance measured under the monotonic load, respectively. One can observe an increase of the transverse displacement and the considerable stiffness degradation with an increasing number of cycles N. Figure 74b shows the secant stiffness of the dowel response after the N^{th} cycle normalized to stiffness at first cycle with the exponent of 4/3 according to Eq. 23, which represents in fact the coefficient η_{cyc}. The results show the larger stiffness degradation for smaller bar diameters. Based on these results, the following coefficient η_{cyc} to account for the number of cycles can be proposed:

$$\eta_{cyc} = 1 - \log N^{\frac{Ø_s}{200}} \tag{43}$$

where N is the number of cycles and $Ø_s$ is the bar diameter.

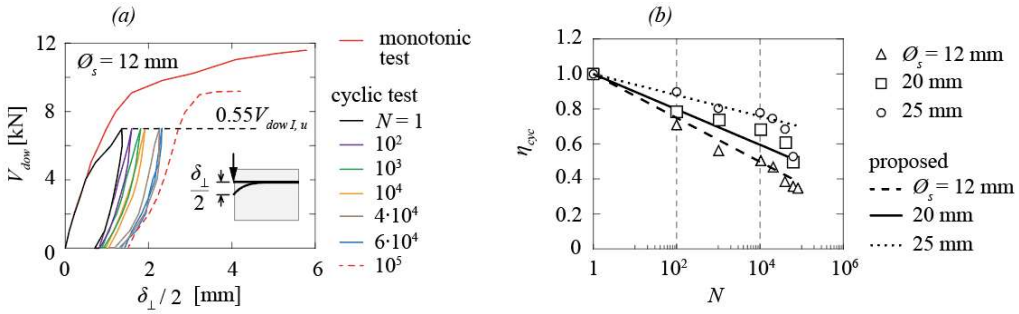

Fig. 74 *(a) Monotonic and corresponding cyclic dowel test after different numbers of cycles N (adapted from Li et al. [217]) and (b) proposed coefficient η_{cyc} as a function of the number of cycles (the abscissa is in a logarithmic scale).*

It must be noted that this expression is based on a small number of tests, so that an additional investigation in the future is needed, including the larger range of cyclic conditions.

7.2.8 Validation of the enhanced expression for the bearing stiffness k_c

In Fig. 75, the proposed bearing stiffness k_c according to Eq. 35 is compared with the stiffness derived using Winkler's model calculated to fit with the experimental V_{dow} - $\delta_\perp$ curves (brown solid line). The results, normalized by the ratio $Ø_s$ / E_c, are shown for the DP tests presented in Section 6 and other tests from the literature as a function of the transverse displacement $\delta_\perp$. The considered tests had various geometrical and material properties (bar diameter, angles θ, etc.). One can observe a good agreement between the fitted curves from the experimental data and the proposed prediction for the depicted range of the transverse displacement $\delta_\perp$. For a comparison, the predictions by Brenna et al. [222] and Soltani et al.[215] are also shown.

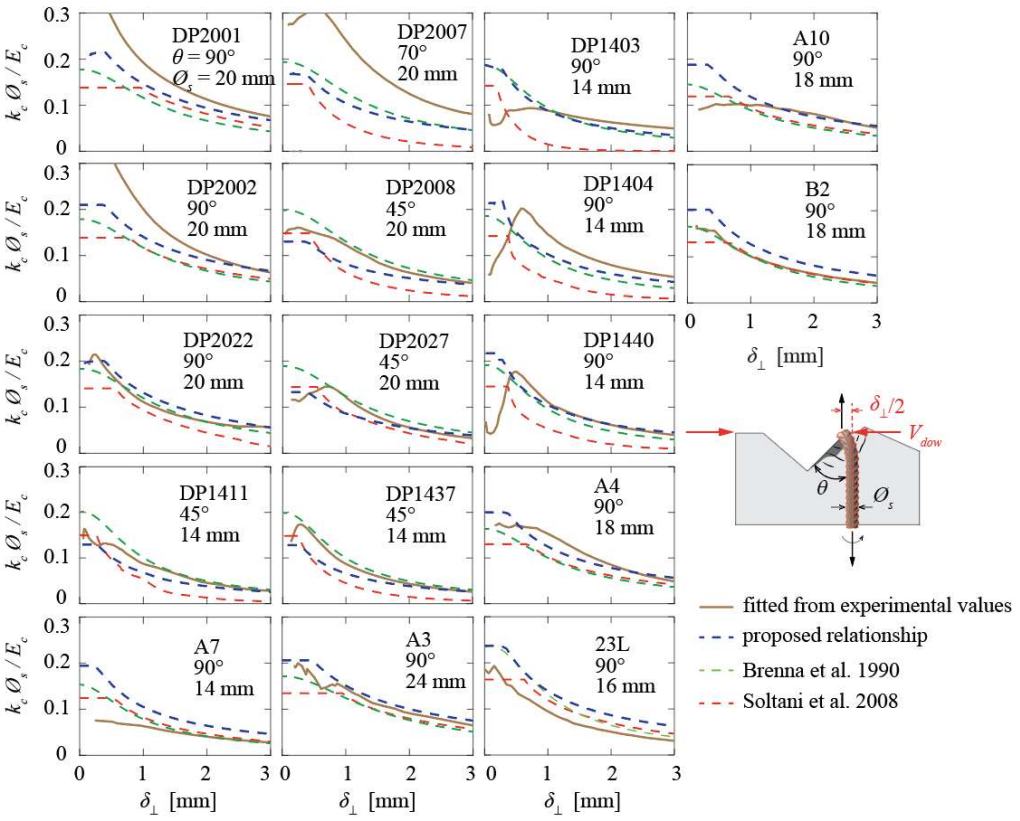

***Fig. 75** Comparison between the predicted and the experimental bearing stiffness (fitted from the experimental V_{dow} - $\delta_\perp$ curves).*

Figure 76 shows for the same tests the experimental curves (V_{dow} - $\delta_\perp$) and the curves according to various models. The first yielding of the reinforcing bar, measured by optical fibres, is identified with a red solid marker. One can observe a good agreement between the test results and the prediction according to Eq. 35 for all tests.

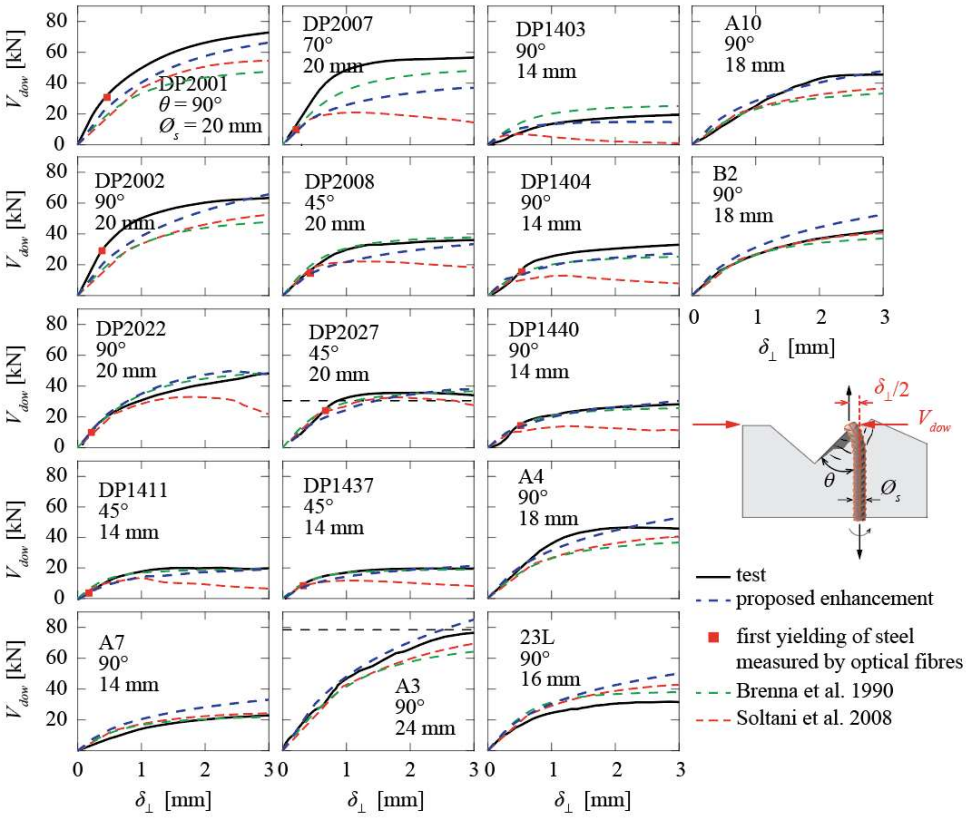

Fig. 76 *Comparison between experimental and predicted V_{dow} - $\delta_{\perp}$ curves.*

Figure 77 compares the model's prediction with the proposed stiffness to the optical fibre measurements for test DP2027: the normalized axial stress due to bending (Fig. 77d, assuming elastic behaviour), the normalized curvature (Fig. 77d), the rotation (Fig. 77d) and the deformed shape of the reinforcing bar (Fig. 77d). The results are shown for five different load levels including the dowel resistance $V_{dow\,l,u}$. The enhanced model shows a good agreement with the presented measurements for all considered parameters.

Figures 77g,h show the comparison between the predicted and measured distance between the crack and the most stressed cross-section in the bar x_{max} as a function of the angle θ and the bar diameter $\varnothing_s$. Again, one can observe a good correspondence between the model and the test results.

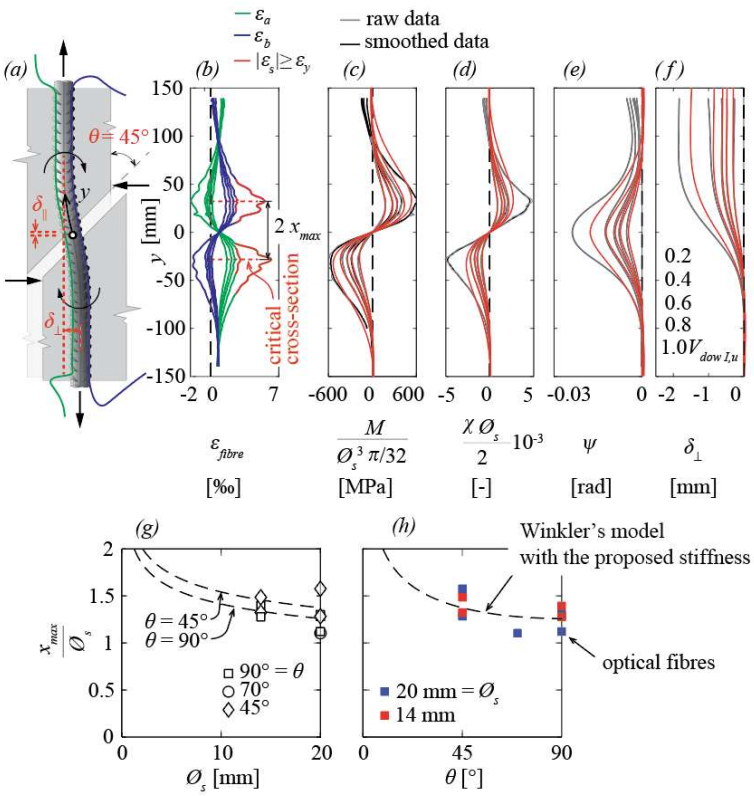

Fig. 77 *Comparison between the optical fibre measurements and the prediction by Winkler's model with the proposed concrete stiffness: (a) bar deformation and parameter definitions; (b) measured strains; (c) normalized moment (stress assuming an elastic behaviour; red line indicates the prediction); (d) normalized curvature; (e) bar rotation; (f) transverse displacement; (g) distance between the crack and the critical cross-section as a function of the bar diameter and (h) as a function of angle between the crack and the bar ((a)-(f): test DP2027 with* $Ø_s$ *= 20 mm and* θ *= 45°, see Section 6).*

In a similar manner, the enhanced model is also validated against a representative cyclic test in Fig.78. Here again, the model provides accurate estimates of the behaviour.

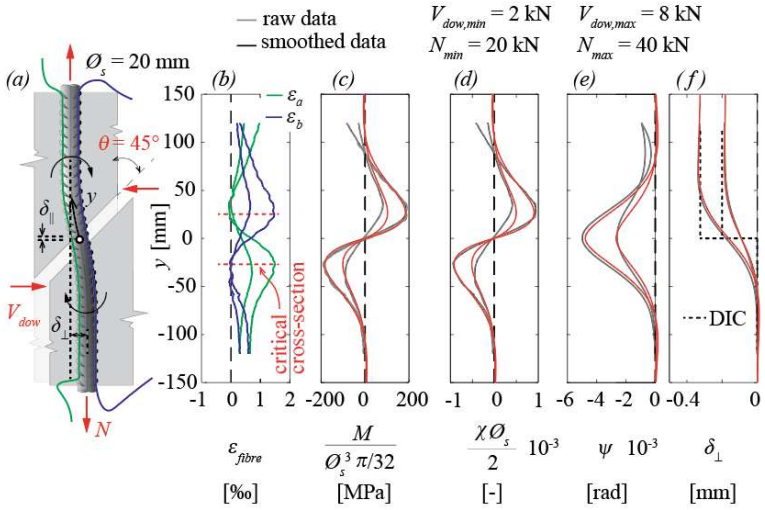

Fig. 78 *Comparison between the enhanced model and the optical fibre measurements: (a) bar deformation and parameter definitions; (b) measured strains; (c-f) derived parameters (specimen* $DP2027_{cyc}$*).*

Figure 79 compares the predicted peak longitudinal stress $\sigma_{s,flex}$ at the critical cross-section to the fibre measurements normalized with the yield strength f_y. The results are presented for all monotonic tests at five load levels including the dowel resistance $V_{dow\,I,u}$ (with a step of $0.2V_{dow\,I,u}$) and for the cyclic tests for the minimum and maximum load levels within a constant V_{dow} / N cycle combination. One can observe a good agreement between the prediction and the measurements with an average of the measured-to-predicted stress ratio of 0.95 and a coefficient of variation CoV =12.8% for the considered tests.

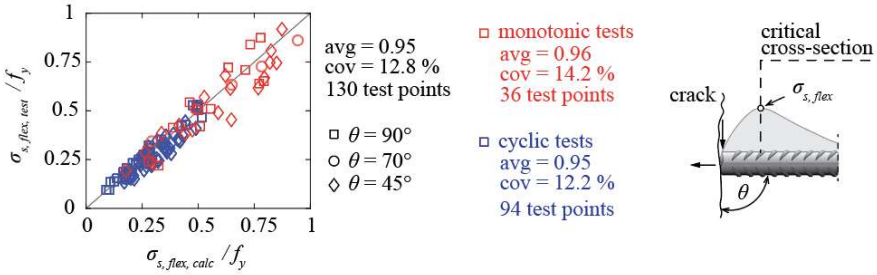

***Fig. 79** Comparison between the predicted and measured peak longitudinal stress $\sigma_{s,flex}$ at the critical cross-section (red markers represent monotonic tests and blue markers cyclic tests).*

7.2.9 Different bearing stiffness on opposite sides of the crack

It has been shown in Subsection 7.2.4 that the presence of a free surface near to the bar and the direction of the dowel force with respect to the free surface can affect the bearing stiffness and thus the dowel behaviour. As described above, since in actual structures, different cases occur at the two sides of a crack (namely A with D; B with C; E with H; and F with G), the bearing stiffness on both sides of the crack can be different. Such an example is shown in Fig. 80a, where the bearing stiffness is expected to be smaller on the side where the bar pushes against the concrete cover (the case G in Fig. 69b) compared to the opposite side where the bar pushes away from the cover (the case F in Fig. 69b). This asymmetry in the bearing stiffness results in different dowel behaviours on opposite crack sides, leading to different distributions of the bending moment and the corresponding stress $\sigma_{s,flex}$ along the bar (Fig. 80a,b).

To predict the dowel behaviour in this case, Winkler's model can be adapted considering two different bearing stiffnesses $\bar{k}_c$ and k_c on either crack side, where $\bar{k}_c \le k_c$, to be used in the parameters $\bar{\beta} = \sqrt[4]{\frac{\bar{k}_c \varnothing_s}{4E_s I_s}}$ and $\beta = \sqrt[4]{\frac{k_c \varnothing_s}{4E_s I_s}}$, respectively. The ratio between the two parameters is defined as $\tilde{\beta} = \frac{\bar{\beta}}{\beta}$. In this case, the transverse displacement at the crack interface of the bar with the larger bearing stiffness of concrete (Fig. 80a) can be calculated as $\delta_\perp \tilde{\beta} / \left(1+\tilde{\beta}\right)$, where $\delta_\perp$ is transverse component of the relative displacement of the two crack lips. The distance between the crack and the position of the maximum bending moment along the bar which occurs at the side with the largest bearing stiffness (Fig. 80a) can be calculated as:

$$x_{\max} = \frac{\arctan \tilde{\beta}}{\beta} \tag{44}$$

The maximum bending moment along the bar can thus be calculated as:

$$M_{\max} = -2E_s I_s \beta^2 \delta_\perp e^{-\arctan \tilde{\beta}} \frac{\tilde{\beta}^2}{1+\tilde{\beta}} \frac{1}{\sqrt{1+\tilde{\beta}^2}} \tag{45}$$

Consequently, the maximum elastic stress in the bar (Fig. 80b) becomes:

$$\sigma_{s,flex} = \frac{32 M_{\max}}{\varnothing_s^3 \pi} \tag{46}$$

For the same bearing stiffness on both sides of the crack ($\tilde{\beta} = 1$), this solution becomes symmetric, as previously presented.

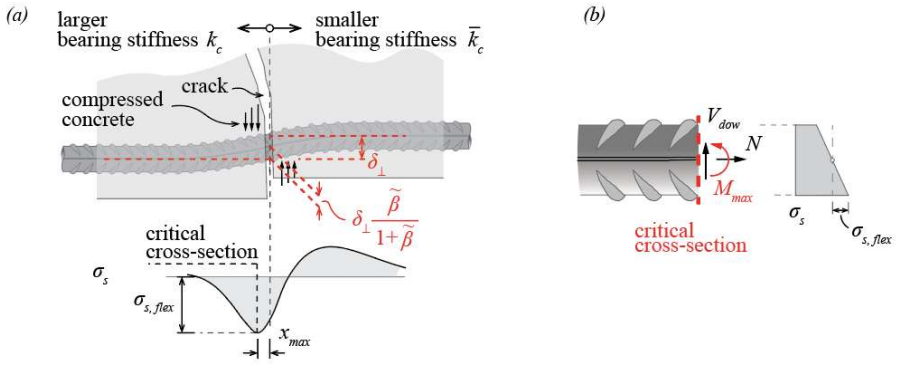

Fig. 80 *(a) Asymmetric dowel behaviour due to the different bearing stiffness on the opposite sides of the crack and (b) stress $\sigma_{s,flex}$ at the critical cross-section.*

7.3 Shear resistance of dowels

The first-order dowel resistance $V_{dow\,I,u}$ can be predicted using the model proposed by Rasmussen [185] which was derived on the basis of the limit analysis approach (plastic behaviour of the dowel bar, with a bending resistance $M_p = f_y \varnothing_s^3 / 6$, and a uniformly distributed contact pressure between concrete and bar. The expression for the case where the point of contraflexure in the bar is at the concrete edge (crack) is given by:

$$V_{dow\,I,u} = \varnothing_s^2 \sqrt{\frac{\eta_3 f_c f_y}{3}} \tag{47}$$

where η_3 is a coefficient accounting for the concrete strength increase due to the triaxial stress state in concrete under the dowel (calibration parameter according to the Rasmussen's approach) and f_y is the yield strength of the bar. Figure 81 shows the comparison between the model's predictions and a database of 121 dowel tests with $\theta = 90°$. For tests where the point of contraflexure in the bar does not correspond to the concrete edge, Equation (47) is adapted according to the original model by Rasmussen [185]. Three values of the coefficient η_3 are used for this comparison. The first value (Fig. 81a), $\eta_3 = 5.1$ as proposed by Rasmussen based on his tests, provides slightly unconservative results (average value of the measured-to-predicted resistance ratio of 0.91) and a relatively large scatter (CoV = 19.9%). In Fig. 81b, the comparison is conducted assuming $\eta_3 = 3.0$ (in accordance with Tanaka et al. [192]). In this case, the coefficient of variation is reduced to 16.8% and the average value of the measured-to-predicted resistance ratio is 1.14. Assuming $\eta_3 = 4.0$ as observed in the CP test series of this work (see Fig. 63b), the statistical values become CoV = 18.1% and avg = 1.0 (see Fig.81c for comparison). It must be noted that this model was originally developed for bars perpendicular to cracks (or concrete edges, $\theta = 90°$) and without applied axial force.

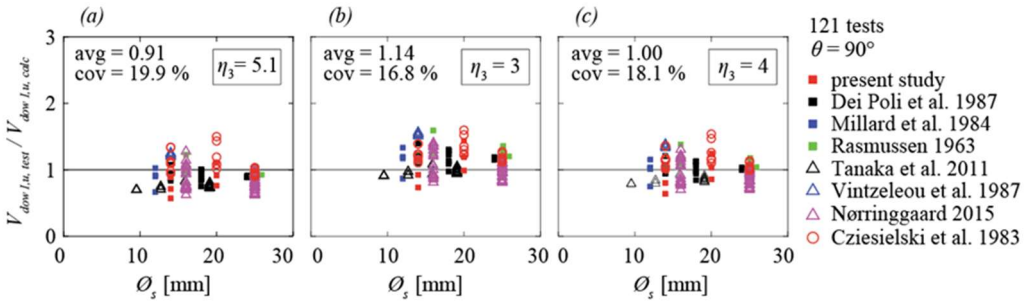

Fig. 81 *Comparison of Rasmussen's model with the considered database of dowel tests with θ = 90°.*

For other crack angles ($\theta < 90°$), the first-order dowel resistance $V_{dow\,I,u}$ can be predicted using the expression proposed by Dulacska [187]:

$$V_{dowI,u} = \varnothing_s^{\,2} k_N k_{cal} f_y \eta_3 \cos\theta \left(\sqrt{1 + \frac{f_{c,cube}}{3 k_N k_{cal}^2 f_y \eta_3 \cos^2\theta}} - 1 \right) \qquad (48)$$

where $k_N = 1 - (N / N_p)^2$ is a parameter which accounts for the axial force in the bar (with N being the axial force and N_p being the axial resistance), $k_{cal} = 0.05$ is a calibration coefficient proposed by Dulacska based on their tests, $\eta_3 = 4$ and $f_{c,cube}$ is the concrete strength measured on 150 mm cubes. Figure 82 shows the comparison between the predictions and 21 dowel tests with $\theta < 90°$. The expression provides fairly good results, with an underestimation of resistances for tests with relatively large axial forces in the bar (few tests from the present study). The average value of the measured-to-predicted resistance ratio is 1.09 and the coefficient of variation is 21.3%.

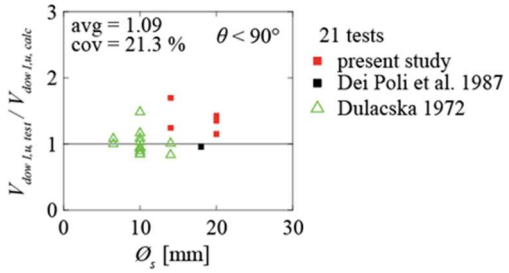

Fig. 82 *Comparison of Dulacska's model [187] with the considered dowel tests with θ < 90°.*

The plastic dowel response including the activation of the catenary action can be predicted by the model proposed by Sørensen et al.[188] which is also based on the limit analysis approach. Figure 83a shows a comparison of this model with the experimental responses of the present study. The model's prediction is accompanied by an envelope accounting for the various test variables. Its lower and upper boundaries account for the prediction considering the bar's yield and tensile strength, respectively. Figure 83b shows the main parameters of the model. For the concrete confinement coefficient, $\eta_3 = 4.0$ is assumed. The model's prediction shows a relatively good agreement with the final catenary load stages. It is important to note that also this model was developed for the bars perpendicular to cracks or concrete faces.

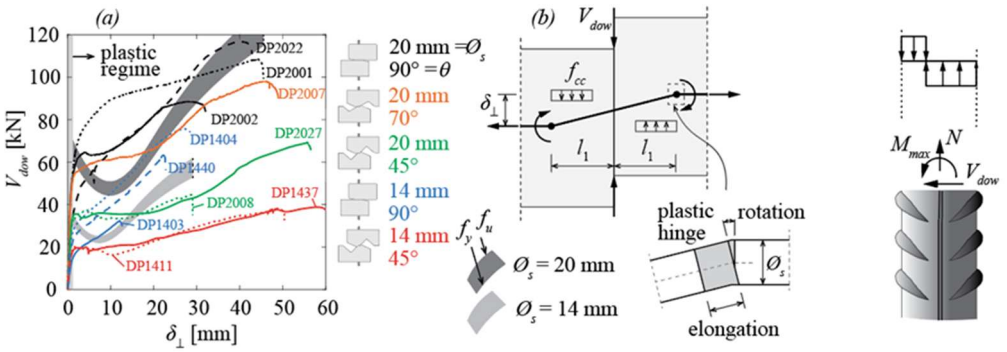

Fig. 83 *(a) Comparison of the model proposed by Sørensen et al. [188] with the performed dowel tests and (b) model's hypotheses.*

Previous comparisons show that existing models correctly predict the capacity of reinforcing bars to carry shear forces related to dowel action. With respect to the influence of a free surface near to the doweled bar, due to the less ductile behaviour related to spalling of the concrete cover before yielding of the reinforcing bar, Rasmussen's model cannot be applied.

7.4 Conclusions

This section presents a new formulation for the bearing stiffness of concrete under the reinforcing bar to be used in Winkler's model as well as a comparison of the dowel resistance according to Rasmussen's model with available tests. The formulation for the bearing stiffness accounts for various effects and it is calibrated based on mechanical considerations and optical fibres measurements. The main conclusions are:

1. The new formulation for the bearing stiffness of concrete in Winkler's model is enhanced to account for various effects: angle between the reinforcing bar and the crack, concrete strength, casting conditions, concrete cover and reduction of the stiffness due to a large number of cycles, as well as due to secondary cracks caused by the axial force.
2. The bearing stiffness under a ribbed bar in case of an imposed crack opening was observed to be slightly smaller than under a smooth. This difference is probably due to the secondary cracks which develop near to ribs due to bond generated by the imposed crack opening.
3. Similar to bond (top bar effect), casting conditions have an influence on the bearing stiffness. Compared to good casting conditions, in case of poor casting conditions, the bearing stiffness is reduced more than 50%, leading to smaller steel stresses due to local bending activated for the same transverse imposed displacement.
4. In case of bars near to a free surface, the bearing stiffness increases with the cover-to-bar diameter ratio $c / \varnothing_s$. The stiffness reaches its maximum value for approximately $c / \varnothing_s = 3$.
5. The enhanced bearing stiffness formulation to be used in Winkler's model shows a good prediction compared to tests with respect to shear force-transverse displacement response (V_{dow} - $\delta_\perp$) and the peak longitudinal stress $\sigma_{s,flex}$ due to bending measured in the monotonic and low-stress cyclic tests presented in Section 6.
6. Rasmussen's and Dulacska's model provide reasonably accurate predictions of the dowel resistance for the angles between the bar and the crack $\theta = 90°$ and $\theta < 90°$, respectively.

7.5 Outlook and future works

Several questions regarding the dowel modelling for fatigue and ultimate limit state still remain open. In the following, some aspects that should be further studied are outlined:

- The impact of secondary cracks resulting from axial forces in ribbed bars on the bearing stiffness of concrete requires deeper investigation. For this purpose, an experimental campaign should be performed encompassing both smooth and ribbed bars of varying diameters, subject to different imposed crack openings.
- The influence of cyclic loading on the bearing stiffness needs to be further investigated. To that aim, an experimental campaign should be conducted including cyclic conditions in the range of service loads with a large number of cycles. Various material and geometrical properties could be considered.
- The influence of the concrete strength on the bearing stiffness needs to be further corroborated with additional tests. These tests could include concrete prisms with various concrete strengths in which short rebars are pressed to reproduce the dowel behaviour as well as dowel tests.
- Winkler's assumption of the uniform bearing stiffness along the bar could be explored. By considering a non-uniform stiffness distribution, solving the beam equation might yield results that capture the local behaviour of the concrete near the crack.
- The influence of the casting conditions and the concrete cover on the bearing stiffness and on the dowel resistance need to be investigated more in detail and the case with corner reinforcing bars deserved to be investigated experimentally.

8 Steel stress calculation, general conclusion

In the previous sections, the forces and stresses in the reinforcement bars induced by a crack opening and sliding were investigated. The effects of the crack displacement components parallel ($\delta_{\parallel}$) and perpendicular to the bar axis ($\delta_{\perp}$) were investigated separately, due to the complexity of each phenomenon.

Firstly, the relationship between the crack displacement component parallel to the bar axis ($\delta_{\parallel}$) and the axial force (N) in the bar was investigated in Sections 4 and 5. The results show that the uniform longitudinal stress in the bar due to the axial force ($\sigma_{s,tens}$) at the crack location can be estimated using Eq. 14 with an average bond stress estimated using Eq. 20. The experimental results have also shown that bond is deteriorated mostly in the region within approximately one bar diameter from the crack location. This leads to axial stress distributions with smooth peaks as schematically shown in Fig. 84b. Consequently, the axial force remains fairly constant in the crack region.

Secondly, the relationship between the crack displacement component perpendicular to the bar ($\delta_{\perp}$) and the bending moment (M) was investigated in Sections 6 and 7. The results have shown that Winkler's model (beam on elastic foundation) is suitable to describe the behaviour of the bar due to dowel action. This model can be used to estimate the distribution of bending moment in the bar, including the maximum bending moment (M_{max}) and its distance from the crack (x_{max}), as shown in Fig. 84c. The position of the maximum bending moment corresponds to the critical cross-section and its distance from the crack can be determined using Eq. 44. This cross-section is typically located at around 1 to 1.5Ø from the crack. The additional stress ($\sigma_{s,flex}$) caused by the maximum bending moment can be estimated using Eq. 46.

Based on these observations, it is justified to estimate the total stress variations in the bar at the critical cross-section due to dowel action, assuming that the stress due to the axial force corresponds to the values at the crack location. Due to the low bond stress activation near the crack (caused by the secondary cracks), this approach does not result in an excessive overestimation. Furthermore, this would provide a somewhat conservative estimation of the stress variation due to the measured crack kinematics.

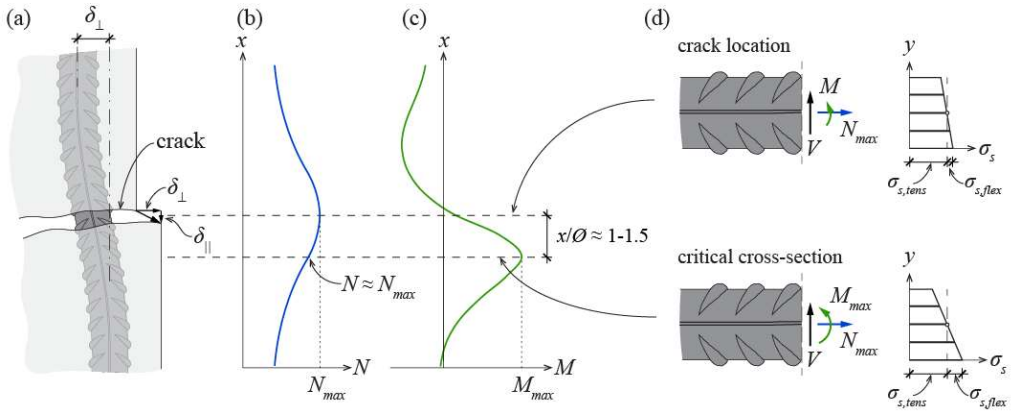

Fig. 84 *Forces and stresses in the bar due to the crack opening: (a) definition of the crack opening components; (b) axial force N in the bar; (c) bending moment M in the bar; and longitudinal stress distribution in the cross-section (d) at the crack location and (e) at the critical cross-section.*

An example of application of the proposed model is described in the following paragraphs. Assuming the following geometrical and mechanical properties are obtained from an inspection:

- Bar diameter $\emptyset$ = 20 mm
- Clear cover c = 40 mm
- Concrete compressive strength f_{cm} = 30 MPa
- Good casting conditions (from the position within the section)

The measured characteristics of the crack are:

- Initial crack displacement in the direction of the bar $\delta_{\parallel}$ = 0.2 mm
- Initial crack displacement in the direction perpendicular to the bar $\delta_{\perp}$ = 0 mm
- Crack displacement variations due to traffic loads $\Delta\delta_{\parallel}$ = 0.05 mm and $\Delta\delta_{\perp}$ = 0.03 mm
- Crack spacing s_{cr} = 200 mm
- Angle between the crack and the bar θ = 90°
- No longitudinal cracks along the bar observed w_{lc} = 0 mm

Other reasonable assumptions for relevant parameters are:

- Bar elastic modulus E_s = 200 GPa
- Shrinkage strain ε_{cs} = 0‰
- Bond index f_R = 0.08 and number of lugs n_l = 2
- Number of cycles 1

Other mechanical parameters can be estimated based on code formulations

- Concrete elastic modulus E_c = 31072 MPa
- Effective reinforcement ratio ρ_t = 1%

The initial stress can be estimated using the aforementioned approach:

$$\tau_{bu,po} = 0.5 f_{cm}\left(\frac{30}{f_{cm}}\right)^{1/6}\left(\frac{20}{\emptyset}\right)^{1/8} = 0.5\cdot 30\cdot 1\cdot 1 = 15 \text{ MPa}$$

$$\delta_{sc1,po} = 1.0\cdot\frac{\emptyset}{20}\cdot\left(\frac{30}{f_{cm}}\right)^{1/3}\left(\frac{0.08}{f_R}\right)^{1/5} = 1\cdot 1\cdot 1\cdot 1 = 1 \text{ mm}$$

$$\tau_{b,avg} = \eta_2\cdot k_{sr}\cdot k_{lc}\cdot k_{cyc}\cdot\tau_{bu,po}\frac{1-\alpha}{1+\alpha}\left(\frac{\delta_{\parallel,0}}{2\cdot\delta_{sc1,po}}\right)^{\alpha} = 1\cdot 1.3\cdot 1\cdot 1\cdot 15\cdot\frac{1-0.4}{1+0.4}\left(\frac{0.2}{2\cdot 1}\right)^{0.4} = 3{,}33 \text{ MPa} \quad (49)$$

$$\sigma_{s,tens0} = \frac{\delta_{\parallel}}{s_{cr}}E_s + \frac{s_{cr}\tau_{b,avg}}{\emptyset}\frac{1+(n-1)\rho}{1-\rho} + E_s\varepsilon_{cs} = \frac{0.2}{200}200000 + \frac{200\cdot 3.33}{20}\frac{1+(6.44-1)0.01}{1-0.01} = 235 \text{ MPa}$$

$$\sigma_{s,flex0} = 0 \text{ MPa}$$

The stress variation due to the crack displacement in the direction of the bar measured under traffic ($\Delta\delta_{\parallel}$) can be estimated analogously. In this case, the assumption of N = 1 might be overconservative.

$$\Delta\sigma_{s,tens} = \frac{0.05}{200}200000 + \frac{200\cdot 3.33}{20}\frac{1+(6.44-1)0.01}{1-0.01} = 85 \text{ MPa} \quad (50)$$

A more realistic estimation could probably be obtained assuming the effect of cyclic loading. For example, for a bridge that has been in service for 50 years and assuming a traffic of 250 trucks per day, the crack would have been subjected to around N = 4.46 million cycles. Using the cyclic factor defined in Eq. 15 would be k_{cyc} = 0.47. The stress variation would be:

$$\tau_{b,avg} = 3.33\cdot 0.47 = 1.56$$

$$\Delta\sigma_{s,tens} = \frac{0.05}{200}200000 + \frac{200\cdot 1.56}{20}\frac{1+(6.44-1)0.01}{1-0.01} = 66 \text{ MPa} \quad (51)$$

The variation of the maximum bending moment due to the measured crack displacement in the direction perpendicular to the bar due to the traffic load ($\Delta\delta_\perp$) can be estimated using the aforementioned approach:

$$\begin{aligned}
\overline{k}_c &= 0.2\ \frac{E_c}{\varnothing_s}\eta_\theta \cdot \eta_\delta \cdot \eta_c \cdot \eta_{cast} \cdot \eta_{fc} \cdot \eta_{bond} \cdot \eta_{cyc} = 0.2 \cdot \frac{31072}{20} \cdot 1 \cdot 1 \cdot 0.8 \cdot 1 \cdot 1 \cdot 0.87 \cdot 1 = 217\ \frac{\text{MPa}}{\text{mm}} \\
k_c &= 0.2 \cdot \frac{31072}{20} \cdot 1 \cdot 1 \cdot 1 \cdot 1 \cdot 1 \cdot 0.87 \cdot 1 = 271\ \frac{\text{MPa}}{\text{mm}} \\
\overline{\beta} &= \sqrt[4]{\frac{\overline{k}_c \varnothing_s}{4E_s I_s}} = \sqrt[4]{\frac{217 \cdot 20}{4 \cdot 200000 \cdot 7854}} = 0.0288\ \frac{1}{\text{mm}} \\
\beta &= \sqrt[4]{\frac{k_c \varnothing_s}{4E_s I_s}} = \sqrt[4]{\frac{271 \cdot 20}{4 \cdot 200000 \cdot 7854}} = 0.0305\ \frac{1}{\text{mm}} \\
\tilde{\beta} &= \frac{\overline{\beta}}{\beta} = 0.95 \\
\Delta M_{\max} &= -2E_s I_s \beta^2 \delta_\perp e^{-\arctan\tilde{\beta}} \frac{\tilde{\beta}^2}{1+\tilde{\beta}} \frac{1}{\sqrt{1+\tilde{\beta}^2}} = 13717\ \text{Nmm}
\end{aligned} \tag{52}$$

Consequently, the corresponding maximum stress variation in the bar and its distance from the crack can be calculated as:

$$\begin{aligned}
\Delta\sigma_{s,flex} &= \frac{32M_{\max}}{\pi \cdot \varnothing_s^3} = \frac{32 \cdot 13717}{\pi \cdot 20^3} = 17\ \text{MPa} \\
x_{\max} &= \frac{\arctan\tilde{\beta}}{\beta} = \frac{\arctan(0.95)}{0.0305} = 24.9\ \text{mm} \rightarrow \frac{x_{\max}}{\varnothing_s} = 1.24
\end{aligned} \tag{53}$$

Appendixes

I In-plane alignment of the marker coordinates

Given a group of coplanar points P_n with coordinates [x_n y_n z_n], the best fitting plane and the correspondent planar coordinates can be calculated using the following steps.

1. The normal vector of the plane is computed:

$$A = \begin{bmatrix} x_1 & y_1 & 1 \\ \vdots & \vdots & \vdots \\ x_n & y_1 & 1 \end{bmatrix} \tag{54}$$

$$\underline{n} = -\left(A^T A\right)^{-1} A^T \begin{bmatrix} z_1 \\ \vdots \\ z_n \end{bmatrix} \tag{55}$$

2. The relative angles between the normal vector and a vertical vector are computed:

$$\begin{bmatrix} \theta_x \\ \theta_y \\ 0 \end{bmatrix} = \arctan\left(\frac{\underline{n} \times [0 \quad 0 \quad 1]^T}{\underline{n} \cdot [0 \quad 0 \quad 1]^T} \right) \tag{56}$$

3. The rotation matrix which transforms the plane to a horizontal position is determined:

$$Q = \begin{bmatrix} 1 & 0 & 0 \\ 0 & \cos\theta_x & -\sin\theta_x \\ 0 & \sin\theta_x & \cos\theta_x \end{bmatrix} \begin{bmatrix} \cos\theta_y & 0 & \sin\theta_y \\ 0 & 1 & 0 \\ -\sin\theta_y & 0 & \cos\theta_y \end{bmatrix} \tag{57}$$

4. The marker coordinates can be rotated to a best-fit horizontal plane as follows.

$$\begin{bmatrix} x'_n \\ y'_n \\ z'_n \end{bmatrix} = Q \begin{bmatrix} x_n \\ y_n \\ z_n \end{bmatrix} \tag{58}$$

II Calculation of crack kinematics using the marker-based technique

II.1 Best-fit uniform dilation

This subsection provides the steps required to calculate the best-fit scaling matrix and translation to transform the makers in the reference position ($A_{n,ref}$ with coordinates $\underline{a}_{n,ref}$ and $B_{m,ref}$ with coordinates $\underline{b}_{m,ref}$) to their deformed position ($A_{n,def}$ with coordinates $\underline{a}_{n,def}$ and $B_{m,def}$ with coordinates $\underline{b}_{m,def}$). The crack points in the reference position C_l have coordinates $\underline{c}_{l,ref}$.

1. The mean distance d_1 between the centroid of a given group of markers and each of the given markers is used as an indicator of the relative change of temperature between reference and deformed states. Eq. 59 is used to obtain $d_{1,ref}$ and $d_{1,def}$.

$$d_1 = \frac{1}{2n}\sum_{i=1}^{n}\left\|\left(\frac{1}{n}\sum_{i=1}^{n}\underline{a}_i\right)-\underline{a}_i\right\| + \frac{1}{2m}\sum_{i=1}^{m}\left\|\left(\frac{1}{m}\sum_{i=1}^{m}\underline{b}_i\right)-\underline{b}_i\right\| \tag{59}$$

2. The scaling matrix is determined by:

$$S = \begin{bmatrix} d_{1,def}/d_{1,ref} & 0 \\ 0 & d_{1,def}/d_{1,ref} \end{bmatrix} \tag{60}$$

3. The translation vector $\underline{t}_S$ necessary to perform the scaling operation around the centroid of the crack points $\overline{c}_{l,ref}$ is:

$$\underline{t}_s = \frac{1}{l}\sum_{i=1}^{l}\underline{c}_{i,ref} - S\cdot\frac{1}{l}\sum_{i=1}^{l}\underline{c}_{i,ref} \tag{61}$$

4. The scaled coordinates of the markers in the reference state are:

$$\begin{aligned} \underline{a}^s_{n,ref} &= \underline{S}\cdot\underline{a}_{n,ref} + \underline{t}_S \\ \underline{b}^s_{m,ref} &= \underline{S}\cdot\underline{b}_{m,ref} + \underline{t}_S \end{aligned} \tag{62}$$

II.2 Best-fit in-plane rigid body motion

This appendix presents the steps to compute the rotation matrix R and the translation vector $\underline{t}$ to transform a group of markers with coordinates ($\underline{e}_1$, …, $\underline{e}_n$) into a group of markers with coordinates ($\underline{f}_1$, …, $\underline{f}_n$). The equations are adapted from the solution of Sorkine-Hornung [227]. The equations for this type of calculations were presented by [147] for use with the DEMEC and adapted by Gehri et al. [41] for use with DIC measurements.

1. The centroid of both groups of markers is computed.

$$\begin{aligned} \overline{e} &= \frac{1}{n}\sum_{i=1}^{n}\underline{e}_i \\ \overline{f} &= \frac{1}{n}\sum_{i=1}^{n}\underline{f}_i \end{aligned} \tag{63}$$

2. The coordinates of the markers relative to the centroid are computed.

$$\begin{aligned} \underline{e}_{i,rel} &= \underline{e}_i - \overline{e} \\ \underline{f}_{i,rel} &= \underline{f}_i - \overline{f} \end{aligned} \tag{64}$$

3. The covariance matrix is computed.

$$M = \left[\underline{e}_{1,rel} \cdots \underline{e}_{n,rel}\right]\left[\underline{f}_{1,rel} \cdots \underline{f}_{n,rel}\right]^T \tag{65}$$

4. The singular value decomposition is computed.

$$M = U\Sigma V^T \tag{66}$$

5. The rotation matrix is obtained as follows.

$$R = V\begin{bmatrix} 1 & 0 \\ 0 & \det\left(VU^T\right) \end{bmatrix}U^T \tag{67}$$

6. The translation vector necessary to superimpose the centroids of both groups is:

$$\underline{t} = \overline{f} - R\frac{1}{n}\sum_{i=1}^{n}\underline{e}_i \tag{68}$$

II.3 Crack displacement

The crack lip displacements can be calculated following the next steps:

1. The deformed position of the crack points is computed by first applying the scaling operation (S, $\underline{t}_s$) which describes the effect of temperature and then the relative displacement of the crack lips (R, $\underline{t}$) to the coordinates of the crack points $\underline{c}_{l,ref}$:

$$\underline{c}_{i,def} = R\left(S\underline{c}_{i,ref} + \underline{t}_s\right) + \underline{t} \tag{69}$$

2. The translation between $\underline{c}_{l,ref}$ and the obtained coordinates $\underline{c}_{l,def}$ is the crack displacement:

$$\underline{\delta}_i = \underline{c}_{i,def} - \underline{c}_{i,ref} \tag{70}$$

III Zero Displacement and Zero Strain Tests

III.1 Zero Displacement Test

The Zero Displacement Test (ZDT) is used to characterise the noise. Between 50 and 100 images of a set of markers should be captured without any applied displacement in between images. For a group of *I* markers, the plane coordinates of a given marker *i* for the *n* images are called ($\underline{m}_{i,1}$, …, $\underline{m}_{i,n}$).

1. The coordinates relative to the average of the measurements is computed.

$$\left[\underline{dm}_{i,1} \cdots \underline{dm}_{i,n}\right] = \frac{1}{n}\sum_{j=1}^{n} m_{i,j} - \left[\underline{m}_{i,1} \cdots \underline{m}_{i,n}\right] \tag{71}$$

2. The noise is quantified by the zero displacement deviation $NV_{N,i}$.

$$NV_{N,i} = \sqrt{\frac{1}{n}\sum_{j=1}^{n} \left\|\underline{dm}_{i,j}\right\|} \tag{72}$$

A spatial distribution of $NV_{N,i}$ across the field of vision can be assessed. The total NV_N can simply be defined as the average of the $NV_{N,i}$ of all the markers.

$$NV_N = \frac{1}{I}\sum_{i=1}^{I} NV_{N,i} \tag{73}$$

III.2 Zero Strain Test

The Zero Strain Test (ZST) is used to characterise the bias. Between 50 and 100 images of a set of markers should be captured with different positions of the markers. The displacements should be of small amplitude so that the markers stay in their direct vicinity.

In each position, 10 images are averaged to reduce the noise. For a group of *I* markers, the averaged coordinates of a given marker *i* in the *p* positions are ($\underline{o}_{i,1}$, …, $\underline{o}_{i,p}$). For each position, all the markers are used to compute the best-fit rigid-body motion necessary to map them back to position 1. The procedure detailed in Appendix II can be used for this. The coordinates of marker *i* mapped to position 1 are ($\underline{o}'_{i,1}$, …, $\underline{o}'_{i,p}$).

1. The coordinates relative to the average of the measurements are computed and the zero displacement deviation $NV_{B,i}$ obtained.

$$\left[\underline{do}'_{i,1} \cdots \underline{do}'_{i,n}\right] = \frac{1}{p}\sum_{j=1}^{p} m_{i,j} - \left[\underline{o}'_{i,1} \cdots \underline{o}'_{i,p}\right] \tag{74}$$

2. The bias is quantified by the zero displacement deviation $NV_{B,i}$.

$$NV_{B,i} = \sqrt{\frac{1}{p}\sum_{j=1}^{p} \left\|\underline{do}'_{i,j}\right\|} \tag{75}$$

A spatial distribution of $NV_{N,i}$ across the field of vision can be assessed. The total NV_N can simply be defined as the average of the $NV_{N,i}$ of all the markers.

$$NV_B = \frac{1}{I}\sum_{i=1}^{I} NV_{B,i} \tag{76}$$

IV Pull-out test results

Detailed crack patterns and fibre optical measurement results for all the specimens of series PC01, PC02 and CM11.

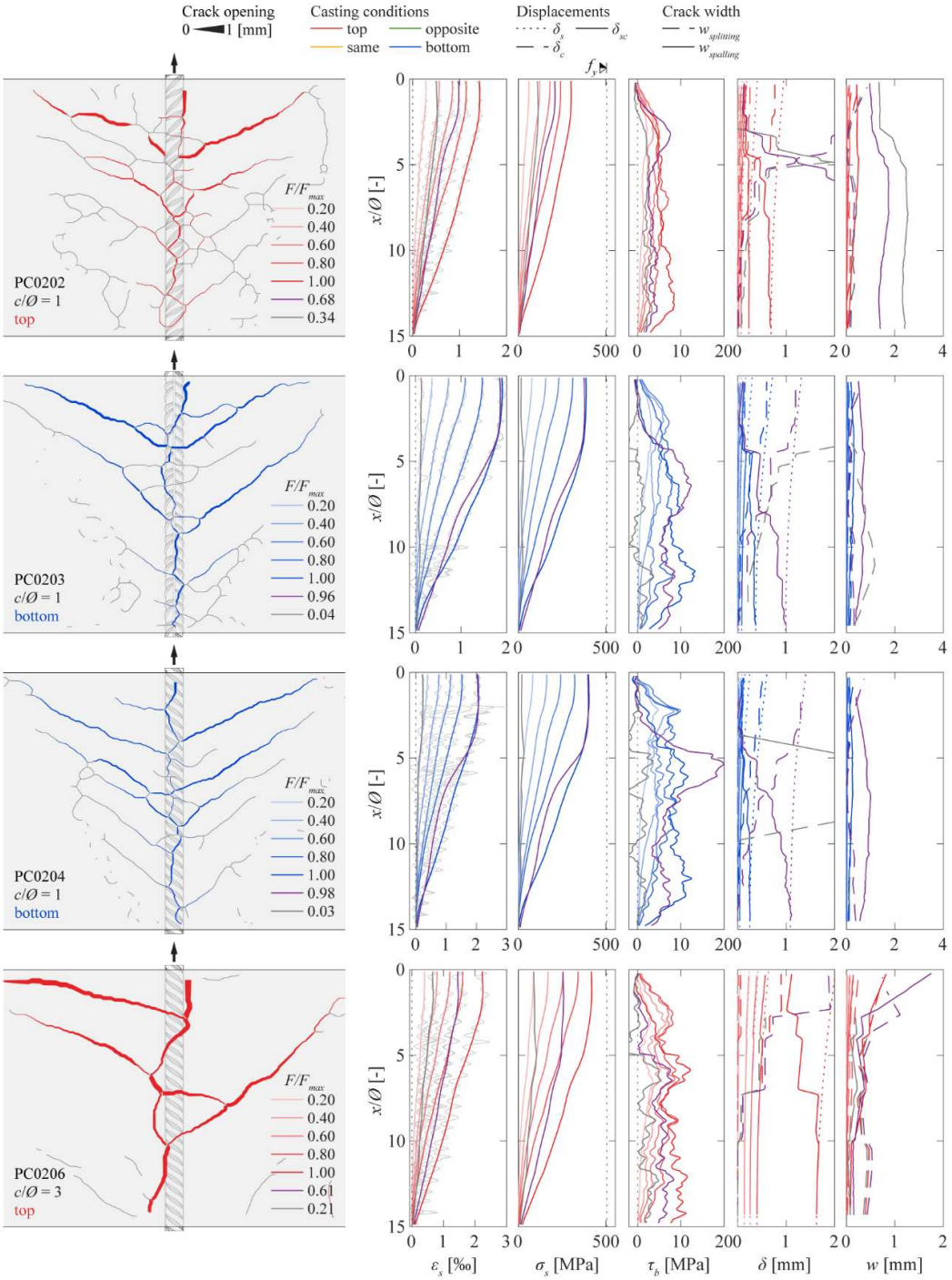

Fig. 85 *Cracking pattern and distribution along the anchorage length of axial steel strains, axial steel stresses, bond stresses, slip and crack widths for specimens: PC0202, PC0203, PC0204 and PC0206.*

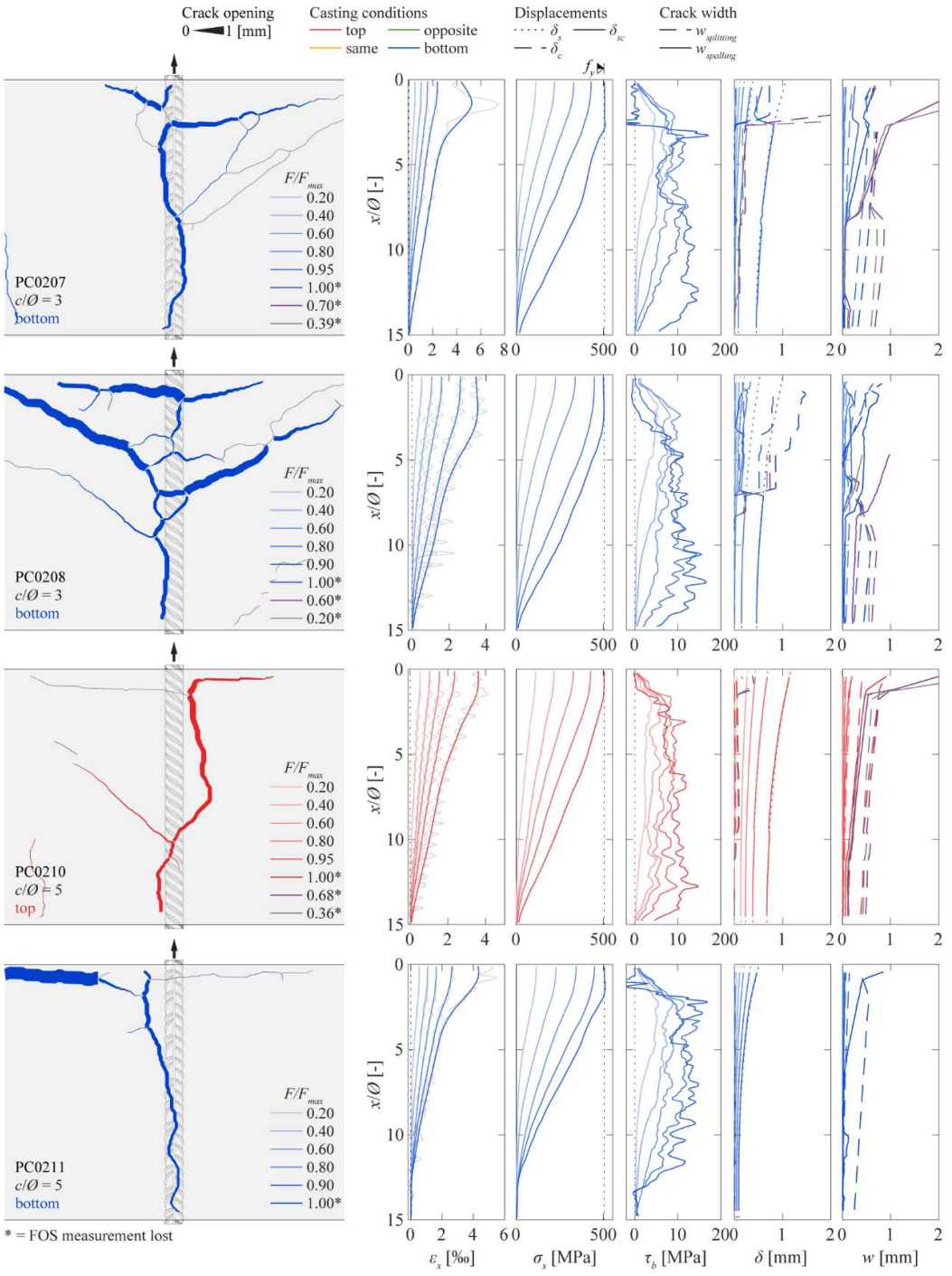

Fig. 86 *Cracking pattern and distribution along the anchorage length of axial steel strains, axial steel stresses, bond stresses, slip and crack widths for specimens: PC0207, PC0208, PC0210 and PC0211.*

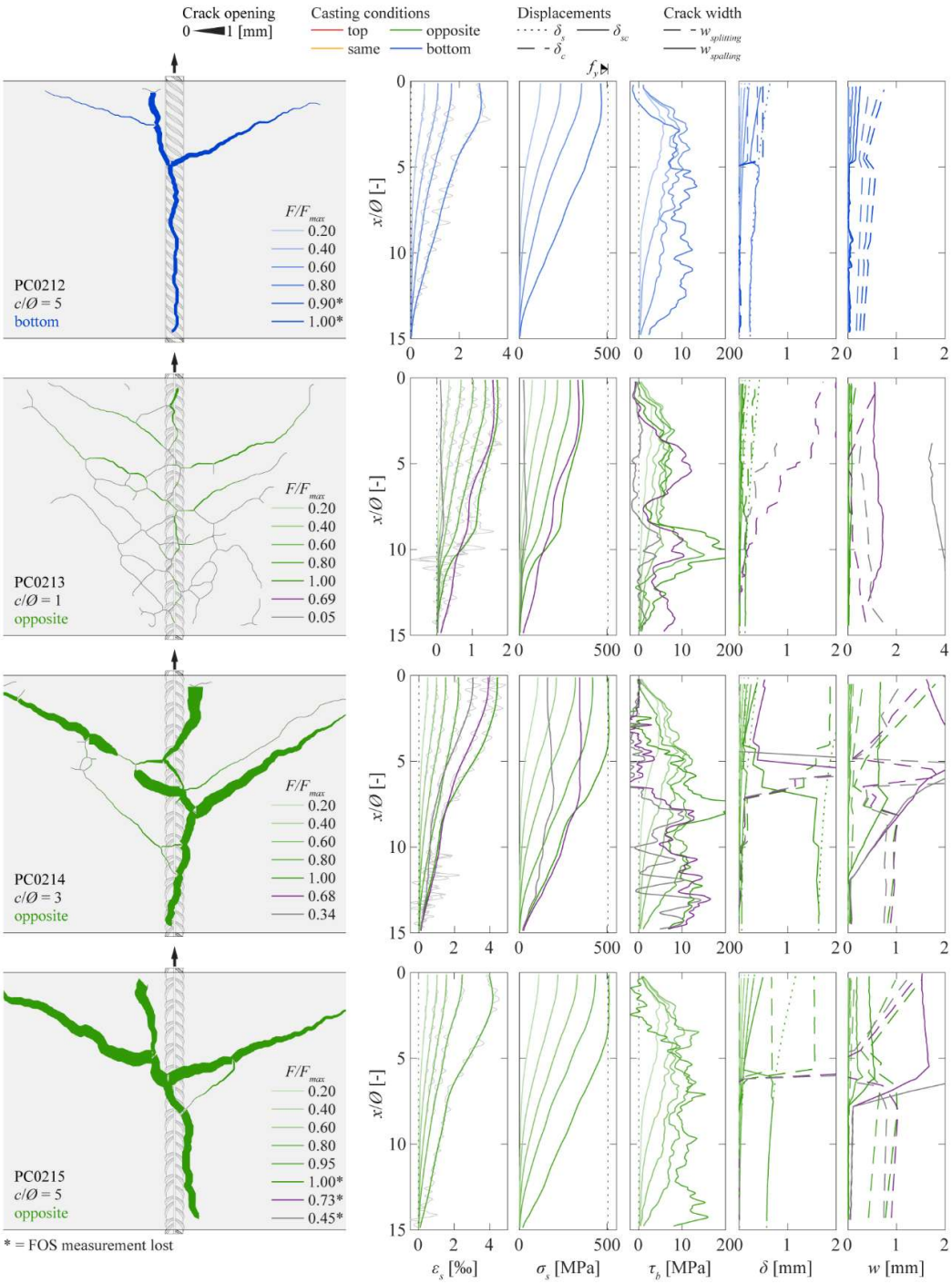

Fig. 87 *Cracking pattern and distribution along the anchorage length of axial steel strains, axial steel stresses, bond stresses, slip and crack widths for specimens: PC0212, PC0213, PC0214 and PC0215.*

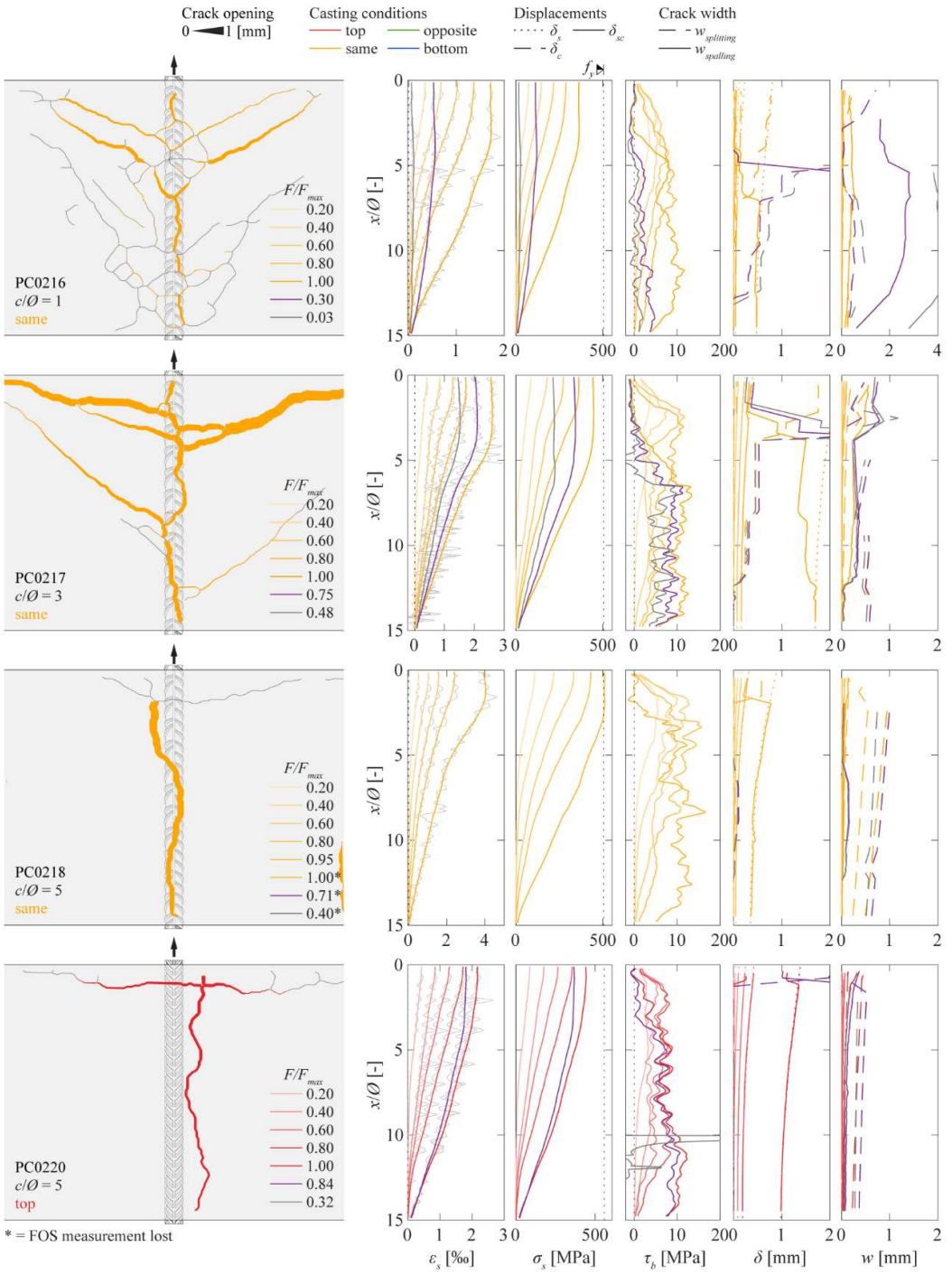

Fig. 88 *Cracking pattern and distribution along the anchorage length of axial steel strains, axial steel stresses, bond stresses, slip and crack widths for specimens: PC0216, PC0217, PC0218 and PC0220.*

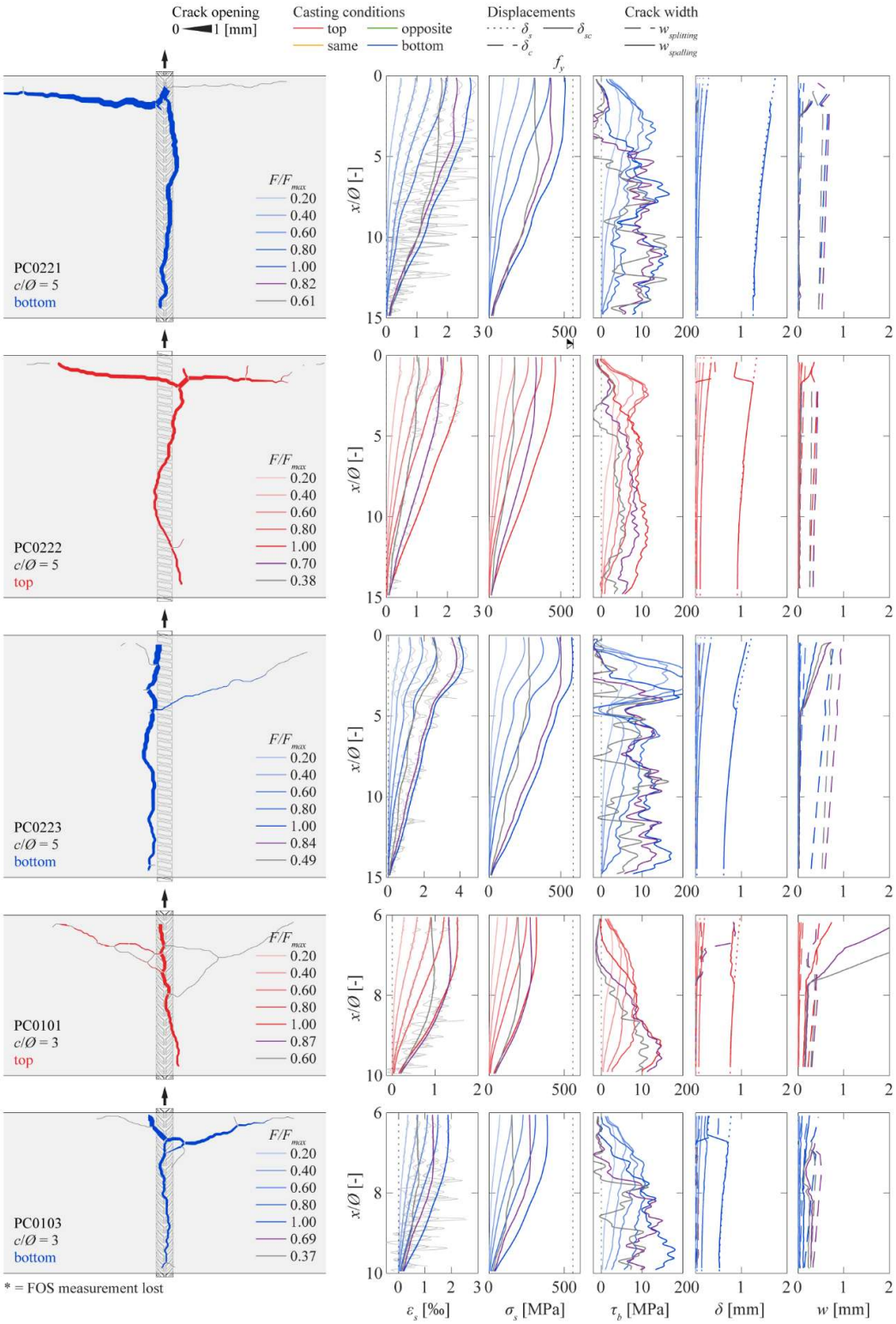

Fig. 89 *Cracking pattern and distribution along the anchorage length of axial steel strains, axial steel stresses, bond stresses, slip and crack widths for specimens: PC0221, PC0222, PC0223, PC0101 and PC0103.*

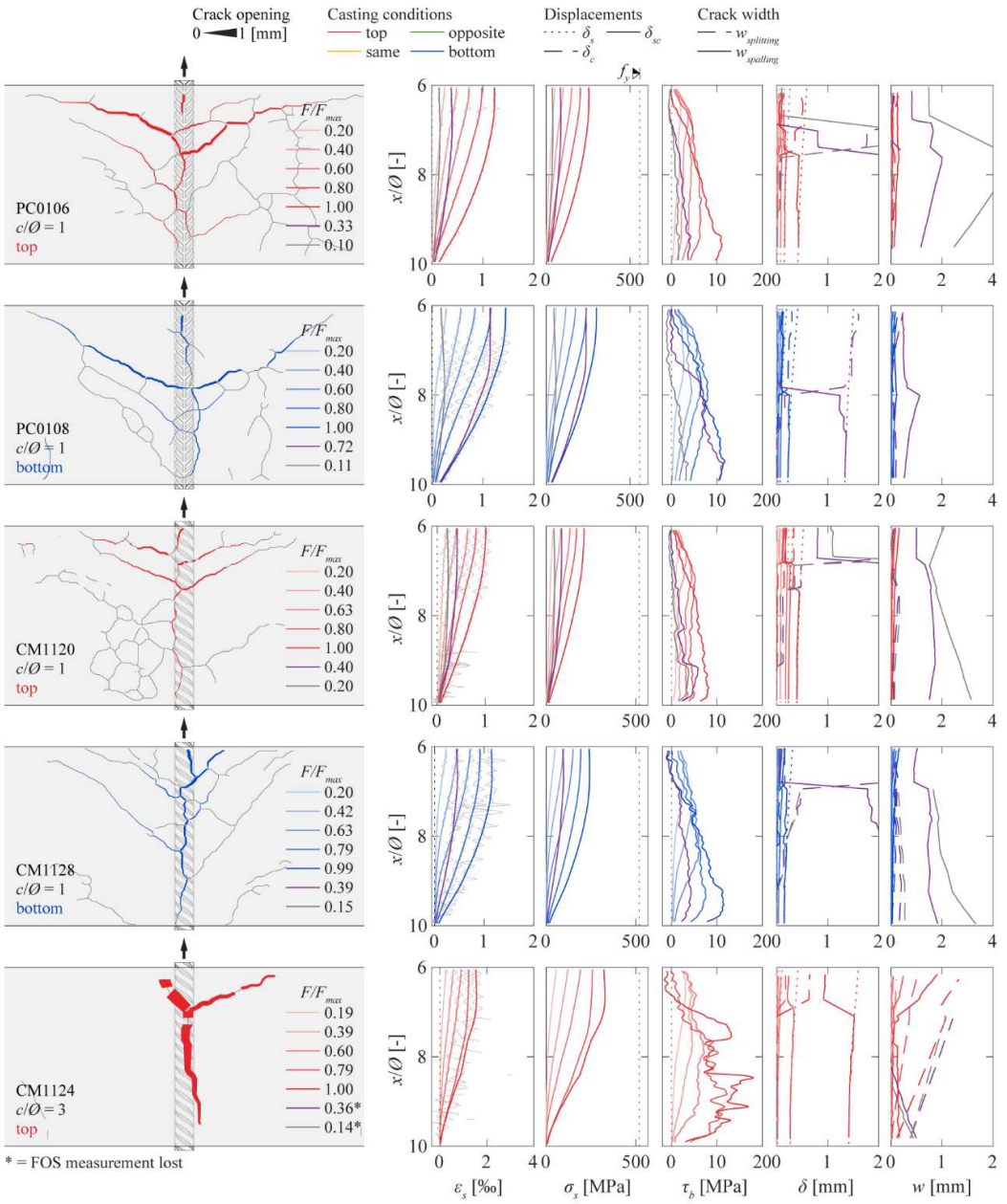

Fig. 90 *Cracking pattern and distribution along the anchorage length of axial steel strains, axial steel stresses, bond stresses, slip and crack widths for specimens: PC0106, PC0108, CM1120, CM1128 and CM1124.*

V Bar stress - crack width analytical expression development

Based on the equilibrium and compatibility conditions of the differential element shown in Fig. 31b and assuming a linear elastic behaviour of both steel and concrete and no external forces acting on the element, the differential equation governing the tie segment response is given by Eq. 77.

$$\frac{d^2\delta_{sc}}{dx^2} = \frac{4\tau_b(x)}{\emptyset E_s} + \frac{\pi \emptyset \tau_b(x)}{A_c E_c} \tag{77}$$

Assuming that the first crack appears when the concrete stress reaches f_{ct}, due to compatibility of deformations the cracking axial force is determined by Eq. 78. The stress in the reinforcement before and after cracking can be calculated using Eq. 79 and 80 at the cracked section:

$$N_{cr} = \frac{f_{ct}}{E_c}(A_c E_c + A_s E_s) \tag{78}$$

$$\sigma_{sB} = \frac{f_{ct}}{E_c} E_s = \varepsilon_{cr} E_s \tag{79}$$

$$\sigma_{sC} = \frac{f_{ct}}{\rho}[1 + (n-1)\rho] \tag{80}$$

Given the stress variation, the required transfer length l_{cr} as a function of the average bond stress $\tau_{b,avg}$ can be determined using Eq. 81:

$$l_{cr} = \frac{\emptyset}{4\tau_{b,avg}} \Delta\sigma_s = \frac{\emptyset f_{ct}}{4\tau_{b,avg}} \frac{1-\rho}{\rho} \tag{81}$$

The crack width in the crack formation stage is therefore:

$$\delta_{||} = \frac{l_{cr}\sigma_{sC}}{E_s} = \frac{\emptyset f_{ct}^2}{4\tau_b E_s} \frac{(1-\rho)(1+(n-1)\rho)}{\rho^2} \tag{82}$$

This expression can be generalized for any stress σ_{sC}, as shown in Eq. 83:

$$\delta_{||} = \frac{\emptyset \sigma_{sC}^2}{4\tau_b E_s} \frac{1-\rho}{1+(n-1)\rho} \tag{83}$$

In the stabilized cracking stage, the distance between cracks is smaller than the transfer length. Therefore, the tensile strength of the concrete cannot be reached between cracks and no further principal crack develops (secondary cracks may develop). In these conditions, the crack width for a given stress can be calculated considering that the maximum axial force that can be taken by the concrete as a function of the crack spacing and the average bond stress. The resulting equation is:

$$\delta_{||} = \frac{s_{cr}}{E_s}\left[\sigma_{sC} - \frac{s_{cr}\tau_{b,avg}}{\emptyset} \frac{1+(n-1)\rho}{1-\rho}\right] \tag{84}$$

Due to the reinforcement, the shrinkage strains ($\varepsilon_{cs} < 0$) are partially restrained, which causes tensile forces in the concrete and compression in the reinforcement. From compatibility and equilibrium conditions, the initial strain can be determined using Eq. 85:

$$\varepsilon_{ci} = \varepsilon_{si} = \frac{1-\rho}{1+(n-1)\rho}\varepsilon_{cs} \tag{85}$$

As a consequence of this initial stress-state, the cracking force is reduced:

$$N_{cr,cs} = N_{cr}\left[1+\frac{n\rho}{1+(n-1)\rho}\frac{\varepsilon_{cs}}{f_{ct}/E_c}\right] \tag{86}$$

Nevertheless, both the cumulative difference of strains remains the same because both strain diagrams are shifted by the unrestrained shrinkage strain (see Fig. 31c,d). Consequently, assuming the same bond distribution, the anchorage length and the crack width are the same for a lower stress in the reinforcement. For the stabilized cracking phase, the effect of shrinkage affects the average concrete strains as shown in Eq. 87:

$$\delta_{\|} = \frac{s_{cr}}{E_s}\left[\sigma_{sC} - \frac{s_{cr}\tau_{b,avg}}{\emptyset}\frac{1+(n-1)\rho}{1-\rho} - E_s\varepsilon_{cs}\right] \tag{87}$$

Inversely, the bar stress as a function of the crack width can be calculated using Eq. 88:

$$\sigma_{sC} = \frac{\delta_{\|}}{s_{cr}}E_s + \frac{s_{cr}\tau_{b,avg}}{\emptyset}\frac{1+(n-1)\rho}{1-\rho} + E_s\varepsilon_{cs} \tag{88}$$

VI Local bond-slip relationship

The bond-slip relationships for monotonic loading were investigated by the authors in a separate publication [158]. The general expression of the segments composing the curve is defined in Eq. 89 (see Fig. 41a):

$$\begin{aligned}
&\tau_b = \tau_{b,max}(\delta_{sc} / \delta_{sc,1})^{\alpha} \\
&\tau_b = \tau_{b,max} \\
&\tau_b = \tau_{bmax} - (\tau_{bmax} - \tau_{bf})(\delta_{sc} - \delta_{sc2}) / (\delta_{sc3} - \delta_{sc2}) \\
&\tau_b = \tau_{bf}(1 - (\delta_{sc} - \delta_{sc3}) / (\delta_{sc4} - \delta_{sc3}))
\end{aligned} \tag{89}$$

The factor to account for the cover and transverse reinforcement proposed in MC2010 is used for the definition of the confinement conditions [94]. This factor is limited to a value of 1.7 [99], that corresponds to the confinement when c = 5Ø. A minimum value of 1 is set, that corresponds to the confinement when c = 1Ø. The normalized factor can be determined using Eq. 90, where c_{min} and c_{max} are minimum and maximum covers (including the horizontal c_x, vertical cover c_y or half of the bar spacing c_s). The component accounting for the stirrup contribution [94] is not considered as discussed in Sections 5.4.2 and 5.5:

$$\begin{aligned}
&k_{conf} = \frac{1}{0.7}\left[\left(\frac{c_{\min}}{\varnothing}\right)^{0.33}\left(\frac{c_{\max}}{c_{\min}}\right)^{0.1} - 1\right] \quad k_{conf} \in [0,1] \\
&c_{\min} = \min(c_s / 2, c_x, c_y) \\
&c_{\max} = \min(c_s / 2, c_x, c_y)
\end{aligned} \tag{90}$$

Three confinement conditions are defined accordingly:

- Well-confined conditions: k_{conf} = 1, corresponding to covers ≥ 5Ø.
- Unconfined conditions: k_{conf} = 0, corresponding to covers ≤ 1Ø.
- Moderately confined conditions: 0 < k_{conf} < 1, intermediate situations.

The main parameters of the proposed bond-slip relationship for the three types of confinement are summarized in Tab. 12.

***Tab. 12** Bond-slip relationship definition (see Notation for the definition of the parameters)*

Parameter	Well-confined	Moderate confinement	Unconfined
τ_{bu}	$\tau_{bu,po} = 0.5 f_{cm}\left(\frac{30}{f_{cm}}\right)^{1/6}\left(\frac{20}{\varnothing}\right)^{1/8}$	$\tau_{bu,sc} = \tau_{bu,su} + (\tau_{bu,po} - \tau_{bu,su})k_{conf}$	$\tau_{bu,su} = 7.1\left(\frac{f_{cm}}{30}\right)^{0.25}\left(\frac{20}{\varnothing}\right)^{0.2}$
τ_{bf}	$0.4 \cdot \tau_{bu}$	$\tau_{bf,sc} = \tau_{bf,su} + (\tau_{bf,po} - \tau_{bf,su})k_{conf}$	0
δ_{sc1}	$1.0 \cdot \frac{\varnothing}{20} \cdot \left(\frac{30}{f_{cm}}\right)^{1/3}\left(\frac{0.08}{f_R}\right)^{1/5}$	$\delta_{sc1,sp} = \delta_{sc1,po}\left(\frac{\tau_{bu,sp}}{\tau_{bu,po}}\right)^{1/\alpha}$	$\delta_{sc1,po}\left(\frac{\tau_{bu,su}}{\tau_{bu,po}}\right)^{1/\alpha}$
δ_{sc2}	$2 \cdot \delta_{sc1}$	$\delta_{sc2,sc} = \delta_{sc2,su} + (\delta_{sc2,po} - \delta_{sc2,su})k_{conf}$	δ_{sc1}
δ_{sc3}	c_{clear}	$\delta_{sc3,sc} = \delta_{sc3,su} + (\delta_{sc3,po} - \delta_{sc3,su})k_{conf}$	$1.2 \cdot \delta_{sc1}$
δ_{sc4}	$2 \cdot c_{clear}$	$\delta_{sc4,sc} = \delta_{sc4,su} + (\delta_{sc4,po} - \delta_{sc4,su})k_{conf}$	$1.2 \cdot \delta_{sc1}$
α	0.4	0.4	0.4

VII Failure pattern of DP test series

The monotonic dowel tests which experienced the rupture of the reinforcing bar allowed observing the concrete spalling patterns. They are shown in Fig. 91 in a crack plan view in terms of normalized coordinates.

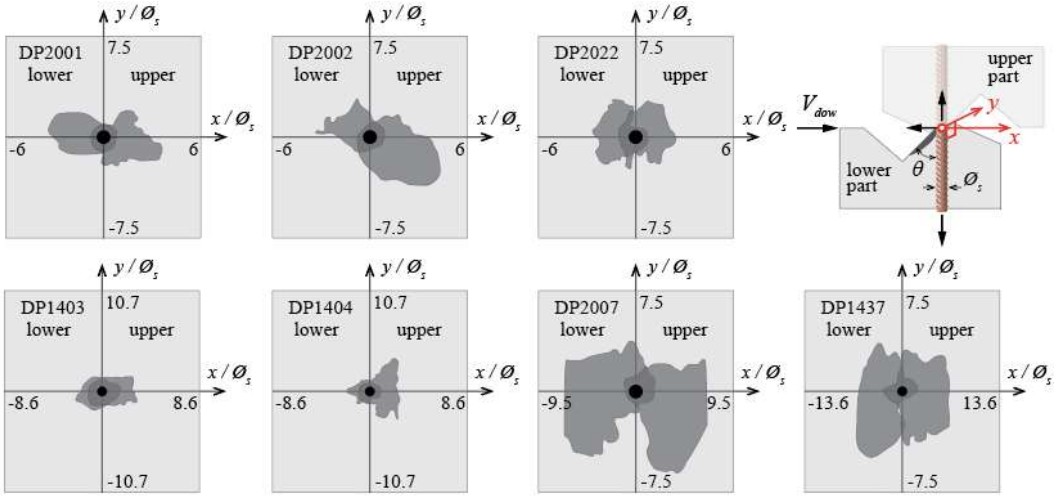

Fig. 91 *Concrete spalling patterns of monotonic dowel tests after catenary rupture.*

VIII Optical fibre measurements of DP series

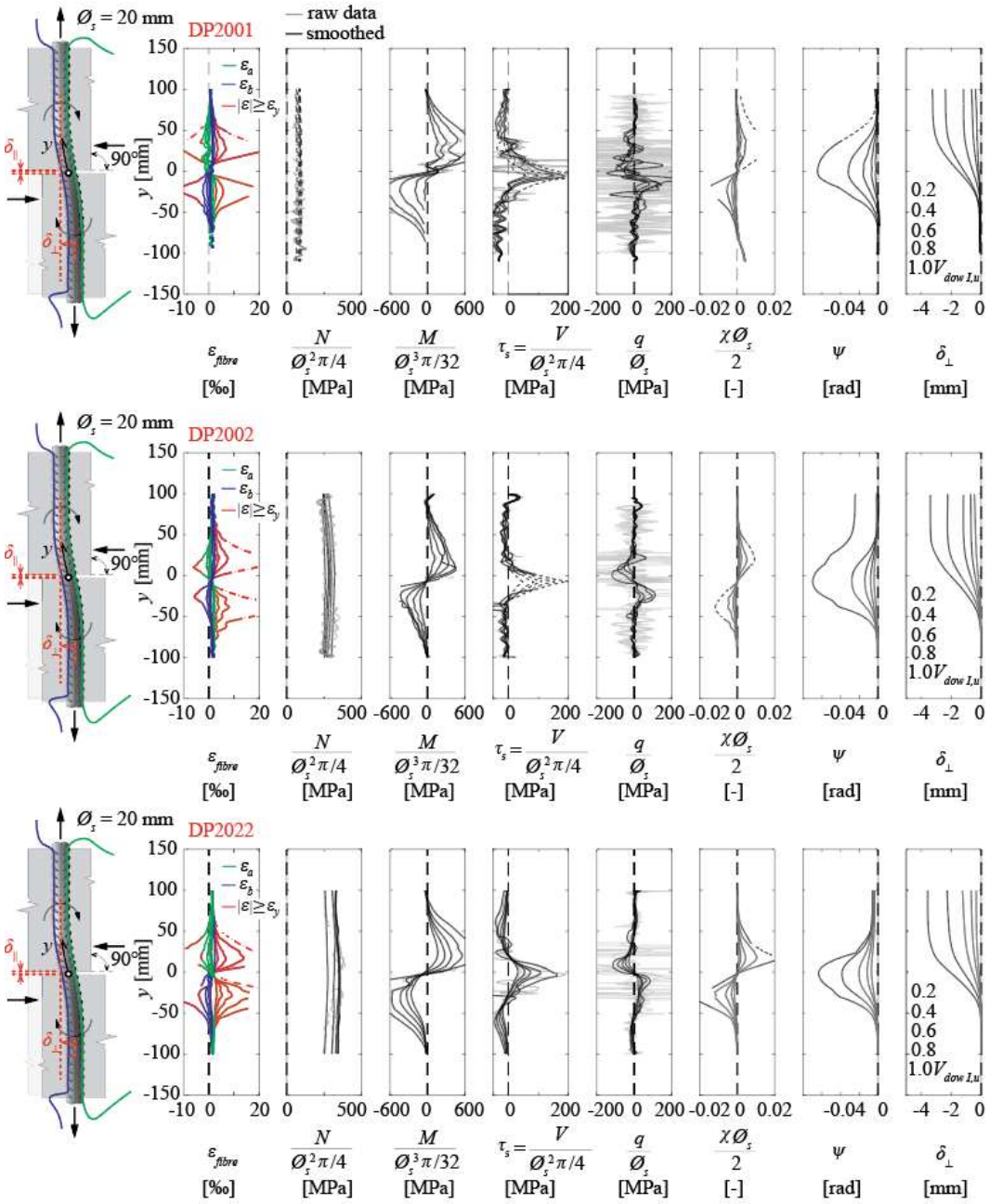

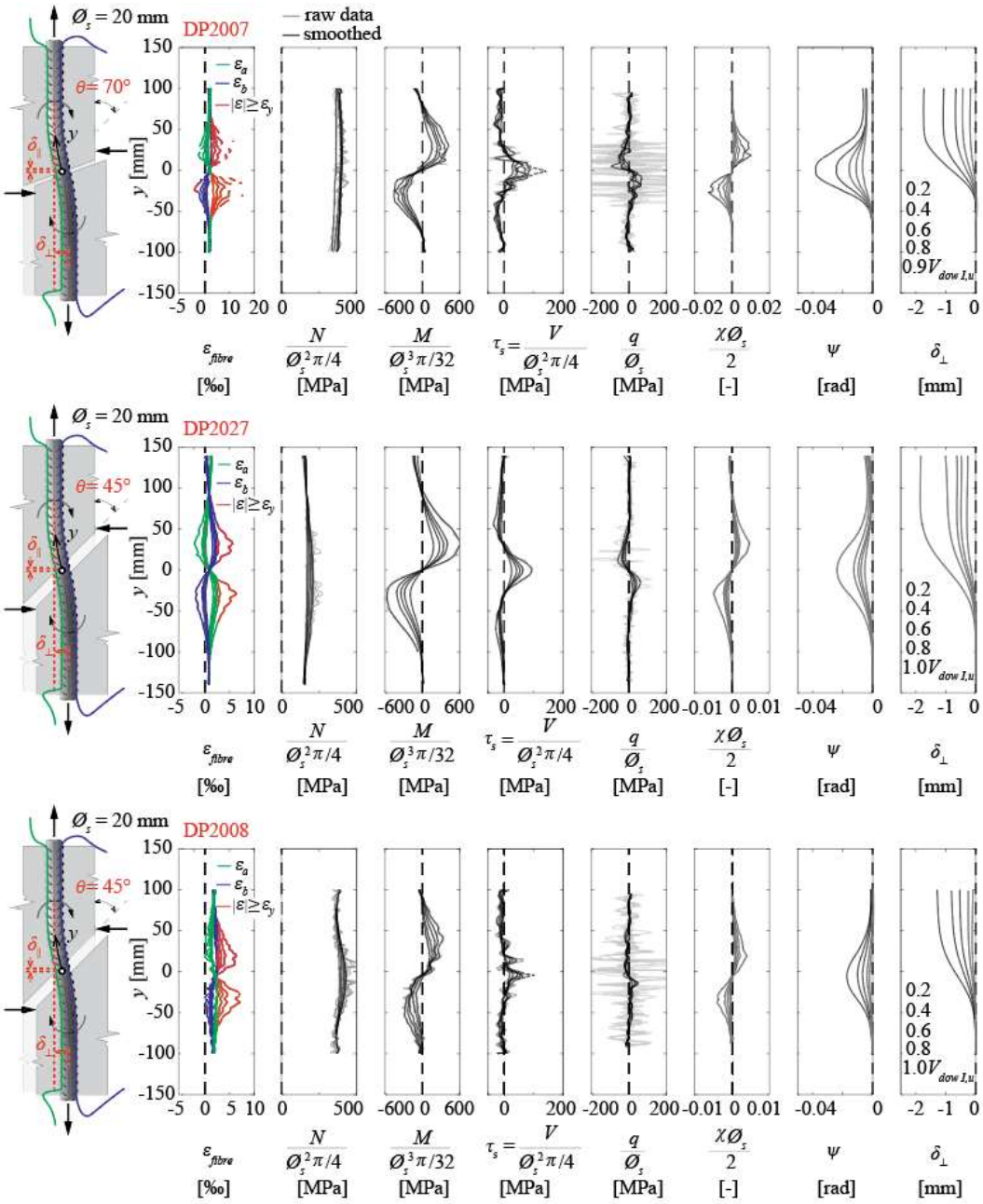
Ø_s = 20 mm
DP2007
raw data
smoothed
θ = 70°
DP2027
θ = 45°
DP2008
θ = 45°
y [mm]
ε_fibre [‰]
N/(Ø_s²π/4) [MPa]
M/(Ø_s³π/32) [MPa]
τ_s = V/(Ø_s²π/4) [MPa]
q/Ø_s [MPa]
χØ_s/2 [-]
ψ [rad]
δ⊥ [mm]
0.9V_dow I,u
1.0V_dow I,u

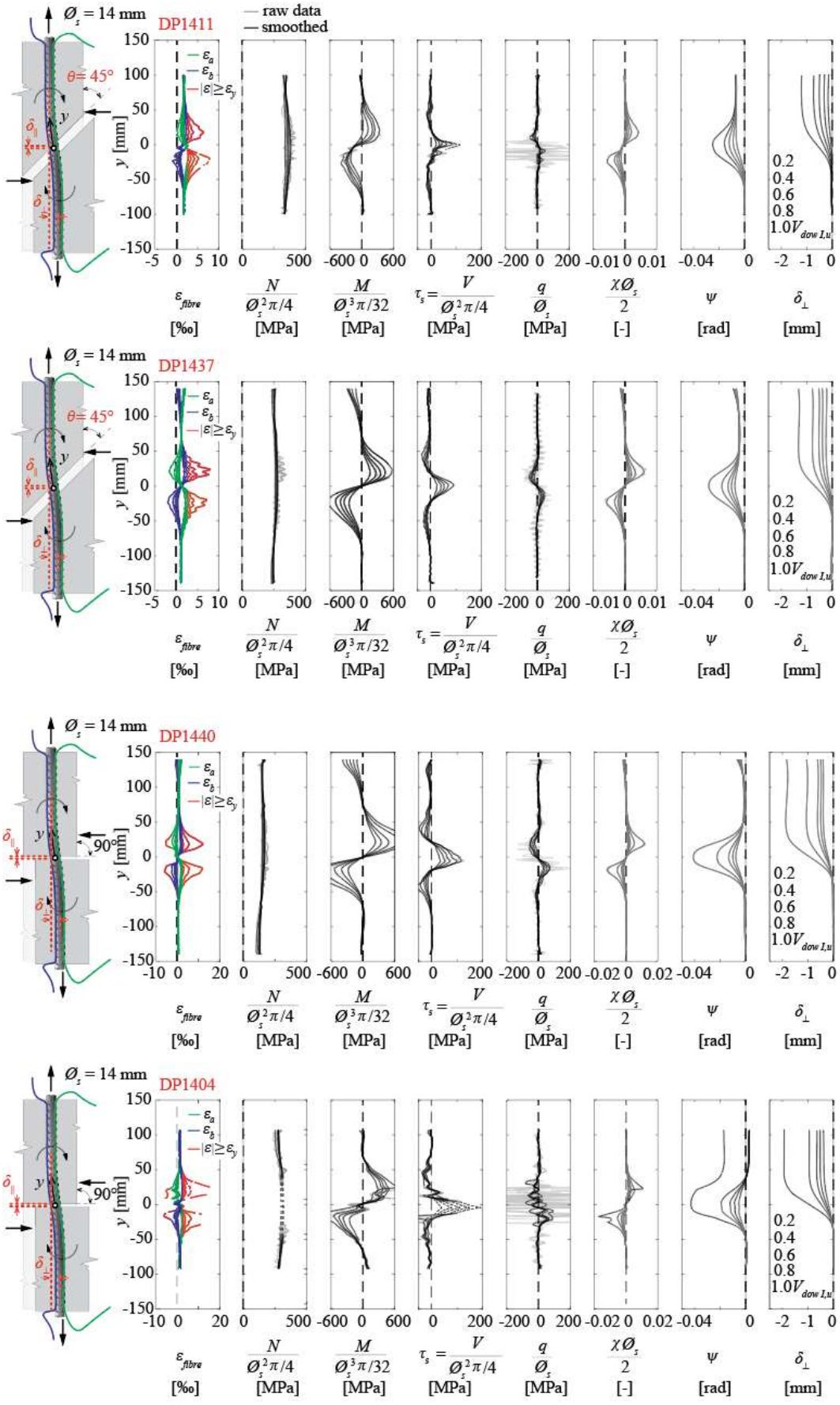

Fig. 92 *Optical fibre measurements and derived parameters in monotonic dowel tests.*

IX Spalling pattern at peak load in CP tests

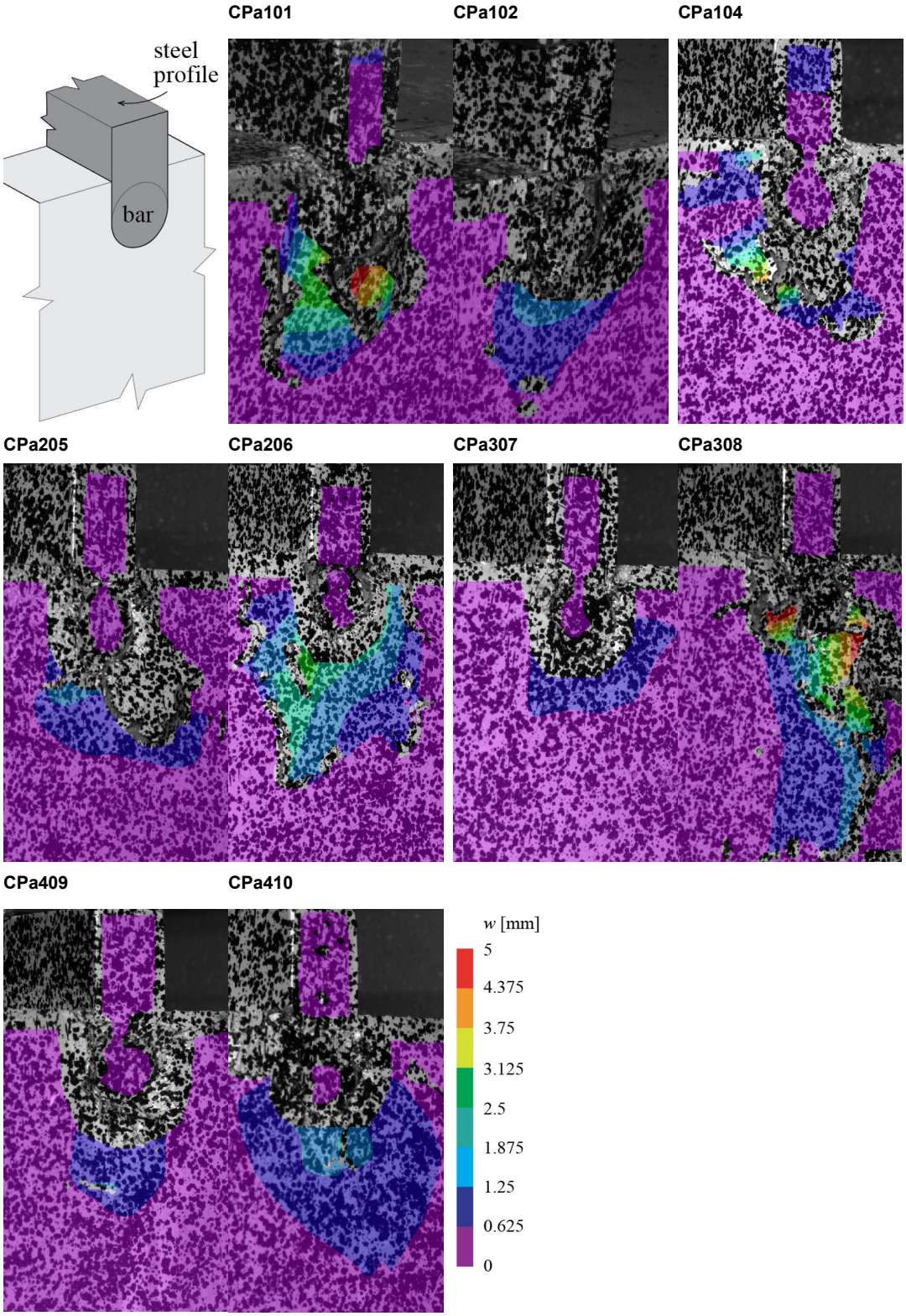

Fig. 93 *Spalling pattern at peak load in CP tests: front face of specimens where the penetration of the bar in reported with respect to the applied force in Fig. 62a.*

Notation

Notation for Section 2	
Symbol	**Meaning**
u	In-plane horizontal displacement.
v	In-plane vertical displacement
w	Out-of-plane displacement
NV_{uv}	Standard deviation to quantify the in-plane measurement uncertainty
NV_{w}	Standard deviation to quantify the out-of-plane measurement uncertainty
δ_n	Crack opening perpendicular to the crack direction
δ_t	Crack sliding parallel to the crack direction

Notation for Section 3	
Symbol	**Meaning**
d_1	Average distance from the markers to the centroid of the group of markers
d_2	Distance between centroids of the two groups of markers
$\underline{t}$	Translation vector
x	Coordinate along the x axis
y	Coordinate along the y axis
w_D	Detected crack width using the image processing algorithms
$w_{M,avg}$	Average of the measurements of the crack width
A_n	Markers on the fixed side of the crack
B_m	Markers on the moveable side of the crack
C_l	Crack points
NV_N	Standard deviation to quantify the in-plane noise in the marker detection
NV_B	Standard deviation to quantify the in-plane bias in the marker detection
S	Scaling transformation matrix
R	Rotation transformation matrix
β	Reduction factor due to the addition of quantities with different standard deviations
δ_n	Crack opening perpendicular to the crack direction
δ_t	Crack sliding parallel to the crack direction
δ_x	Crack opening in the horizontal direction
δ_y	Crack opening in the vertical direction
θ	Rotation
$\sigma(x)$	Standard deviation of variable x

Notation for Section 4	
Symbol	**Meaning**
b	rib width
c	clear concrete cover
c_{clear}	clear rib spacing
f_c	cylinder compressive strength of concrete

f_R	bond index
f_t	tensile strength of reinforcement
f_y	yield strength of reinforcement
h	distance from the bar surface to the bottom of the formwork
$h_{R,avg}$	average rib height
$h_{R,max}$	maximum rib height
l_b	bonded length
n_l	number of lugs that compose the rib
n_s	number of transverse reinforcement stirrups
n_t	number tests
s_{ps}	plastic settlement strain
s_R	transverse rib spacing
w	crack width
x	coordinate
A_c	rib contact area
F_{max}	maximum pull-out force
α	exponent for the ascending branch of the bond-slip relationship of MC2010
α_R	transverse rib flank inclination
β	transverse rib angle
δ_s	bar displacement
δ_c	concrete displacement
δ_{sc}	relative slip
$\delta_{sc}(\tau_{b,max})$	slip corresponding to the maximum bond stress
$\delta_{sc,end}$	relative slip at the unloaded end of the bar
δ_{sc1}	slip at the end of the ascending branch of the local bond-slip relationship
δ_{sc2}	slip at the end of plateau of the local bond-slip relationship
δ_{sc3}	slip at the beginning of the residual frictional branch
ε_s	bar axial strain
η_2	bond stress reduction factor for poor casting conditions
$\eta_{spl\text{-}spa}$	bond stress reduction factor due to splitting and spalling cracks
θ	ratio between splitting and spalling components of the crack width
κ_f	proportionality factor
κ_m	factor to account for the presence of multiple cracks
σ_s	bar axial stress
σ_{sR}	maximum stress at the loaded end of the bar
τ_b	bond stress
τ_{b0}	reference bond stress
$\tau_{b0.1}$	bond stress corresponding to a slip at the unloaded end of 0.1 mm
τ_{bf}	residual frictional bond strength
$\tau_{b,avg}$	average bond stress over the bonded length
$\tau_{b,max}$	maximum bond stress
$\varnothing$	bar diameter

Notation for Section 5	
Symbol	**Meaning**
b_w	Beam width
c	Clear concrete cover
c_{clear}	Clear rib spacing at the top of the lugs
d	Beam effective depth
f_c	Concrete compressive strength
f_{cm}	Mean concrete cylinder compressive strength
f_{ct}	Concrete tensile strength
f_{ctm}	Mean concrete tensile strength
f_R	Bond index of the reinforcement
f_{ym}	Mean yield strength of the longitudinal reinforcement
f_{ywm}	Mean yield strength of the shear reinforcement
h	Beam height
h_c	Depth of the compression zone in a section subjected to bending
k_{cyc}	Average bond stress reduction factor due to cyclic loading
k_{lc}	Average bond stress reduction factor due to longitudinal cracks along the bar
k_{sr}	Average bond stress adjustment factor
l_{cr}	Transfer length
n	Ratio of the steel elastic modulus divided by the concrete elastic modulus
n_l	Number of lugs composing the rib
s	Stirrup spacing
s_{cr}	Crack spacing
v	Beam test mid-span deflection
w_{lc}	Crack width of the longitudinal crack along the reinforcements
x	Coordinate along x axis
A	Transverse cross section
A_c	Concrete area in the transverse cross section
E_c	Elastic modulus of the concrete
E_s	Elastic modulus of the reinforcement
F	Tensile force applied to the concrete ties
N	Number of cycles
V	Shear force
$V_{cyc,max}$	Maximum shear force during cyclic loading
$V_{cyc,min}$	Minimum shear force during cyclic loading
V_{max}	Maximum measured shear force
δ_{sc}	Bar-to-concrete slip
$\delta_{\|}$	Crack displacement component in the direction of the reinforcement (also referred to as crack width in Section 5)
ε_c	Concrete strain
ε_{cs}	Unrestrained shrinkage strain
ε_s	Steel strain
η_2	Factor for to account for casting position

λ	Bond reduction factor near the crack
$\varnothing$	Nominal bar diameter
ρ_f	Flexural reinforcement ratio $A_s/(d \cdot b_w)$
ρ_t	Tensile reinforcement ratio A_s/A
ρ_w	Shear reinforcement ratio $A_{sw}/(s \cdot b_w)$
$\sigma_{cyc,max}$	Maximum nominal stress in the reinforcement for the maximum force during cyclic loading
$\sigma_{cyc,min}$	Minimum nominal stress in the reinforcement for the maximum force during cyclic loading
τ_b	Local bond stress
$\tau_{b,avg}$	Average bond stress over a certain length
$\tau_{bu,po}$	Maximum bond stress for pull-out failure
$\tau_{bu,sc}$	Maximum bond stress for splitting with confinement
$\tau_{bu,su}$	Maximum bond stress for splitting in unconfined conditions
χ_s	Reinforcement bar curvature

Notation for Section 6

Symbol	**Meaning**
a	distance of the concentrated load from the bar end
f_{cm}	mean uniaxial compressive concrete strength on day of testing
f_u	tensile strength of the rebar
f_y	yield strength of the rebar
k_c	bearing concrete stiffness under a rebar
k_{sec}	secant slope of pressure curves
q / $\varnothing_s$	local contact pressure between concrete and the rebar
q_{max} / $\varnothing_s$	peak contact pressure between concrete and the rebar
w	out-of-plane displacement (spalling)
x_{max}	position of the critical cross-section in the rebar
A_s	area of the bar cross-section
E_c	elastic modulus of concrete
E_s	elastic modulus of the rebar
F	point load in CP tests
F_u	peak force in CP tests
M	bending moment in the rebar
M_{max}	maximum bending moment in the rebar
M_p	plastic bending moment of the rebar
N	global axial force in the rebar
N'	inclined local axial force in the rebar
N_{init}	initial global axial force
$N_{min\ /\ max}$	minimum / maximum axial force within a cyclic combination
N_p	axial resistance of the rebar
V	shear force in the rebar
V_{dow}	dowel force
$V_{dow\ I}$	first-order dowel force
$V_{dow\ I,u}$	ultimate first-order dowel force

$V_{dow,\ min\ /\ max}$	minimum / maximum shear force within a cyclic combination
$V_{dow,cat}$	catenary action
α	angle defining the applied crack kinematics in monotonic dowel tests
δ	penetration of the bar end in concrete
$\delta_{\|\|}$	crack opening component in the direction of the rebar
$\delta_{\|\|,\ init}$	initial crack opening component in the direction of the rebar
$\delta_{\|\|min\ /\ max}$	minimum / maximum crack opening component in the direction of the rebar
$\delta_{\perp}$	transverse displacement
$\delta_{\perp min\ /\ max}$	minimum / maximum transverse displacement
$\varepsilon_{fibre\ /\ a\ /\ b}$	strains measured by optical fibres on both sides of the rebar
ε_s	strain in the rebar
$\varepsilon_{s,avg}$	average longitudinal strain in the rebar
$\varepsilon_{s,flex}$	longitudinal strain in the the rebar due to bending
ε_y	yield strain in the rebar
θ	angle between the crack and the rebar
$\sigma_{c,pl}$	plastic stress in concrete
σ_s	stress in the rebar
$\sigma_{s,avg}$	average axial stress in the rebar
$\sigma_{s,flex}$	nominal longitudinal stress due to bending at the edge of the bar cross-section
χ	curvature of the rebar
ψ	rotation of the rebar
CP	tests of the concrete behaviour under a rebar
DIC	Digital Image Correlation
DP	dowel tests
MI	Mode I
MII	Mode II
MM	Mixed-Mode
$\varnothing_s$	diameter of the dowel bar

Notation for Section 7

Symbol	**Meaning**
c	concrete cover
$c_{x,\ y}$	concrete cover in two orthogonal directions
f_c	uniaxial compressive concrete strength
$f_{c,cube}$	uniaxial concrete strength measured on cubes
f_u	tensile strength of the rebar
f_y	yield strength of the rebar
k_c	bearing concrete stiffness under the rebar
k_{cal}	constant in accordance with Dulacska's model
k_N	$= 1 - (N / N_p)^2$ in Dulacska's model
p	internal pressure
$q / \varnothing_s$	contact pressure between concrete and the rebar

x_{max}	position of the critical cross-section in the rebar
$\bar{k}_c$	= $k_c \varnothing_s / E_c$
E_c	elastic modulus of concrete
E_s	elastic modulus of the rebar
I_s	moment of inertia of the rebar
M	bending moment in the rebar
M_{max}	maximum bending moment in the bar
M_p	plastic bending moment of the rebar
N	axial force in the rebar; number of cyclic loads
$N_{min\ /\ max}$	minimum / maximum axial force within a cyclic combination
V	shear force in the rebar
V_{dow}	dowel force
$V_{dow\ l,u}$	ultimate first-order dowel force
$V_{dow,\ min\ /\ max}$	minimum / maximum shear force within a cyclic combination
β	stiffness parameter in Winkler's model
δ	measured displacement
$\delta_{\parallel}$	crack opening component in the direction of the rebar
$\delta_{\perp}$	transverse displacement
$\Delta\delta_{\perp}$	variation of the transverse displacement
$\Delta\sigma_{s,flex}$	variation of the longitudinal stress in the rebar due to bending at the critical cross-section
$\varepsilon_{fibre\ /\ a\ /\ b}$	strains measured by optical fibres on both sides of the rebar
$\eta 3$	concrete confinement factor
η_{bond}	coefficient accounting for secondary cracks due to the axial force
η_c	coefficient accounting for the thickness of the concrete cover
η_{cast}	coefficient accounting for the casting conditions
η_{cyc}	coefficient accounting for the number of cyclic loads
η_{fc}	coefficient accounting for the concrete strength
η_δ	coefficient accounting for the bearing stiffness reduction due to the transverse displacement
η_θ	coefficient accounting for the angle between the bar and the crack
θ	angle between the crack and the rebar
λ	coefficient accounting for the spring length
$\sigma_{c,\ avg}$	average stress in concrete under the rebar
$\sigma_{s,flex}$	longitudinal stress in the rebar due to bending at the critical cross-section
χ	curvature of the rebar
ψ	rotation of the rebar
$\tilde{\delta}_{\perp}$	local transverse displacement
CP	tests of the concrete behaviour under a rebar
DP	dowel tests
$\varnothing_s$	diameter of the dowel bar

References

References for Chapter 1

[1] Zaborac J., Athanasiou A., Salamone S., Bayrak O., Hrynyk T. D., **"Evaluation of Structural Cracking in Concrete"**, Center for Transportation Research at The University of Texas at Austin, Final Report (FHWA/TX-19/0-6919-1), 172 p., Austin, USA, 2019.

[2] OFROU, **"Directive ASTRA 62016: Guide pour les inspecteurs d'ouvrages d'art"**, Office fédéral des routes, Édition 2021 V1.20, 85 p., Switzerland, 2021.

[3] Monney F., Fernández Ruiz M., Muttoni A., **"Influence of amount of shear reinforcement and its post-yield response on the shear resistance of reinforced concrete members"**, Structural Concrete, pp. 1-33, 2022.

[4] Bell B., **"European Railway Bridge Demography D1.2"**, Sustainable Bridges – Assessment for Future Traffic Demands and Longer Lives, 15 p., 2004.

[5] Office Fédéral des Routes, **"Rapport sur l'état du réseau des routes nationales"**, Édition 2019, 46 p., Switzerland, 2019.

[6] Capros P., De Vita A., Tasios N., Papadopoulos D., **"EU Energy, Transport and GHG Emissions Trends to 2050"**, European Commission, Directorate-General for Energy, Directorate-General for Climate Action and Directorate-General for Mobility and Transport, 173 p., 2013.

[7] Croce P., **"Impact of Road Traffic Tendency in Europe on Fatigue Assessment of Bridges"**, Applied Sciences, Vol. 10, 30 p., 2020.

[8] CEB, **"Fatigue of concrete structures"**, CEB Bulletin d'Information, 188, 300 p., 1988.

[9] Tilly G. P., **"Fatigue of steel reinforcement bars in concrete: a review"**, Fatigue of Engineering Materials and Structures, Vol. 2, pp. 251-268, 1979.

[10] Lenschow R., **"Fatigue of concrete structures"**, IABSE Report, 37, pp. 15-24, Zürich, Switzerland, 1982.

[11] Rehm G., **"Kriterien zur Beurteilung von Bewehrungsstäben mit hochwertigen Verbund"**, Stahlbetonbau, Berichte aus Forschung und Praxis, Verlag Wilhelm Ernst & Sohn, pp. 79-96, Berlin, Germany, German, 1969.

[12] Eurocode 2, **"Design of concrete structures-Part 1-1: General rules and rules for buildings"**, European Committee for Standardization (CEN), 225 p., Brussels, Belgium, 2004.

[13] Cantone R., Fernández Ruiz M., Muttoni A., **"A detailed view on the rebar-to-concrete interaction based on refined measurement techniques"**, Engineering Structures, Vol. 226, 19 p., 2020.

[14] Galkovski T., Mata Falcón J., Kaufmann W., **"Effective reinforcement ratio of RC beams: Validation of modelling assumptions with high-resolution strain data"**, Structural Concrete, Vol. 23, No 3, pp. 1353-1369, 2022.

References for Chapter 2

[15] Abdel-Qader I., Abudayyeh O., Kelly M. E. , **"Analysis of Edge-Detection Techniques for Crack Identification in Bridges"**, ASCE Journal of Computing in Civil Engineering, Vol. 17, No 4, pp. 255-263, 2003.

[16] Oliveira H., Lobato Correia P., **"Automatic Road Crack Detection and Characterization"**, IEEE Transactions on Intelligent Transportation Systems, Vol. 14, No 1, pp. 155-168, 2013.

[17] Dias da Costa D., Valença J., Júlio E. N. B. S., **"Laboratorial test monitoring applying photogrammetric post-processing procedures to surface displacements"**, Measurement, Vol. 44, No 3, pp. 527-538, 2011.

[18] Morice P. B., Base G. D., **"The design and use of a demountable mechanical strain gauge for concrete structures"**, Magazine of concrete research, Vol. 5, No 13, pp. 37-42, 1953.

[19] Mohan A., Poobal S., **"Crack detection using image processing: A critical review and analysis"**, Alexandria Engineering Journal, Vol 57, No 2, pp. 787-798, 2018.

[20] Sutton M. A., Orteu J.-J., Schreier H. W., **"Image correlation for shape, motion and deformation measurements : basic concepts, theory and applications"**, Springer, 321 p., 2009.

[21] Sutton M. A., Matta F., Rizos D., **"Recent Progress in Digital Image Correlation: Background and Developments since the 2013 W M Murray Lecture"**, Experimental Mechanics, Vol. 57, No 1, pp. 1-30, 2017.

[22] Pan B., Qian K., Xie H., **"Two-dimensional digital image correlation for in-plane displacement and strain measurement: a review"**, Measurement Science and Technology, Vol. 20, No 6, 2009.

[23] Mata Falcón J., Haefliger S., Lee M., Galkovski T., Gehri N., **"Combined application of distributed fibre optical and digital image correlation measurements to structural concrete experiments"**, Engineering Structures, Vol. 225, Page: 111309, Amsterdam, 2020.

[24] Berrocal C., Fernandez I., Rempling R., **"Crack monitoring in reinforced concrete beams by distributed optical fiber sensors"**, Structure and Infrastructure Engineering, Vol. 17, No 1, pp. 124-139, UK, 2020.

[25] Murray C., Take W., Hoult N. A., **"Field monitoring of a bridge using digital image correlation"**, Proceedings of the ICE - Bridge Engineering, Vol. 168, pp. 3-12, 2015.

[26] Zahra T., Dhanasekar M., **"Serviceability Assessment of Masonry Arch Bridges Using Digital Image Correlation"**, Journal of Bridge Engineering, Vol. 24, 2018.

[27] Sousa P., Barros F., Tavares P., **"Experimental measurement of bridge deflection using Digital Image Correlation"**, Procedia Structural Integrity, Vol. 17, pp. 806-811, 2019.

[28] Mousa M. A., Yussof M. M., Udi U. J., **"Application of Digital Image Correlation in Structural Health Monitoring of Bridge Infrastructures: A Review"**, Infrastructures, Vol. 6 No 12, p. 176, 2021.

[29] Garnica G., Lantsoght E.O.L., Yang Y., **"Monitoring structural responses during load testing of reinforced concrete bridges: a review"**, Structure and Infrastructure Engineering, Vol. 18, 2022.

[30] Tung S.-H., Weng M.-C., Shih M.-H., **"Measuring the in situ deformation of retaining walls by the digital image correlation method"**, Engineering Geology, Vol. 166, pp. 116-126, 2013.

[31] Barros F., Aguiar S., Sousa P., **"Detection and measurement of beam deflection in the Madeira Airport runway extension using digital image correlation"**, International Journal of Structural Integrity, Vol. 14, 2022.

[32] Küntz M., Jolin M., Bastien J., **"Digital image correlation analysis of crack behavior in a reinforced concrete beam during a load test"**, Canadian Journal of Civil Engineering, Vol. 33, No 11, pp. 1418-1425, 2006.

[33] Elfgren L., Sas G. , Blanksvärd T., **"Photographic strain monitoring during full-scale failure testing of Örnsköldsvik Bridge"**, Structural Health Monitoring, Vol. 11 No. 4, pp. 489-498, 2012.

[34] Reagan D., Sabato A., Niezrecki C., **"Feasibility of using digital image correlation for unmanned aerial vehicle structural health monitoring of bridges"**, Structural Health Monitoring, Vol. 17, No 5, pp. 1056-1072, 2018.

[35] International Digital Image Correlation Society, **"A Good Practices Guide for Digital Image Correlation"**, 110 p., 2018.

[36] VDI, **"Optische Messverfahren - Digitale Bildkorrelation; Grundlagen, Annahme- und Überwachungsprüfung"**, VDI - Verein Deutscher Ing., 51 p., Germany, German/English, 2019.

[37] Correlated Solutions, **"Vic-3D 8 Software Manual"**, Version 8.4, 202 p., 2021.

[38] Correlated Solutions, **"Vic-3D 8 Testing Guide"**, 86 p., 2020.

[39] Busca G., Cigada A., Mazzoleni P., Zappa E., Franzi M., **"Cameras as displacement sensors to get the dynamic motion of a bridge: performance evaluation against traditional approaches"**, Bridge Maintenance, Safety, Management, Resilience and Sustainability, Proceedings of the Sixth International IABMAS Conference, pp. 2835-2841, Stresa, Italy, 2012.

[40] Piguet J.-C., **"Ponts en courbe préfabriqués et construits en encorbellement (exemple de Chillon)"**, Bulletin technique de la Suisse romande, Vol. 9, pp. 128-134, Suisse, 1969.

[41] Gehri N., Mata Falcón J., Kaufmann W., **"Automated crack detection and measurement based on digital image correlation"**, Construction and Building Materials, 256, 14 p., 2020.

[42] Gehri N., Mata Falcón J., Kaufmann W., **"Refined extraction of crack characteristics in large-scale concrete experiments based on digital image correlation"**, Engineering Structures, 251-A, 21 p., UK, 2022.

References for Chapter 3

[43] Wang P., Huang H., **"Comparison Analysis on Present Image-based Crack Detection Methods in Concrete Structures"**, 3rd International Congress on Image and Signal Processing, pp. 2530-2533, 2010.

[44] Jahanshahi M. R., Kelly J. S., Masri S. F., Sukhatme G. S., **"A survey and evaluation of promising approaches for automatic image-based defect detection of bridge structures"**, Structure and Infrastructure Engineering, Vol. 5, No 6, pp. 455-486, 2009.

[45] Jahanshahi M. R., Masri S. F., **"Adaptive vision-based crack detection using 3D scene reconstruction for condition assessment of structures"**, Automation in Construction, Vol. 22, pp. 567-576, 2012.

[46] Dorafshan S., Thomas R. J., Maguire M., **"Comparison of deep convolutional neural networks and edge detectors for image-based crack detection in concrete"**, Construction and Building Materials, Vol. 186, pp. 1031-1045, 2018.

[47] Ito A., Aoki Y., Hashimoto S., **"Accurate Extraction and Measurement of Fine Cracks from Concrete Block Surface Image"**, Proceedings of the 2002 28th Annual Conference of the IEEE Industrial Electronics, pp. 2202-2207, 2002.

[48] Fujita Y., Hamamoto Y., **"A robust automatic crack detection method from noisy concrete surfaces"**, Machine Vision and Applications, Vol. 22, pp. 245-254, 2010.

[49] Kim H., Ahn E., Cho S., Shin M., Sim S.-H., **"Comparative analysis of image binarization methods for crack identification in concrete structures"**, Cement and Concrete Research, Vol. 99, pp. 53-61, 2017.

[50] Roberts L. G., **"Machine perception of three-dimensional solids"**, Massachusetts Institute of Technology, Dept. of Electrical Engineering, 82 p., USA, 1963.

[51] Canny J., **"A Computational Approach to Edge Detection"**, IEEE Transactions on Pattern Analysis and Machine Intelligence, Vol. 6, No 6, pp. 679-698, 1986.

[52] Iyer S., Sinha S. K., **"A robust approach for automatic detection and segmentation of cracks in underground pipeline images"**, Image and Vision Computing, Vol. 23, No 10, pp. 921-933, 2005.

[53] Yamaguchi T., Nakamura S., Saegusa R., Hashimoto S., **"Image-Based Crack Detection for Real Concrete Surfaces"**, IEEJ Transactions on Electrical and Electronic Engineering, Vol. 3, No 1, pp. 128-135, 2007.

[54] Dare P. M., Hanley H. B., Fraser C. S., Riedel B., Niemeier W., **"An Operational Application of Automatic Feature Extraction: The Measurement of Cracks in Concrete Structures"**, Photogrammetric Record, Vol. 17, No 99, pp. 453-464, 2003.

[55] Kaseko M. S., Ritchie S. G., **"A neural network-based methodology for pavement crack detection and classification"**, Transportation Research Part C: Emerging Technologies, Vol. 1, No 4, pp. 275-291, 1993.

[56] Moselhi O., Shehab-Eldeen T., **"Classification of Defects in Sewer Pipes Using Neural Networks"**, Journal of Infrastructure Systems, Vol. 6, No 3, pp. 97-104, 2000.

[57] Chae M. J., Abraham D. M., **"Neuro-Fuzzy Approaches for Sanitary Sewer Pipeline Condition Assessment"**, Journal of Computing in Civil Engineering, Vol. 15, No 1, pp. 4-14, 2001.

[58] Rezaie A., Achanta R., Godio M., Beyer K., **"Comparison of crack segmentation using digital image correlation measurements and deep learning"**, Construction and Building Materials, Vol. 261, 12 p., 2020.

[59] Li H., Wang W., Wang M., Li L., Vimlund V., **"A review of deep learning methods for pixel-level crack detection"**, Journal of Traffic and Transportation Engineering, Vol. 9, No 6, pp. 945-968, 2022.

[60] Wiedemann C., Heipke C., Mayer H., Jamet O., **"Empirical Evaluation Of Automatically Extracted Road Axes"**, Empirical Evaluation Techniques in Computer Vision, pp. 172-187, 1998.

[61] Mosinska A., Marquez-Neila P., Kozinski M., Fua P., **"Beyond the pixel-wise loss for topology-aware delineation"**, Proceedings of the IEEE Conference on Computer Vision and Pattern Recognition, pp. 3136–3145, 2018.

[62] Cavagnis F., Fernández Ruiz M., Muttoni A., **"An analysis of the shear-transfer actions in reinforced concrete members without transverse reinforcement based on refined experimental measurements"**, Structural concrete, Vol. 19, pp. 49-64, 2017.

[63] Shan B., Zheng S., Ou J., **"A Stereovision-based Crack Width Detection Approach for Concrete Surface Assessment"**, KSCE Journal of Civil Engineering , Vol. 20, pp. 803-812, 2015.

[64] Zhu Z., German S., Brilakis I., **"Visual retrieval of concrete crack properties for automated post-earthquake structural safety evaluation"**, Automation in Construction, Vol. 20, No 7, pp. 874-883, 2011.

[65] Lins R. G., Givigi S. N., **"Automatic Crack Detection and Measurement Based on Image Analysis"**, IEEE Transactions on Instrumentation and Measurement, Vol. 65, No 3, pp. 583-590, 2016.

[66] Pantoja-Rosero B. G., dos Santos K. R. M., Achanta R., Rezaie A., Beyer K., **"Determining crack kinematics from imaged crack patterns"**, Construction and Building Materials, 343, 24 p., 2022.

[67] Malesa M., Kujawinska M., **"Deformation measurements by digital image correlation with automatic merging of data distributed in time"**, Applied Optics, Vol. 52, No 19, pp. 4681-4692, 2013.

[68] Ruocci G., Rospars C., Moreau G., **"Digital Image Correlation and Noise-filtering Approach for the Cracking Assessment of Massive Reinforced Concrete Structures"**, Strain, Vol. 52, No 6, pp. 503-521, 2016.

[69] Benning W., Lange J., Schwermann R., **"Monitoring crack origin and evolution at concrete elements using photogrammetry"**, ISPRS Congress Istanbul Commission, 2004.

[70] Valença J., Dias da Costa D., Júlio E. N. B. S., **"Automatic crack monitoring using photogrammetry and image processing"**, Measurement, Vol. 46, No 1, pp. 433-441, 2013.

[71] Nishiyama S., Minakata N., Kikuchi T., **"Improved digital photogrammetry technique for crack monitoring"**, Advanced Engineering Informatics, Vol. 29, No 4, pp. 851-858, 2015.

[72] Germanese D., Pascali M. A., Berton A., **"A preliminary study for a marker-based crack monitoring in ancient structures"**, Proceedings of the 2nd International Conference on Applications of Intelligent Systems, pp. 1-5, 2019.

[73] Wojnarowski A. E., Leonteva A. B., Tyurin S. V., **"Photogrammetric technology for remote high-precision 3D monitoring of cracks and deformation joints of buildings and constructions"**, The International Archives of Photogrammetry, Remote Sensing and Spatial Information Sciences, Vol. 42, pp. 96-101, 2019.

[74] Bal I. E. , Dais D., Smyrou E., **"Novel invisible markers for monitoring cracks on masonry structures"**, Construction and Building Materials, Vol. 300, 2021.

[75] Vincens B., Corres E., Muttoni A., **"Image-based techniques to complement digital image correlation for initial and long-term characterization of cracks in reinforced concrete structures"**, Engineering Structures, 2024.

[76] Iglovikov V., Shvets A., **"TernausNet: U-Net with VGG11 Encoder Pre-Trained on ImageNet for Image Segmentation"**, ArXiv e-prints, 5 p., 2018.

[77] Rezaie A., **"Deep Crack Segmentation GitHub repository"**, https://github.com/amirrezaie1415/Deep-DIC-Crack (visited on 08/05/2023), 2023.

[78] Rezaie A., Achanta R., Godio M., Beyer K., **"Dataset of cracks on DIC images"**, https://zenodo.org/records/4307686 (visited on 08/05/2023), 2023.

[79] Rezaie A., **"Crack Segmentation in Concrete Surfaces GitHub repository"**, https://github.com/amirrezaie1415/Concrete-Crack-Segmentation (visited on 08/05/2023), 2023.

[80] Ozgenel C. F., **"Concrete Crack Segmentation Dataset"**, Mendeley Data, https://data.mendeley.com/datasets/jwsn7tfbrp/1 (visited on 08/05/2023), 2019.

[81] Pantoja-Rosero B. G., **"Crack Kinematics GitHub repository"**, https://github.com/eesd-epfl/crack_kinematics (visited on 08/05/2023), 2022.

[82] Nikon Corporation, **"Nikon D800 Tech Specs"**, https://www.nikonusa.com/en/nikon-products/product-archive/dslr-cameras/d800.html#tab-ProductDetail-ProductTabs-TechSpecs (visited on 10/04/2023), 2023.

[83] OnePlus Technology, **"OnePlus 6 Tech Specs"**, https://www.oneplus.com/us/6/specs (visited on 11/04/2023), 2023.

[84] Cavagnis F., Fernández Ruiz M., Muttoni A., **"Shear failures in reinforced concrete members without transverse reinforcement: An analysis of the critical shear crack development on the basis of test results"**, Engineering structures, Vol. 103, pp. 157-173, UK, 2015.

[85] Ito Y., Ogawa K., Nakano K., **"Fast Ellipse Detection Algorithm Using Hough Transform on the GPU"**, 2011 Second International Conference on Networking and Computing, pp. 313-319, 2011.

[86] Grob J., Thürlimann B., **"Ultimate Strength and Design of Reinforced Concrete Beams Under Bending and Shear"**, IABSE, No. 36, pp. 105-120, 1976.

[87] Thürlimann B., **"Plastic Analysis of Reinforced Concrete Beams"**, IABSE Colloquium, Vol. 28, pp. 71-90, Copenhagen, Denmark, 1979.

References for Chapter 4

[88] FIB, **"Bond of reinforcement in concrete"**, fib bulletin, Fédération Internationale du Béton - fib Bulletin n°10; state-of-art report prepared by Task Group Bond models, 10, 427 p., Lausanne, Switzerland, 2000.

[89] Lindorf A., **"Ermüdung des Verbundes von Stahlbeton unter Querzug"**, Technischen Universität Dresden, Fakultät Bauingenieurwesen, 228 p., Dresden, Germany, German, 2011.

[90] Eligehausen R., Popov P., Bertero V., **"Local bond stress-slip relationships of deformed bars under generalized excitations"**, UCB/EERC, 83/23, Berkeley, USA, 1983.

[91] Shima H., **"Micro and Macro models for bond in Reinforced concrete"**, University of Tokyo, Journal of the Faculty of Engineering; University of Tokyo, XXXIX n° 2, pp. 133-194, Tokyo, Japan, 1987.

[92] Giuriani E., Plizzari G., **"Interrelation of Splitting and Flexural Cracks in RC Beams"**, Journal of Structural Engineering, Vol. 109, No 9, pp. 1032-1049, USA, 1998.

[93] Idda K., **"Verbundverhalten von Betonrippenstählen bei Querzug"**, Institut für Massivbau und Baustofftechnologie, Universität Karlsruhe, 228 p., Karlsruhe, Germany, German, 1999.

[94] FIB, **"fib Model Code for Concrete Structures 2010"**, fib, First Edition, UK, 2013.

[95] SIA, **"SIA 262:2013 - Structures en béton"**, Société suisse des ingénieurs et des architectes, 102 p., Zurich, Switzerland, 2013.

[96] Plizzari G., Metelli G., Cairns J., **"An overview of enhancements to provisions for bond in the draft Fib Model Code 2020"**, Bond in Concrete 2022, pp. 1038-1051, Stuttgart, Germany, 2022.

[97] Eurocode 2, **"Design of concrete structures - Part 1-1: General rules and rules for buildings, bridges and civil engineering structures"**, Final draft FprEN 1992-1-1, European Committee for Standardization (CEN), 405 p., Brussels, Belgium, 2023.

[98] Muttoni A., Cairns J., Goodchild C., Ganz H. R., **"Background document to clauses 11.4 and 11.5 - Anchorage and laps of bars in tension and compression"**, 135 p., Lausanne, Switzerland, 2023.

[99] FIB, **"Bond and anchorage of embedded reinforcement: Background to the fib Model Code for Concrete Structures 2010"**, Fédération Internationale du Béton, fib bulletin, Vol. 72, 161 p., Lausanne, Switzerland, 2014.

[100] RILEM, **"Essais portant sur l'adhérence des armatures du béton - Essais par traction"**, Recommendation RILEM/CEB/FIP - RC6, Matériaux et Constructions, vol. 6, n° 32, 1978.

[101] Goto Y., **"Cracks Formed in Concrete around Deformed Tension Bars"**, ACI Journal, Vol. 68, No 4, pp. 244-251, Japan, 1971.

[102] Metelli G., Plizzari G., **"Influence of the relative rib area on bond behaviour"**, Magazine of Concrete Research, Vol. 66, No 6, pp. 277-294, 2014.

[103] Koschemann M., Curbach M., Marx S., **"Investigation of local bond behavior using distributed optical fiber sensing"**, Bond in Concrete 2022, pp. 133-145, Stuttgart, Germany, 2022.

[104] Lemcherreq Y., Galkovski T., Mata Falcón J., Kaufmann W., **"Application of Distributed Fibre Optical Sensing in Reinforced Concrete Elements Subjected to Monotonic and Cyclic Loading"**, Sensors, Vol. 22, No 5, 28 p., Basel, Switzerland, 2022.

[105] Cairns J., Plizzari G., **"Towards a harmonised European bond test"**, Materials and Structures, Vol. 36, pp. 498-506, 2003.

[106] ASTM, **"Standard Test Method for Comparing Bond Strength of Steel Reinforcing Bars to Concrete Using Beam-End Specimens"**, ASTM, A944-10, 4 p., USA, 2015.

[107] Koschemann M., Curbach M., Marx S., **"Influence of the test setup on the local bond behaviour of ribbed steel bars"**, fib International Congress 2022 Oslo, pp. 349-358, Oslo, Norway, 2022.

[108] Tepfers R., Olsson P.-A., **"Ring test for the evaluation of bond properties of reinforcing bars"**, Bond in Concrete - From Research to Practice, Vol. 1, pp. 89-99, Riga, Latvia, 1992.

[109] Moccia F., Fernández Ruiz M., Metelli G., Muttoni A., Plizzari G., **"Casting position effects on bond performance of reinforcement bars"**, Structural Concrete, Wiley, 21 p., 2021.

[110] Mains R. M., **"Measurement of the Distribution of Tensile and Bond Stresses Along Reinforcing Bars"**, Journal of the American Concrete Institute, Vol. 23, No 3, pp. 225-252, USA, 1951.

[111] Djabry W., **"Contribution à l'étude de l'adhérence des fers d'armature au béton"**, Rapport EMPA N°184, 76 p., Zürich, Switzerland, 1952.

[112] Nilson A. H., **"Internal Measurement of Bond Slip"**, ACI Journal, Vol. 69, No 7, pp. 439-441, USA, 1972.

[113] Bado M. F., Casas J.-R., Kaklauskas G., **"Distributed Sensing (DOFS) in Reinforced Concrete members for reinforcement strain monitoring, crack detection and bond-slip calculation"**, Engineering Structures, Vol. 226, 111385, 13 p., 2021.

[114] Balázs G. L., **"Cracking analysis based on slip and bond stresses"**, ACI Materials Journal, 90 N°1, pp. 340-348, Detroit, USA, 1993.

[115] CEB, **"CEB-FIP Model Code 1990"**, Comité Euro-International du Béton (CEB), 460 p., London, UK, 1993.

[116] Fernández Ruiz M., Muttoni A., Gambarova P., **"Analytical modelling of the pre- and post-yield behaviour of bond in reinforced concrete"**, ASCE Journal of Structural Engineering, Vol. 133, N° 10, pp. 1364-1372, Reston, USA, 2007.

[117] Gambarova P., Paolo Rostasi G., Zasso B., **"Steel-to-concrete bond after concrete splitting: constitutive laws and interface deterioration"**, Materials and Structures, Vol. 22, pp. 347-356, 1989.

[118] Mahrenholtz C., **"Seismic Bond Model for Concrete Reinforcement and the Application to Column-to-Foundation Connections"**, Universität Stuttgart, Institut für Werkstoffe im Bauwesen, 398 p., Stuttgart, Germany, 2012.

[119] Brantschen F., Faria D. M. V., Fernández Ruiz M., Muttoni A., **"Bond Behaviour of Straight, Hooked, U-Shaped and Headed Bars in Cracked Concrete"**, Structural Concrete, 17 No. 5, pp. 799-810, 2016.

[120] Moccia F., Fernández Ruiz M., Muttoni A., **"Spalling of concrete cover induced by reinforcement "**, Engineering Structures, 19 p., 2021.

[121] ISO, **"EN ISO 15630-1 Steel for the reinforcement and prestressing of concrete - Test methods - Part 1 : reinforcing bars, wire rod and wire"**, European Committee For Standardization CEN, 36 p., 2019.

[122] Luna Technologies Inc., **"ODiSI 6000 Series User Guide"**, 99 p., USA, 2020.

[123] Galkovski T., Lemcherreq Y., Mata Falcón J., Kaufmann W., **"Fundamental Studies on the Use of Distributed Fibre Optical Sensing on Concrete and Reinforcing Bars"**, Sensors, Vol. 21, No 22, 24 p., Switzerland, 2021.

[124] Bado M. F., Casas J.-R., Dey A., Berrocal C., Kaklauskas G., Fernandez I., Rempling R., **"Characterization of concrete shrinkage induced strains in internally-restrained RC structures by distributed optical fiber sensing"**, Cement and Concrete Composites, Vol. 120, 12 p., 2021.

[125] Clark A. P., **"Bond of Concrete Reinforcing Bars"**, Journal of Research of the National Bureau of Standards, Vol. 43, pp. 565-579, USA, 1949.

[126] Rehm G., **"Über die Grundlagen des Verbunds zwischen Stahl und Beton"**, Deutscher Ausschuss für Stahlbeton, Vol. 138, 59 p., Berlin, Germany, German, 1961.

[127] Martin H., Noakowski P., **"Verbundverhalten von Betonstahlen Untersuchung auf der Grundlage von Ausziehversuchen"**, Deutscher Ausschuss für Stahlbeton, Vol. 319, 175 p., Berlin, Germany, German, 1981.

[128] Pérez Caldentey A., García R., Gribniak V., Rimkus A., **"Tension versus flexure: Reasons to modify the formulation of MC 2010 for cracking"**, Structural Concrete, Vol. 21, No 5, pp. 2101-2123, 2020.

[129] Kreller H., **"Zum nichtlinearen Trag- und Verformungsverhalten von Stahlbetonstabtragwerken unter Last- und Zwangeinwirkung"**, Institut für Werkstoffe im Bauwesen, Mitteilungen, Universität Stuttgart, 214 p., German, 1989.

[130] Corres E., Muttoni A., **"Validation of bond models for the crack width estimation based on detailed measurements"**, 14th fib International PhD Symposium in Civil Engineering, pp. 138-144, Rome, Italy, 2022.

[131] Cairns J., Jones K., **"Influence of rib geometry on strength of lapped joints: an experimental and analytical study"**, Magazine of Concrete Research, Vol. 47, No 172, pp. 253-262, 1995.

[132] Cairns J., **"Top cast effect: Influence of bond length on splitting mode failure"**, Structural Concrete, Vol. 23, No 5, pp. 2696-2709, 2022.

[133] Corres E., Muttoni A., **"Long anchorage resistance of reinforcement bars derived from local bond-slip relationships for good and poor bond conditions"**, Bond in Concrete 2022, pp. 207-216, Stuttgart, Germany, 2022.

[134] Soretz S., Holzenbein H., **"Influence of Rib Dimensions of Reinforcing Bars on Bond and Bendability"**, ACI Journal Proceedings, Vol. 76, No 1, pp. 111-128, USA, 1979.

References for Chapter 5

[135] Eurocode, **"Eurocode 2: Design of concrete structures - Part 1-1: General rules and rules for buildings"**, European Committee for Standardization (CEN), Brussels, 2004.

[136] Saliger R., **"Hochwertige Stähle im Eisenbetonbau (High-Grade Steel in Reinforced Concrete)"**, Proceedings of the 2nd congress of the International association for bridge and structural engineering (IABSE), Vol. 2, pp. 303-323, Berlin-Munich, Germany, German, 1936.

[137] Thomas F. G., **"Cracking in reinforced concrete"**, The Structural Engineer , Vol. 14, No 7, pp. 298-320, 1936.

[138] Broms B. B., **"Crack width and crack spacing in reinforced concrete members"**, ACI Journal Proceedings, Vol. 62, No. 10, pp. 1237-1256, USA, 1965.

[139] CEB, **"Fissuration"**, Comité Euro-International du béton, Bulletin d'Information, No. 61, 253 p., 1967.

[140] Ferry-Borges J., **"Cracking and deformability of reinforced concrete beams"**, Publications of the International Association of Bridge and Structural Engineering, Vol. 26, pp. 75-95, Zurich, Switzerland, 1966.

[141] Borosnyói A., Balázs G. L., **"Models for flexural cracking in concrete: the state of the art"**, Structural Concrete, Vol. 6, No 2, pp. 53-62, 2005.

[142] Lapi M., Orlando M., Spinelli P., **"A review of literature and code formulations for cracking in R/C members"**, Structural Concrete, vol. 19, No 5, pp. 1255-1535, 2018.

[143] Van der Esch A., Wolfs R., Fennis S., Roosen M., Wijte S., **"Categorization of formulas for calculation of crack width and spacing in reinforced concrete elements"**, Structural Concrete, 17 p., 2023.

[144] Noakowski P., **"Nachweisverfahren für Verankerung, Verformung, Zwangbeanspruchung und Rissbreite"**, Deutscher Ausschuss für Stahlbeton, Vol. 394, 75 p., Germany, German, 1988.

[145] Sigrist V., **"Zum Verformungsvermögen von Stahlbetonträgern"**, Dissertation, No. 11169, ETHZ, 159 p., Zürich, Switzerland, German, 1995.

[146] Corres E., Muttoni A., **"Bond of steel reinforcement based on detailed measurements: Results and interpretations"**, Structural Concrete, Vol. 24, No 6, pp. 7173-7204, 2023.

[147] Campana S., Fernández Ruiz M., Anastasi A., Muttoni A., **"Analysis of shear-transfer actions on one-way RC members based on measured cracking pattern and failure kinematics"**, Magazine of Concrete Research, Vol. 56, No. 6, pp. 386-404, UK, 2013.

[148] Calvi P. M., **"A Theory for the Shear Behaviour of Cracks Providing a Basis for the Assessment of Cracked Reinforced Concrete Structures"**, PhD Thesis, University of Toronto, 367 p., Canada, 2015.

[149] Shima H., Chou L. L., Okamura H., **"Bond characteristics in post-yield range of deformed bars"**, Proceedings of JSCE, Translation, n°378/v-6, pp. 113-124, Japan, 1987.

[150] Maekawa K., Pimanmas A., Okamura H., **"Nonlinear Mechanics of Reinforced Concrete"**, Spon Press, 768 p., 2003.

[151] Brault A., Hoult N. A., Lees J. M., **"Development of a relationship between external measurements and reinforcement stress"**, Proceedings of SPIE, Vol. 9435, 12 p., USA, 2015.

[152] Carmo R. N. F., Valença J., Silva D., Dias da Costa D., **"Assessing steel strains on reinforced concrete members from surface cracking patterns"**, Construction and Building Materials, Vol. 98, pp. 265-275, 2015.

[153] Galkovski T., Mata Falcón J., Kaufmann W., **"Experimental investigation of bond and crack behaviour of reinforced concrete ties using distributed fibre optical sensing and digital image correlation"**, Engineering Structures, Vol. 292, 24 p., 2023.

[154] Lemcherreq Y., Zanuy C., Vogel T., Kaufmann W., **"Experimental and analytical assessment of fatigue damage in reinforced concrete tension members"**, Engineering Structures, Vol. 289, 23 p., 2023.

[155] Poldon J. J., Hoult N. A., Bentz E. C., **"Distributed Sensing in Large Reinforced Concrete Shear Test"**, ACI Structural Journal, 116(5), 235-245, 2019.

[156] Davis M. B., Hoult N. A., Bajaj S., Bentz E. C., **"Distributed Sensing for Shrinkage and Tension Stiffening Measurement"**, ACI Structural Journal, V. 114, pp. 755-766, 2017.

[157] Corres E., Muttoni A., **"Estimation of the bar stress based on crack width measurements in reinforced concrete structures"**, Structural Concrete, 26 p., 2024.

[158] Corres E., Muttoni A., **"Local bond-slip model based on mechanical considerations"**, Engineering Structures, Vol. 314, No 1, 19 p., 2024.

[159] Hordijk D. A., **"Local approach to fatigue of concrete"**, Technische Universiteit Delft, Thesis, Editor W. D. Meinema b. v. Delft, Delft, Netherlands, 1991.

[160] Bischoff P. H., **"Effects of shrinkage on tension stiffening and cracking in reinforced concrete"**, Canadian Journal of Civil Engineering, Vol. 21, No 3, pp. 363-374, 2001.

[161] Gribniak V., Kaklauskas G., Bacinskas D., **"State-Of-Art Review of Shrinkage Effect on Cracking and Deformations of Concrete Bridge Elements"**, The Baltic Journal of Road and Bridge Engineering, Vol. 2, No 4, pp. 183-193, 2007.

[162] García R., Pérez Caldentey A., **"Influence of casting position on cracking behavior of reinforced concrete elements and evaluation of latest proposal for EN-1992 and MC2020: Experimental study"**, Structural Concrete, Vol. 23, No 5, pp. 2910-2927, 2022.

[163] CEN, **"Final draft FprEN 1992-1-1: Design of concrete structures - Part 1-1: General rules and rules for buildings, bridges and civil engineering structures"**, European Committee for Standardization (CEN), 405, Brussels, Belgium, 2023.

[164] Marti P., Alvarez M., Kaufmann W., Sigrist V., **"Tension chord model for structural concrete"**, Structural Engineering International, IABSE, Vol. 8, No. 4, pp. 287-298, USA, 1998.

[165] FIB, **"Constitutive modelling of high strength/ high performance concrete"**, Fédération Internationale du Béton, fib bulletin, Vol. 42, 134 p., Lausanne, Switzerland, 2008.

[166] Husain S. I., Ferguson P. M., **"Flexural crack widths at the bars in reinforced concrete beams"**, Centrale nationale d'alarme, The University of Texas at Austin, 41 p., Austin, USA, 1968.

[167] Yannopoulos P. J., **"Variation of the concrete concrete crack widths through cover to reinforcement"**, Magazine of Concrete Research, Vol. 41, No 147, pp. 63-68, 1989.

[168] Borosnyói A., Snóbli I., **"Crack width variation within the concrete cover of reinforced concrete members"**, Epitoanyag - Journal of Silicate Based and Composite Materials, Vol. 62 (3), pp. 70-74, 2010.

[169] Pérez Caldentey A., Corres Peiretti H., Peset Iribarren J., Giraldo Soto A., **"Cracking of RC members revisited: influence of cover, f/?s,ef and stirrup spacing – an experimental and theoretical study"**, Structural Concrete, Vol. 14, No 1, pp. 69-78, 2013.

[170] Tammo K., **"Crack Behavior near Reinforcing Bars in Concrete Structures"**, ACI Structural Journal, Vol. 106, No 3, pp. 259-267, USA, 2009.

[171] Cavagnis F., Fernández Ruiz M., Muttoni A., **"A mechanical model for failures in shear of members without transverse reinforcement based on development of a critical shear crack"**, Engineering structures, Elsevier, Vol. 157, pp. 300-315, 2018.

[172] Fernández Ruiz M., Muttoni A., Sagaseta J., **"Shear strength of concrete members without transverse reinforcement: A mechanical approach to consistently account for size and strain effects"**, Engineering structures, Vol. 99, pp. 360-372, UK, 2015.

[173] Zheng H., Abel A. A., **"Fatigue Properties of Reinforcing Steel Produced by TEMPCORE Process"**, Journal of Materials in Civil Engineering, Vol. 11, No 2, pp. 158-165, USA, 1999.

[174] Cedolin L., Dei Poli S., Iori I., **"Analisi sperimentale del processo di formazione della frattura nel calcestruzzo"**, Studi E Ricerche, Politecnico di Milano, 3, pp. 47-74, Milan, Italy, Italian, 1981.

[175] Cedolin L., Dei Poli S., Iori I., **"Comportamento a trazione del calcestruzzo"**, Studi E Ricerche, Politecnico di Milano, 5, pp. 23-46, Milan, Italy, Italian, 1983.

[176] Debernardi P. G., Taliano M., **"An improvement to Eurocode 2 and fib Model Code 2010 methods for calculating crack width in RC structures"**, Structural Concrete, Vol. 17, No 3, pp. 365-376, 2016.

[177] Lemcherreq Y., Haefliger S., Kaufmann W., **"Discontinuous yielding in bare and embedded reinforcing bars: Implications on the determination of steel and bond shear stresses from strain measurements"**, Engineering Structures, Vol. 278, 20 p., 2023.

References for Chapter 6

[178] Vintzeleou E., Tassios T.P., **"Mathematical models for dowel action under monotonic and cyclic conditions"**, Magazine of Concrete Research, Vol. 38, No 134, pp. 13-22, 1986.

[179] Marcus H., **"Load Carrying Capacity of Dowels at Transverse Pavement Joints"**, ACI Structural Journal, Vol. 48, No.10, pp. 169-184, 1951.

[180] Krefeld W., Thurston C. W., **"Studies of the shear and diagonal tension strength of simply supported reinforced concrete beams"**, ACI Journal, Vol. 63, No 4, pp. 451-476, 1966.

[181] Taylor H. P. J., **"Investigation of the Dowel Shear Forces Carried by the Tensile Steel in Reinforced Concrete Beams"**, Cement and Concrete Association, Report No. TRA 431, 24 p., London, UK, 1969.

[182] Baumann T., Rüsch H., **"Schubversuche mit indirekter Krafteinleitung: Versuche zum Studium der Verdübelungswirkung der Biegezugbewehrung eines Stahlbetonbalkens"**, Deutscher Ausschuss für Stahlbeton, Heft 210, 83 p., Berlin, Germany, German, 1970.

[183] Dei Poli S., di Prisco M., Gambarova P., **"Cover and Stirrup Effects on the Shear Response of Dowel Bar Embedded in Concrete"**, ACI Structural Journal, Vol. 90, No. 4, pp. 441-450, Farmington Hills, USA, 1993.

[184] Autrup F., Joergensen H. B., Hoang L. C., **"Dowel action of the tensile reinforcement in RC beams without shear reinforcement: Novel experimental investigation and mechanical modelling"**, Engineering Structures, Vol. 279, 115471, pp. 13, 2023.

[185] Rasmussen B. H., **"Strength of transversely loaded bolts and dowels cast into concrete"**, Laboratoriet for Bugningastatik, Denmark Technical University, Meddelelse, Vol. 34, No 2, pp. 39-55, Danish, 1962.

[186] Soroushian P., Obaseki K., Rojas M., Sim Jongsung, **"Analysis of Dowel Bars Acting Against Concrete Core"**, ACI Structural Journal, Vol. 83, No 4, pp. 642-649, 1986.

[187] Dulacska H., **"Dowel Action of Reinforcement Crossing Cracks in Concrete"**, ACI Structural Journal, Vol. 69, No 12, pp. 754-757, 1972.

[188] Sorensen J. H., Hoang L. C., Olesen J. F., Fischer G., **"Testing and modeling dowel and catenary action in rebars crossing shear joints in RC"**, Engineering Structures, Vol. 145, pp. 234–245, 2017.

[189] Dei Poli S., di Prisco M., Gambarova P., **"In tema di trasmissione del taglio negli elementi di calcestruzzo armato. Alcuni risultati sperimentali attinenti alla cosidetta azione di spinotto"**, Studi e ricerche, 303 p., Italian, 1987.

[190] Dei Poli S., di Prisco M., Gambarova P., **"Shear Response, Deformations, and Subgrade Stiffness of a Dowel Bar Embedded in Concrete"**, ACI Structural Journal, Vol. 89, No.6, pp. 665-675, Detroit, USA, 1992.

[191] Hofbeck J. A., Ibrahim I. O., Mattock A. H., **"Shear Transfer in Reinforced Concrete"**, ACI Journal Proceedings, Vol. 66, No 2, pp. 119-128, 1969.

[192] Tanaka Y., Murakoshi J., **"Reexamination of dowel behavior of steel bars embedded in concrete"**, ACI Journal, Vol. 108, No 6, pp. 659–668, 2011.

[193] Pruijessers A. F., **"Aggregate Interlock and Dowel Action Under Monotonic and Cyclic Loading"**, PhD thesis, Delft University, Netherland, 165 p., 1988.

[194] Nørringgaard P., **"Dowel Action in Rebars Embedded in Concrete"**, Master Thesis, 112 p., 2015.

[195] Vintzeleou E., Tassios T.P., **"Behavior of Dowels Under Cyclic Deformations"**, ACI Structural Journal, Vol. 84, No 1, pp. 18-30, 1987.

[196] Cziesielski E., Friedmann M., **"Tragfähigkeit geschweißter Verbindungen im Betonfertigteilbau"**, Ernst & Sohn, DAfStb-Heft 346, 149 p., Berlin, German, 1983.

[197] Vintzeleou E., **"Mechanisms of Load Transfer along Reinforced Concrete Interfaces under Monotonic and Cyclic Actions"**, PhD Thesis, 549 p., National Technical University of Athens, 1984.

[198] Maekawa K., Qureshi J., **"Embedded bar behavior in concrete under combined axial pullout and transverse displacement"**, J. Materials, Conc. Struct., Pavements, 30, pp. 183-195, 1996.

[199] Maekawa K., Qureshi J., **"Computational Model for Reinforcing Bar Embedded in Concrete Under Combined Axial Pullout and Transverse Displacement"**, Journal of JSCE: Materials, Concrete Structures and Pavements, Vol. 31, No 538, pp. 227-239, 1996.

[200] Sharma N. K., **"Splitting Failures in Reinforced Concrete Members"**, PhD Thesis, 424 p., Ithaca, N.Y., USA: Cornell University, 1969.

[201] Kemp E. L., Wilhelm J., **"An Investigation of the Parameters Influencing Bond Behaviour with a View Towards Establishing Design Criteria"**, Department of Civil Engineering, West Virginia University, Report WVDOH 46-2, 244 p., West Virginia, 1977.

[202] Takase Y., **"Testing and modeling of dowel action for a post-installed anchor subjected to combined shear force and tensile force"**, Engineering Structures, Vol. 195, pp. 551–558, 2019.

[203] Soroushian P., Obaseki K., Rojas M., **"Bearing Strength and Stiffness of Concrete Under Reinforcing Bars"**, ACI Structural Journal, Vol. 84, No.3, pp. 179-184, 1987.

[204] Pejatovic M., Muttoni A., **"Experimental investigation of dowel action in reinforcing bars using refined measurements"**, Structural Concrete, 2024.

[205] Nonis C., Niezrecki C., Yu T.-Y., Ahmed S., Su C.-F., **"Structural health monitoring of bridges using digital image correlation"**, Proceedings of SPIE 8695: Health Monitoring of Structural and Biological Systems, Vol. 8695 869507-1, pp. 1-13, San Diego (California), 2013.

[206] Tirassa M., Fernández Ruiz M., Muttoni A., **"An interlocking approach for the rebar-to-concrete contact in bond"**, Magazine of Concrete Research, Vol. 73, No 8, pp. 379-393, 2021.

[207] Correlated Solutions, **"Vic-3D 7 Reference Manual"**, 108 p., 2010.

[208] Luna Technologies Inc., **"Optical Backscatter Reflectometer 4600 User Guide"**, 227 p., Blacksburg, VA, 2013.

[209] Brault A., Hoult N. A., **"Distributed Reinforcement Strains: Measurement and Application"**, ACI Structural Journal, Vol. 116, No. 4, pp. 115-127, 2019.

[210] Bado M. F., Casas J.-R., **"A Review of Recent Distributed Optical Fiber Sensors Applications for Civil Engineering Structural Health Monitoring"**, Sensors, Vol. 21, No 5, pp. 1-83, 2021.

References for Chapter 7

[211] FIB, **"Structural connections for precast concrete buildings, fib bulletin No. 43"**, 370 p., 2008.

[212] Eleiott A. F., **"An experimental investigation of shear transfer across cracks in reinforced concrete."**, M.S. Thesis, Cornell University, Ithaca, 1974.

[213] Stanton J. F., **"An investigation of dowel action of the reinforcement of nuclear containment vessels and their nonlinear dynamic response to earthquake loads"**, 1977.

[214] Jimenez R., White R. N., Gergely P., **"Bond and Dowel Capacities of Reinforced Concrete"**, Vol. 76, No.1, pp. 73-92, 1979.

[215] Soltani M., Maekawa K., **"Path-dependent mechanical model for deformed reinforcing bars at RC interface under coupled cyclic shear and pullout tension"**, Engineering Structures, Vol. 30, pp. 1079–1091, 2008.

[216] Kato B., Akiyama H., Yamanoushi Y., **"Predictable properties of materials under incremental cyclic loading"**, International Association for Bridge and Structural Engineering, Reports of the Working Commissions, Symposium on resistance and ultimate deformability of structures acted on by well-defined repeated loads, Vol. 13, pp. 119-124, 1973.

[217] Li P., Tan N., Wang C., **"Nonlinear Bond Model for the Dowel Action considering the Fatigue Damage Effect"**, Hindawi - Advances in Materials Science and Engineering, 11 p., 2018.

[218] Winkler E., **"Die Lehre von der Elastizitat und Festigkeit"**, Dominicus, 411 p., Prague, Czech Republic, German, 1867.

[219] Zimmermann H., **"Die Berechnung des Eisenbahnoberbaues"**, 308 p., Berlin, Germany, German, 1888.

[220] Timoshenko S., Lessells J. M., **"Applied Elasticity"**, Westinghouse Technical Night School Press, 1925.

[221] Friberg B. F., **"Design of dowels in transverse joints of concrete pavement"**, American Society of Civil Engineers, Vol. 64, No 9, pp. 1809-1828, 1938.

[222] Brenna A., Dei Poli S., di Prisco M., **"Dowel action: some experimental and theoretical results regarding special concrete"**, Studi e Ricerche, School for the design of R/C structures, Milan University of Technology, pp. 321-380, Italian, 1990.

[223] Figueira D., Sousa C., **"Winkler spring behavior in FE analyses of dowel action in statically loaded RC cracks "**, Computers and Concrete, Vol. 21, pp. 593-605, Portugal, 2018.

[224] Moccia F., Kubski X., Fernández Ruiz M., Muttoni A., **"The influence of casting position and disturbance induced by reinforcement on the structural concrete strength "**, Structural Concrete, 1, 28 p., 2020.

[225] Monney F., Fernández Ruiz M., Muttoni A., **"Design against splitting failures in reinforced concrete due to concentrated forces and minimum bend diameter of reinforcement"**, Engineering Structures, Vol. 245, 112902, 23 p., 2021.

[226] Boussinesq V.J., **"Équilibre d'élasticité d'un sol isotrope sans pesanteur, supportant différent poids"**, Comptes Rendus, Vol. 86, pp. 1260-1263, Paris, France, 1878.

References for the Appendices

[227] Sorkine-Hornung O., Rabinovich M., **"Least-squares rigid motion using svd"**, Department of Computer Science, ETH Zurich, 5 p., 2017.

Projektabschluss

Formular 3 ARAMIS SBT als PDF (Das Formular einscannen, dann das PDF öffnen und dann mit dem Schnappschuss-Werkzeug (Fotoapparat) die Seiten markieren und dann hier einfügen).

Schweizerische Eidgenossenschaft
Confédération suisse
Confederazione Svizzera
Confederaziun svizra

Département fédéral de l'environnement, des transports, de l'énergie et de la communication DETEC
Office fédéral des routes OFROU

RECHERCHE DANS LE DOMAINE ROUTIER DU DETEC

Version du 09.10.2013

Formulaire N° 3 : Clôture du projet

établi / modifié le : 4.6.2025

Données de base

Projet N° :	AGB 2019/017
Titre du projet :	Contribution to the assessment of the safety and fatigue of concrete structures based on advanced in-situ measurements
Echéance effective :	4.12.2025

Textes :

Résumé des résultats du projet :

Regarding the use of DIC in existing structures, the limits of applicability of this technique have been studied through systematic tests and complementary techniques are proposed to overcome some of its limitations. The effect of known factors affecting the precision of 3D DIC measurements has been quantified. The effect of lighting was evaluated. It was concluded that the algorithms included in most commercial DIC measurement systems can satisfactorily minimize the effect of the overall variation in lighting. However, non-uniform lighting conditions on the measurement surface can lead to different measurement accuracies in the studied region. The effect of vibrations of the measurement system was quantified. The results show that the measurement accuracy is lower than in laboratory conditions but satisfactory to measure relative displacements in the studied region. Its application to measure absolute displacements is highly dependent on the required accuracy and site-specific conditions. These results were tested in the Chillon Viaduct where the DIC system was able to capture crack displacements of ±15 µm (0.015 mm) under the passage of heavy trucks.
Regarding the techniques to overcome current DIC limitations, two techniques have been tested and validated, showing an improvement in measurement accuracy and resolution with respect to conventional measurement techniques. The first technique to characterize the existing crack is based on processing the pixels of a standard digital image and provides a measurement accuracy of ±2 pixels. The second technique for long-term measurements is based on marker detection and results in measurement accuracies of ±1/20 to ±1/150 of a pixel.
Regarding the enhancement of relationship between the crack opening in the direction of the bar and the longitudinal stresses generated in the bar, an experimental program and a revision of the mechanical models were conducted. The experimental program includes pull-out tests, tension tests and beam tests. The experimental results show bond stresses that differ considerably with the typically assumed values in the mechanical models. A new model to estimate the bond stresses is proposed. The use of the mechanical model with the measured crack spacings and the proposed bond model improves the steel stress estimation with respect to current code formulations, particularly for small crack widths.
To better understand the relationship between the crack kinematic component perpendicular to the bar and the resulting longitudinal stresses in the bar, both experimental and analytical research were conducted. The experimental work includes two test series to investigate the behavior: 1) of a reinforcing bar under dowel action subjected to monotonic or low-level cyclic loading with both longitudinal and transverse crack openings, 2) of concrete beneath the reinforcing bar under point loads applied at various positions through the bar.
This experimental work led to the following results.
Measurements of displacements using optical fibres glued in surface grooves on the concrete showed a strong dependency on test variables: bar diameter, crack kinematics, and bar-to-crack angle. Larger dowel resistance was observed with larger bar diameters and larger bar-to-crack angles. First-order dowel resistance involved concrete crushing near the crack and bar yielding due to bending. Additional resistance was mobilized through catenary action with significant transverse displacements. Optical fibre data revealed peak bending stresses about 1.5 bar diameters from the crack. Concrete stiffness began degrading significantly at 40–60% of the first-order dowel resistance.
And regarding the behaviour of concrete beneath the reinforcing bar under point loads, an increase in both peak force and initial stiffness was observed when the load was applied farther from the concrete edge, due to a larger concrete area carrying the force. The tests were found to reproduce results comparable to dowel tests when the load was applied at a position 0.9 times the bar diameter from the edge. This corresponds approximately to the location of the resultant pressure distribution observed in the dowel tests.
In the analytical research on dowel action, a new formulation for the bearing stiffness of concrete beneath the reinforcing bar is proposed for use in Winkler's model (beam on elastic foundation). It accounts for factors such as the angle between the crack and the bar, bar diameter, concrete strength, casting conditions, concrete cover thickness, load cycles, and secondary cracks near ribs due to axial force. Good casting conditions yielded roughly twice the stiffness compared to poor casting conditions. Stiffness increases with concrete cover, reaching the peak value at a cover-to-bar diameter ratio of about 3. As transverse displacement increases, stiffness decreases due to splitting cracks, crushing, and spalling near the crack. This reduction is captured by an empirical expression calibrated using optical fibre data. The improved model accurately predicts shear force–transverse displacement in monotonic tests and peak longitudinal stress in both monotonic and cyclic tests.
Regarding the ultimate limit state, Rasmussen's model based on limit analysis is used to evaluate dowel resistance for a 90° angle between the bar and the crack, considering various confinement factors. For angles smaller than 90°, Dulacska's model is applied. Both models show good agreement with the experimental results.

Schweizerische Eidgenossenschaft
Confédération suisse
Confederazione Svizzera
Confederaziun svizra

Département fédéral de l'environnement, des transports, de l'énergie et de la communication DETEC
Office fédéral des routes OFROU

Atteinte des objectifs :

The research objectives were attained. The possibilities and limits of applicability of DIC measurements on existing structures have been clearly studied and established. Two techniques are proposed to overcome two limitations inherently related to the principles of DIC measurements. Clear recommendations for its applicability are provided. Furthermore, an example of application of these techniques to characterize the response of a crack in an existing bridge is provided, showing high accuracy results.
The relationships between the crack opening in the directions parallel and perpendicular to the bar and the longitudinal stresses generated in the bar have been thoroughly investigated. The main influencing parameters have been identified and new formulations to estimate these parameters have been proposed and validated against experimental results. The resulting models improve the estimations of the stresses in the reinforcement compared with alternative formulations from the literature. Most of the results have been already published in international scientific journals. Considering the complexity of these mechanism, the research objectives have been attained as an improvement of current formulations has been achieved. However, it must be noted that the uncertainty of these estimations remains considerable and further research is required to improve and validate these models for its application on the field.

Déductions et recommandations :

This research has shown the potential of state-of-the-art measurement techniques for understanding existing structures and to obtain highly detailed experimental data from complex mechanisms. However, the studied mechanisms that determine the relationship between the crack displacements and the bar stresses are complex and are affected by a large number of influencing factors. The amount of available experimental data is limited, and further experimental works are required to validate some of the proposed factors. Particularly, in the case of the bond stresses around reinforcing bars, the effect of cyclic loading is critical and needs further validation. Regarding dowel action, several questions about its mechanism and modelling for fatigue and ultimate limit states remain open. This is mostly due to the limited experimental data available and the complexity of the local behaviour, which is influenced by multiple factors. For this reason, additional experimental research is required to thoroughly study the influence of factors such as secondary cracks resulting from axial forces in ribbed bars on the bearing stiffness of concrete, the effect of cyclic loading on bearing stiffness, the impact of casting conditions, and the role of concrete cover on bearing stiffness.

Publications :

[1] Vincens B., Corres E., Muttoni A., "Image-based techniques for initial and long-term characterization of crack kinematics in reinforced concrete structures", Engineering Structures, Volume 317, 2024
[2] Corres E., Muttoni A., "Bond of steel reinforcement based on detailed measurements: Results and interpretations", Structural Concrete, Volume 24, Issue 6, p. 7173-7204, 2023.
[3] Corres E., Muttoni A., "Local bond-slip model based on mechanical considerations", Engineering Structures, Volume 314, 2024.
[4] Corres E., Muttoni A., "Estimation of the bar stress based on crack width measurements in reinforced concrete structures", Structural Concrete, Volume 25, Issue 6, p. 4454-4479, 2024.
[5] Pejatović M., Muttoni A., "Experimental investigation of dowel action in reinforcing bars using refined measurements", Structural Concrete, Volume 25, Issue 4, p. 2732–2758, 2024.
[6] Pejatović M., Muttoni A., "Steel stresses and shear forces in reinforcing bars due to dowel action", Structural Concrete, Volume 25, Issue 6, p. 4956–4974, 2024.

Chef/cheffe de projet :

Nom : Muttoni Prénom : Aurelio

Service, entreprise, institut : IBETON, EPFL-ENAC-IIC

Signature du chef/de la cheffe de projet :

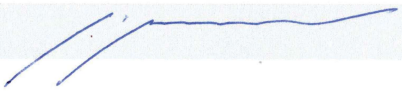

Schweizerische Eidgenossenschaft
Confédération suisse
Confederazione Svizzera
Confederaziun svizra

Département fédéral de l'environnement, des transports, de l'énergie et de la communication DETEC
Office fédéral des routes OFROU

RECHERCHE DANS LE DOMAINE ROUTIER DU DETEC

Formulaire N° 3 : Clôture du projet

Appréciation de la commission de suivi :

Evaluation :

Les différents objectifs de la recherche ont été atteints et la commission relève la qualité de cette dernière. Elle salue notamment la méthodologie mise en oeuvre, tant au niveau des campagnes d'essais effectuées que des études et des développements théoriques.
Concernant l'utilisation de la DIC dans le contexte de l'évaluation de structures existantes, son potentiel ainsi que ses limites sont bien cernés et clairement décrits, et des techniques destinées à surmonter certaines de ces limites ont fait l'objet de tests et de validations.
Les études des relations entre l'ouverture de fissures et les contraintes dans la barre d'armature, étayées par des campagnes d'essais, débouchent sur des améliorations sensibles de la compréhension des mécanismes qui se mettent en oeuvre, sur une meilleure identification et estimation des paramètres ies influençant ainsi que sur une amélioration des modèles théoriques existants.
L'important apport de la recherche dans le domaine de la compréhension, description et modélisation de l'influence de 'l'effet goujon' est également salué par la commission.

Mise en oeuvre :

Basé sur les conclusions de la recherche, le potentiel de l'utilisation de la DIC dans le cadre de l'évaluation de structures existantes s'inscrit comme une voie prometteuse dans la pratique.
Complétés par les conclusions de futures recherches complémentaires, identifiées dans le projet, les résultats de la présente recherche en matière d'évaluation de contraintes dans la barre d'armature et dans le béton pourront être intégrés dans le domaine normatif et seront très utiles dans la pratique de l'ingénieur.

Besoin supplémentaire en matière de recherche :

Les besoins en matière de recherche future sont identifiés et décrits en conclusion de la recherche.
Ils concernent notamment la validation de certains facteurs influençant les déplacements lors de la fissuration du béton et les contraintes afférentes dans la barre d'armature, les effets de chargements cycliques ou encore l'influence de fissures secondaires.

Influence sur les normes :

Les résultats de la présente recherche, complétés par ceux de future recherche, serviront à l'élaboration, dans le cadre normatif, de compléments et/ou d'actualisations de dispositions existantes.

Président/Présidente de la commission de suivi :

Nom : Putallaz Prénom : Jean-Christophe

Service, entreprise, institut : Ingénieur EPFZ / SIA, Sion

Signature du président/ de la présidente de la commission de suivi :